

Electronic Thesis and Dissertation Repository

4-23-2014 12:00 AM

Computational Techniques to Predict Orthopaedic Implant Alignment and Fit in Bone

Seyed Kamaledin Mostafavi Yazdi, *The University of Western Ontario*

Supervisor: Dr. Remus Tutunea-Fatan, *The University of Western Ontario*

Joint Supervisor: Dr. James Johnson, *The University of Western Ontario*

A thesis submitted in partial fulfillment of the requirements for the Doctor of Philosophy degree in Mechanical and Materials Engineering

© Seyed Kamaledin Mostafavi Yazdi 2014

Follow this and additional works at: <https://ir.lib.uwo.ca/etd>



Part of the [Biomechanics and Biotransport Commons](#)

Recommended Citation

Mostafavi Yazdi, Seyed Kamaledin, "Computational Techniques to Predict Orthopaedic Implant Alignment and Fit in Bone" (2014). *Electronic Thesis and Dissertation Repository*. 1998.
<https://ir.lib.uwo.ca/etd/1998>

This Dissertation/Thesis is brought to you for free and open access by Scholarship@Western. It has been accepted for inclusion in Electronic Thesis and Dissertation Repository by an authorized administrator of Scholarship@Western. For more information, please contact wlsadmin@uwo.ca.

COMPUTATIONAL TECHNIQUES TO PREDICT ORTHOPAEDIC IMPLANT
ALIGNMENT AND FIT IN BONE

(Thesis format: Integrated)

by

Seyed Kamaledin Mostafavi Yazdi

Graduate Program in Mechanical and Materials Engineering

A thesis submitted in partial fulfillment
of the requirements for the degree of
Doctor of Philosophy

The School of Graduate and Postdoctoral Studies
The University of Western Ontario
London, Ontario, Canada

© Seyed Kamaledin Mostafavi Yazdi 2014

Abstract

Among the broad palette of surgical techniques employed in the current orthopaedic practice, joint replacement represents one of the most difficult and costliest surgical procedures. While numerous recent advances suggest that computer assistance can dramatically improve the precision and long term outcomes of joint arthroplasty even in the hands of experienced surgeons, many of the joint replacement protocols continue to rely almost exclusively on an empirical basis that often entail a succession of trial and error maneuvers that can only be performed intraoperatively. Although the surgeon is generally unable to accurately and reliably predict *a priori* what the final malalignment will be or even what implant size should be used for a certain patient, the overarching goal of all arthroplastic procedures is to ensure that an appropriate match exists between the native and prosthetic axes of the articulation.

To address this relative lack of knowledge, the main objective of this thesis was to develop a comprehensive library of numerical techniques capable to: 1) accurately reconstruct the outer and inner geometry of the bone to be implanted; 2) determine the location of the native articular axis to be replicated by the implant; 3) assess the insertability of a certain implant within the endosteal canal of the bone to be implanted; 4) propose customized implant geometries capable to ensure minimal malalignments between native and prosthetic axes. The accuracy of the developed algorithms was validated through comparisons performed against conventional methods involving either contact-acquired data or navigated implantation approaches, while various customized implant designs proposed were tested with an original numerical implantation method.

It is anticipated that the proposed computer-based approaches will eliminate or at least diminish the need for undesirable trial and error implantation procedures in a sense that present error-prone intraoperative implant insertion decisions will be at least augmented if not even replaced by optimal computer-based solutions to offer reliable virtual “previews” of the future surgical procedure. While the entire thesis is focused on the elbow as the most challenging joint replacement surgery, many of the developed approaches are equally applicable to other upper or lower limb articulations.

Keywords

Computer-assisted surgery; total elbow arthroplasty; flexion-extension axis; implant malalignment; humerus; computed tomography; insertion trajectory; implant design; numerical optimization

Co-Authorship Statements

- Chapter 1: Kamal Mostafavi - sole author.
- Chapter 2: Kamal Mostafavi - study design, analysis, wrote manuscript; Evgueni Bordatchev – data collection, reviewed manuscript; James Johnson – study design, reviewed manuscript; Remus Tutunea-Fatan – study design, reviewed manuscript.
- Chapter 3: Kamal Mostafavi - study design, analysis, wrote manuscript; Emily Lalone – data collection, reviewed manuscript; Graham King - study design, reviewed manuscript; James Johnson – study design, reviewed manuscript; Remus Tutunea-Fatan- study design, reviewed manuscript.
- Chapter 4: Kamal Mostafavi - study design, analysis, wrote manuscript; James Johnson – study design, reviewed manuscript; Remus Tutunea-Fatan – study design, reviewed manuscript.
- Chapter 5: Kamal Mostafavi - study design, analysis, wrote manuscript; James Johnson – study design, reviewed manuscript; Remus Tutunea-Fatan- study design, reviewed manuscript.
- Chapter 6: Kamal Mostafavi - sole author.

Acknowledgments

I would first and foremost like to thank my supervisors Dr. Remus Tutunea-Fatan and Dr. James Johnson. During my Ph.D they have always supported and encouraged me to progress in my research. I would also like to thank them for dedicating their time for having individual weekly meetings, their great comments and contribution in my research and toward progressing my thesis. They always provided invaluable feedback in every single step of my work and helped me in various ways to solve the issues I faced during this research.

I would like to further thank Dr. Tutunea-Fatan for his great contribution during my research, for his time that spent every single day from the beginning of my research and being a wonderful supervisor all the time supporting me.

I would also like to thank Emily Lalone for her great support in providing information and data on specimens all the time and also helping me in understanding this information and answering my questions. Thank you to Colin McDonald for his great feedbacks and support through the experimental setup and corresponding information.

At the end I would like to thank my lovely wife, Fatemeh, for always being there for me and providing love, support and guidance and helping me a lot during my Ph.D. Thank you to my mom and dad who dedicated their lives to their children. You are my inspiration and my mentors.

Table of Contents

Abstract.....	ii
Co-Authorship Statements.....	iv
Acknowledgments.....	v
Table of Contents.....	vi
List of Tables.....	x
List of Figures.....	xi
Chapter 1.....	1
1 Introduction.....	1
1.1 Overview.....	1
1.2 Joints and Implants.....	1
1.3 Elbow.....	2
1.3.1 Anatomy and Biomechanics.....	2
1.3.2 Motion and kinematics.....	7
1.3.3 Disorders.....	9
1.4 Medical Imaging.....	10
1.4.1 Radiographs.....	10
1.4.2 Computed Tomography.....	12
1.4.3 Digital Imaging and Communication in Medicine (DICOM).....	12
1.4.4 Edge Detection Methods.....	15
1.5 Total Elbow Arthroplasty.....	19
1.5.1 Surgical Techniques.....	21
1.5.2 Implant Types.....	21
1.5.3 Complications.....	23
1.6 Component Alignment and Collision Detection.....	24

1.7 Thesis Rationale.....	27
1.7.1 Motivation.....	27
1.7.2 Objectives and Hypothesis.....	28
1.7.3 Contributions.....	29
1.7.4 Outline.....	30
1.8 References.....	32
Chapter 2.....	38
2 B-Spline-Based Representations of Humeral Bone.....	38
2.1 Overview.....	38
2.2 Introduction.....	38
2.3 Segmentation of Bone Contours.....	42
2.4 Planar B-Spline Fitting Through Deformable Control Polygon Technique.....	49
2.4.1 Closed B-Spline Formulation.....	50
2.4.2 Determination of the Control Polygon.....	53
2.4.3 Robustness of the Proposed Approach.....	58
2.5 Accuracy of the Proposed Bone Reconstruction Technique.....	64
2.5.1 Pair-wise Registration of Point Datasets.....	65
2.5.2 Comparison with Contact-Acquired Data.....	67
2.6 Conclusion.....	77
2.7 References.....	79
Chapter 3.....	82
3 Determination of Elbow Flexion-Extension Axis Based on Planar and Closed B-Splines.....	82
3.1 Overview.....	82
3.2 Introduction.....	82
3.3 B-spline Based Determination of Flexion- Extension axis.....	87

3.3.1	Detection of Outer Cortical Bone Contours.....	87
3.3.2	Planar and Closed B-Spline Fitting by Control Polygon Deformation.....	89
3.3.3	Automated Detection of Relevant Features through Local Curvature Analysis.....	96
3.4	Conventional Voxel-based Determination of FE axis	99
3.5	Results and discussion	100
3.6	Conclusions.....	104
3.7	References.....	104
Chapter 4	107
4	Assessment of the insertability of a certain implant within the endosteal canal of the bone	107
4.1	Overview.....	107
4.2	Introduction.....	107
4.3	Genetic Algorithm Based Search on the feasibility of the Implant Insertion	114
4.3.1	Materials	114
4.3.2	Elbow Implants	116
4.3.3	Bone Geometry Reconstruction.....	119
4.3.4	Genetic Algorithm	123
4.3.5	Experimental Setup.....	133
4.4	Result	133
4.5	Discussion.....	149
4.6	References.....	151
Chapter 5	153
5	On the Design of Customized Implant Geometries	153
5.1	Overview.....	153
5.2	Introduction.....	153
5.3	Optimization Techniques on Elbow Implant Shape	158

5.3.1	Stem-Focused Optimization.....	160
5.3.2	Spool-Focused Optimization	164
5.3.3	Overall Implant Optimization.....	167
5.3.4	Customized Implant Design.....	172
5.4	Result	176
5.5	References.....	186
Chapter 6.....		188
6	Conclusion	188
6.1	Overview.....	188
6.2	Limitations	192
6.3	Future Direction	194
6.4	References.....	196
Curriculum Vitae		197

List of Tables

Table 2.1: The comparison of the proposed B-Spline method against uniform, chordal and centripetal methods	62
Table 3.1: Quantitative comparisons between B-Spline and voxel-based methods	102
Table 5.1: Summary of the best three implant designs with minimum malalignment developed by the stem-focused optimization method.....	177
Table 5.2: Summary of the best three implant designs with minimum malalignment developed by the spool-focused optimization method.....	177
Table 5.3: Summary of the best three implant designs with minimum malalignment developed by the overall implant optimization method.....	178
Table 5.4: Summary of the best three implant designs with minimum malalignment developed by the customized implant design method.	178

List of Figures

Figure 1.1: Elbow anatomy: (a) anterior view of right arm, showing the three elbow bones: humerus, radius and ulna, and (b) the three joints of elbow: radiohumeral, humeroulnar and radioulnar joints.	4
Figure 1.2: Anterior view of the distal humerus.	6
Figure 1.3: Motion of the elbow: (a) flexion-extension movement, and (b) supination-pronation movement.	8
Figure 1.4: X-ray of a total elbow arthroplasty.....	11
Figure 1.5: (a) 3D representation of distal humerus acquired by CT scanner, and (b) the distal humerus cross section in transverse, sagittal and coronal planes.	14
Figure 1.6: Comparison of different edge detection techniques; (a) original sample image, adapted from [http://en.wikipedia.org/wiki/Statue_of_Liberty], (b) Prewitt, (c) Canny, (d) Sobel, (e) Roberts, and (f) LOG methods.	18
Figure 1.7: (a) Anatomical features of the native elbow joint, and (b) elbow joint after total elbow arthroplasty with prosthetic components.	20
Figure 2.1: Segmentation of the bone contours: a) overall positioning of the analyzed axial CT slice, b) raw DICOM image of the axial slice, c) thresholded outer and inner bone contours, and d) detailed bone contour data points.....	44
Figure 2.2: 2D pixel intensity mapping in CT slices.	46
Figure 2.3: Bone contours extracted through the proposed approach from representative: a) middle, and b) extreme distal cross sections of the humerus.....	47
Figure 2.4: Comparison of the proposed segmentation (blue and green contours) against conventional edge detection methods: a) Canny, b) Prewitt, c) Laplacian of Gaussian, d) Roberts, and e) Sobel.	48

Figure 2.5: Parametric formulation of a closed B-Spline.	51
Figure 2.6: Control polygon deformation through global modification.	56
Figure 2.7: Control polygon deformation through local modification.	58
Figure 2.8: Closed B-Spline fitting through control polygon deformation: a) to ..) global modification; ...) to h) local modification.	59
Figure 2.9: Local behavior of closed B-Spline approximants: a) outer, and b) inner bone contours.	60
Figure 2.10: Graphical comparison between the tested closed B-Spline fitting methods.	63
Figure 2.11: Pair-wise registration of two correlated point datasets.	66
Figure 2.12: Separation of humeral fragment of interest: a) approximate location of detached humeral segment within the overall distal humerus, and b) detail view of the reduced humeral specimen.	69
Figure 2.13: Typical cross sections through reduced humeral specimen as obtained in principal CT planes.	70
Figure 2.14: Contact data acquisition setup: a) overview of Kugler CNC measurement system, and b) kinematics of the measurement process.	72
Figure 2.15: Comparison between contact-acquired data and proposed bone reconstruction method: a) CMM point dataset, b) B-Spline fitting technique, and c) overlay of the two datasets.	74
Figure 2.16: Deviation between reconstructed geometry and contact-acquired data: a) sample of relative positioning between CMM points and parametric curves; and b) variation of the deviation around outer contour circumference.	76
Figure 3.1: Anatomical position and orientation of the flexion-extension axis: (a) medial, (b) anterior, and (c) lateral views of the distal humerus.	84

Figure 3.2: Representative axial cross sections through distal humerus: (a) raw CT slices, and (b) parametric curve-approximated outer bone contours.....	88
Figure 3.3: Progressive adaptation of the fitted B-Spline curve shape: (a) initial set of segmented CT points, (b) approximating curve after one global modification iteration (one Step 2), (c) approximating curve at the end of the global modification phase (end of Step2), and (d) final shape of the approximating curve (end of Step 3).	95
Figure 3.4: Sample of local curvature pattern along distal humeral B-Splines.	96
Figure 3.5: Determination of the geometric characteristics of FE axis through least squares fitting.....	98
Figure 3.6: Qualitative comparisons between the resulting point datasets obtained through B-Spline (green) and conventional (blue) approaches achieved through: (a)-(d) combined fitted features and bone overlay, (e)-(h) direct result overlay.....	102
Figure 4.1: : Latitude implant configurations: (a) unlinked, and (b) linked versions.....	115
Figure 4.2: Implant Components: (a) small, medium, large and X-large spool sizes, (b) anterior, centered and posterior offset spools, (c) different stem locations based on offset spools, and (d) small, medium and large stem sizes.	117
Figure 4.3: 3D representations of the humeral implant and the distal humerus: (a) Latitude humeral portion components containing humeral implant, spool and screw, and (b) anterior view of the distal humerus.	118
Figure 4.4: Relative position of Latitude humeral implant in: (a) medial-lateral (ML) view (b) anterior-posterior (AP) view of the distal humerus, and (c) 3D model of implant position in medullary canal of the humerus.....	120
Figure 4.5: (a) Implant penetration into the humerus due to improper fitting, and (b) 3D model of implant penetration, showing interference areas in red.....	121
Figure 4.6: Reconstruction of the distal humerus geometry: (a) DICOM images of the humerus acquired from CT scan, (b) generated inside and outside contours from DICOM	

images using developed control polygon technique, and (c) full 3D model of the humerus from contours.	122
Figure 4.7: Reconstructed bone model: (a) control polygon form and (b) selection of three critical cross sections as the GA input.	125
Figure 4.8: Selection of two distal and proximal ends of humeral implant stem as the GA input.	126
Figure 4.9: Genetic algorithm iteration in generating populations and selecting proper.....	127
Figure 4.10: Bone and implant coordinate systems: (a) three critical bone cross sections in local Bone Coordinate System (BCS) and implant position in local Implant Coordinate System (ICS). BCS is located in centroid of bone bottom cross section while ICS is at the implant capitellum center, and (b) Implant position in BCS. In order to position the implant in initial position for GA technique, the centroid of implant bottom cross section should match the centroid of bone top cross section.	128
Figure 4.11: Implant Coordinate System (ICS) orientation with respect of Bone Coordinate System (BCS) over: (a) θ rotation about X_{BCS} axis, (b) ω rotation about Y_{BCS} axis, and (c) ϕ rotation about Z_{BCS} axis.	129
Figure 4.12: Geometric interpretation of implantation malalignment: (a) 3D view of implant position in bone cavity showing the translation error d_{CC} , (b) anterior-Posterior view of implant insertion showing varus-varus angulation error α_{VV} , (c) medial-lateral view of implant insertion showing flexion-extension angle α_{FE} and (d) distal-proximal view of implant insertion showing internal-external angulation error α_{IE}	132
Figure 4.13: Implant insertion procedure using GA technique: (a) 3D view of the humeral implant from initial to final position, and (b) intermediate steps of implant insertion.	135
Figure 4.14: Schematic presentation of GA algorithm.	136
Figure 4.15: Validation of the developed method results in comparison with experimental setup results: (a) implant alignment error in translation (mean + 1 standard deviation) for both developed method and experimental setup. Translational malalignment was reported in	

three directional components of medial-lateral (MED) error, anterior-posterior (ANT) error and proximal-distal (PROX) error while Total represents square root of error components, and (b) implant alignment error in rotation (mean + 1 standard deviation) for both developed method and experimental setup. Rotational malalignment was reported in two components of varus-valgus (VV) error and internal-external (IE) error while Total represents square root of error components in rotation. 138

Figure 4.16: Definition of minimum implant distance to bone: (a) d1 to d4 represent the distances of each implant corner to bone inner boundary in one cross section while d1 denotes the minimum implant distance to bone, (b) relation between slice numbers and bone model, and (c) minimum implant distance to bone in each cross section from distal to proximal end of the bone. 141

Figure 4.17: Definition of area ratio: (a) A1 denotes implant area while A2 represents bone area delimited within the parametric definition of bone inner boundary in one cross section, (b) relation between slice numbers and bone model , and (c) Area ratio of implant to bone behaviour from distal to proximal end of bone..... 143

Figure 4.18: Impact of implant/spool size change in objective function value and final implant position 145

Figure 4.19: Repeatability test: (a) implant alignment error in translation (mean + 1 standard deviation) for developed method starting from the same implant position in 5 runs, and (b) implant alignment error in rotation (mean + 1 standard deviation) for developed method starting from the same implant position in 5 runs..... 146

Figure 4.20: Sensitivity to initial implant position in the developed GA technique: (a) implant alignment error in translation (mean + 1 standard deviation) for developed method starting from different implant orientation in 5 runs, and (b) implant alignment error in rotation (mean + 1 standard deviation) for developed method starting from different implant position and orientation implant position in 5 runs. 148

Figure 5.1: Stem-focused optimization variables: (a) Stem Coordinate System (SCS) located in the centroid of distal implant cross section, and (b) and (c) represent two translational and three rotational variables defined for the change in the shape of the stem. 162

Figure 5.2: Spool-focused optimization method representation: (a) change in the position of the capitellum and trochlea centers of the current shape of the implant, (b) current design of the implant with its FE axis, and (c) new design for the implant distal part (where spool is attached) with new FE axis. 165

Figure 5.3: Overall implant optimization method representation: (a) change in the positions of the capitellum and trochlea centers and also centroids of the distal and proximal cross sections of stem for current shape of the implant, (b) current design of the implant with its current FE axis and current stem shape and (c) new design for the implant with new FE axis and new stem shape. 168

Figure 5.4: Schematic chart of the first three methods (stem-focused, spool-focused and overall implant optimization) for optimizing the shape of the implant. 171

Figure 5.5: Customized implant design method representation: (a) finding the proper 3D axis that represents the largest common area of the bone cross sections, and (b) the resultant envelope along the 3D axis. 174

Figure 5.6: Comparison of the developed implant design in the stem-focused optimization method versus current design (green): (a) 3D view, and (b) side views of this comparison implant designs. 180

Figure 5.7: Comparison of the developed implant design in the spool-focused optimization method versus current design (green): (a) 3D view, and (b) side views of this comparison implant designs. 181

Figure 5.8: Comparison of the developed implant design in the overall implant optimization method versus current design (green): (a) 3D view, and (b) side views of this comparison implant designs. 182

Figure 5.9: Comparison of the developed implant design in the customized implant design method versus current design (green): (a) 3D view, and (b) side views of this comparison implant designs. 183

Figure 5.10: Comparison of the four developed implant designs versus current design (green): (a) 3D view, and (b) side views of the comparison of all implant designs. 184

Chapter 1

1 Introduction

1.1 Overview

This introductory chapter reviews elbow anatomy, elbow disorders and total elbow arthroplasty. This chapter also highlights the challenges involved in total elbow arthroplasty.

1.2 Joints and Implants

Joints articulate with bones of the human body and are responsible for movement. Joints can be classified functionally and structurally based on the range of motion and type of joint, respectively. Functionally, joints can be classified into three classes; 1) synarthrosis joints with no movement, (2) amphiarthrosis or joints with slight amount of movement, and (3) diarthrosis or freely movable joints. The last group of joints such as the elbow, knee, shoulder and hip are more prone to different dislocations and injuries.

Orthopedic implants are incorporated to restore normal kinematic and range of motion of the diseased joint. Although employing these implants reduces the pain and replicate the motion of the damaged joint, they may loosen, wear or break in place. Proper and efficient positioning of an implant into the cavity of the bone of a joint, not only contributes to suppressing all these defects, but it also helps to reform the normal functional joint.

In the recent years, computer-assisted surgery has been employed clinically in some centers for the placement of the implants to improve the accuracy and precision of orthopedic implant positioning, even in the hands of experienced surgeons. Freely

movable joints of the human body vary markedly in terms of degrees of freedom, complexity, overall size, bone structure and also canal shape. The current research which investigates the interaction between the implant and bone focuses on the elbow joint and the humeral canal with a more kinematic complexity, complicated canal shape and smaller size. However, the general methodology related to implant-bone contact/collision of this research is applicable to all other joints of the body.

1.3 Elbow

1.3.1 Anatomy and Biomechanics

The elbow joint, one of the most complicated joints of the body, connects the upper arm to the forearm [Bernardino, 2010]. The humerus of the upper arm, and the ulna and radius from the forearm, are three bones that form this synovial hinge joint. Structurally, the elbow joint is a synovial joint, while functionally behaves as a hinge joint. As a synovial joint, which is the most common and movable type of joints in human body, the elbow is capable of achieving movement at the contact point of the articulating bones. In order to ease this movement, articular cartilage covers the surfaces of the bones where they meet and acts as a smooth substance which protects the bones during movement. As one of the characteristics of synovial joints, all remaining surfaces inside the elbow joint are also covered by a thin smooth tissue, called synovial membrane. Muscles, ligaments, and tendons hold the elbow structure together to provide stability.

The human elbow is comprised of 3 articulations/joints; The humeroulnar joint in which trochlear notch of the ulnar articulates with trochlea of the humerus, the radiohumeral joint in which the concavity on the superior aspect of the radius head

articulates with capitulum of the humerus, and the radioulnar joint in which the head of the radius articulates with radial notch of the ulna (Figure 1.1). Although there are three joints performing in the elbow, they provide two different motions only. The first two joints (humeroulnar and radiohumeral joints) are in fact two hinge joints, which together function as a hinge joint, providing flexion-extension movement for the elbow, while the radioulnar joint is a pivot joint and responsible for supination-pronation motion. Traditionally, the two hinge joints of the elbow are considered as the representation of the elbow because the major task of the joint is to properly place the hand in space, while the radioulnar joint does not have any share in this functionality [Palastanga and Soames, 2012].

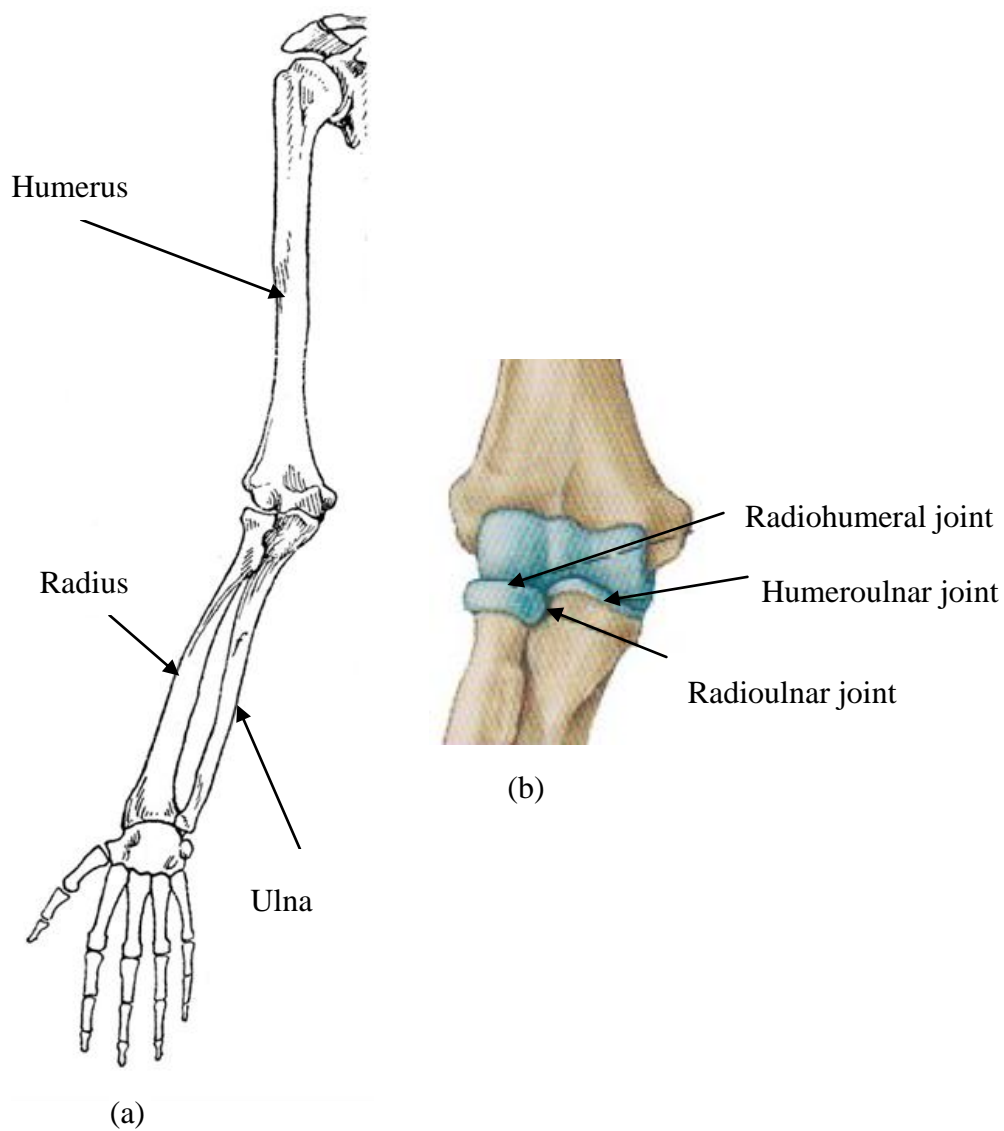


Figure 1.1: Elbow anatomy: (a) anterior view of right arm, showing the three elbow bones: humerus, radius and ulna, and (b) the three joints of elbow: radiohumeral, humeroulnar and radioulnar joints.

Adapted from [<http://www.cea1.com/anatomy-sistems/skeleton-of-the-arm/>;
<http://phs.psd3.org/science/anatomy/notes/skelenotes.html>]

The humerus is the longest bone in the upper limbs consisting of a body and two extremities, which connects to shoulder joint from upper (proximal) side and to the elbow joint from lower (distal) side. The body is composed of a cylindrical compact cortical bone, thicker at the center while the structure of the two extremities is cancellous tissue covered by a thin and compact layer. The cylindrical shaft contains an inner endosteal medullary canal that runs along the length of the diaphysis. Cross-sections of the humerus for both the periosteal shaft and medullary canal are not circles since the humerus is wider in medial-lateral direction rather than in anterior-posterior, especially close to the elbow.

The inner shape of endosteal canal is significantly important in positioning of the humeral implant during elbow replacement surgeries. On the other side, the lower extremity (distal) of the humerus plays a crucial role in surgical exposures since it contains several anatomical features that help surgeons to identify native regions of the elbow joint. These landmarks include two lateral and medial epicondyles which are located on each side of the distal humerus, two articular surfaces which are capitellum and trochlea, and three fossae comprised of the radial fossa, coronoid fossa and olecranon fossa (Figure 1.2). The articular surfaces are a bit lower than (distal to) the epicondyles. The lateral portion of the articular surfaces is a smooth rounded feature named the capitellum, while the medial part is a hyperbolic concaved surface, named the trochlea, which is separated by a groove called the trochlea sulcus. The capitellum articulates with the radius to form the radiohumeral joint. The trochlea of the humerus articulates with the ulna to represent the humeroulnar joint [Morrey and Bryan, 1982]. As reported previously [Amis, 2012], the transmission of loads to these joints is different, where 57%

of the load applied to the hand is transmitted through the radiohumeral joint and the rest is transmitted through the humeroulnar joint [Bernardino, 2010].

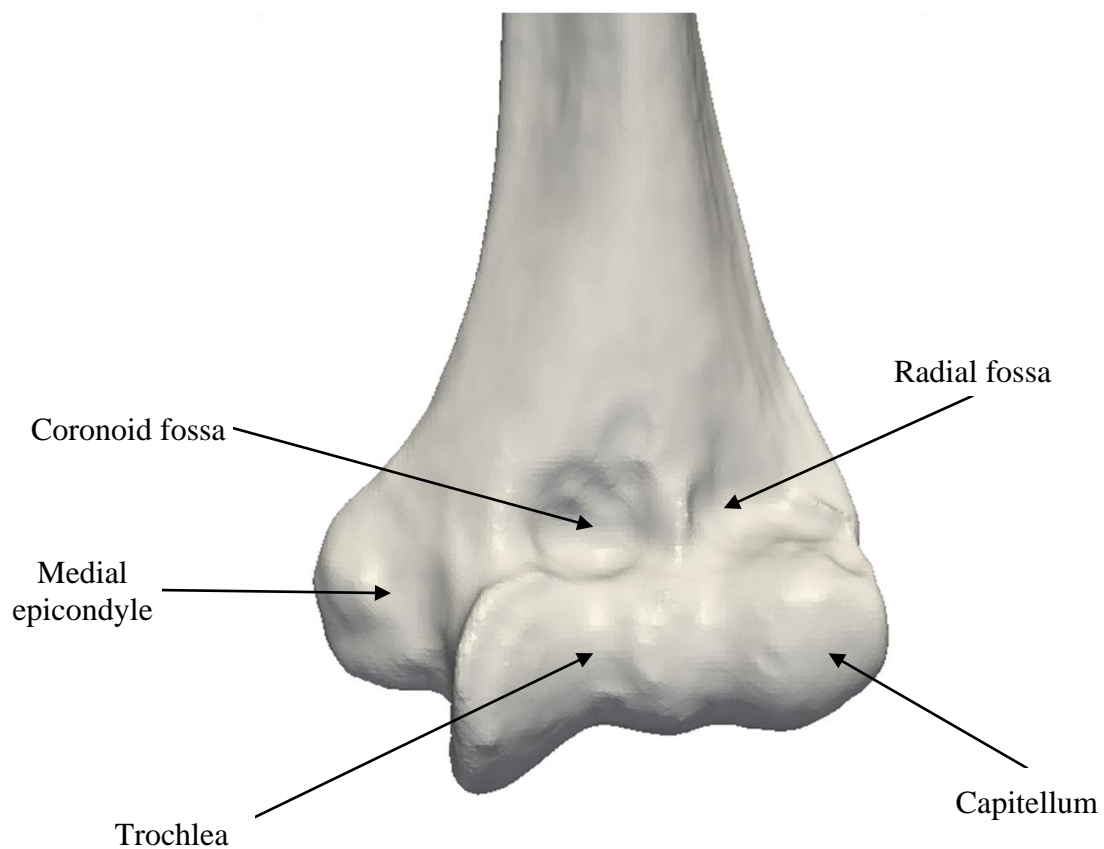


Figure 1.2: Anterior view of the distal humerus.

1.3.2 Motion and kinematics

The motions of the elbow joint consists of the flexion-extension movement provided by the humeroulnar and radiohumeral hinge joints and the pronation-supination movement provided by the radioulnar pivot joint (Figure 1.3). The flexion-extension motion occurs over an axis of rotation which is in fact the axis of the elbow hinge joint. In order to study the exact location of this axis, concurrent study of the centers of motions for both engaged joints (humeroulnar and radiohumeral joints) is required. The center of motion for the humeroulnar joint was reported to coincide with the center of trochlea sulcus arc for the majority of the flexion-extension range of motion, while the center of motion for the radiohumeral joint was reported to almost match the center of capitulum arc. As a result, the flexion-extension axis is a unique line that passes through arc centers described by trochlea sulcus and capitulum, except at extremes of flexion and extension [London, 1981]. Further details will be discussed in Chapter 3.

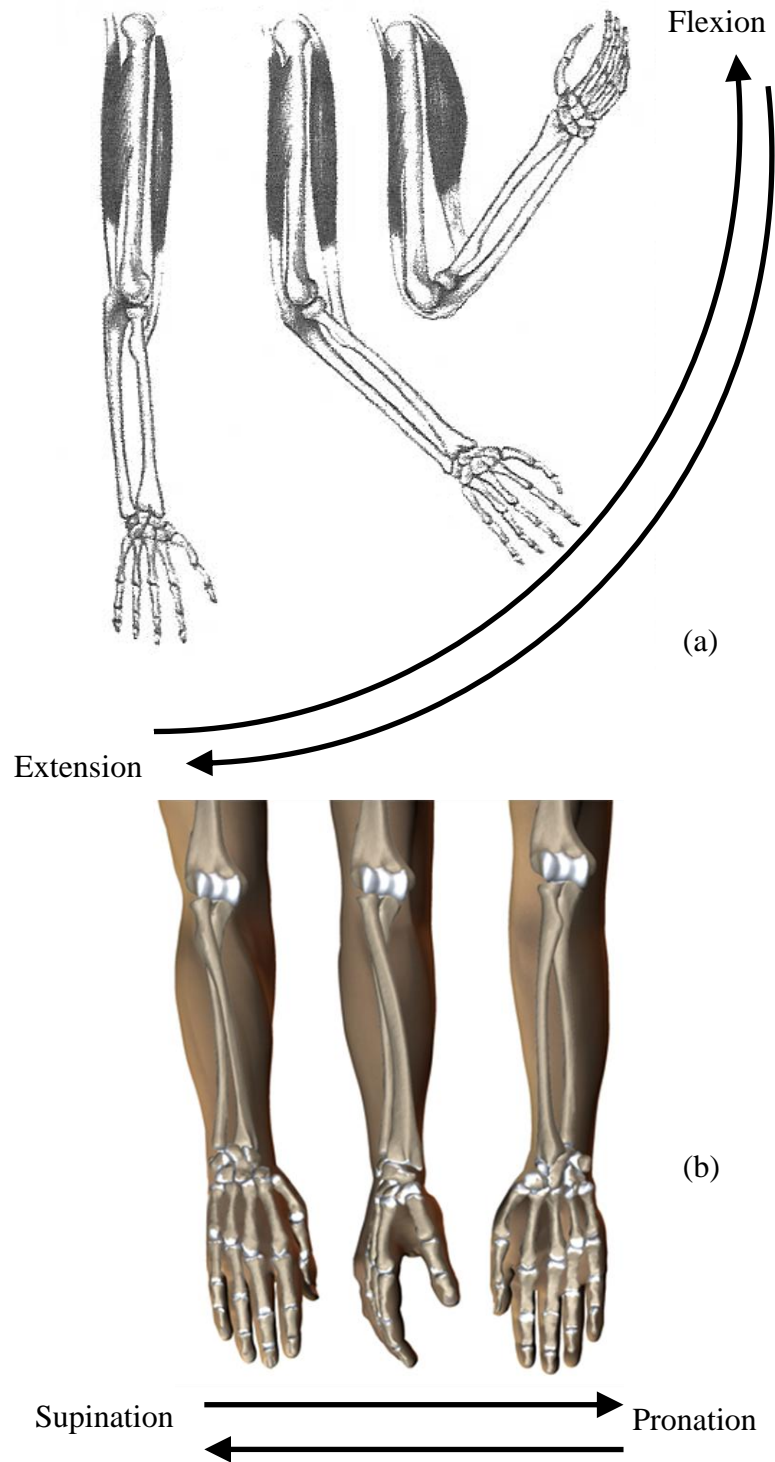


Figure 1.3: Motion of the elbow: (a) flexion-extension movement, and (b) supination-pronation movement.

Adapted from [<http://www.eorthopod.com/content/adolescent-osteochondritis-dissecans-of-the-elbow>; http://www.arn.org/docs/glicksman/eyw_040901.htm]

1.3.3 Disorders

The study of biomechanics of the elbow can help surgeons to plan surgeries and apply suitable treatments in difficult clinical problems, similar to other joints of the body. Many routine activities highly depend on the performance and functionality of the elbow joint, which is affected by both osseous and soft tissue structures. In the occurrence of different types of disorders, the large ranges of motion are subject to significant losses and they can impair the functionality of the elbow [Amis *et al.*, 1982]. There are three major groups of elbow disorders consisting of different types of arthritis, tumors, fractures, and dislocations.

Arthritis involves inflammation in the joint. Swelling, joint stiffness, difficulty with moving the joint, and muscle ache are other symptoms. One typical treatment option with overall satisfactory results for patients with osteoarthritis is total elbow arthroplasty, however, depending on the age and stage of the disease other treatment options might be recommended [Baksi, 1998; Throckmorton *et al.*, 2010]. Fractures can also lead to joint replacement. Radial head and neck, olecranon, coronoid, the distal humerus, and condylar fractures are common elbow fractures. In adults radial head fracture is the most common fracture, while distal humerus fracture can be more challenging in elderly patients, especially when associated with previous damages such as rheumatoid arthritis [Antuna *et al.*, 2012]. As one of the first studies, Cobb *et al.* [Cobb and Morrey, 1997] suggested total elbow arthroplasty for elderly patients with the distal humerus fractures and reported successful results after the surgery. As a result, replacement surgeries are more and more accepted for the elbow as the use of hip replacement surgeries for elderly patients with femoral neck fracture is fairly well accepted [Cobb and Morrey, 1997]. Due to high rate

of complications for open reduction and internal fixation, total elbow arthroplasty as a treatment decision for extensively comminuted fractures of the distal humerus is highly recommended. The rate of this type of surgery for these patients is increasing due chiefly to the rise in elderly population [Ali *et al.*, 2010].

1.4 Medical Imaging

Medical Imaging is an important tool in the diagnosis and planning for joint replacement. There are different methods, processes and instruments involved in creating the medical images, among which X-ray, Computed Tomography (CT), Magnetic Resonance Imaging (MRI), and ultrasound are the most common techniques.

1.4.1 Radiographs

In the X-ray technique, a source emits X-rays to the human body and on the other side a recording film produces X-ray images from the patient. Depending on the absorption rate of the different parts of the body, X-rays are absorbed or reflected and therefore the X-rays that reach the recording film make the film dark. In this way, the recording film records the attenuation of the X-rays, passing through human body. The resolution of the image depends on the amount of energy generated by X-ray source, tube current, and exposure time (Figure 1.4).



Figure 1.4: X-ray of a total elbow arthroplasty.

Adapted from [<http://www.orthop.washington.edu/?q=patient-care/hand/elbow-arthritis.html>]

1.4.2 Computed Tomography

Computed Tomography (CT) is a non-invasive medical examination procedure that uses specialized X-ray equipment to produce cross-sectional images of the body. The difference between CT and X-ray is that CT produces multi-sliced 3D images, while X-ray is a 2D representation of the human body (Figure 1. 5). In this technique, a detector rotates around the patient and as a result takes images at different angles. All the images are processed and reconstructed into multiple cross sectional (slices) images. Obviously, 3D image comparing to a 2D image delivers larger amount of information.

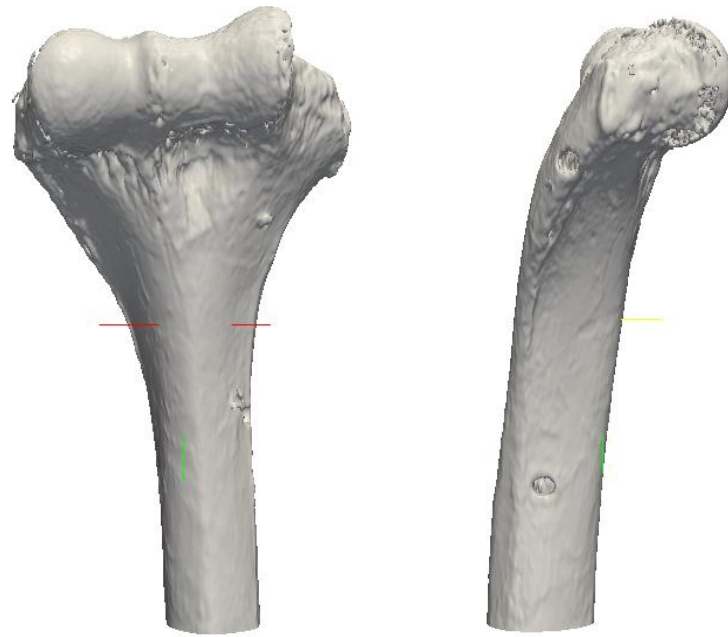
In orthopedics-related CT applications [Wang, 2009], accurate representation of the endosteal cavity of the humerus is a mandatory and preliminary step for positioning of the humeral implants during total elbow arthroplasty. Furthermore, this information is critical in determination of optimized implant stem. This calls for an accurate geometric representation of the cortical bone as one of the decisive premises of successful reconstruction.

1.4.3 Digital Imaging and Communication in Medicine (DICOM)

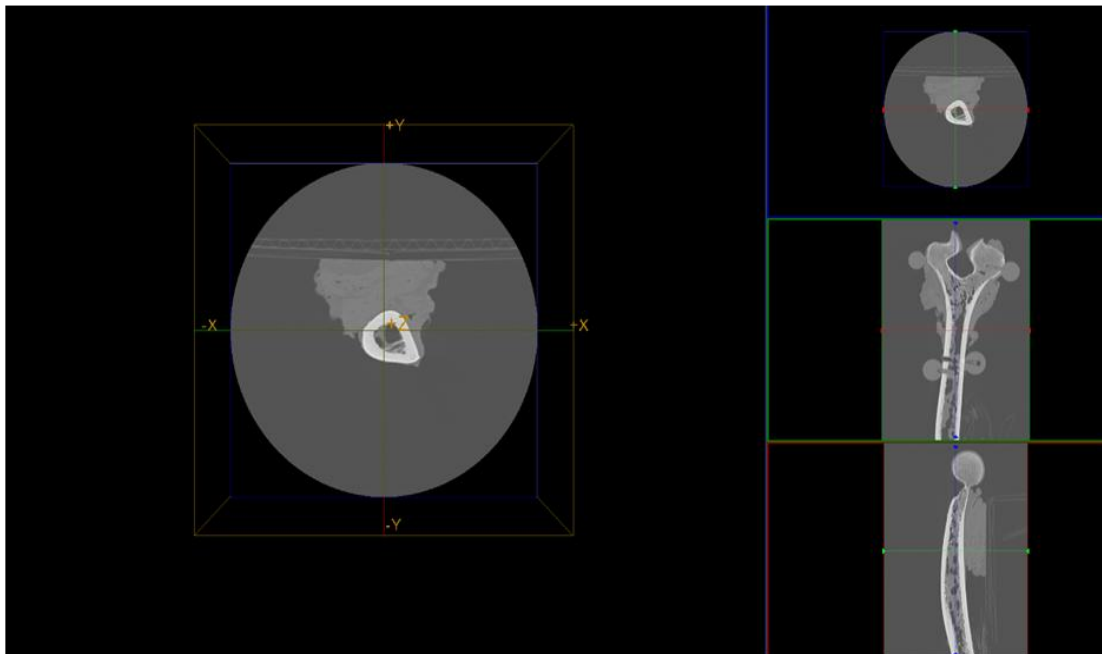
In 1983, the American college of Radiology (ACR) and National Electrical Manufacturers Association (NEMA) introduced the first standard named Digital Imaging and Communication in Medicine (DICOM), capable of storing, handling, and transmitting information in medical imaging. DICOM became the global format for encoding the images acquired from different system. DICOM enables integration of

different scanners, work-stations, and servers from multiple manufacturers into a Picture Archiving and Communication System (PACS).

Each DICOM file contains grids of pixels which depending on the density of the tissue forms a grayscale spectrum (Figure 1.5). One of the applications of DICOM files in orthopedics field is to extract the 3D geometry of the bone from a stack of DICOM slices. In order to accomplish this, pixels belonging to outside and inside boundaries of the cortical bone are detected in each single DICOM file and then these boundaries are assembled to reconstruct the bone geometry.



(a)



(b)

Figure 1.5: (a) 3D representation of distal humerus acquired by CT scanner, and (b) the distal humerus cross section in transverse, sagittal and coronal planes.

1.4.4 Edge Detection Methods

Edge detection aims at identifying points/pixels in a digital image at which sharp changes in image intensity occurs. Edge detection techniques benefit from a set of mathematical methods to locate the boundaries of objects within an image which are characterized by abrupt discontinuities due to change in image brightness [Nadernejad *et al.*, 2008; Maini and Aggarwal, 2009]. Edge detection filters and keeps important structural properties (*i.e.*, boundaries of objects). Detecting the edges/boundaries is an essential step in image segmentation and image reconstruction. All the methods in edge detection employ either gradient-based method which searches for maximum or minimum in first derivative of an image, or Laplacian-based technique which employs zero crossings in the second derivative of an image.

Canny, Sobel, Prewitt, Robert, and Laplacian of Gaussian are the major edge detection techniques in image processing. The Canny edge detector method [Canny, 1986] is known as the standard technique. The Canny algorithm is based on converting the edge detection problem into a signal processing optimization problem in which there is a minimum deviation between the distance of the edge pixels, found by the algorithm, and the actual edge [Canny, 1986; Maini and Aggarwal, 2009]. As the first step of this algorithm, the Canny algorithm smoothens the image with a two-dimensional Gaussian to eliminate the noise, and then calculates the gradient of the image in both directions to identify regions with high spatial derivatives. Since edges occur at points where the generated gradient is a maximum, Canny applies a non-maximum suppression to eliminate non-maximum pixels. Canny then uses high and low thresholds (named as hysteresis) to generate edges among candidate pixels. Sobel [Matthewes, 2002] uses a

simple 3*3 convolution kernels to create a series of gradients in both x and y directions. These magnitudes of gradients are plotted at the end to represent edges/boundaries of an image. The main characteristic of Sobel technique is that it is incredibly sensitive to noises in images. Prewitt technique [Seitz *et al.*, 2010; Shirvakshan, 2012] is similar to the Sobel algorithm in terms of kernels involved in generating gradient values. Unlike Sobel technique, the Prewitt operator is a fast operator that does not put emphasis on pixels that are close to the center of the masks and therefore it is only suitable for well-contrasted noiseless images. The Roberts algorithm [Roberts, 1965] benefits from 2*2 convolution kernels to calculate 2D spatial gradient measurements. The Roberts technique highlights regions of high spatial frequency which at the end correspond to edges. The most common use of this technique is its application on grayscale images as input and output [Shirvakshan, 2012]. Laplacian of Gaussian function known as LOG function employs a smoothing filter, performed by convolution with a Gaussian function and followed by a derivative operation. The LOG operator is a 2D isotropic measure of the 2nd derivative of an image, which is sensitive to noises [Juneja and Sandhu, 2009].

It is really essential to understand the differences between different edge detection techniques, their advantages, disadvantages, and their special applications (Figure 1.6). Typically, gradient-based algorithms such as Prewitt are sensitive to noise although they might work faster than others. It is reported in [Juneja and Sandhu, 2009] that under noisy conditions, Canny, Robert, and Sobel represent better performance respectively. The other factor, which is important, is the quality of output images, which under these circumstances Sobel, Prewitt, and Roberts provide low quality images comparing to other

methods. Canny algorithm depends heavily on adjustable factors such as standard deviation for the Gaussian filter and threshold values. Although Canny method is computationally more expensive comparing to the others, it performs accurate edge detection on images [Miani and Aggarwal, 2009; Juneja and Sandhu, 2009; Nadernejad *et al.*, 2008; Shirvakshan, 2012] (Figure 1.6).

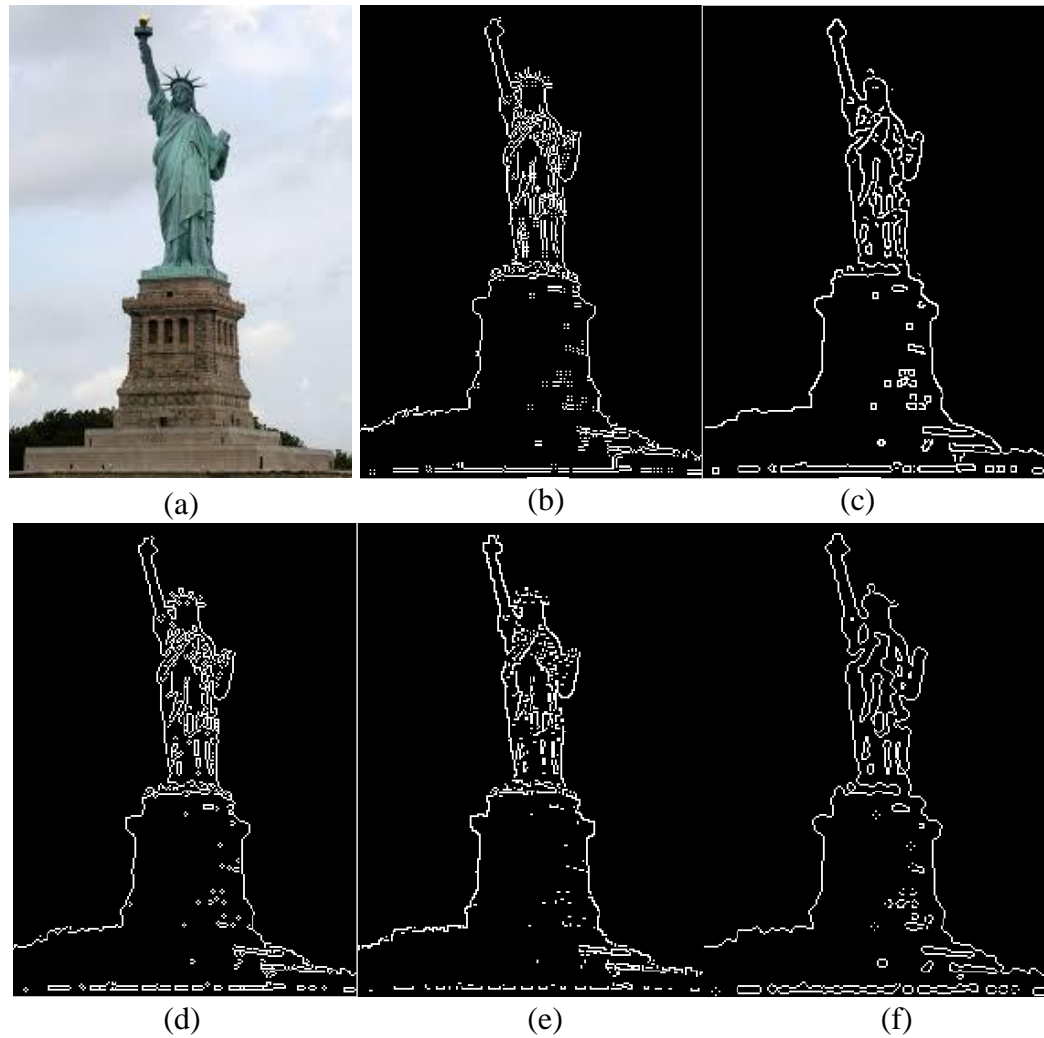


Figure 1.6: Comparison of different edge detection techniques; (a) original sample image, adapted from [http://en.wikipedia.org/wiki/Statue_of_Liberty], (b) Prewitt, (c) Canny, (d) Sobel, (e) Roberts, and (f) LOG methods.

1.5 Total Elbow Arthroplasty

Total Elbow Arthroplasty (TEA) involves replacement of the damaged elbow joint with artificial components (implants) aiming at restoring elbow function and relieving pain in the patient (Figure 1.7). Operatively, surgeons identify the native articulation axis and remove diseased portions of the elbow and then prosthetic replacement is performed for the humeral and ulnar sides. Implant stems are inserted into the medullary canals of the corresponding bones and fixed by cement while surgeon ensures the flexion-extension axis best matches the native articulation axis of the elbow [Brownhill, 2007]. The implant configuration/alignment inside the bone canals affects the kinematics and load transfer of the elbow after surgery. The crucial issue here is to replicate the same kinematics and load transfer system as accurate as possible to avoid potential failure [Bauer and Schils, 1999; Brownhill, 2007].

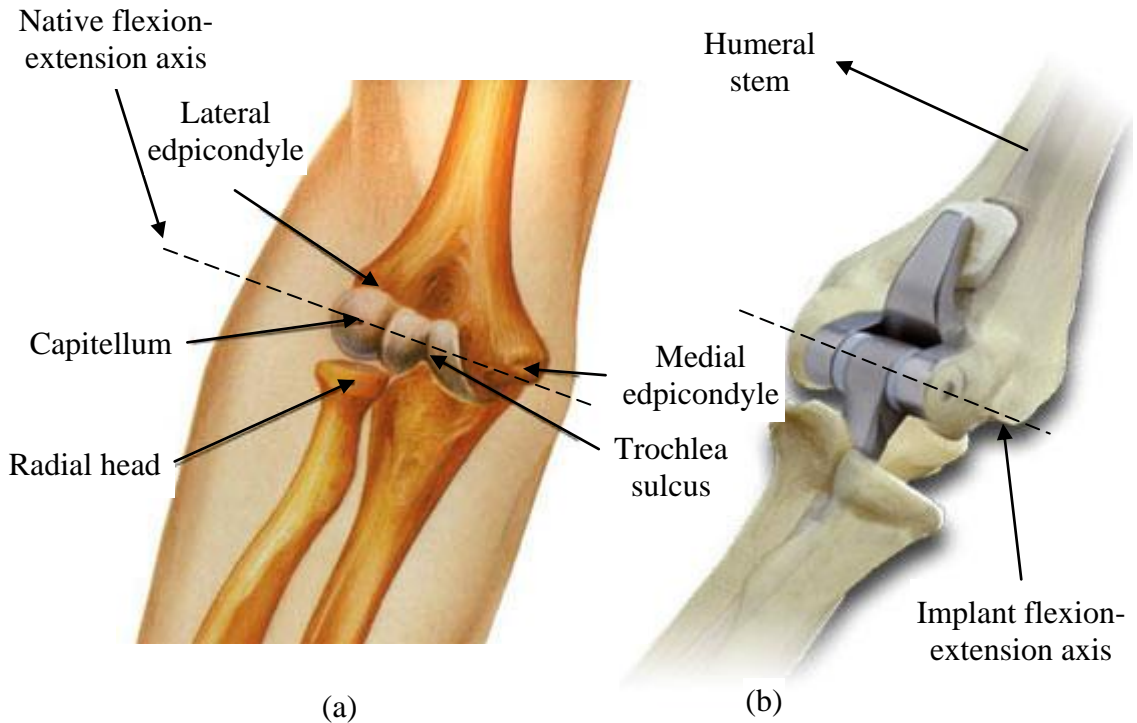


Figure 1.7: (a) Anatomical features of the native elbow joint, and (b) elbow joint after total elbow arthroplasty with prosthetic components.

Adapted from [<http://www.doctorre.com/commoninjuries/elbow/>;
<http://www.littleastonoasis.com/Pages/ElbowReplacement.aspx>]

1.5.1 Surgical Techniques

Following joint exposure, component sizing is performed by comparing humeral spool size with articulation of the distal humerus from medial to lateral since the width of the component is more important than spool diameter. The size of the spool determines the size of the humeral, ulnar, and radial head components [Marsh and King, 2013; Gramstad *et al.*, 2005]. The flexion-extension axis is then determined by a line from the center of the capitellum to the anterior-inferior aspect of the medial epicondyle. The humeral implant is then inserted into the canal and the ulnar component is implanted into the ulnar medullary canal. When trial components are in place and linked together to form the trial elbow joint, the elbow is placed through a range of motion and tested for stability [Marsh and King, 2013; Gramstad *et al.*, 2005]. The spool is fixed to the humeral stem first by a screwdriver and the radial head is snapped onto the stem.

1.5.2 Implant Types

Implants used in total elbow arthroplasty can be divided into two general categories; linked (coupled) and unlinked implants. The distinction between these two groups is the way humeral and ulnar implants are linked [Little *et al.*, 2005; Sanchez-Sotelo, 2011]. For linked implants, humeral and ulnar components are connected via a physical linking (*i.e.* screw) to avoid further dislocation between them. Linked implants can also be divided into two groups; fixed hinge/constrained implants that are early generations of linked implants and sloppy hinge implants that are current type of linked implants. Since the main kinematic characteristic of the elbow is the flexion-extension movement, early designs for linked implants were considered to contain a simple fixed hinge joint as linking joint representing native kinematics of the elbow. The main two drawbacks of

such design are transmitting higher stresses to implant/cement and cement/bone interfaces and also high rate of failure in total elbow arthroplasty [Little *et al.*, 2005; Sanchez-Sotelo, 2011]. As reported in [Little *et al.*, 2005], the overall functionality of fixed hinge implants is lower than sloppy hinge or unlinked implants with higher loosening rate of 11% and lower successful results of 73%. The majority of loosening comes from the humeral stem rather than the ulnar component, which might be increased to 25%, due to high amount of forced transferred to the joint [Morrey and Bryan, 1982]. Therefore, current linked implants are semi-constrained implants with sloppy hinge of linking mechanism, which allows internal-external rotational laxity and varus-valgus play of 5^0 - 10^0 degrees [Baksi, 1998; Hastings, 2004; Lee *et al.*, 2005; Little *et al.*, 2005]. Since rotational and varus-valgus forces in a native elbow joint are dispersed through surrounding soft tissue and not the articulation mechanism, sloppy hinge implants are designed to replicate this semi-constrained native kinematics of the elbow and to reduce the amount of forces being applied on joint articulation [Gramstad *et al.*, 2005; Morrey and Bryan, 1982; Little *et al.*, 2005]. It is believed that semi-constrained implants lead to a long-term fixation due to less transmission of stress to implant articulation interfaces and also more and more advances in geometric and mechanical design [Sanchez-Sotelo, 2011]. Coonrad-Morrey, Discovery, GSB III, Norway, Pritchard Mark II, and Pritchard Walker are common linked implants available for total elbow arthroplasty, among which Coonrad-Morrey is the major one in this type of group and widely used in current TEA [Sanchez-Sotelo, 2011; Prasad and Dent, 2008; Mansat *et al.*, 2013; Gill and Morrey, 1998; An, 2005].

Unlike semi-constrained implants, unlinked/resurfacing implants (also termed unconstrained implants) do not have a mechanical connection between the humeral and ulnar components. The articulation consists of two curved surfaces that slide on each other to replicate the elbow motion. The stability of unlinked implant is achieved by accurate positioning of each component, ligament integrity and muscle stability [Sanchez-Sotelo, 2011]. Theoretically, unlinked implants lead to a lower loosening rate comparing to linked implants due to lower implant/cement and cement/bone interfaces stresses [Kamineni *et al.*, 2005]. As a contradiction to unlinked implants, extensive loss of bone for implant preparation and ligamentous support can be a source of instability for this type of implant. Capitellocondylar, iBP, Kudo, Norway, Pritchard II, Sorbie and Souter-Strathclyde are current options for unlinked implants to be used in total elbow arthroplasties among which Kudo, Sorbie and Souter-Strathclyde are the more common from other options [Sanchez-Sotelo, 2011; An, 2005; Kamineni *et al.*, 2005].

The new generation of implants are termed convertible implants due to the fact that these new types of implants can be both linked and unlinked implants depending on the intra-operative decision of surgeon in terms of stability for TEA. Comparing to existing linked and unlinked implants, convertible implants include a better bearing surface design and a geometrical design with the focus on anatomic reconstruction. The Latitude is the major available option for these convertible implants [Sanchez-Sotelo, 2011; Gramstad *et al.*, 2005].

1.5.3 Complications

Despite of the advancements in implant designs and surgical techniques, the rate of complications after total elbow arthroplasty is 25% as reported in [Voloshin *et al.*, 2011]

while some studies show a high rate of 45% [Gschwend *et al.*, 1996]. Studies on complications after TEA vary in terms of number of patients, number of months followed after surgery, indication of TEA, age of patients, year of surgery and patients referral to the same hospital for revision surgery and as a result a wide range of complication rate is reported in different studies [Voloshin *et al.*, 2011; Gschwend *et al.*, 1996; Seitz *et al.*, 2010; Wright *et al.*, 2000; Morrey and Bryan, 1982; Mansat *et al.*, 2013]. However, common complications are aseptic loosening, deep infection, ulnar nerve lesions, bushing wear/failure, implant fracture, dislocation and intra-operative fractures. As previously indicated, these can be attributed to varied extents to implant alignment in bone.

Aseptic loosening is the most prominent complication occurring mostly about humeral component due to insufficient bone stock, ligament instability, improper cement fixation and failure of bone/cement interface [Voloshin *et al.*, 2011; Gschwend *et al.*, 1996]. Unlike semi-constrained implants, unlinked prostheses lead to less aseptic loosening due to reductions in stress at the cement-bone interface.

Several studies investigated the intrinsic constraints and attributes of various types of implants utilized in total elbow arthroplasty through cadaveric studies [An, 2005; Kamineni and Morrey, 2008; Brownhill, 2007]. These studies can help surgeons to decide which implant types better replicate the kinematics of the elbow, despite of various geometric designs and in vitro biomechanical behavior of implants.

1.6 Component Alignment and Collision Detection

The final position of humeral implant in the humeral canal during TEA determines the flexion-extension (FE) axis of the joint, however, the overall success of determination of

the optimal insertion path of the implant into the intramedullary convoluted canal with no collision is the challenging step in implantation. Determination of the optimal insertion trajectory is a part of classical peg-in-hole path planning problem, in which the primary goal is to determine a collision-free trajectory of a moving object (peg) from an outside position to the final inside position within confined spaces (hole). This is where calculation of collision detection is relevant. This is a fundamental problem in Computer-Aided Design and Machining (CAD/CAM), robotics, automation, manufacturing, computer graphics, animation and computer simulated environments. The major goal of collision detection is to identify a geometric contact when collision is about to occur [Lin and Gottschalk, 1998]. As an example, in robotics, motion planning of robots depends highly on collision detection technique aiming at maneuvering the robot away from obstacles. Generally speaking, determination of a collision-free trajectory involves identification within the pool of instantaneously possible object position and orientations (*i.e.* poses or postures) of those who are characterized by a non-overlapping status with neighboring objects.

Typically, various model representations define collision detection algorithms, however the desired query types and simulation environments are essential parameters. There are many model representations in CAD/CAM, while polygonal models, constructive solid geometry, implicit surfaces and parametric surfaces are important ones. Most of earlier studies in collision detection focused on algorithms for convex polytopes [Dobkin and Kirkpatrick, 1990; Gilbert *et al.*, 1988; Seidel, 1990; Lin and Gottschalk, 1998].

Gottschalk *et al.* introduced RAPID algorithm in which collision detection was based on oriented bounding boxes. K-DOPs method was introduced by Klosowski *et al.* which used discrete orientation polytopes for approximating bounded geometry. In the context of non-polygonal models, there are several attempts for computing the intersection of surfaces represented as splines or algebraic surfaces [Krishnan and Manocha, 1997]. We can divide non-polygonal models into three groups; 1) Constructive Solid Geometry (CSG) models, (2) Parametric surfaces and (3) Implicit surfaces. In CGS models, efficient and accurate computation of the boundary is a challenging area. S-bounds were introduced by Cameron to speed up the intersection testing by one or two orders of magnitude on CSG systems, using limited sample points [Cameron and Culley, 1986]. In the Duff approach [Duff, 1992] interval arithmetic was used to evaluate implicit function in box-like regions which is in fact extended version of classical point classification scheme. By using this technique, he could determine whether regions lie inside or outside or lay across the boundaries.

Four techniques are common algorithms for collision detection in parametric surfaces: subdivision methods, analytic methods, lattice methods and tracing methods. Subdivision methods subdivide the domain of two surface patches in tandem and then inspect the relationship between these patch subsections [Snyder *et al.*, 1993]. Lattice methods try to find specific points on the preimage curve of the intersection curve of two surfaces in the domain of both surfaces. In this method, many isoparametric curves are defined to criss-cross the surface like a lattice-work [Prasad and Dent, 2008]. Tracing methods start from a given point on the intersection curve of two surfaces and then try to trace the intersection curve in small steps [Krishnan and Manocha, 1997]. In analytic

methods, the parametric representation of the curve is substituted for the implicit function to end up with a scalar function in terms of parametric variables. The locus of roots of this scalar function maps out the preimage intersection curve of two surfaces [Manocha and Canny, 1991]. To accomplish collision detection for implicit surfaces, [Pentland and Williams, 1989] used point samples and implicit functions to represent the shape of the intersection curve.

1.7 Thesis Rationale

1.7.1 Motivation

Implant alignment is a critical factor in replicating native kinematics of the elbow and durability of the artificial components. In order to better position the implant into medullary canals of the elbow bones, both anatomical understanding of the bones and biomechanical properties should be considered [Schunid *et al.*, 1995; Figgie *et al.*, 1986]. Brownhill and colleagues [Brownhill *et al.*, 2012a] studied the anatomical perspective of the distal humerus and derived geometric features of the distal humeral canal, to better investigate implant positioning. It was shown that the anteriorposterior curvature of medullary canal of the distal humerus along with FE axis anterior offset from axis of this canal play an important role in the design and implantation of distal humerus implants [Brownhill *et al.*, 2012b].

Collision detection can have broad applications in medical area and so many studies were conducted in this area. In a study by Tutunea-Fatan *et al.* [Tutunea-Fatan *et al.*, 2010], collision detection was utilized to assess the insertability of the stem in the humeral canal during total elbow arthroplasty. In this study CEA software was used to

accomplish the insertion. As another application, collision detection was used in virtual surgery simulators in [Lombardo *et al.*, 1999] to train surgeons on virtual patients. Nowadays, since non-invasive surgeries contain a majority of surgeries, practicing with various tools during surgery is essential in which surgical simulators can be a great help.

Successful clinical outcome of surgical joint arthroplasty is decisively influenced by the pre-operative planning procedures aiming to establish an optimized implant insertion trajectory into the bone cavity. Since computation of the insertion path of a body into a cavity represents a traditional instance of a path planning problem often encountered in robotics field, the proposed research is expected to reinforce the importance of engineering approaches in the context of Computer-Aided Orthopaedic Surgery (CAOS). The use of collision detection algorithms – involving advanced geometric representations and/or computations will enable the determination of optimal implant insertion trajectory with significant implications with respect to preoperative prediction of implant alignment and optimal implant design.

1.7.2 Objectives and Hypothesis

The main objective of the proposed research is to develop a library of numerical algorithms that will constitute the core of a computationally-intensive geometry visualization module capable of achieving accurate predictions related to implant insertability into the bone's endosteal canal as defined by patient-specific CT scans.

The methods to be developed within the scope of the proposed research will permit the replacement of error-prone implant insertion decisions made preoperatively by the surgeon with optimized computer-based solutions. This approach will eliminate or at

least diminish the need for unreliable and undesirable trial and error validation procedures. Over the long term, it is expected that the knowledge generated through this study will be incorporated into a complex virtual total arthroplasty training simulator that will integrate these geometry-based modules with elements of haptic feedback.

The central hypothesis of the proposed research is that by analyzing preoperatively the implant and medullary canal geometries involved in total elbow arthroplasty, an accurate prediction can be made with respect to their relative fit. To address this hypothesis, the objectives are:

- 1) To develop a computer-aided method capable to reconstruct with minimal user intervention accurate parametric-based representations of the bone geometry starting from computer tomography (CT) data;

- 2) To assess the insertability of particular implant geometry in the context of a specific humeral specimen by means of numerical techniques; and

- 3) To use the developed numerical algorithms as validation tools for new implant stem geometries.

1.7.3 Contributions

The major contributions emerging from this thesis are related to the development of several numerical techniques of performing aforementioned tasks. Indeed, the developed techniques within the scope of this study were aimed to automatically represent humeral canal in a parametric format and determine FE axis and to derive

optimal insertion trajectory pre-operatively to serve surgeons have an efficient plan for intra-operative surgery.

This work is one of the first attempts in the context of implant insertion into the cavity of bone with minimum malalignment benefiting from a computer-assisted technique. As such, by utilizing the developed technique surgeons can assess insertability of different implant sizes while investigating malalignment between native FE axis and bone implant axis to achieve optimal final position for implant and consequently better final outcome of TEA.

1.7.4 Outline

Chapter 2 outlines a numerical algorithm developed initially for a highly accurate and automatic conversion of source CT data into parametric (B-Spline/NURBS-based) data. The automatic DICOM to B-Spline conversion entails determination of an appropriate thresholding method, to be followed by an edge detection procedure required to establish inner and outer cortical bone boundaries.

Chapter 3 contains a numerical algorithm to determine the theoretical/ideal location of the flexion-extension (FE) axis of the humeral bone based on reconstructed geometry of the bone. The output of this algorithm was compared and validated against conventional FE axis determination methods employing marching cube approaches followed by least square fitting methods through extracted VTK data points.

Chapter 4 is focused on the final posture of the implant to match the natural FE axis of the bone, provided that this constitutes a feasible solution for analyzed bone canal geometry. Then, the optimal insertion trajectory was analyzed in reversed motion (final to

initial) in order to reduce the amount of computational time required to detect inaccessible final implant orientations located – most likely – towards the end of the insertion trajectory.

Chapter 5 explores new geometry for stems by benefiting from the previously developed computational tool in conjunction with various implant stem geometries and a broad variety of humeral bones in an optimization process.

Chapter 6 provides the conclusion of the thesis.

1.8 References

- Ali, A., Shahane, Sh., and Stanley, D. (2010) Total elbow arthroplasty for distal humeral fractures: Indications, surgical approach, technical tips, and outcome. *J.Shoulder.Elbow.Surg.* 19, 53-58.
- Amis, A.A. (2012) Biomechanics of the elbow. In: Stanley D, Trail I, editors. *Operative elbow surgery*. Edinburgh: Churchill Livingstone Elsevier. 29-44.
- Amis, A.A., Hughes, S. J., Miller, J. H., and Wright, V. (1982) A functional study of rheumatoid elbow. *Rheumatology and Rehabilitation*, 21, 151-157.
- An, K.N. (2005) Kinematics and constraint of total elbow arthroplasty. *J.Shoulder.Elbow.Surg.* 14[1 Suppl S], 168S-173S.
- Antuna, S.A., Laakso, R.B., Barrera, J.L., Espiga, X., and Ferreres, A. (2012) Linked total elbow arthroplasty as treatment of distal humerus fractures. *Acta Orthop. Belg.* 78, 465-472.
- Athwal, G.S., Chin, P.Y., Adams, R.A., and Morrey, B.F. (2005) Coonrad-Morrey total elbow arthroplasty for tumours of the distal humerus and elbow. *J. Bone Joint Surg. Br.* 87[10], 1369-1374.
- Baksi, D.P. (1998) Sloppy hinge prosthetic elbow replacement for post-traumatic ankylosis or instability. *J.Bone Joint Surg.Br.* 80[4], 614-619.
- Bauer, T.W. and Schils, J. (1999) The pathology of total joint arthroplasty.II. Mechanisms of implant failure. *Skeletal Radiol.* 28[9], 483-497.
- Bernardino, S. (2010) Total elbow arthroplasty: history, current concepts, and future. *Clin Rheumatol* ,29,1217–1221.
- Boone, D.C. and Azen, S.P. (1979) Normal range of motion of joints in male subjects. *J.Bone Joint Surg.Am.* 61 [5], 756-759.
- Brownhill, J.R. (2007) The Development of Computer-Assisted Techniques for Total Elbow Arthroplasty. PhD The University of Western Ontario.
- Brownhill, J.R., King, G.J., and Johnson, J. A. (2007) Morphologic analysis of the distal humerus with special interest in elbow implant sizing and alignment. *J.Shoulder.Elbow.Surg.* 16[3 Suppl], S126-S132.
- Brownhill, J.R., McDonald, C.P., Ferreira, L.M., Pollock, J.W., Johnson, J. A., and King, G.J. (2012a) Kinematics and laxity of a linked total elbow arthroplasty following computer navigated implant positioning. *Computer Aided Surgery*, 17[5], 249–258.
- Brownhill, J.R., Pollock, J.W., Ferreira, L.M., Johnson, J. A., and King, G.J. (2012b) The effect of implant malalignment on joint loading in total elbow arthroplasty: an in vitro study. *J Shoulder Elbow Surg*, 21, 1032-1038.

- Cameron S., and Culley, R. K. (1986) Determining the minimum translational distance between two convex polyhedra. *Proceedings of International Conference on Robotics and Automation*, 591-596.
- Canny, J. (1986) A computational approach to edge detection. *IEEE Transactions on pattern analysis and machine intelligence*, 8[6], 679-698.
- Cesar, M., Roussanne, Y., Bonnel, F., and Canovas, F. (2007) GSB III total elbow replacement in rheumatoid arthritis. *J.Bone Joint Surg.Br.* 89[3], 330-334.
- Celli, A., Morrey, B.F. (2009) Total elbow arthroplasty in patients forty years of age or less. *The Journal of Bone and Joint Surgery*, 91, 1414-1418.
- Chan, R.K.W., and King, G.J. (2012) The management of the failed total elbow arthroplasty. In: *Stanley D, Trail I, editors. Operative elbow surgery; Elsevier*, 665-694.
- Choo, A., and Ramsey, M.L. (2013) Total elbow arthroplasty; Current options. *J Am Acad Orthop Surg.* 21, 427-437.
- Cobb, T.K., Morrey, B.F. (1997) Total elbow arthroplasty as primary treatment for distal humeral fractures in elderly patients. *The Journal of Bone and Joint Surgery*, 826-832.
- Deland, J.T., Garg, A., and Walker, P.S. (1987) Biomechanical basis for elbow hinge distractor design. *Clin. Orthop.Relat Res.* [215], 303-312.
- Dobkin, D. P., and Kirkpatrick, D. G. (1990) Determining the separation of preprocessed polyhedral. *Lecture Notes Comput. Sci.*, 443,400-413.
- Duck, T.R., Dunning, C.E., Armstrong, A.D., Johnson, J.A., and King, G.J. (2003) Application of screw displacement axes to quantify elbow instability. *Clin.Biomech. (Bristol, Avon.)* 18[4], 303-310.
- Duff, T. (1992) Interval arithmetic and recursive subdivision for implicit functions and constructive solid geometry. *ACM Computer Graphics*, 26(2),131-139.
- Ericson, A., Arndt, A., Stark, A., Wretenberg, P., and Lundberg, A. (2003) Variation in the position and orientation of the elbow flexion axis. *J.Bone Joint Surg.Br.* 85[4], 538-544.
- Ferlic, D.C., and Clayton, M.L. (1995) Salvage of failed total elbow arthroplasty. *J ShoulderElbow Surg*, 4, 290-297.
- Fevang, B.S., Lie, S.A., Havelin, L.I., Skredderstune, A., Furnes, O. (2009) Results after 562 total elbow replacements: A report from the Norwegian Arthroplasty Register. *J ShoulderElbow Surg*, 18, 449-456.
- Figgie, H.E., Inglis, A.E., and Mow, C. (1986) A critical analysis of alignment factors affecting functional outcome in total elbow arthroplasty. *J Arthroplasty*, 1, 169-173.
- Gay, D.M., Lyman, S., Do, H., Kotchkiss, R.N., Marx, R.G., and Dauliski, A. (2010) Indications and Reoperation Rates for Total Elbow Arthroplasty: An Analysis of Trends in New York State. *The Journal of Bone and Joint Surgery*, 94, 110-117.

- Gilbert, E. G., Johnson, D. W., and Keerthi, S. S. (1988) A fast procedure for computing the distance between objects in three-dimensional space. *IEEE J. Robotics and Automation*, RA-4,193-203.
- Gill, D.R. and Morrey, B.F. (1998) The Coonrad-Morrey total elbow arthroplasty in patients who have rheumatoid arthritis. A ten to fifteen-year follow-up study. *J.Bone Joint Surg.Am.* 80[9], 1327-1335.
- Goto, A., Moritomo, Ft., Murase, T., Oka, K., Sugamoto, K., Arimura, T., Nakajima, Y., Yamazaki, T., Sato, Y., Tamura, S., Yoshikawa, H., and Ochi, T. (2004) In vivo elbow biomechanical analysis during flexion: three-dimensional motion analysis using magnetic resonance imaging. *J.Shoulder.Elbow.Surg.* 13[4], 441-447.
- Gschwend, N., Simmen, B.R., Matejovsky, Z. (1996) Late complications in elbow arthroplasty. *J. Shoulder Elbow Surg.*5[2], 86-96.
- Gramstad, G.D., King, G.J., O'Driscoll, S.W., and Yamaguchi, K. (2005) Elbow arthroplasty using a convertible implant. *Tech.Hand Up Extrem.Surg.* 9[3], 153-163.
- Halls, A.A. and Travil, A. (1964) Transmission of pressures across the elbowjoint. *Anat.Rec.* 150, 243-247.
- Hastings, H. (2004) Minimally constrained elbow implant arthroplasty: the discovery elbow system. *Tech.Hand Up Extrem.Surg.* 8[1], 34-50.
- Hildebrand, K.A., Patterson, S.D., Regan, W.D., MacDermid, J.C., and King, G.J. (2000) Functional outcome of semiconstrained total elbow arthroplasty. *J. Bone Joint Surg.Am.* 82-A[10], 1379-1386.
- Jenkins, P.J., Watts, A.C., Norwood, T., Duckworth, A.D., Rymaszewski, L.A., and McEachan, J.E. (2013) Total elbow replacement: outcome of 1,146 arthroplasties from the Scottish arthroplasty Project. *Acta Orthopaedica* ,84 [2], 119–123.
- Juneja, M., and Sandhu, P.S. (2009) Performance Evaluation of Edge Detection Techniques for Images in Spatial Domain. *International Journal of Computer Theory and Engineering*, 1[5], 614-621.
- Kamineni, S. and Morrey, B.F. (2004) Distal humeral fractures treated with noncustom total elbow replacement. *J.Bone Joint Surg.Am.* 86-A[5], 940-947.
- Kamineni, S., O'Driscoll, S.W., Urban, M., Garg, A., Berglund, L.J., Morrey, B.F., and An, K.N. (2005) Intrinsic constraint of unlinked total elbow replacements—the ulnotrochlear joint. *J.Bone Joint Surg.Am.* 87[9], 2019-2027.
- Kelly, E.W., Coghlan, J., and Bell, S. (2004) Five- to thirteen-year follow-up of the GSB III total elbow arthroplasty. *J.Shoulder.Elbow.Surg.* 13[4], 434-440.
- Kim, J.M., Mudgal, Ch. S., Konopka, J.D., and Jupiter, J.B. (2011) Complications of Total Elbow Arthroplasty. *J Am Acad Orthop Surg*, 19, 328-339.
- Krishnan S., and Manocha, D. (1997) An efficient surface intersection algorithm based on the lower dimensional formulation. *ACM Transactions on Graphics*, 16(1), 74-106.

- Lin, M.C., and Gottschalk, S. (1998) Collision detection between geometric models; a survey. *Proc. of IMA Conference on Mathematics of Surfaces*.
- Lee, B.P., Adams, R.A., and Morrey, B.F. (2005a) Polyethylene wear after total elbow arthroplasty. *J.Bone Joint Surg.Am.* 87[5], 1080-1087.
- Little, C.P., Graham, A.J., and Carr, A.J. (2005) Total elbow arthroplasty: a systematic review of the literature in the English language until the end of 2003. *J.Bone Joint Surg.Br.* 87[4], 437-444.
- Loebenberg, M.I., Adams, R., O'Driscoll, Sh. W., Morrey, B.F. (2005) Impaction grafting in revision total elbow arthroplasty. *The journal of bone and joint surgery*, 87-A[1], 99-106.
- Lombardo, J., Cani, M., and Neyret, F. (1999) Real time collision detection for virtual surgeries. *In Proc. of Computer Animation*.
- London, J.T. (1981) Kinematics of the elbow. *J.Bone Joint Surg.Am.* 63[4], 529-535.
- Maini, R., Aggarwal, H. (2009) Study and comparison of various image edge detection techniques. *International Journal of Image Processing*, 3[1], 1-12.
- Malone, A.A., Sanchez, J.S., Adams, R., Morrey, B.F. (2011) Revision of total elbow replacement by exchange cementing. *J Bone Joint Surg Br*, 94-B, 80-85.
- Manocha D., and Canny, J.F. (1991) A new approach for surface intersection. *International Journal of Computational Geometry and Applications*, 1(4),491-516.
- Mansat, P., Bonneville, N., Rongieres, M., Mansat, M., and Bonneville, P. (2013) Experience with the Coonrad-Morrey total elbow arthroplasty: 78 consecutive total elbow arthroplasties reviewed with an average 5 years of follow-up. *J Shoulder Elbow Surg*, 22, 1461-1468.
- Marsh, J.P., and King., G.J. (2013) Total elbow arthroplasty. *Operative Techniques in Orthopedics*, 23, 253-264.
- Matthews, J. (2002) An introduction to edge detection: The sobel edge detector. Available at <http://www.generation5.org/content/2002/im01.asp>, 2002.
- Morrey, B.F. and Bryan, R.S. (1982) Complications of total elbow arthroplasty. *Clin.Orthop.RelatRes.* [170], 204-212.
- Nadernejad, E., Sharifzadeh, S., and Hassanpour, H. (2008) Edge detection techniques: Evaluations and comparisons. *Applied Mathematical Sciences*, 2[31] 1507-1521.
- Palastanga, N., and Soames, R. (2012). *Anatomy and Human Movement: Structure and Function* (6th ed.). Elsevier. ISBN 9780702040535.
- Park, S., Kim, J., Cho, S., Rhee, S., and Kwon, S. (2013) Complications and revision rate compared by type of total elbow arthroplasty. *J Shoulder Elbow Surg*, 22, 1121-1127.
- Pentland, A., and Williams, J. (1989) Good vibrations: Modal dynamics for graphics and animation. *In Computer Graphics (SIGGRAPH '89 Proceedings)*, 23, 215-222.

- Prasad, N., and Dent, C. (2008) Outcome of total elbow replacement for distal humeral fractures in the elderly. *J Bone Joint Surg*,90-B,343-348.
- Roberts, L.G. (1965) Machine perception of 3-D solids. *ser. Optical and Electro-Optical Information Processing. MIT Press.*
- Ramsey, M.L., Adams, R.A., and Morrey, B.F. (1999) Instability of the elbow treated with semiconstrained total elbow arthroplasty. *J.Bone Joint Surg.Am.* 81 [1], 38-47.
- Sanchez-Sotelo, J. (2011) Total elbow arthroplasty. *The Open Orthopaedics Journal*, 5, 115-123.
- Schunid, F., O'Driscoll, S., Korinek, S., An, K.N., and Morrey, B.F. (1995) Loose-hinge Total Elbow Arthroplasty; An Experimental Study of the Effects of Implant Alignment on Three-dimensional Elbow Kinematics. *The Journal of Arthroplasty*, 10 (5), 670-678.
- Seidel, R. (1990) Linear programming and convex hulls made easy. *In Proc. 6th Ann. ACM Conf. on Computational Geometry*, 211-215.
- Seif, A., Salut, M.M., and Marsono, M.N. A hardware architecture of Prewitt edge detection, *Sustainable Utilization and Development in Engineering and Technology (STUDENT), 2010 IEEE Conference, Malaysia*, 99 – 101, 20-21 Nov. 2010.
- Seitz, W.H., Bismar, H., and Evans, P.J. (2010) Failure of the hinge mechanism in total elbow arthroplasty . *J Shoulder Elbow Surg*,19, 368-375.
- Shirvakshan, G.T. (2012) A comparison of various edge detection techniques used in image processing. *International Journal of Computer Science Issues*, 9[5], 269-276.
- Stokdijk, M., Nagels, J., Garling, E.H., and Rozing, P.M. (2003) The kinematic elbow axis as a parameter to evaluate total elbow replacement: A cadaver study of the iBP elbow system. *J.Shoulder.Elbow.Surg.* 12[1], 63-68.
- Sneftrop, S.B., Jensen, S.L., Johannsen, H.V., and Sojbjerg, J.O. (2005) Revision of failed total elbow arthroplasty with use of a linked implant. *J Bone Joint Surg*, 88-B, 78-83.
- Snyder, J. M., Woodbury, A. R., Fleischer, K., Currin, B., & Barr, A. H. (1993, September). Interval methods for multi-point collisions between time-dependent curved surfaces. *In Proceedings of the 20th annual conference on Computer graphics and interactive techniques* (pp. 321-334). ACM.
- Thomas, M. (2013) Interposition arthroplasty of the elbow. *ORTHOPAEDICS AND TRAUMA* 27[1], 42-49.
- Throckmorton, T., Zarkadas, P., Sanchez-Sotelo, J., and Morrey, B.F. (2010) Failure Patterns After Linked Semiconstrained Total Elbow Arthroplasty for Posttraumatic Arthritis. *J Bone Joint Surg Am*, 92,1432-1441.

- Tutunea-Fatan, O.R., Bernick, J.H., Lalone, E., King, G.J., Johnson, J.A. (2010) Application of Collision Detection to Assess Implant Insertion in Elbow Replacement Surgery. SPIE.
- Voloshin, I., Schippert, D.W., Kakar, S., Kaye, E.K., and Morrey B.F. (2011) Complications of total elbow replacement: A systematic review. *J Shoulder Elbow Surg* , 20, 158-168.
- Wang, J. (2009) Precision of cortical bone reconstruction based on 3D CT scans. *Comput Med Imaging Graph*, 33(3), 235-241.
- West, C.C. (1945) Measurement of joint motion. *Arch Phys Med*, 26(7),414-425.
- Willing, R., King, G.J., and Johnson, J.A. (2012) Computer Methods in Biomechanics and Biomedical Engineering (2012): The effect of implant design of linked total elbow arthroplasty on stability and stress: a finite element analysis, Computer Methods in Biomechanics and Biomedical Engineering, DOI: 10.1080/10255842.2012.739161
- Wright, T.W., Wong, A.M., and Jaffe, R. (2000) Functional outcome comparison of semiconstrained and unconstrained total elbow arthroplasties. *J. Shoulder. Elbow. Surg.* 9[6], 524-531.
- Wright, T.W. and Hastings, H. (2005) Total elbow arthroplasty failure due to overuse, Cring failure, and/or bushing wear. *J.Shoulder.Elbow.Surg.* 14[1], 65-72.

Chapter 2

2 B-Spline-Based Representations of Humeral Bone

2.1 Overview

This chapter proposes an accurate B-Spline fitting technique based on deformable control polygon approach to reconstruct the humerus geometry in a user-independent manner. This technique was then validated by comparison against data points of outer bone surface acquired from CMM. This validation revealed that the developed technique is capable of accurate replication of the geometry of the bone.

2.2 Introduction

As the boundaries between engineering and medical disciplines fade away, new fields began to emerge by providing links between once disjoint areas. One of good examples in this category is represented by Bio-CAD, a field found at the confluence of several established research domains including: mathematics, engineering, computer science, medicine, etc. While it is still relatively difficult to define such a novel and broad topic in just few words, it can be probably briefly stated here that one of the main objectives of Bio-CAD is to propose efficient and accurate ways for computer-assisted representation and visualization of anatomical structures associated with various forms of life. As outlined out by Sun *et al.* [Sun *et al.*, 2005], this form of computer-aided representation has begun to play an increasingly important role in numerous biomedical applications focused on design and fabrication of the artificial human tissue replacements [Sun *et al.*, 2005], manufacturing of the prosthetic implants and fixation systems [Singare *et al.*, 2006; Liao *et al.*, 2009] and preoperative surgical planning [Singare *et al.*, 2009].

However, regardless of the application focus, one of the mandatory steps to be completed resides in fast and precise geometric reconstruction of the analyzed anatomical features of the human body, whose dimensions broadly vary since dental [Wu *et al.*, 2007], osseous [Singare *et al.*, 2006; Singare *et al.*, 2006; Liao *et al.*, 2009; Au *et al.*, 2008] or even full body modeling might be necessary [Gayzik *et al.*, 2011]. While soft tissues could be part of the developed geometric representation [Gayzik *et al.*, 2011], numerous research studies focus exclusively on bone geometry [Singare *et al.*, 2006; Singare *et al.*, 2006; Liao *et al.*, 2009; Au *et al.*, 2008]. It is perhaps of importance to note here that while pixel/voxel-based representations of the geometry are also suitable for visualization of the biomedical structures, they generally lack the accuracy of detail, formulation brevity, scalability, topological context and mathematical rigorousness that are characteristic to parametric-based data which constitutes the foundation of modern CAD [Grove *et al.*, 2011]. Furthermore, once the geometry of the anatomical features has been converted to CAD-based representations, they can be further investigated by means of conventional mechanical engineering tools that are now embedded in most commercial CAD systems: dimensional and strength analysis, motion simulation, and so on.

The techniques developed so far for geometry reconstruction of various components of the human skeleton rely on relatively diverse approaches. Regardless of their specifics, all existent bone reconstruction methods fall under the general category of reverse engineering, and they all have as an input the initial cloud of points generally placed on the delimiting surfaces of the osseous feature of interest. However, unlike in the reverse engineering of the mechanical components in which the initial dataset can be acquired through contact (e.g. coordinate measurement) or non-contact (e.g. laser

scanning) methods, Bio-CAD relies on an input consisting of a cloud of points determined through segmentation of the stack of images obtained through CT scanning of the relevant human body part. The accurate segmentation of CT data constitutes the object of an extensive area of research in medical imaging, in an attempt to precisely detect the boundaries of the scanned anatomical features since the CT data acquired for clinical purposes is generally noisy due to the limitations imposed on the scanner power.

So far, the process of “reverse engineering” in the context of Bio-CAD relied either on commercial CAD software [Singare *et al.*, 2006; Singare *et al.*, 2006; Liao *et al.*, 2009; Au *et al.*, 2008; Gayzik *et al.*, 2011; Starly *et al.*, 2005; Viceconti *et al.*, 1998] or on custom-written codes aiming to enhance the accuracy and efficacy of the fitting for segmented data. While each of the two approaches has its own advantages and disadvantages, it could be probably safely assumed that while the first technique will enable faster implementations and thereby solutions, the latter will provide more accurate answers to a certain problem, since all parameters are accessible to the user who often shares the code/method developer status. Numerous studies have proposed custom-written CT data fitting algorithms focused on determination of the most suitable expressions for the parametric curves [Wytyczak-Partyka and Klempous, 2012; Wu *et al.*, 2007], or surface patches [Grimm *et al.*, 2002; Jaillet and Vandorpe, 1997; Yoo, 2011] to approximate the given dataset. Furthermore, some of the newer Bio-CAD techniques advocate for generation of heterogeneous models to incorporate both geometry and material properties [Kou and Tan, 2007; Warkhedkar and Bhatt, 2009; Grove *et al.*, 2012].

Despite the relatively large number of research studies focused on the reconstruction of the bone geometry from CT data, only a very limited subset of works was concerned with the accuracy of the model generated with respect to its physical counterpart. While the correspondence between real and virtual shapes of human body parts is relatively hard to establish in case of soft tissues that tend to deform under the external action of the measurement probe, this is not the case with bone. The techniques that have been used to verify the precision of the reconstructed geometric models often rely on optical/non-contact measurement approaches that could involve a broad variety of equipment ranging from simple flatbed scanners [Aamodt *et al.*, 1999] to more advanced options involving laser probes mounted on a coordinate measurement machine (CMM) frame [Gelaude *et al.*, 2008]. Since – debatable to some extent – the precision of non-contact methods would be always somewhat lower than that of contact-based approaches, a number of researchers have validated their bone reconstruction algorithms by means of “hard” measurements performed either with calipers used on phantoms [Noser *et al.*, 2011] and bones [Laine *et al.*, 1997] or with CMM [Au *et al.*, 2008]. For accessibility reasons, contact measurement points can only be acquired on the outer (periosteal) surface.

The accuracy of the bone reconstruction from CT slices is dependent on a number of parameters, among which the value of segmentation threshold along with the overall precision of the reverse engineering process – essentially set by the fitting tolerance – are probably the most important ones. So far, the reported mean reconstruction error for outer bone surface has varied broadly from 0.3-0.4 mm [Au *et al.*, 2008] up to 1.2-1.5 mm [Laine *et al.*, 1997], most likely as a consequence of the conceptual differences between

the techniques used. However, as Au *et al.* [Au *et al.*, 2008] noted, when it comes to shape reconstruction, the inner (i.e. canal or endosteal) surface of the bone is relatively difficult to capture due to the inherent segmentation difficulties.

Building on this, the current study proposes an automated bone reconstruction technique based on a B-Spline fitting method involving a novel deformable control polygon (DCP) approach to eliminate the need for powerful, but rather unspecialized commercial CAD software. To better control the overall precision of the reconstruction a straightforward, but effective CT segmentation will be used as part of the bone reconstruction method. The technique to be introduced further will be validated through comparisons with CMM-acquired data points placed on the outer surface of the bone, a feature that is generally lacking from studies focused on the development of custom-written CT data fitting numerical procedures. Although the overall surgical context in which this work was performed imposed a strict focus on humeral reconstruction, the techniques detailed further can be effortlessly extrapolated to other osseous geometries.

2.3 Segmentation of Bone Contours

Determination of the bone contours through numerical processing methods represents an active area of medical-oriented imaging research. While segmentation, edge detection, and contour extraction are presently being used to denote this process, its essence is always the same, namely to enable meaningful divisions or partitions of the digital images acquired through various noninvasive body scanning techniques (e.g. CT, MRI, X-ray, ultrasound, etc.) that can also be used on live organisms. In the context of the current study, segmentation constitutes an indispensable phase of “reverse engineering” of the bone geometry since it provides the cloud of points to be subsequently used during

for fitting purposes. While – by contrast with the vast majority of the segmentation proposed so far – the approach used here for segmentation might be regarded as relatively effortless, its accuracy will be demonstrated later. Evidently, it is important to note that the simplicity of the bone detection method presented hereafter is tightly related to the characteristics of the CT data being analyzed.

The principal steps of the bone segmentation process – typically performed sequentially on each axial bone slice – are outlined in Figure 2.1. The value of the threshold applied in step c) is critical for the generation of an accurate representation of the bone geometry since small variations in its value could cause important underestimations or overestimations of the object size, to be further amplified through subsequent fitting. As it can be noticed from Figure 2.1b, the precise determination of bone contours is made extremely difficult by the relatively large noise and low resolution of the CT data acquired, which is mainly caused by the restrictions imposed on the power of the CT scanning procedure when used for clinical purposes.

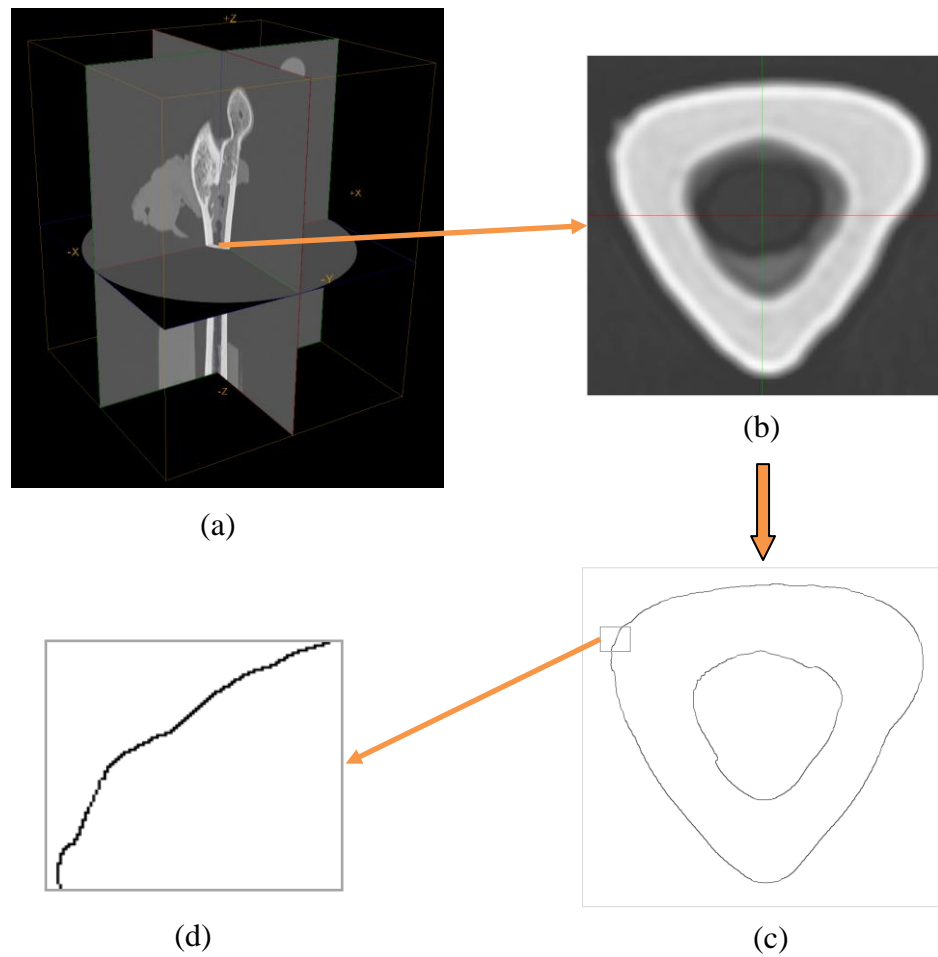


Figure 2.1: Segmentation of the bone contours: a) overall positioning of the analyzed axial CT slice, b) raw DICOM image of the axial slice, c) thresholded outer and inner bone contours, and d) detailed bone contour data points.

By following Hangartner's suggestions for accurate geometric representations [Hangartner, 2007], the threshold was set at a fixed percentage of the brightest pixel intensity as determined through the scan of the analyzed DICOM slice. Since typical CT slices are acquired as grayscale images characterized by two-dimensional arrays:

$$\mathbf{I}_{\text{CT}} = [I_{ab}] \quad (2.1)$$

where $a \in \mathbf{A}, b \in \mathbf{B}$ with $\mathbf{A}, \mathbf{B} \subset \mathbb{N}$ and $a \leq a_{\max_x}$ and $b \leq b_{\max_y}$. The a_{\max_x} and b_{\max_y} constitute pixel limits on X and Y directions respectively that are generally set by the resolution of the CT scanner (Figure 2.2). Furthermore, the common definition of grayscale images relies on 12 bits/pixel to store pixel intensity, such that $I_{ab} \in \mathbb{N}^0$ (nonnegative integers) with $I_{ab} \leq 4095$.

Based on the results of an extensive heuristic search on the values, the threshold value was set in this study at:

$$I_{\text{threshold}} = 0.6 \cdot \max_{a \in \mathbf{A}, b \in \mathbf{B}} (I_{ab}) = I_{\alpha\beta} \quad (2.2)$$

such that pixels located on outer and inner bone contours can be identified through their α and β pairs of coordinates ($\alpha \in \mathbf{A}, \beta \in \mathbf{B}$). However, to be subsequently useful for geometry reconstruction purposes, each of the thresholded pixels has to be mapped back into Cartesian coordinate system:

$$\mathbf{P}_{D_i} = [X_{D_i} \quad Y_{D_i} \quad Z_{D_i}]^T, i \in \mathbb{N}^0, i \leq n_D$$

$$X_{D_i} = (\alpha - 0.5) \frac{X_{\max_{\text{voxel}}}}{a_{\max_X}} \quad (2.3)$$

$$Y_{D_i} = (\beta - 0.5) \frac{Y_{\max_{\text{voxel}}}}{b_{\max_Y}}$$

where $X_{\max_{\text{voxel}}}$ and $Y_{\max_{\text{voxel}}}$ are the maximum limits of the voxel acquired through CT scanning. Since this fast, but rather simplistic thresholding method seemed to be capable to identify relatively accurate bone boundaries – as assessed through qualitative visual comparisons (Figure 2.3) – the proposed threshold was qualitatively compared against few conventional edge detection algorithms [Trichili *et al.*, 2002] as shown in Figure 2.4. Given the relative match between the proposed and conventional methods, the extracted data was taken into further processing.

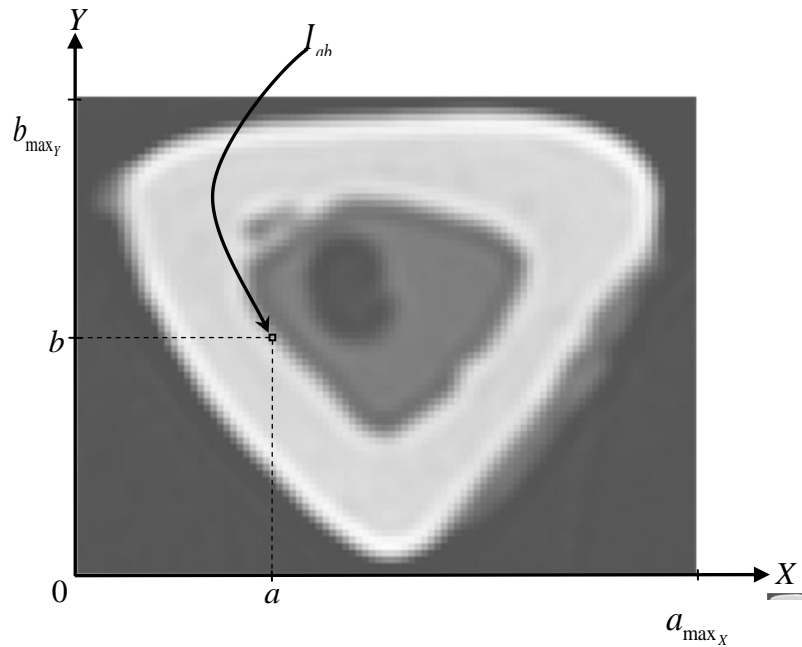
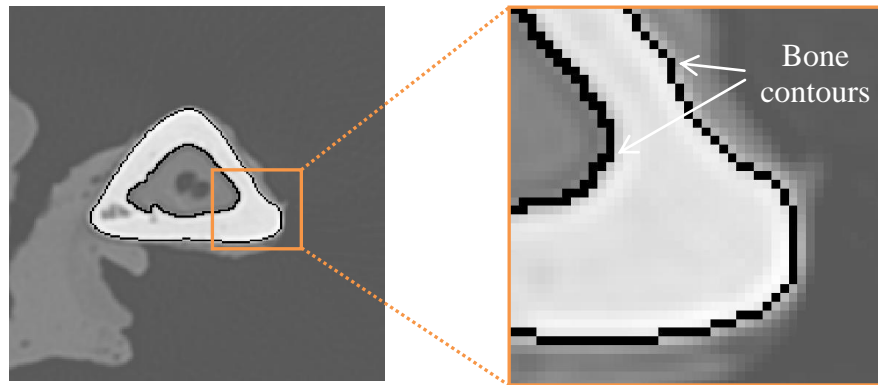
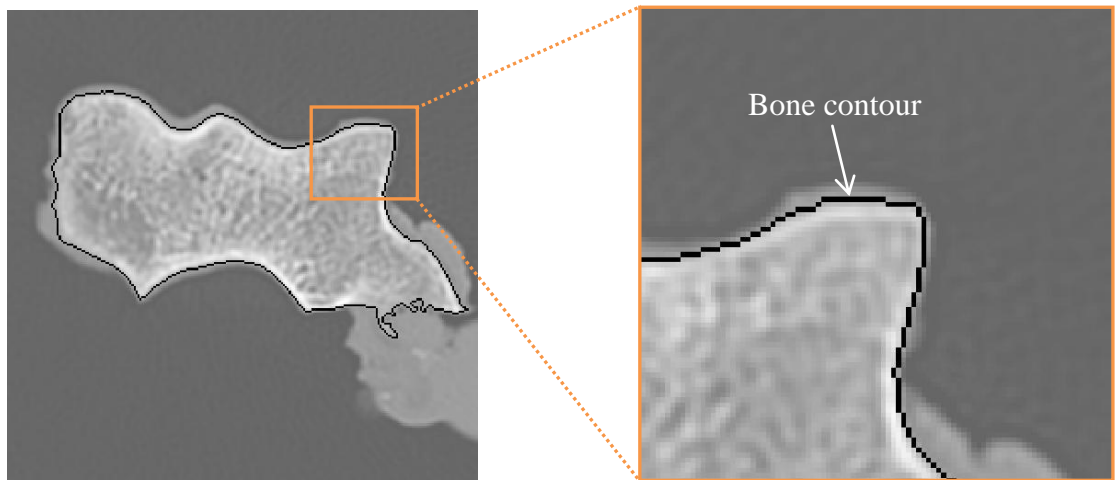


Figure 2.2: 2D pixel intensity mapping in CT slices.



(a)



(b)

Figure 2.3: Bone contours extracted through the proposed approach from representative: a) middle, and b) extreme distal cross sections of the humerus.

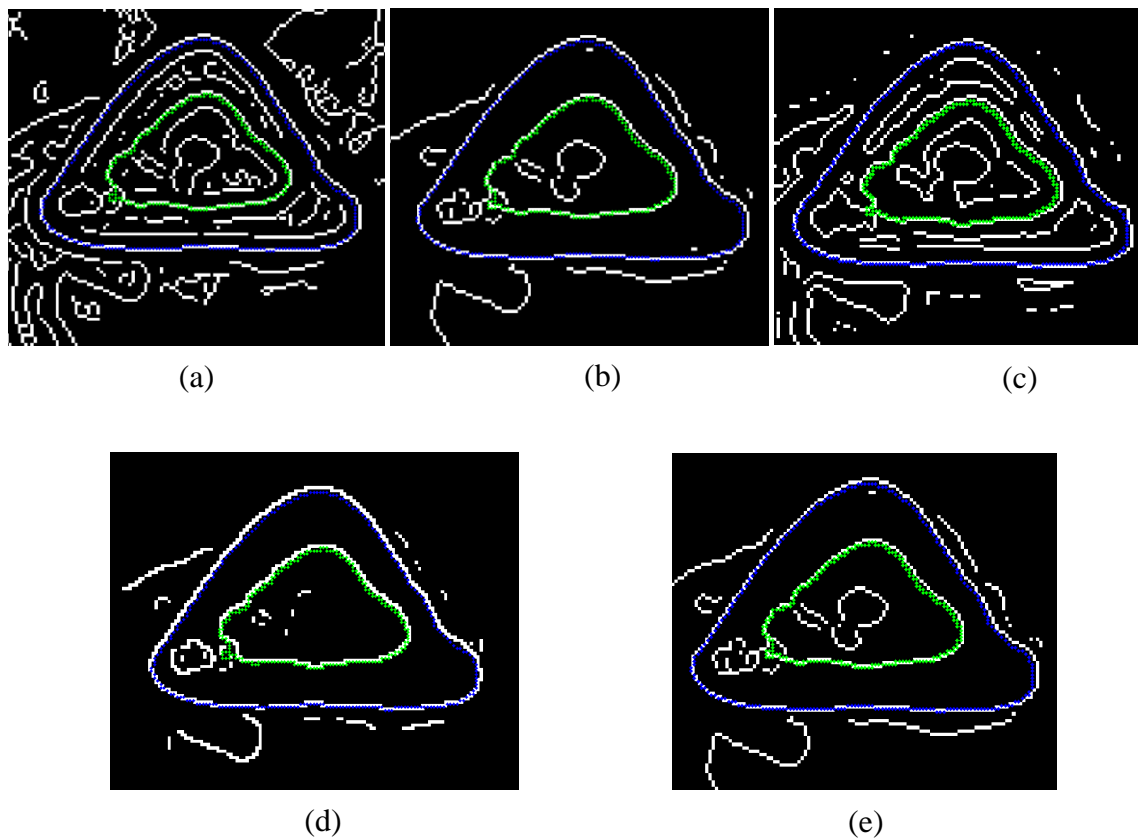


Figure 2.4: Comparison of the proposed segmentation (blue and green contours) against conventional edge detection methods: a) Canny, b) Prewitt, c) Laplacian of Gaussian, d) Roberts, and e) Sobel.

2.4 Planar B-Spline Fitting Through Deformable Control Polygon Technique

Assuming inner and outer contours of the bone have been extracted in a discrete point-based form, the next task to be accomplished consists of fitting of planar curves to extracted data points. As mentioned above, in addition to parametric data fitting options offered by commercial CAD software, a number of custom solutions have been proposed in the past to address the specifics of CT bone datasets [Grove *et al.*, 2011; Wytyczak-Partyka and Klempous, 2012; Wu *et al.*, 2007]. Furthermore, a number of imaging-oriented techniques based on classical snake or B-snake formulations have been developed for similar reasons, but in addition to their known drawbacks [Wu *et al.*, 2007], their interfacing with general purpose CAD/Bio-CAD modules remains difficult. Generally speaking, the wide majority of existent B-Spline fitting algorithms rely on one of the two approaches detailed in the comprehensive monograph on NURBS [Piegl and Triller, 1997] involving either knot removal or degree elevation techniques. However, none of these two methods seems to work well for CT-originated data points, such that supplementary smoothing and/or fairing operations are typically required [Grove *et al.*, 2011]. Alternate B-Spline fitting techniques involved either Bezier into B-Spline merging [Deng and Yang, 2008] or iterative square-distance minimization (SDM) methods as initially proposed by Pottmann *et al.* [Pottmann *et al.*, 2002] and later enhanced by others [Yang *et al.*, 2004; Wang *et al.*, 2006].

Perhaps important to mention, the view taken in [Pottmann *et al.*, 2002; Yang *et al.*, 2004; Wang *et al.*, 2006] differs significantly by others in a sense that the significance of intrinsic B-Spline parametrization based on given data points location is

greatly reduced owed to SDM approach, such that faster and better convergences are ensured [Yang *et al.*,2004]. Following up on this concept, the current study proposes a novel B-Spline fitting method based on control deformation. The main idea of the proposed method was originally mentioned by Floater [Floater, 2008] who has indicated that for fitting purposes, a good curve will not deviate too much from its control polygon. This view will be speculated in the context of the current work by enforcing that control points (CP) of approximating B-Spline are nothing but a subset of the initial CT dataset. Then, if the curve does not deviate much from its control polygon, it is reasonable to expect that it will also not deviate more from the data points to be approximated.

2.4.1 Closed B-Spline Formulation

According to classic parametric curve theory, the general formulation of a closed B-Spline curve whose shape is determined by $n+1, n \in \mathbb{N}$ control points

$\mathbf{P}_{\text{CP}_i} = [X_{\text{CP}_i} \quad Y_{\text{CP}_i} \quad Z_{\text{CP}_i}]^T$ as shown in Figure 2.5 is:

$$\mathbf{P}_B(u) = \sum_{i=0}^n N_{i,k}(u) \cdot \mathbf{P}_{\text{CP}_i}, \quad u \in [u_p, u_{n+1}] \quad (2.4)$$

where $k = p+1$ represents the order of the p -th degree curve. Although particularities of CT data approximation require a more narrow focus on planar B-Spline case ($Z_{\text{CP}_i} = 0$) only, it can be assumed that many of the upcoming considerations are extendable to non-planar situations.

In Eq. (2.5), $N_{i,k}$ are B-Spline blending functions defined by the well-known Cox-deBoor recursion:

$$N_{i,j} = \frac{u - u_i}{u_{i+j} - u_i} \cdot N_{i,j-1}(u) + \frac{u_{i+j+1} - u}{u_{i+j+1} - u_{i+1}} \cdot N_{i+1,j-1}(u) \quad (2.5)$$

that is valid for $i, j \in \mathbb{N}^0, i \leq (n+k-j-1)$ and $j \leq k$ and assumes $\frac{0}{0} = 0$. The initial

conditions of the recursion are set by:

$$N_{i,1} = \begin{cases} 1, & \text{when } u \in [u_i, u_{i+1}) \\ 0, & \text{otherwise} \end{cases} \quad (2.6)$$

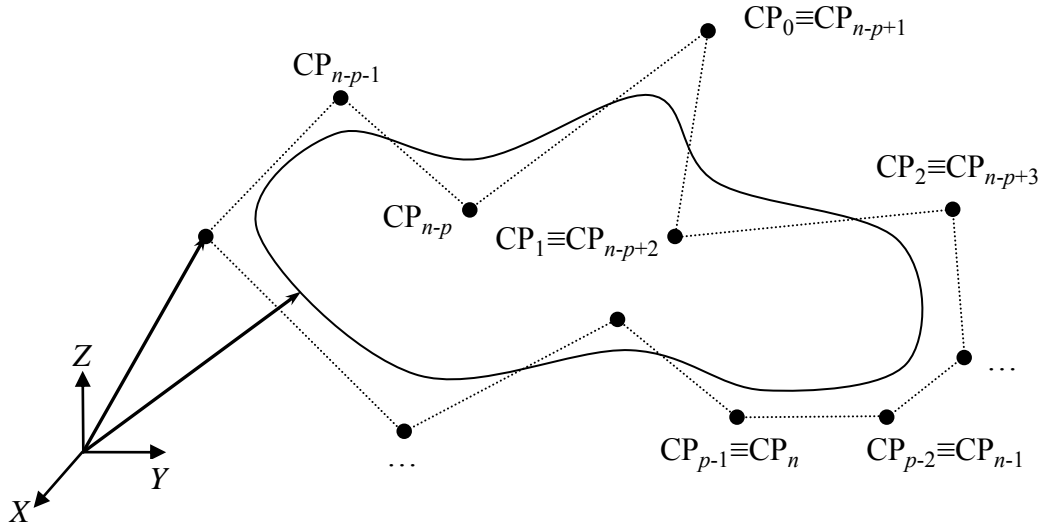


Figure 2.5: Parametric formulation of a closed B-Spline.

For closed and planar B-Spline formulations built through the control point wrapping technique described by Alavala [Alavala, 2008], although the total length of knot vector $\mathbf{U} = \{u_0 \ u_1 \ \dots \ u_m\}$ is $m = n + k + 1$, the feasible range of parameter u is restricted to $[u_p, u_{n+1}]$ range, to a total of $m - 2p$ knots. The aforementioned technique assumes a perfect overlap between the first and last p control points of the control polygon of an initially open B-Spline:

$$\mathbf{P}_{\text{CP}_i} = \mathbf{P}_{\text{CP}_{n-p+1+i}}, i \in \mathbb{N}^0, i \leq (p-1) \quad (2.7)$$

Evidently, the definition of a closed B-Spline implies that $\mathbf{P}_B(u_p) = \mathbf{P}_B(u_{n+1})$. Based on Eq. (2.4-7) it becomes clear that three elements are required to uniquely define its shape: i) order (degree); ii) knot vector \mathbf{U} ; and iii) control polygon \mathbf{P}_{CP} .

When it comes the degree of the approximating B-Spline, most of the studies in the area have already pointed out that there are little incentives to explore anything else beyond cubics. As such, the current study makes no exception from selection of cubics ($p = 3$). On the other hand, when it comes to B-Spline parametrization, the issues are not as straightforward and hence a number of alternate parametrization schemes have been explored in addition to the classical uniform, chordal and centripetal [Floater *et al.*, 2008]. However, as pointed out in [Haron *et al.*, 2012], with few exceptions [Park, 2001] most of prior work on parametrization was devoted to general (*i.e.* open) curves and ultimately “the best parametrization” continues to remain a somewhat subjective notion that is highly dependent on the designer [Haron *et al.*, 2012].

As such, only the three more conventional types of parametrizations (*e.g.* uniform, chordal and centripetal) have been investigated by the present study, while the latter two of them merely for comparison purposes. All these parametrizations are encompassed by the following generic formulation:

$$u_{i+1} = u_i + t_i, i \in \mathbb{N}^0, i \leq (m-1) \quad (2.8)$$

where u_i are the components of knot vector \mathbf{U} that correspond to known curve points \mathbf{P}_{B_i} such that $\mathbf{P}_B(u_i) = \mathbf{P}_{B_i}$. In Eq. (2.8), t_i represents the consecutive knot increments as determined by the following recursive relationship:

$$t_i = |\mathbf{P}_{B_{i+1}} - \mathbf{P}_{B_i}|^\alpha \quad (2.9)$$

where $\alpha = 0$ corresponds to uniform, $\alpha = 0.5$ to centripetal, and $\alpha = 1$ to chordal parametrization, respectively. However, by taking the view expressed by Yang *et al.* [Yang *et al.*, 2004] according to which the knot sequence should be straightforward, fixed and independent of the shape of the approximating curve, the developed B-Spline fitting technique was built around the uniform knots:

$$u_{i+1} = u_i + 1, i \in \{p, (p+1), \dots, n\} \quad (2.10)$$

2.4.2 Determination of the Control Polygon

The accuracy of the fitting is controlled at two different levels via global (or “rough”) and local (or “finish”) tolerances defined as functions of the Euclidian distance between the analyzed data points to be approximated D_i and their respective projections $\text{Proj}_B(D_i)$ on the current B-Spline shape:

$$\begin{aligned} \mathcal{E}_{\text{global}} &= \frac{1}{n_D + 1} \sum_{i=0}^{n_D} |\mathbf{P}_{D_i} - \mathbf{P}_{\text{proj}_B(D_i)}| \\ \mathcal{E}_{\text{local}} &= \max_{i \in \{0, 1, \dots, n_D\}} (|\mathbf{P}_{D_i} - \mathbf{P}_{\text{proj}_B(D_i)}|) \end{aligned} \quad (2.11)$$

As already mentioned, $\{CP\} \subset \{D\}$ such that each control point of the approximating B-Spline can be identified within the initial array of given data points: $CP_i \equiv D_{CP_i} \equiv D_l$, with $D_l \in \{D\}$. Data point projection $\text{Pr}_{\text{oj}}(D_i)$ is calculated through a nonlinear constrained optimization technique based on Newton's method, although more advanced methods can be used [Chen *et al.*, 2008].

With these theoretical notions at hand, the algorithm developed to determine the location of the control points relies on the following three major steps:

1. *Initialization*: Build a cubic B-Spline based on the location of four control points located at extreme X and Y positions of the CT point dataset:

$$\begin{aligned}
 CP_0 &\equiv \{D_i \mid X_{D_i} = \min_D(X)\} \\
 CP_1 &\equiv \{D_i \mid Y_{D_i} = \max_D(Y)\} \\
 CP_2 &\equiv \{D_i \mid X_{D_i} = \max_D(X)\} \\
 CP_3 &\equiv \{D_i \mid Y_{D_i} = \min_D(Y)\}
 \end{aligned} \tag{2.12}$$

2. *Global modification*: Ensure that at the end of this step the resulting curve has the mean deviation $\varepsilon_{\text{global}}$ smaller than a predefined limit Δ_{global} :

$$\varepsilon_{\text{global}} \leq \Delta_{\text{global}} \tag{2.13}$$

The verification of the tolerance condition is performed before performing a new iterative “round check” of the entire control polygon. If the global tolerance condition is not satisfied at the current iteration level, new control points are being inserted between each pair of consecutive control points. The new control points D_{max} inserted

between $\text{CP}_i^{\text{curr}}$ and $\text{CP}_{i+1}^{\text{curr}}$ for the next iterative “round check” are those located at the maximum distance from the analyzed side of the current (*i.e.* “curr”) control polygon:

$$\text{CP}_{i,i+1}^{\text{new}} \equiv \{D_{\max} \mid \|\mathbf{P}_{D_{\max}} - (\mathbf{P}_{\text{CP}_{i+1}^{\text{curr}}} - \mathbf{P}_{\text{CP}_i^{\text{curr}}})\| = \max_{j \in \{j_{\min}, \dots, j_{\max}\}} (\|\mathbf{P}_{D_j} - (\mathbf{P}_{\text{CP}_{i+1}^{\text{curr}}} - \mathbf{P}_{\text{CP}_i^{\text{curr}}})\|\)} \} \quad (2.14)$$

where

$$\text{CP}_i^{\text{curr}} \equiv D_{j_{\min}}, \text{CP}_{i+1}^{\text{curr}} \equiv D_{j_{\max}} \text{ for } i \in \{0, 1, \dots, n_D^{\text{curr}}\} \quad (2.15)$$

As soon as the last pair of control points has been analyzed at the current iterative cycle ($i+1 = n^{\text{cur}}$), the current array of control points is updated along with its total length n^{curr} that will include for the next iterative cycle all newly identified points $\text{CP}_{i,i+1}^{\text{new}}$ (Figure 2.6). After a number of “round check”, Eq. (2.13) will be satisfied, case in which the developed numerical algorithm will advance to the local modification phase. The primary reason for adoption of this particular type of control polygon deformation strategy resides in its efficiency, an essential attribute at the current “rough” data fitting phase whose primary role is to quickly reshape the curve according to the actual location of the data points to be approximated.

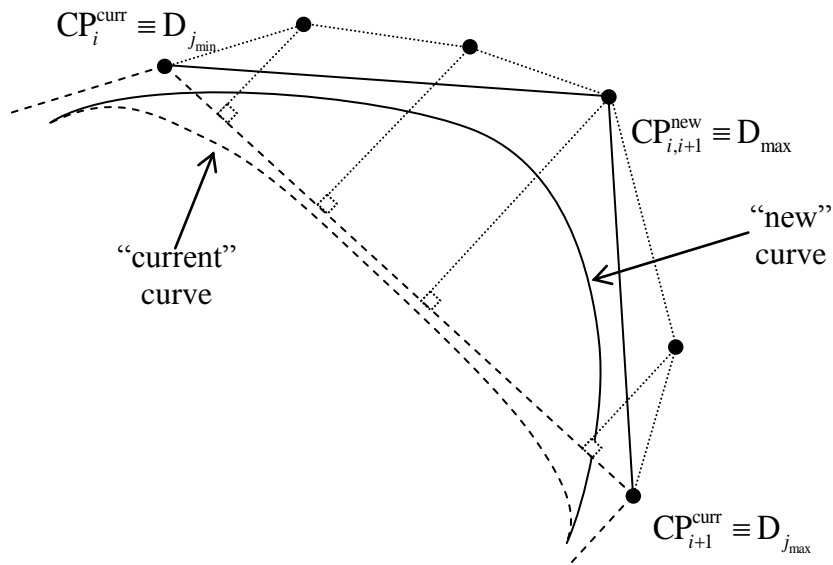


Figure 2.6: Control polygon deformation through global modification.

3. *Local modification:* Once the global tolerance constraint is satisfied, a check is being performed to verify that B-Spline approximates all given data points with a tolerance smaller than a certain preset value Δ_{local} :

$$\varepsilon_{\text{local}} \leq \Delta_{\text{local}} \quad (2.16)$$

The goal of this test is to eliminate CT data points that are more than Δ_{local} away from the current B-Spline approximant simply by including them in the revised version of the control polygon. More specifically, if Eq. (2.16) is not satisfied for the current shape of the B-Spline, the new points to be added to the revised version of the control polygon are exactly those found in a violation of the tolerance constraint. As such, all D_{max} points found to obey the following condition:

$$\begin{aligned}
\text{CP}_{i,i+1}^{\text{new}} \equiv \{ & \text{D}_{\text{max}} \mid \left| \mathbf{P}_{\text{D}_{\text{max}}} - \mathbf{P}_{\text{B proj}(\text{D}_{\text{max}})} \right| = \max_{j \in \{j_{\text{min}}, \dots, j_{\text{max}}\}} (|\mathbf{P}_{\text{D}_j} - \mathbf{P}_{\text{B proj}(\text{D}_j)}|) \\
& \text{and } |\mathbf{P}_{\text{D}_{\text{max}}} - \mathbf{P}_{\text{B proj}(\text{D}_{\text{max}})}| > \Delta_{\text{local}} \}
\end{aligned} \tag{2.17}$$

are automatically inserted between $\text{CP}_i^{\text{curr}}$ and $\text{CP}_{i+1}^{\text{curr}}$ for the next “round check” iteration (Figure 2.7). After a number of alterations performed to each of the segments of the current control polygon, Eq. (2.16) will be satisfied. At the end of the current “finish” fitting phase, no CT points to be approximated should be than Δ_{local} further away from the resulting curve. Given the known local modification properties associated with B-Splines, multiple control polygon deformations can be performed in a single “round” pass.

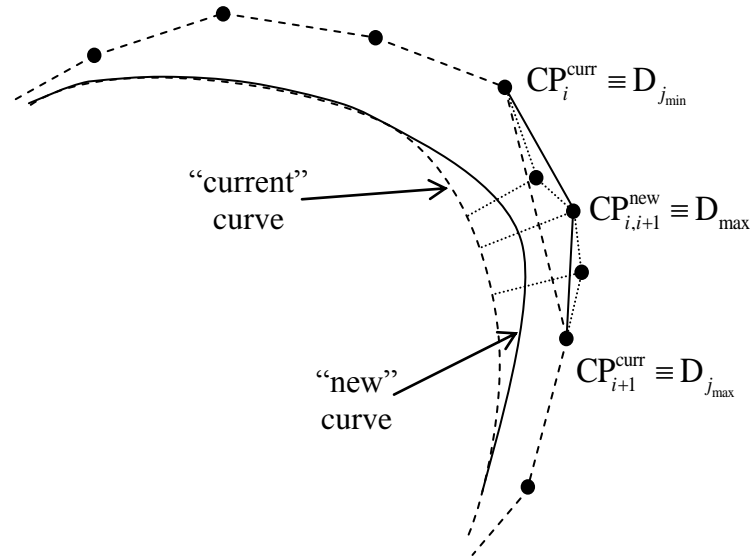


Figure 2.7: Control polygon deformation through local modification.

2.4.3 Robustness of the Proposed Approach

As an overall illustration of the control polygon deformation concept, Figure 2.8 depicts the gradual evolution of the closed B-Spline shape as a result of the continuous deformation of the control polygon subjected to global and local modification techniques. To achieve the desired final precision Δ_{local} , extensive testing has shown that global tolerance should be set at values larger than the local one:

$$\Delta_{local} < \Delta_{global} \quad (2.18)$$

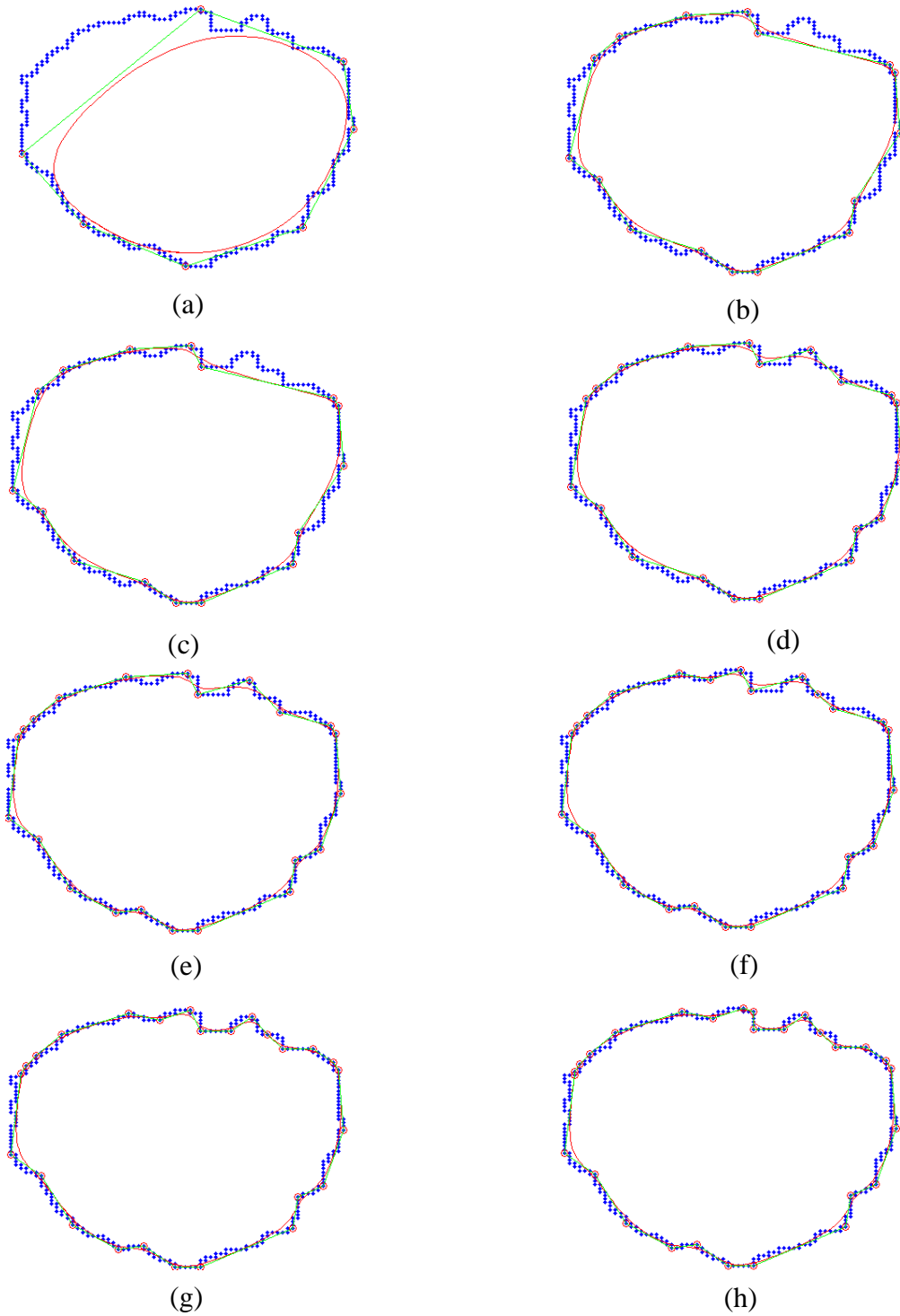


Figure 2.8: Closed B-Spline fitting through control polygon deformation: a) to b) global modification; c) to h) local modification.

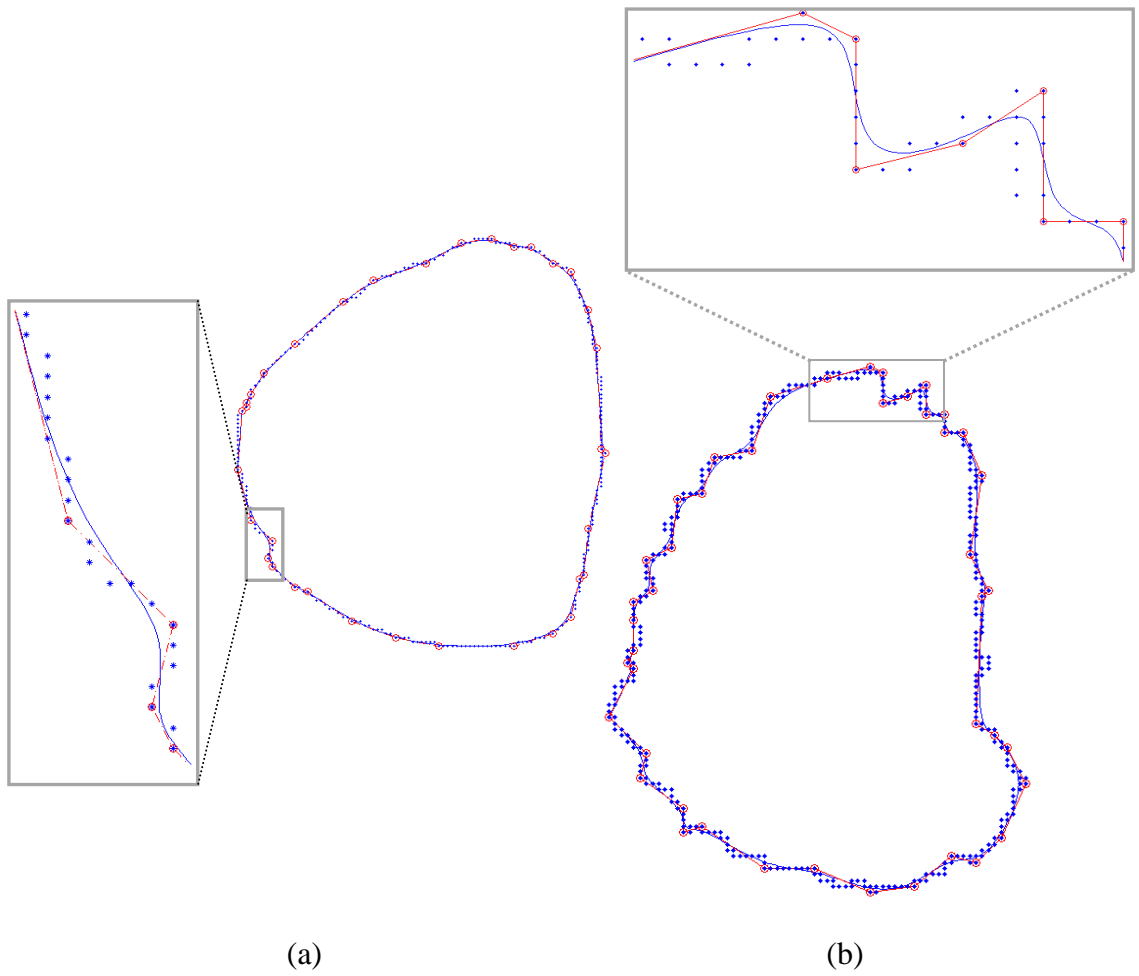


Figure 2.9: Local behavior of closed B-Spline approximants: a) outer, and b) inner bone contours.

While large number of control points will generally translate into superior fitting accuracies, they also tend to cause unnecessary undulations of the curve, especially when approximating the more complex configuration of the endosteal surface that is characterized by uneven/rougher walls. On the other hand, large numbers of control points are undesirable for data manipulation purposes, such that their number should be kept at a minimum, but this should not happen on the expense of the fitting precision. Extensive testing performed on outer and inner bone contours has shown that a judicious allocation of the two tolerances will enable smooth fitting curves for both outer and inner bone contours (Figure 2.9). Obviously, the geometric complexity of the inner contour warrants its representation through a larger number of control points but – as the detail in Figure 2.9b reveals –the fitted curve follows smoothly and closely the segmented data points.

The method described in previous sections was also compared to alternate but approximately similar techniques, in which the successive adjustments performed on the control points were substituted by those performed on knot points (KP) themselves. Here, knot points were defined as:

$$\mathbf{P}_{\text{KP}_i} = \{\mathbf{P}_B(u_i) \mid u_i \in \mathbf{U} \text{ and } \mathbf{P}_B(u_i) \in \mathbf{D}\} \quad (2.19)$$

where $i \in \mathbb{N}^0, i \leq (m-1)$. The initial set of knot points was chosen in a manner analogous with the one described by Eq. (2.12), while parametrizations have followed the three cases encompassed by Eq. (2.9). Under these conditions, the problem at hand is a classical closed B-Spline fitting problem in which the location of the control points can be determined from:

$$[\mathbf{P}_{CP}] = [\mathbf{N}]^{-1} \cdot [\mathbf{P}_{KP}] \quad (2.20)$$

where $[\mathbf{N}]$ and $[\mathbf{P}_{KP}]$ are blending functions and knot point matrices, respectively. While no supplementary details on their expression will be provided here, the reader is referred to [Piegl and Triller, 1997] for further information on the curve fitting topic.

Since in this case the global modifications based on the evaluation of the distances between data points and control polygon sides were inefficient for fitting purposes, the last two steps of the approach above were merged into a single “round check” that – after the initial fit of the closed B-Spline through the “current” knot points – will add to the updated knot array $\mathbf{P}(\mathbf{U}^{\text{new}})$, all data points located at the maximum distance with respect to the “current” curve:

$$\mathbf{KP}^{\text{new}} \equiv \{D_{\max} \mid \|\mathbf{P}_{D_{\max}} - \mathbf{P}_{\text{proj}_B(D_{\max})}\| = \max_{j \in \{0,1,\dots,n_D\}} (\|\mathbf{P}_{D_j} - \mathbf{P}_{\text{proj}_B(D_j)}\|)\} \quad (2.21)$$

The algorithm will continue to add knot points as long as both local and global tolerances determined through Eqs. (2.13) and (2.16) will remain unsatisfied.

Table 2.1: The comparison of the proposed B-Spline method against uniform, chordal and centripetal methods

Method	Average number of control points for outside boundary	Average number of control points for inside boundary	Time [s]
Uniform	24	46	158
Chordal	15	44	124
Centripetal	11	46	122
Proposed B-Spline	35	47	91

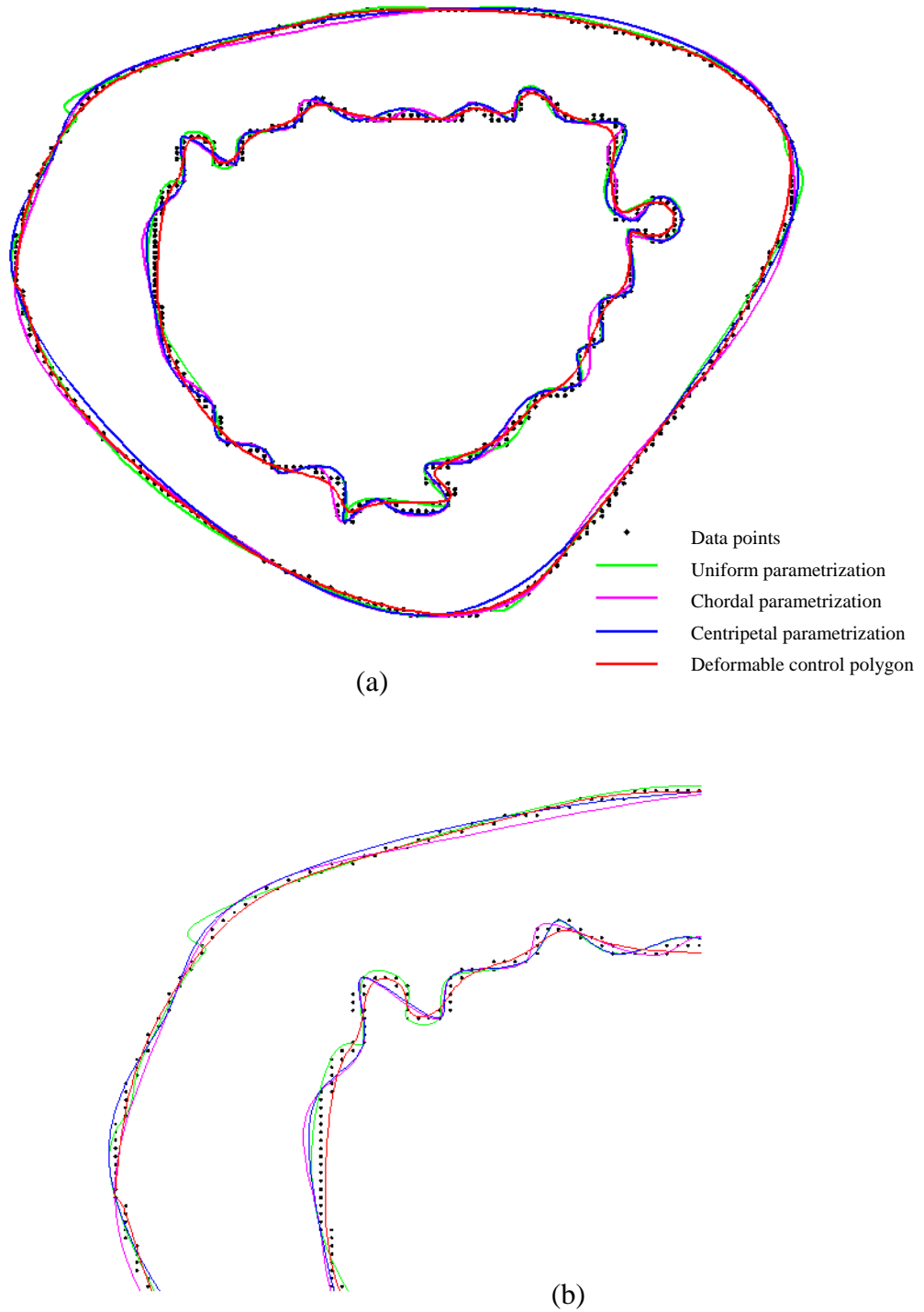


Figure 2.10: Graphical comparison between the tested closed B-Spline fitting methods.

The qualitative comparison of the four different curve fitting approaches analyzed in this study (Figure 2.10) revealed that with the exception of uniform parametrization, all other three methods seem to arguably follow reasonably well the subset of segmented data points, regardless if used for inner or outer bone contours. All fittings were performed with identical local and global fitting tolerances. However, even if no notable graphical differences can be distinguished between three of the approaches used, Table 2.1 implies that – if nothing else – the proposed method is at least 25% faster than all other analyzed fitting methods even if the final number of control points was approximately identical for all analyzed cases. As expected, B-Spline representations cause dramatic reductions in the amount of data points required to define the shape of inner and outer bone contours that decrease from 200 – 300 range to the values illustrated in Table 2.1. As a final comment on the topic of comparison, it could be asserted – on a somewhat subjective visual basis – that the approximating curves generated through the proposed deformable control polygon technique are typically smoother than their counterparts.

2.5 Accuracy of the Proposed Bone Reconstruction Technique

Traditionally, the topic of accuracy tends to be overlooked when it comes to geometric reconstruction of the osseous specimens. Intentionally or not, many of the previously proposed methods in this category were primarily focused on the computational efficiency of the algorithms proposed, and less concerned with the precision of the generated geometric dataset as compared with its physical counterpart – although this

represents one of the common concerns of any shape-oriented reverse engineering process.

By contrast, imaging-focused approaches have attempted more frequently to compare digital and physical models, although the latter ones were sometimes measured with rather imprecise devices, regardless if contact [Laine *et al.*,1997] or non-contact [Aamodt *et al.*, 1999]. Unlike this, newer studies seem to regard the coordinate measurement machine (CMM) as a veritable “gold standard” to be used towards the dimensional characterization of the physical objects [Au *et al.*, 2008]. Based on these considerations, comparisons of the proposed bone reconstruction method against contact-acquired data were included in the present study. However, since the two sets of data involved in the aforementioned side-to-side comparisons were referencing different coordinate systems, registration of the two point datasets had to be performed prior to the intended error analysis.

2.5.1 Pair-wise Registration of Point Datasets

According to the common taxonomy of the field, pair-wise registration is equivalent with the process of geometrical alignment of two correlated datasets between which the initial relative pose is known [Huber and Hebert, 2003] as depicted in Figure 2.11. Given the wealth of resources available on this topic [Rueckert and Schnabel, 2011], it will be briefly reminded ere that the key components of a pair-wise registration are: fixed (${}^F\mathbf{P}_D$) and moving (${}^M\mathbf{P}_D$) sets of data, coordinate transformation (typically of affine/rigid type), similarity assessment, and alignment optimization. The transformation of coordinates involved in a pair-wise registration is given by:

$${}^F\mathbf{P}_D = {}^F_M[\mathbf{T}] \cdot {}^M\mathbf{P}_D \quad (2.22)$$

where ${}^F_M[\mathbf{T}]$ represents the homogeneous matrix to convert point coordinates from moving to fixed coordinate systems.

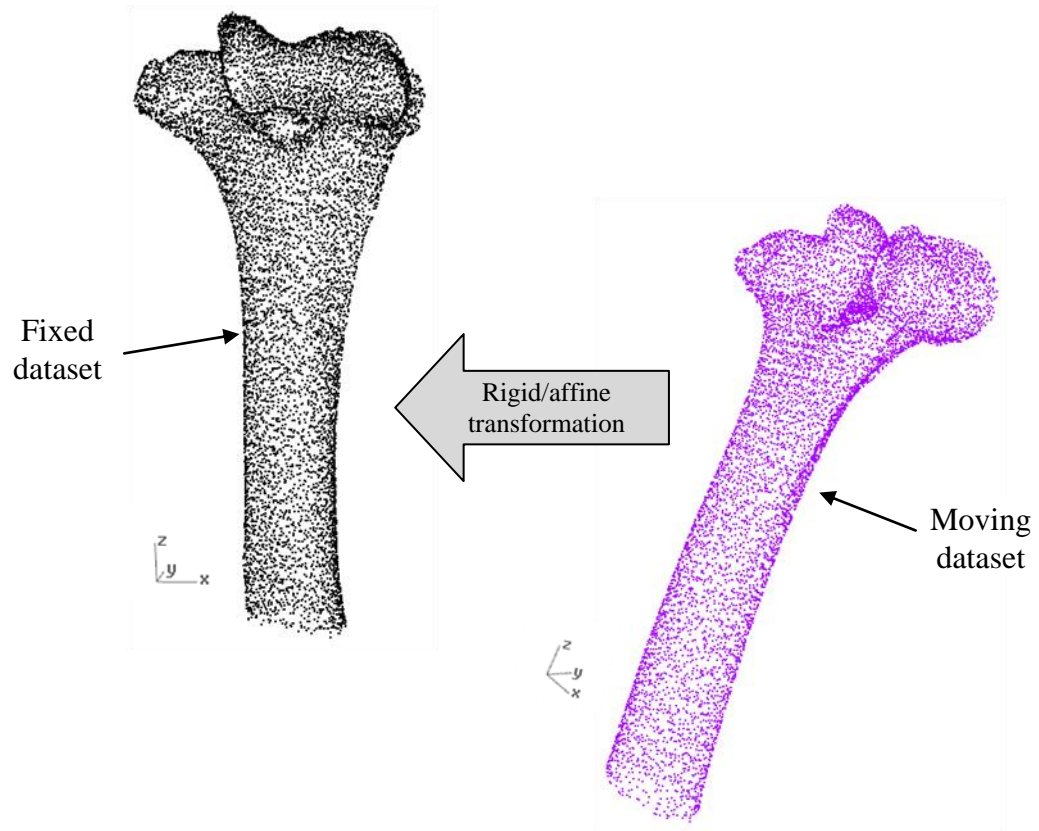


Figure 2.11: Pair-wise registration of two correlated point datasets.

Given the ubiquity of registration problems in computer vision and medical imaging, a broad palette of numerical techniques have been developed to determine ${}^F_M[\mathbf{T}]$. Among them, those comprised from a sequence of coarse and fine registration steps seem to provide the best outcome in terms of stability and accuracy in case of non-correspondent datasets [Salvi *et al.*, 2007]. Based on these considerations, the current study has employed a succession of principal component analysis (PCA) and iterative closest point (ICP) methods to determine the required coordinate transformation matrix. Since both approaches are well described in literature, no further details on them will be provided here and the reader is referred to appropriate bibliographic resources instead [Besl and McKay, 1992; Salvi *et al.*, 2007]. As a closing comment on this topic it will be stated here that similar to prior observations, the lack of a “perfect” correspondence between the pairs of datasets involved in the present work has largely prevented the convergence of ICP when used alone. By contrast, the use of PCA as a fast, but relatively inaccurate initial estimate for ICP has yielded plausible results.

2.5.2 Comparison with Contact-Acquired Data

The precision of the developed technique was tested against data collected through “hard contact” measurements performed with CMM. However, the finite length of the CMM probe combined with the large anatomical irregularity of the inner bone surface makes its measurement impractical. As such, the comparison to be further outlined was solely restricted to outer bone surface. While the collection of both inner and outer bone data would have been a preferable scenario, it is reasonable to anticipate that – given the consistency of approaches used for outer and inner contour reconstruction – the results obtained for outer bone profile are comparable to those applicable to endosteal canal.

To acquire the data, the extreme portions of the humeral specimens were first removed through disk sawing (Figure 2.12). This trimming operation was necessary because of the limitations of the subsequent contact measurement procedure whose precision decreases considerably at larger overhang lengths of the specimen. After that, the reduced humeral specimen was scanned with a GE Discovery 750 HD CT scanner set at a field of view of 97×97 mm. The scanner generated monochrome 16-bit CT slices of 512×512 pixels (0.189 mm/pixel) and voxels of 0.625 mm thickness. Approximately 70 slices were acquired in the region of interest with a beam set at 120 kVp and 240 mA to maintain the clinical relevance of the data (Figure 2.13).

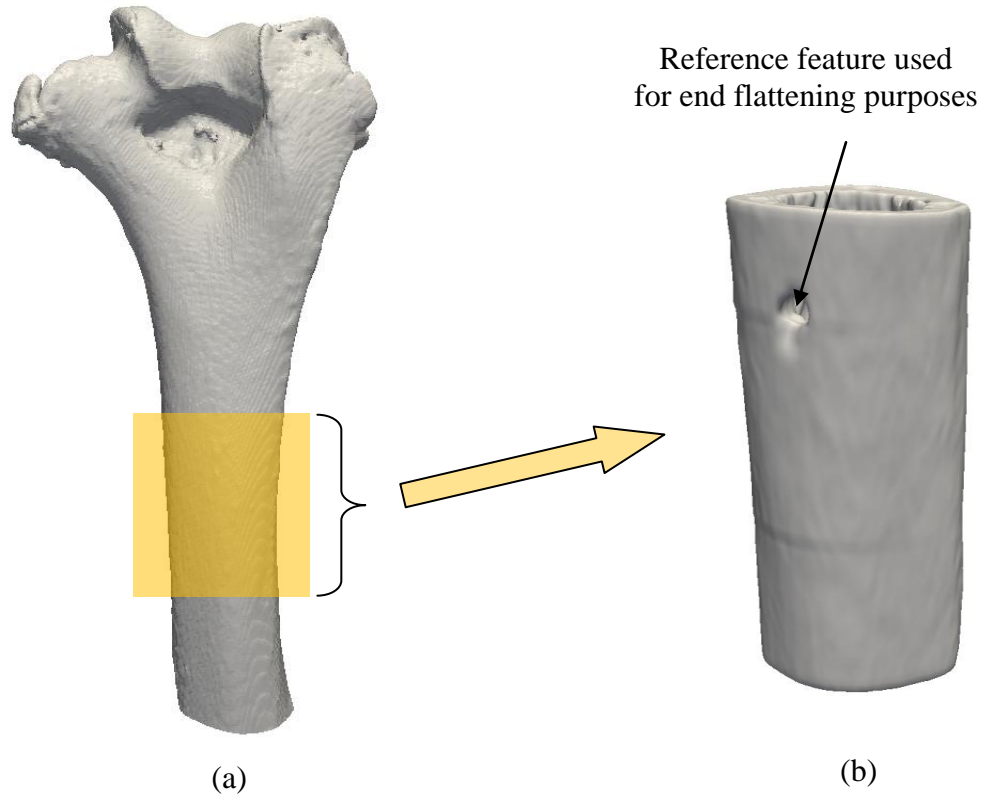


Figure 2.12: Separation of humeral fragment of interest: a) approximate location of detached humeral segment within the overall distal humerus, and b) detail view of the reduced humeral specimen.

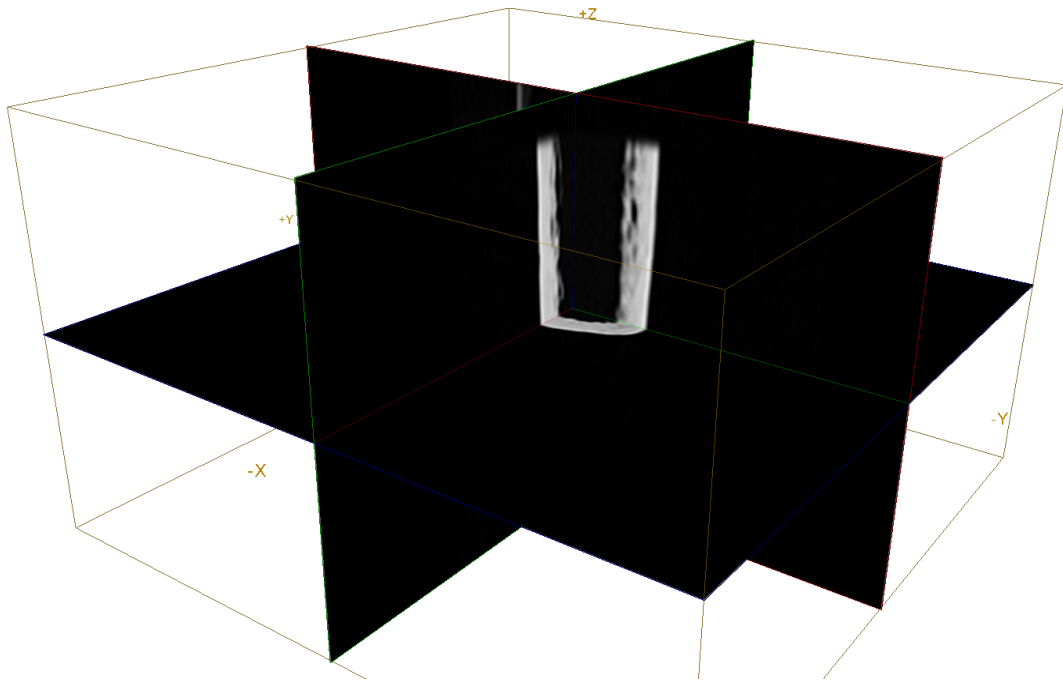


Figure 2.13: Typical cross sections through reduced humeral specimen as obtained in principal CT planes.

After the completion of the CT scanning, the top and bottom surfaces of the reduced humeral specimen were flattened at minimal depths through milling operations performed with the periphery of an end mill while the specimen was mounted – with appropriate precautions – in a chuck-like fixture. To ensure a better quality of the contact data acquired, flattening was performed in planes approximately parallel to the direction of the CT scanning planes. For this purpose, appropriate measuring references set with respect to the extremities of the specimen were used and its pre-cut orientation with respect to the milling tool was continuously adjusted by means of a rotary/swivel-tilt table installed on a Kugler Microgantry Nano5X machine tool. The system allows a simultaneous five-axis positioning with an accuracy of $\pm 1 \mu\text{m}$ and resolution of 1 nm and is equipped with a multifunctional head that includes a high speed spindle as well as a contact measurement probe. One important observation has to be made with respect of the relative order in which the flattening and CT scanning were performed. Although – in principle – these operations could have been performed in reversed order (*i.e.* end flattening first), the positioning/guiding features available on clinical CT scanners are insufficiently precise to enable a reliable alignment between CT scanning planes and top/bottom surfaces of the reduced specimen.

To allow the acquisition of CMM data, the reduced specimen was mounted in a horizontal position on the rotary table of the five-axis machine, such that outer surface points can be easily contacted through the rotation of the osseous sample (Figure 2.14). The overall kinematics of the measurement process resembles that of a four-axis machining operation. The specimen was positioned in such a way that the center of mass for its mounting face was reasonably close to the rotational axis invoked during

measurements, such that the location of the probe contact points did not have unnecessarily large deviations which in turn would have translated in longer than necessary measuring times.

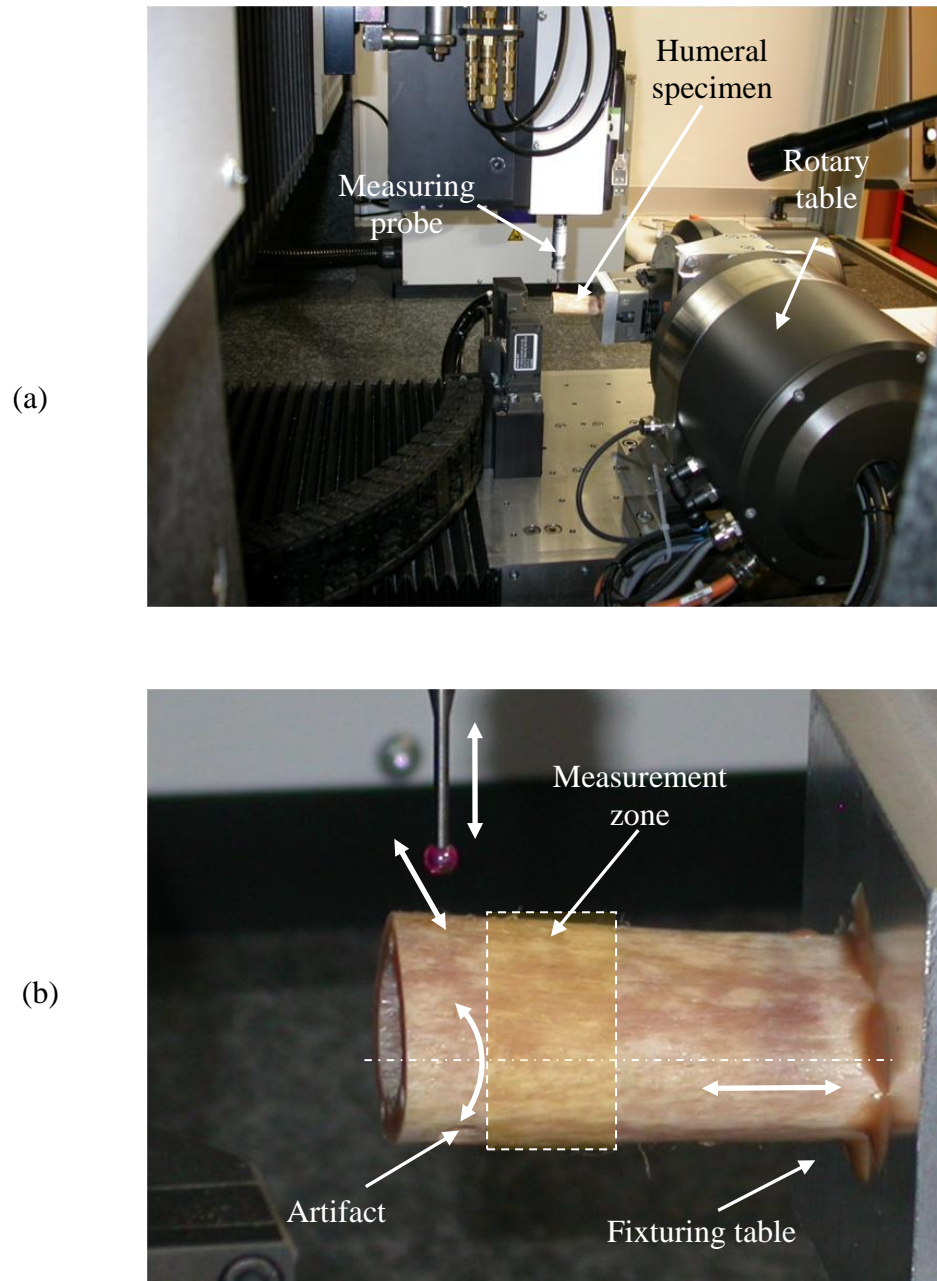
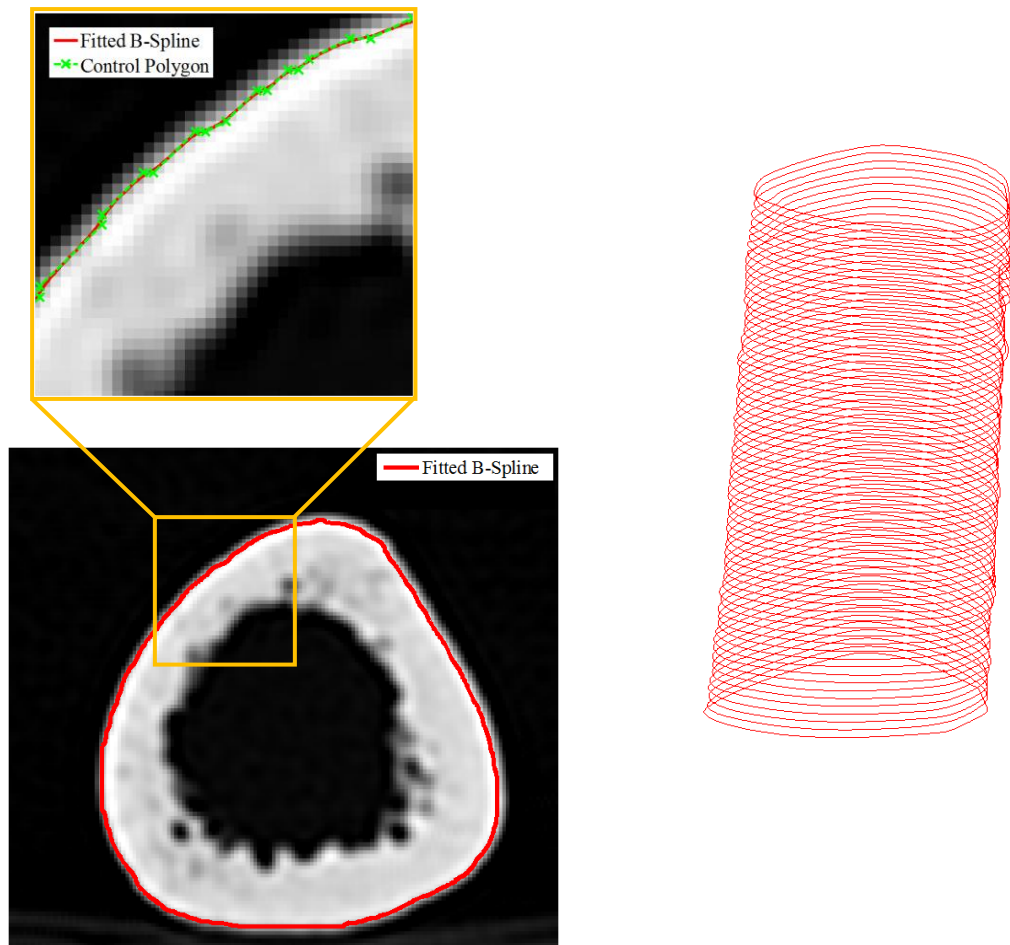
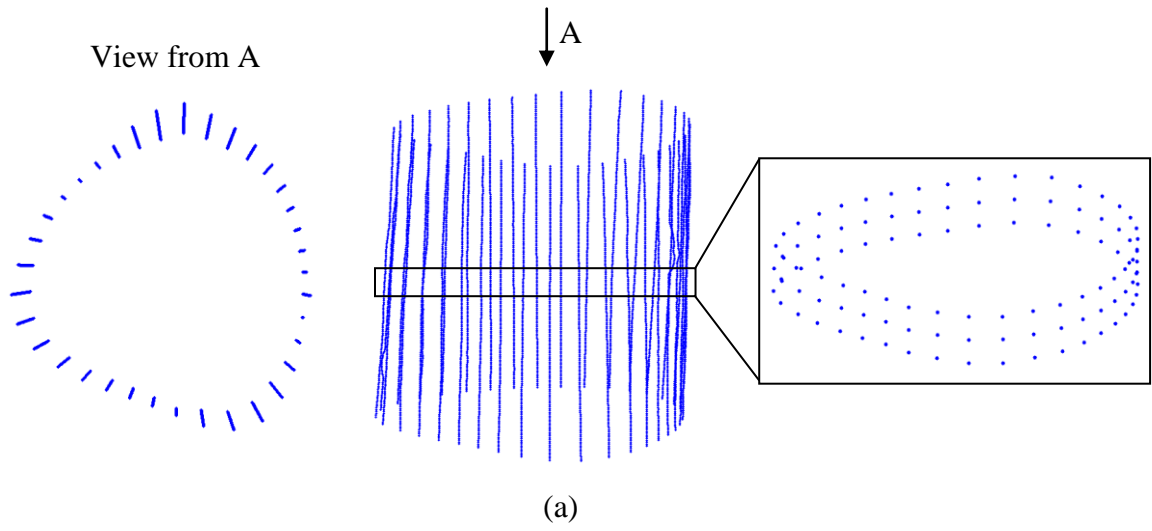


Figure 2.14: Contact data acquisition setup: a) overview of Kugler CNC measurement system, and b) kinematics of the measurement process.



(b)

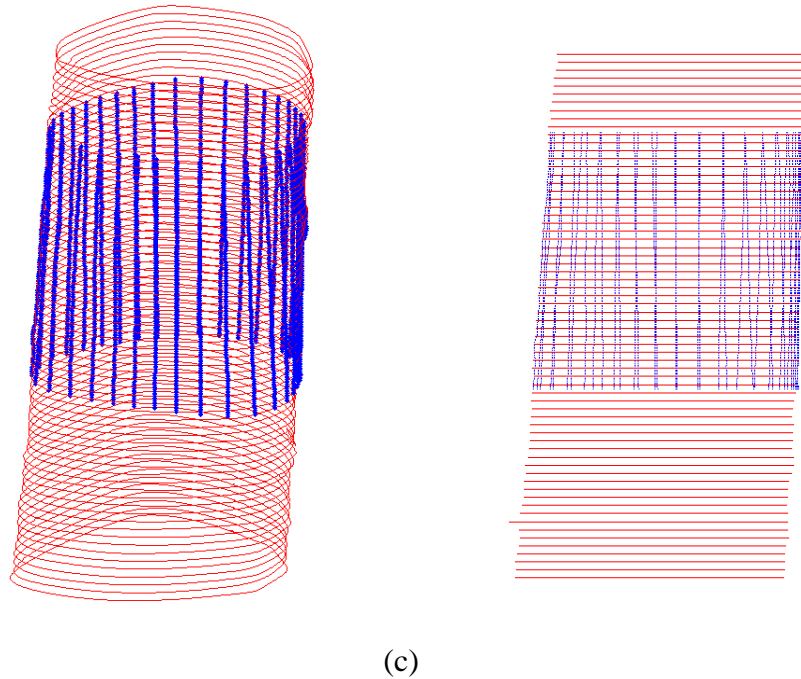


Figure 2.15: Comparison between contact-acquired data and proposed bone reconstruction method: a) CMM point dataset, b) B-Spline fitting technique, and c) overlay of the two datasets.

A total number of 5,760 points over 160 planes (36 points/plane = 10° indexing rotation) located at 0.125 mm apart from each other were collected over approximately 21 hours by means of a measurement script that was run for each of the analyzed specimens (Figure 2.15a). The large amount of data acquired was meant to facilitate the subsequent pair-wise registration between the two datasets. Few prior trials revealed that lower resolutions of the CMM data were unable to yield accurate/reliable registrations results. The contact points were acquired over a humeral length of approximately 20 mm that was located in the median zone of the osseous specimen, in an attempt to avoid both

some pre-existing artifacts (*e.g.* fixturing holes) and collisions between contact probe holder and fixturing table.

After the bone data collected through the transmissive approach was segmented by means of the method outlined in Section 2.3, outer contours were fitted with B-Splines determined with the proposed deformable control polygon technique described in Section 2.4 (Figure 2.15b). To ensure accurate comparisons between the two datasets, CMM points were registered via the combined PCA + ICP approach detailed at Section 2.5.1 to the cloud of points yielded through the discretization of the aforementioned B-Splines with a parametric increment $\Delta u = 0.01$ (Figure 2.15c).

After registration, the deviation between the CMM points and the parametric curves approximating the segmented CT data was assessed in each of the 33 CT planes located in the measurement zone of the CMM. It is important to note here that since pairwise registration was unable to ensure a perfect correspondence/coincidence between CMM and CT planes – characterized by angular deviations of $0.3 - 0.9^\circ$ between their normals – the CMM points located in the close vicinity of CT planes had to be projected on them to enable deviation evaluation. The positioning error of the CMM points caused by registration imperfections was estimated as being less than 0.002 mm ($= 0.125 \cdot \tan(0.9^\circ)$).

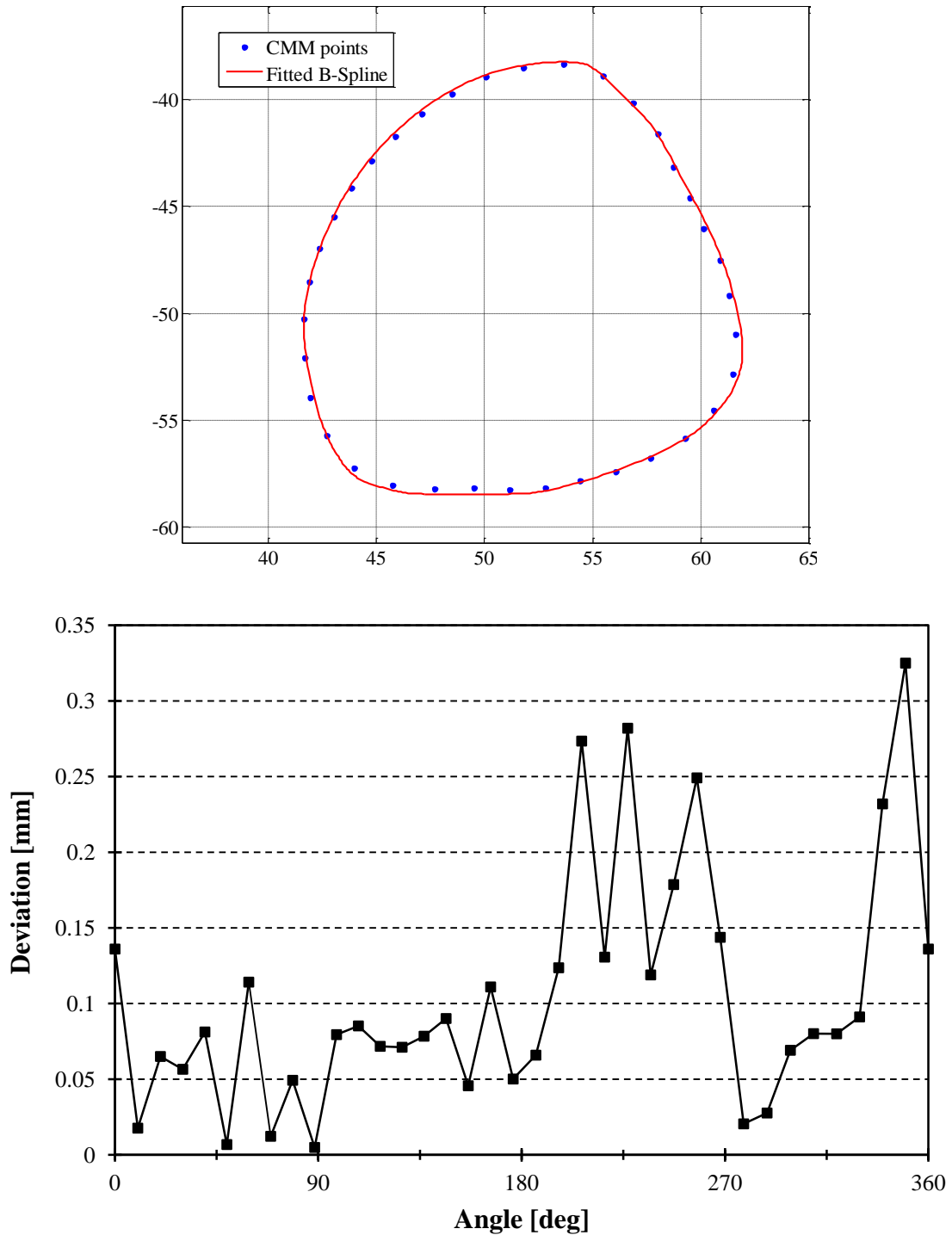


Figure 2.16: Deviation between reconstructed geometry and contact-acquired data:
a) sample of relative positioning between CMM points and parametric curves; and
b) variation of the deviation around outer contour circumference.

For all CT plane-projections of the CMM points, the deviation was defined with respect to their corresponding footprints on the neighboring parametric curves (Figure 2.16). The iterative assessment performed on three different humeral specimens revealed that the mean deviation between the outer bone geometry reconstructed through the proposed approach and the baseline/“gold standard” data acquired with precise contact measurement equipment was 0.187 ± 0.106 mm with a maximum outlier of 0.376 mm. These results suggest that the proposed bone reconstruction technique is capable to replicate with sufficient accuracy the physical geometry of the analyzed humeral specimens.

2.6 Conclusion

The present study presents a numerical algorithm capable to develop for a highly accurate and automatic conversion of raw CT data into B-Spline data. The automatic raw DICOM to B-Spline conversion entailed determination of an appropriate thresholding method, to be followed by an edge detection procedure required to establish inner and outer cortical bone boundaries. Once these boundaries have been identified, a novel curve fitting technique based on closed B-Spline was passed through each of the two sets of extracted CT points defining inner and outer bone surfaces in each of the analyzed CT slices. The primary goal of this curve fitting procedure was to generate high accuracy representations of the bone geometry with reduced computational loads. Various available classic methods were also investigated for this operation, ranging from conventional NURBS-based global interpolation methods to imaging-specific ones like B-snakes. To verify the accuracy of the automatic conversion technique, the generate parametric representation of the bone geometry was compared against physical point data sets acquired with a five-

axis Coordinate Measuring Machine (CMM). The alignment between pairs of planar data sets was achieved through a combination of principal axis of inertia and iterative closest point (ICP) techniques. As a result, the proposed thresholding method was capable to generate clean (minimal noise) data that is suitable for further parametric curve fitting procedures and also the developed curve fitting technique was able to accurately reconstruct the bone geometry.

2.7 References

- Aamodt, A., Kvistad, K. A., Andersen, E., Lund-Larsen, J., Eine, J., Benum, P., and Husby, O. S. (1999). Determination of the Hounsfield value for CT-based design of custom femoral stems. *Journal of Bone & Joint Surgery, British Volume*, 81(1), 143-147.
- Alavala, C. R. (2008). CAD/CAM: Concepts and applications. PHI Learning Pvt. Ltd..
- Au, A. G., Palathinkal, D., Liggins, A. B., Raso, V. J., Carey, J., Lambert, R. G., and Amirfazli, A. (2008). A NURBS-based technique for subject-specific construction of knee bone geometry. *Computer methods and programs in biomedicine*, 92(1), 20-34.
- Besl, P. J., and McKay, N. D. (1992, April). Method for registration of 3-D shapes. In *Robotics-DL tentative* (pp. 586-606). International Society for Optics and Photonics.
- Chen, X. D., Yong, J. H., Wang, G., Paul, J. C., and Xu, G. (2008). Computing the minimum distance between a point and a NURBS curve. *Computer-Aided Design*, 40(10), 1051-1054.
- Deng, C., and Yang, X. (2008). A local fitting algorithm for converting planar curves to B-splines. *Computer Aided Geometric Design*, 25(9), 837-849.
- Floater, M. S. (2008). On the deviation of a parametric cubic spline interpolant from its data polygon. *Computer Aided Geometric Design*, 25(3), 148-156.
- Floater, M. S., and Surazhsky, T. (2006). Parameterization for curve interpolation. *Studies in Computational Mathematics*, 12, 39-54.
- Gayzik, F. S., Moreno, D. P., Geer, C. P., Wuertzer, S. D., Martin, R. S., and Stitzel, J. D. (2011). Development of a full body CAD dataset for computational modeling: a multi-modality approach. *Annals of biomedical engineering*, 39(10), 2568-2583.
- Gelaude, F., Vander Sloten, J., and Lauwers, B. (2008). Accuracy assessment of CT-based outer surface femur meshes. *Computer Aided Surgery*, 13(4), 188-199.
- Grimm, C., Laidlaw, D., and Crisco, J. (2002). Fitting manifold surfaces to 3d point clouds. *Journal of Biomechanical Engineering*, 124(1), 136-140.
- Grove, O., Rajab, K., and Piegl, L. A. (2012). Heterogeneous modeling of medical image data using B-spline functions. *Proceedings of the Institution of Mechanical Engineers, Part H: Journal of Engineering in Medicine*, 226(10), 737-751.
- Grove, O., Rajab, K., Piegl, L. A., and Lai-Yuen, S. (2011). From CT to NURBS: contour fitting with B-spline curves. *Computer-Aided Design and Applications*, 8(1), 3-21.
- Hangartner, T. N. (2007). Thresholding technique for accurate analysis of density and geometry in QCT, pQCT and İCT images. *Journal of Musculoskeletal and Neuronal Interactions*, 7(1), 9-16.
- Haron, H., Rehman, A., Adi, D. I. S., Lim, S. P., and Saba, T. (2012). Parameterization method on B-spline curve. *Mathematical Problems in Engineering*.

- Hill, D. L., Batchelor, P. G., Holden, M., and Hawkes, D. J. (2001). Medical image registration. *Physics in medicine and biology*, 46(3), R1.
- Huber, D. F., and Hebert, M. (2003). Fully automatic registration of multiple 3D data sets. *Image and Vision Computing*, 21(7), 637-650.
- Jaillet, F., Shariat, B., and Vorpe, D. (1997, August). Periodic b-spline surface skinning of anatomic shapes. In *CCCG*.
- Kou, X. Y., and Tan, S. T. (2007). Heterogeneous object modeling: A review. *Computer-Aided Design*, 39(4), 284-301.
- Laine, H. J., Kontola, K., Lehto, M. U. K., Pitkänen, M., Jarske, P., and Lindholm, T. S. (1997). Image processing for femoral endosteal anatomy detection: description and testing of a computed tomography based program. *Physics in medicine and biology*, 42(4), 673.
- Liao, S. H., Tong, R. F., and Tang, M. (2009, October). Computer aided design and evaluation of new anatomic fixation system on entire pelvic model. In 2009 SIAM/ACM Joint Conference on Geometric and Physical Modeling (pp. 331-336). ACM.
- Noser, H., Heldstab, T., Schmutz, B., and Kamer, L. (2011). Typical accuracy and quality control of a process for creating CT-based virtual bone models. *Journal of digital imaging*, 24(3), 437-445.
- Park, H. (2001). Choosing nodes and knots in closed B-spline curve interpolation to point data. *Computer-Aided Design*, 33(13), 967-974.
- Piegl, L., and Tiller, W. (1997) *The NURBS book* (2nd ed.), Springer-Verlag New York, Inc.
- Pottmann, D., Leopoldseder, S., and Hofer, M. (2002). Approximation with active B-spline curves and surfaces. In *Computer Graphics and Applications, 2002. Proceedings. 10th Pacific Conference on* (pp. 8-25). IEEE.
- Salvi, J., Matabosch, C., Fofi, D., and Forest, J. (2007). A review of recent range image registration methods with accuracy evaluation. *Image and Vision Computing*, 25(5), 578-596.
- Singare, S., Lian, Q., Wang, W. P., Wang, J., Liu, Y., Li, D., and Lu, B. (2009). Rapid prototyping assisted surgery planning and custom implant design. *Rapid Prototyping Journal*, 15(1), 19-23.
- Singare, S., Yaxiong, L., Dichen, L., Bingheng, L., Sanhu, H., and Gang, L. (2006). Fabrication of customised maxillo-facial prosthesis using computer-aided design and rapid prototyping techniques. *Rapid Prototyping Journal*, 12(4), 206-213.
- Sun, W. (2005). Bio-CAD. *Computer-Aided Design*, 37(11), 1095-1096.
- Sun, W., Starly, B., Nam, J., and Darling, A. (2005). Bio-CAD modeling and its applications in computer-aided tissue engineering. *Computer-Aided Design*, 37(11), 1097-1114.

- Trichili, H., Bouhlel, M. S., Derbel, N., and Kamoun, L. (2002, October). A survey and evaluation of edge detection operators application to medical images. In *Systems, Man and Cybernetics, 2002 IEEE International Conference on* (Vol. 4, pp. 4-pp). IEEE.
- Tutunea-Fatan, O. R., Bernick, J. H., Lalone, E., McDonald, C. P., King, G. J., and Johnson, J. A. (2013). Assessing the performances of collision driven numerically-simulated implantation in elbow replacement surgery. *International Journal of Computer Aided Engineering and Technology*, 5(4), 263-290.
- Viceconti, M., Zannoni, C., and Pierotti, L. (1998). TRI2SOLID: an application of reverse engineering methods to the creation of CAD models of bone segments. *Computer methods and programs in biomedicine*, 56(3), 211-220.
- Wang, W., Pottmann, H., and Liu, Y. (2006). Fitting B-spline curves to point clouds by curvature-based squared distance minimization. *ACM Transactions on Graphics (ToG)*, 25(2), 214-238.
- Warkhedkar, R. M., and Bhatt, A. D. (2009). Material-solid modeling of human body: A heterogeneous B-spline based approach. *Computer-Aided Design*, 41(8), 586-597.
- Wu, X., Gao, H., Heo, H., Chae, O., Cho, J., Lee, S., and Lee, Y. K. (2007). Improved B-spline contour fitting using genetic algorithm for the segmentation of dental computerized tomography image sequences. *Journal of Imaging Science and Technology*, 51(4), 328-336.
- Wytyczak-Partyka, A., and Klempous, R. (2012, June). Application of B-splines in modelling anatomic shapes from CT scans. In *Intelligent Engineering Systems (INES), 2012 IEEE 16th International Conference on* (pp. 501-504). IEEE.
- Yang, H., Wang, W., and Sun, J. (2004). Control point adjustment for B-spline curve approximation. *Computer-Aided Design*, 36(7), 639-652.
- Yoo, D. J. (2011). Three-dimensional surface reconstruction of human bone using a B-spline based interpolation approach. *Computer-Aided Design*, 43(8), 934-947.

Chapter 3

3 Determination of Elbow Flexion-Extension Axis Based on Planar and Closed B-Splines

3.1 Overview

This chapter covers a novel technique for determination of elbow flexion-extension axis from acquired CT slices related to the distal humerus. The validation of this method was performed by comparing the results of three specimen against a conventional voxel-based determination. The developed technique is capable of accurate automatic determination of the flexion-extension axis of the elbow based on employing the curve fitting technique described in Chapter 2 followed by employing least squares fitting method.

3.2 Introduction

Among human body joints, elbow is generally regarded as the articulation with the most complex anatomy. The role of the elbow within the complex kinematics and dynamics of the upper limb is often more prominent than that of the wrist and shoulder. As such, any impairments of its functionality, caused either by accidents or by various pathological conditions (fractures, arthritis, bone tumors, etc.) have to be addressed promptly.

One of common surgical procedures aiming to restore much of the lost functionality of middle articulation of the upper extremity is total elbow arthroplasty. Within the scope of this procedure, the damaged elbow articulation is partially or totally replaced by an artificial prosthetic device attempting to match its native equivalent. One of the main factors contributing to the successful long term outcome of the surgical arthroplastic procedure is related to the accurate replication of the primary rotational axis

of the elbow [Gramstad *et al.*, 2005], commonly termed flexion-extension (FE) axis. Indeed, the misalignment between native and artificial FE axes alters elbow kinematics and eventually leads to implant failures, whose avoidance is highly desirable from both patient and health care economics perspectives [McDonald *et al.*, 2010].

In conventional biomechanics, the FE axis is somewhat axiomatically defined as the line that connects the centers of a spherical-like and circular-like feature which are easily identifiable on the anatomy of the distal humerus and are termed capitellum and trochlear sulcus, respectively (Figure 3.1). Historically, one of the first studies to characterize the direction of FE axis belongs to [London, 1981] who showed that the elbow rotates as a uniaxial joint. London proposed to define its rotational axis as the line passing through the centers of the arcs outlined by the bottom of the trochlear sulcus and the periphery of the capitellum. Further attempts to determine the location of the FE axis were performed *in vitro* by [Shiba *et al.*, 1988] who used milled slices of cadaveric humeral specimens to obtain points along the line connecting the proposed geometric centers. While the development of modern electromagnetic and radiostereometric devices allow “online” *in vivo* determinations of the perhaps variable FE axis posture (*i.e.* position and orientation) [Stokdijk *et al.*, 1999; Ericson *et al.*, 2003], these methods rely heavily on the accuracy of the equipment used and are relatively difficult to instrument in a clinical setting.

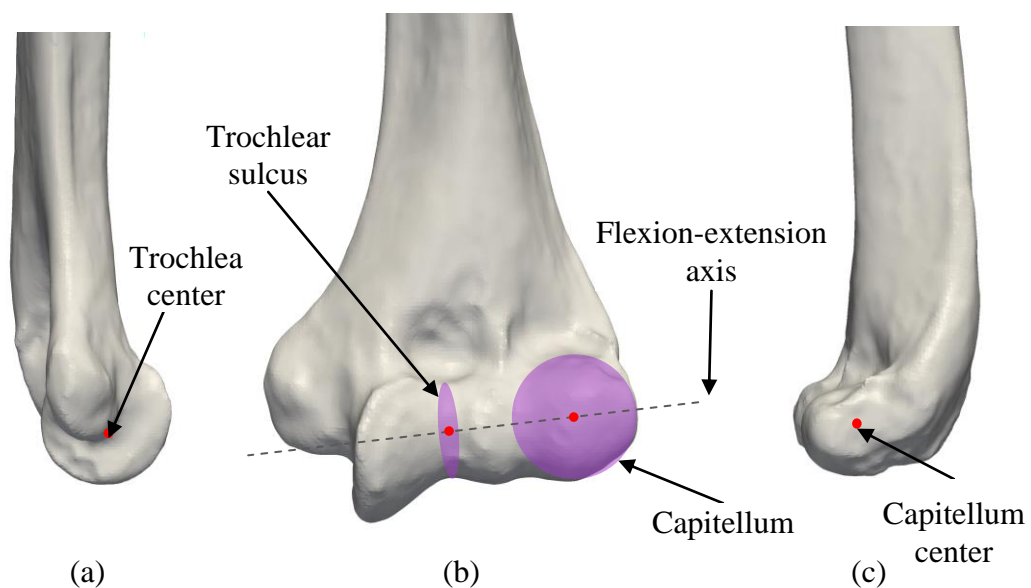


Figure 3.1: Anatomical position and orientation of the flexion-extension axis: (a) medial, (b) anterior, and (c) lateral views of the distal humerus.

Since accurate determination of the FE axis is of paramount importance during the elbow replacement procedure, surgeons are generally required to establish intraoperatively its position based on alternate humeral bony landmarks that are exposed and thereby visible during surgery [Morrey and Hotchkiss, 2000]. However, the inherent subjectivity of this approach makes it susceptible for generation of clinically significant implant alignment errors [Bhatt and Warkhedkar, 2008].

A different approach for FE axis determination relies on the use of alternate methods to reconstruct the shape of the distal humerus, followed by geometry-specific techniques to locate the position of the two relevant centers. While simple quasi-lateral radiographic images could be sufficient to establish the position of the two anatomical landmarks [Bottlang *et al.*, 2000], other types of digital data would also be suitable for

more precise and in-depth analyses of the FE axis posture. One of the first ideas in this regard was to digitize the anatomy of the capitellum and trochlea by means of a contact-based stylus, followed by the use of least-square fitting method to determine the corresponding geometric centers [King *et al.*, 1999; Duck *et al.*, 2003]. However, since this approach is only possible in context of *in vitro* studies, its later enhancements relied on CT-acquired data [Brownhill *et al.*, 2007; McDonald *et al.*, 2008; McDonald *et al.*, 2010]. One of the major advantages of the “offline” imaging-based methods is that after the incipient *in vitro* development and validation, they can be subsequently extended to patients by means of conventional fiducial-based registration procedures [McDonald *et al.*, 2008]. On the other hand, since in this case user interaction along with manual manipulation of the data is required, it is relatively difficult to preserve the consistency of the results among users with undesirable consequences on FE axis posture accuracy.

To address this issue, automated shape recognition methods based on imaging techniques could be employed [Mundy, 2006], especially when combined with appropriate orientation estimation techniques that are specifically oriented towards anatomical structures [Bagci *et al.*, 2011]. However, when it comes to practical engineering applications, the effectiveness of voxel-originated representations – regardless if surface or volume-based - that are omnipresent in medical imaging is at least questionable for at least two reasons [Anderson and Crawford-Hines, 2000; Grove *et al.* 2011]. On one hand, the accuracy of voxel-originated data is direct proportional with its overall size. Moreover, its accuracy is inherently limited by the initial size of the pixel/voxel used during body scan procedure that in turn cannot be decreased too much due to patient radiation overexposure concerns. Because of this, while the advancements

in computer graphics might be arguably capable to keep up with the data volume requirements, resolution restrictions are unavoidable. Secondly, the use of the pixel/voxel-originated data within the wide range engineering applications available is impossible, since many of them require parametric (B-Spline/NURBS) data formats in order to make full use of their capabilities.

Numerous attempts were made to develop heterogeneous parametric representation of various human body external or internal elements/organs [Bhatt and Warkhedkar, 2008]. In most studies, parametric models were generated through specialized reverse engineering operations performed on data acquired via CT or MRI scans. Very often, the reconstruction of the human anatomical features comes down to approximation of the planar segmented point datasets with parametric curves determined by means of custom-written routines [Ane and Roller, 2010; Grove *et al.* 2011] or commercial CAD software [Ameddah and Assas, 2011].

The survey of the available literature reveals that in relatively rare instances the precision of the parametric models of the human body-originated shapes was checked either against their physical correspondent or against alternate imaging-based methods. Within the scope of the current study, an automated technique was developed to establish the orientation of the elbow FE axis based on the parametric models of the distal humerus. The position of the two geometric centers involved in FE axis determination was tested against a conventional method involving medical imaging-specific data and procedures. More details about the developed FE axis determination technique will be provided in the subsequent sections.

Accurate determination of the flexion-extension axis of the elbow affects the outcome of implant replacement. This study proposes an automated approach capable of determining the FE axis based on a stack of axial computer tomographic (CT) imaging slices of the distal humerus. The core of the algorithm consists of an original technique employing control polygon deformation used to approximate the segmented outer cortical bone points with closed B-Splines, followed by curvature-based and least squares fitting methods for determination of the two relevant geometric centers. The new approach was validated against a conventional voxel-based FE axis determination procedure involving marching cubes algorithm.

3.3 B-spline Based Determination of Flexion- Extension axis

In order to determine the location of the two geometric centers that are determinant for the direction of the elbow FE axis, the first task to be accomplished is generation of a parametric representation of the distal humerus based on an input consisting of axial slices of the bone acquired through CT scanning.

3.3.1 Detection of Outer Cortical Bone Contours

The method used in this study to extract the outer contours of the cortical bone represents a direct derivation of the concept proposed by [Hangartner, 2007], according to which an accurate threshold for geometric segmentation purposes has to be set at 49% of the difference of the density between the adjacent tissues. It is important to outline here that when CT data is acquired with low power – which is generally the case in clinical settings – the resulting images are blurred and this has a significant impact on the

dimensional precision of the segmented bone contours. Specifically, when segmentation threshold value is set too high, the resulting representation of the bone will be smaller than its physical correspondent, whereas when threshold value is set too low, CT bone model will yield larger than the actual object.

The thresholding technique used in this study was based on the percentage of the brightest pixel identified in each of the CT slices analyzed. After performing a series of preliminary tests involving outer bone contour segmentation with various thresholds, followed by verification against the scanned humeral specimen, it was established that the best dimensional match between digital and physical representations of the bone is achieved when 40% from the brightest pixel intensity is used as a cutoff value. By employing this threshold value, the segmentation algorithm zigzagged through the columns of the 2D matrix of pixels characteristic to each CT slice and retained the row of the first and last pixel of each column satisfying the set thresholding condition. Obviously, no pixels were extracted for columns placed away from bone cross sectional area (Figure 3.2a).

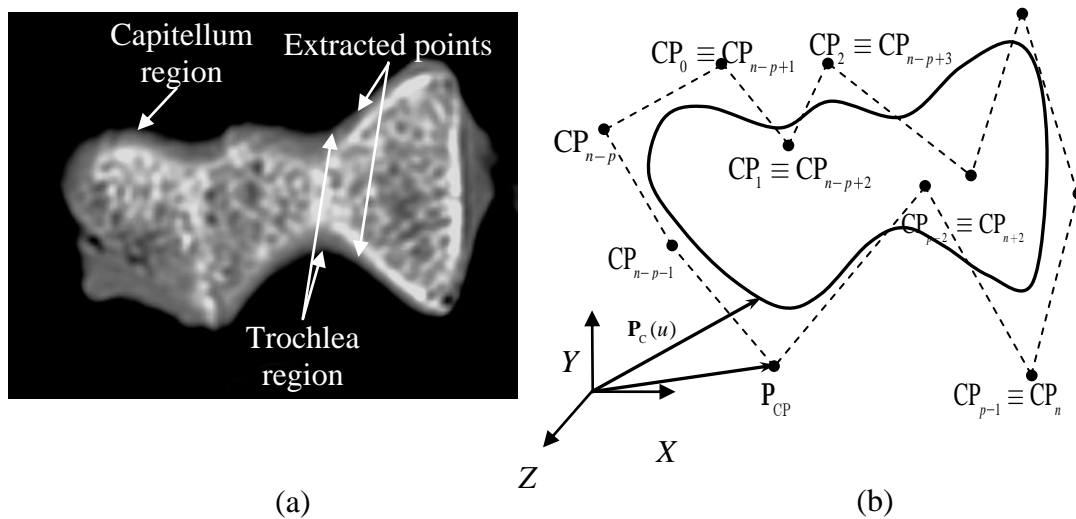


Figure 3.2: Representative axial cross sections through distal humerus: (a) raw CT slices, and (b) parametric curve-approximated outer bone contours.

Furthermore, the characteristics of the scanning (column zig-zag and horizontal left-right) process performed on the 2D matrix of pixels ensure that segmented CT data points form an array that can be easily ordered based on their X (or Y) coordinates, such that geometrically adjacent/neighbors points become consecutively placed in the array. This sequentiality bears a particular importance from the perspective of the curve fitting technique to be detailed below.

3.3.2 Planar and Closed B-Spline Fitting by Control Polygon Deformation

Given the level of maturity acquired by the parametric representations in context of engineering applications, this type of curves was chosen to approximate the point dataset extracted through the thresholding technique outlined at previous chapter. Furthermore, among the existing pool of parametric curves, planar and closed B-Splines are deemed to be capable to trace the outer contours of distal humerus with sufficient precision. Both planar and closed characteristics of the parametric curves used are dictated by the intrinsic features of the acquired CT slices and humeral cross sections, respectively.

According to generic computer-aided geometric modeling theory, the parametric form of planar and closed B-Splines (Figure 3.2b) is:

$$\mathbf{P}_B(u) = \sum_{i=0}^n N_{i,k}(u) \cdot \mathbf{P}_{CP_i} \quad (3.1)$$

where $\mathbf{P}_{CP_i} = \begin{Bmatrix} X_{CP_i} \\ Y_{CP_i} \\ Z_{CP_i} \end{Bmatrix}$ are the $n+1$ vertices of the control polygon, and $u \in [u_p, u_{n+1}]$ is the

inherent parameter of the curve. In Eq. (3.1) $k = p+1$ represents the order of the p -th

degree curve. The present study relied on the control point wrapping technique to generate the parametric expression of closed and planar ($Z_{CP_i} = \text{const.}$) B-Splines as described by [Alavala, 2008]. According to this method, the last p points are to coincide with the first p points of the control polygon in order to close an initially open B-Spline:

$$\mathbf{P}_{CP_i} = \mathbf{P}_{CP_{n-p+i}}, \text{ for } i \in \{0, 1, \dots, (p-1)\} \quad (3.2)$$

The closed form of the curve implies that

$$\mathbf{P}_B(u_p) = \mathbf{P}_B(u_{n+1}) \quad (3.3)$$

The $N_{i,k}(u)$ parametric functions used to blend the influence of $n+1$ control points \mathbf{P}_{CP_i} in Eq. (3.1) are defined by the well known Cox-de Boor recursive formula:

$$N_{i,j}(u) = \frac{u - u_i}{u_{i+j} - u_i} N_{i,j-1}(u) + \frac{u_{i+j+1} - u}{u_{i+j+1} - u_{i+1}} N_{i+1,j-1}(u) \quad (3.4)$$

for $j \in \{0, 1, \dots, k\}$ and $i \in \{0, 1, \dots, (n+k-j-1)\}$

with initial conditions set by:

$$N_{i,1}(u) = \begin{cases} 1, & \text{if } u \in [u_i, u_{i+1}), \text{ for } i \in \{0, 1, \dots, (n+k-2)\} \\ 0, & \text{otherwise} \end{cases} \quad (3.5)$$

$$\frac{0}{0} = 0$$

It is important to emphasize here that while the total length of the knot vector $\mathbf{U} = \{u_0 \ u_1 \ \dots \ u_m\}$ of the cubic B-Spline curve is $m = n + k + 1$, the active range of its

closed form is defined only between u_p and u_{n+1} , to a total of $m - 2p$ knots. The planar and closed B-Splines built on these theoretical premises are C^{p-1} continuous.

When it comes to the actual determination of knot values, numerous attempts were made to propose robust parametrization schemes capable to trace even highly sparse and/or unevenly distributed datapoints. While the number of studies focused on determination of adequate parametrizations for closed B-Spline is considerably smaller, some progress in this direction was also reported in the literature [Park, 2001]. Within the limited scope of the current study and by taking into consideration the relative uniformity and density of the datapoints to be approximated by the closed B-Spline, just uniform parametrization was tested:

$$u_{i+1} = u_i + 1, \text{ for } i \in \{p, (p+1), \dots, n\} \quad (3.6)$$

Based on mathematical formulation outlined by Eqs. (3.1-7) above, planar and closed B-Spline curves are fully determined once their control polygon and knot vector are known. Because of this, the current problem at hand comes down eventually to the development of a robust B-Spline fitting technique, capable to approximate with a certain tolerance/accuracy a given of extracted data points. Many of the presently available solutions in this regard rely or are derived – to a larger or a lesser extent – on the knot removal techniques as originally detailed by [Piegl and Tiller, 1997] in their comprehensive monograph on NURBS. Nevertheless, the current work employed a completely different approach, essentially inspired from a recent observation according to which a “good” B-Spline would not deviate much from its control polygon [Floater, 2008].

The novel approach developed in the framework of the present study for B-Spline fitting purposes is based on a knot insertion technique performed to support a deforming control polygon whose length increases progressively to enable a superior approximation of the given datapoints. The continuous reshaping of the closed B-Spline is controlled at two different levels, via global and local tolerances, respectively. To satisfy this condition, global control $\varepsilon_{\text{mean}}$ is defined as a mean deviation of all given CT data points D_i to the closed B-Spline curve:

$$\varepsilon_{\text{mean}} = \frac{1}{n_D} \cdot \sum_{i=0}^{n_D} |\mathbf{P}_{D_i} - \text{proj}_{\mathbf{B}}(\mathbf{P}_{D_i})| \quad (3.7)$$

where n_D represents the number of extracted CT data points, and $\text{proj}_{\mathbf{B}}(\mathbf{P}_{D_i})$ represents the location of the projection (footprint) of D_i on the closed B-Spline curve. For each analyzed data point, the projection is determined through a nonlinear bounded optimization technique employing golden section search and parabolic interpolation while seeking for the point on the curve whose normal passes through D_i . As expected, $|\mathbf{P}|$ in Eq. (3.7) represents the Euclidian norm of the three-dimensional vector \mathbf{P} .

In addition to $\varepsilon_{\text{mean}}$, a local control was also used:

$$\varepsilon_{\text{max}} = \max_{i \in \{0, \dots, n_D\}} (|\mathbf{P}_{D_i} - \text{proj}_{\mathbf{B}}(\mathbf{P}_{D_i})|) \quad (3.8)$$

The core of the developed curve fitting algorithm consists in the iterative addition of new control points that are selected in a manner capable to gradually reduce the distance between given dataset and approximating curve. Following Floater's idea [Floater, 2008], control points are in fact intentionally chosen to be a subset of the data

points to be approximated ($CP_i \in \{D_0, D_1, \dots, D_{n_D}\}$). Due to the particularities of the CT thresholding method used, each control point of the approximating B-Spline can be uniquely identified within the initial array of given data points ($CP_i \equiv D_{CP_i} \equiv D_i$).

The algorithm used to fit a closed and planar cubic B-Spline to the segmented points of the distal humerus consists of the three major steps:

Step 1: Initialization.

The algorithm starts off by generating a closed B-Spline whose shape is determined by the location of four control points selected in extreme positions with respect to the initial dataset of segmented CT points (Figure 3.3a):

$$\begin{aligned}
 \mathbf{P}_{CP_0} &= \mathbf{P}_{D_i} \mid X_{D_i} = \min_{j \in \{0, \dots, n_D\}} (X_{D_j}) \\
 \mathbf{P}_{CP_1} &= \mathbf{P}_{D_i} \mid X_{D_i} = \max_{j \in \{0, \dots, n_D\}} (Y_{D_j}) \\
 \mathbf{P}_{CP_2} &= \mathbf{P}_{D_i} \mid Y_{D_i} = \max_{j \in \{0, \dots, n_D\}} (X_{D_j}) \\
 \mathbf{P}_{CP_3} &= \mathbf{P}_{D_i} \mid Y_{D_i} = \min_{j \in \{0, \dots, n_D\}} (Y_{D_j})
 \end{aligned} \tag{3.9}$$

Step 2: Global modification.

This step ensures that the mean error defined by Eq. (3.7) becomes smaller than a certain predefined tolerance:

$$\varepsilon_{\text{mean}} \leq \Delta_{\text{global}} \tag{3.10}$$

To achieve this goal, a new control point is dichotomically added between each pair of successive control points, such that each control point segment is practically replaced by two new ones. The new points added to the control dataset in each iteration are those

located at maximum distances with respect to the current location of the control polygon segments according to the following relationship:

$$\mathbf{P}_{\text{CP}_i^{\text{new}}} = \mathbf{P}_{\text{D}_{\text{max}}} \left| \left| \mathbf{P}_{\text{D}_{\text{max}}} - (\mathbf{P}_{\text{CP}_{i+1}} - \mathbf{P}_{\text{CP}_i}) \right| = \max_{j \in \{l, \dots, (l+1)\}} (|\mathbf{P}_{\text{D}_j} - (\mathbf{P}_{\text{CP}_{i+1}} - \mathbf{P}_{\text{CP}_i})|) \right. \quad (3.11)$$

This step iterates around the contour of the bone until global tolerance condition in Eq. (3.10) is satisfied. The new control point $\mathbf{P}_{\text{CP}_i^{\text{new}}}$ is inserted in the control point array between \mathbf{P}_{CP_i} and $\mathbf{P}_{\text{CP}_{i+1}}$.

Step 3: Local modification.

Once the global condition of tolerance was met, fitting algorithm moves in the local modification stage, according to which a new preset modifier is being enforced:

$$\varepsilon_{\text{max}} \leq \Delta_{\text{local}} \quad (3.12)$$

The maximum distance condition between given points and fitted B-Spline expressed through the definition of ε_{max} in Eq. (3.8) is now being checked around the entire contour of the parametric curve. A new control point is added to the dataset whenever the condition outlined by Eq. (3.12) is not verified. The new control point to be included for the next iterative representation of the fitted curve represents precisely the point located at the maximum distance with respect to the

$$\mathbf{P}_{\text{CP}_i^{\text{new}}} = \mathbf{P}_{\text{D}_{\text{max}}} \left| \left| \mathbf{P}_{\text{D}_{\text{max}}} - \text{proj}_{\text{B}}(\mathbf{P}_{\text{D}_{\text{max}}}) \right| = \max_{j \in \{l, \dots, (l+1)\}} (|\mathbf{P}_{\text{D}_j} - \text{proj}_{\text{B}}(\mathbf{P}_{\text{D}_j})|) \right. \quad (3.13)$$

Similar to the global modification phase, the new control points identified in a certain iterative step are always inserted in the control point array according to their

sequential position, *i.e.* between CP_i and CP_{i+1} which correspond to l and $l+1$ counters in Eq. (3.13), respectively. Based on the known local modification properties of the B-Spline curves, each iterative step around the closed contour performs a gradually decreasing number of control point additions until the local tolerance condition is met.

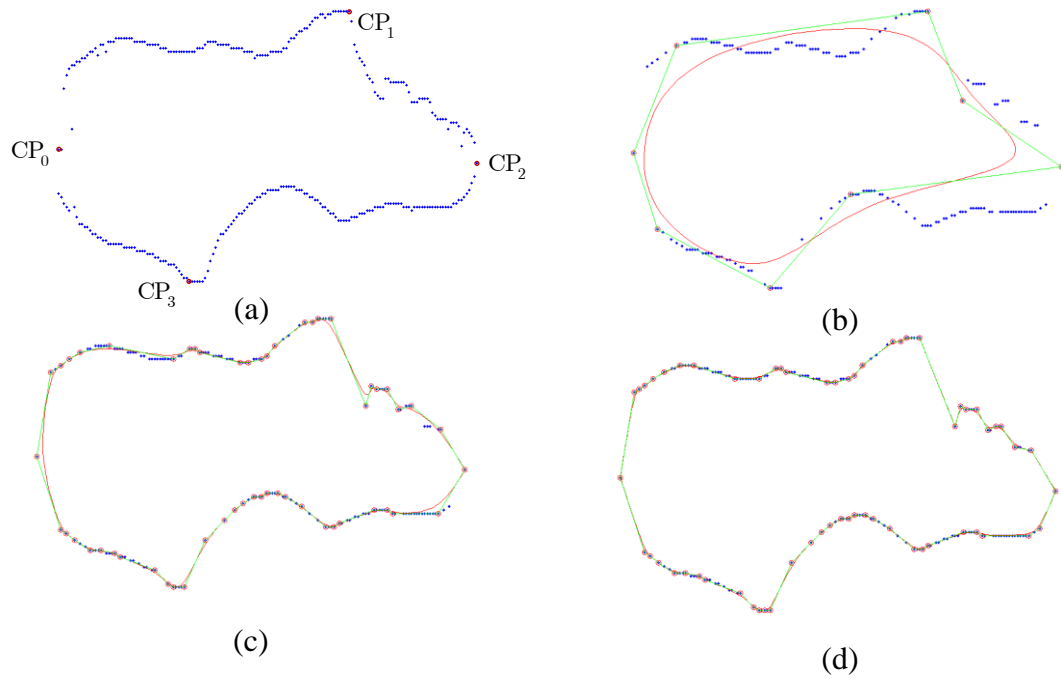


Figure 3.3: Progressive adaptation of the fitted B-Spline curve shape: (a) initial set of segmented CT points, (b) approximating curve after one global modification iteration (one Step 2), (c) approximating curve at the end of the global modification phase (end of Step 2), and (d) final shape of the approximating curve (end of Step 3).

The iterative application of the B-Spline fitting technique based on control polygon deformation enables a progressive wrapping of the control polygon around the extracted CT points, as depicted in Figure 3.3. All decisions made during technique development phase were meant to ensure the efficiency, simplicity and precision of the

proposed approach, but at the same time one of the major objectives of the novel curve fitting method was to reduce the need for subsequent B-Spline fairing/smoothing.

3.3.3 Automated Detection of Relevant Features through Local Curvature Analysis

Once the outer contours of the distal humerus were approximated with planar and closed cubic B-Splines, the next task comes down to identification of their regions with relevance in FE axis position determination. Given the fact that capitellum and trochlea regions (Figure 3.2a) are involved in sphere and circle fitting respectively, a number of points have to be placed on the parametric curves in appropriate locations. In the current approach, determination of the regions of interest of the B-Splines has been performed through an in-depth analysis of their local curvature pattern. Figure 3.4 illustrates the variation of the local curvature along a sample B-Spline whose nonessential lateral portion was trimmed off for clarity purposes.

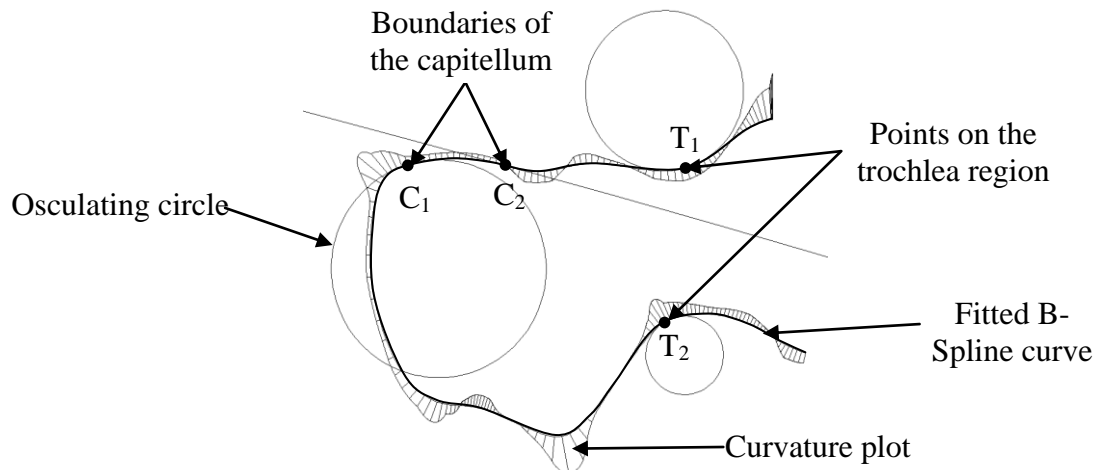


Figure 3.4: Sample of local curvature pattern along distal humeral B-Splines.

As it can be observed, all significant points of the analyzed planar B-Spline slices (C_1, C_2, T_1, T_2) are in fact associated with major changes in the curvature variation. As such, their spatial location can be uniquely specified in conjunction with curvature-related conditions.

According to the fundamentals of differential geometry, the curvature of a parametrically-expressed planar curve can be determined with:

$$\kappa_B(u) = \frac{\frac{dX_B(u)}{du} \cdot \frac{d^2Y_B(u)}{du^2} - \frac{d^2X_B(u)}{du^2} \cdot \frac{dY_B(u)}{du}}{\left[\left(\frac{dX_B(u)}{du} \right)^2 + \left(\frac{dY_B(u)}{du} \right)^2 \right]^{\frac{3}{2}}} \quad (3.14)$$

where $X_B(u)$ and $Y_B(u)$ constitute the components of the general B-Spline curve defined by Eq. (3.1). Since this signed value can be easily calculated for each of the reconstructed B-Splines of the distal humerus, the geometric position of the four points with relevance in FE axis determination can be established based on the following criteria:

$$\begin{aligned} \mathbf{P}_{T_1} &= \mathbf{P}_B(u_{T_1}) \Big| \kappa(u_{T_1}) = \max_{X_T < X_{CP_1}} (|\kappa(u_T)|) \\ \mathbf{P}_{T_2} &= \mathbf{P}_B(u_{T_2}) \Big| \kappa(u_{T_2}) = \max_{X_T > X_{CP_3}} (|\kappa(u_T)|) \\ \mathbf{P}_{C_{1,2}} &= \mathbf{P}_B(u_{C_{1,2}}) \Big| \kappa(u_{C_2}) = 0, X_{T_1} > X_{C_2} > X_{C_1}, u \in (u_{C_1}, u_{C_2}) \Big| \kappa(u_T) \approx \text{const.} \end{aligned} \quad (3.15)$$

For the two points outlining the trochlea region (T_1, T_2) as well as for one of the bounds of the capitellum region (C_2), numerical searches based on golden section search were used to determine their corresponding parameter values ($u_{T_1}, u_{T_2}, u_{C_2}$) along the analyzed B-Spline. These searches were facilitated by the local extremum or zero conditions outlined by Eq. (3.15), as well as by the particular position of these points with

respect with cross sectional landmarks defined by Eq. (3.9), which essentially became the initial guess points of the numerical technique. A special mention has to be made about C_2 , which actually requires a triple pass through zero curvature condition, while the trochlea points T_1, T_2 were found at the first curvature extremum encountered at the left of CP_1 and at the right of CP_3 , respectively. Here, the “left” and “right” directions are associated with search direction expressed in terms of parameter u , which decreases in both situations. Once C_2 was found, C_1 will be always located at the left end of the approximately constant curvature region of the B-Spline. This represents a direct consequence of the spherical geometry of the capitellum. Once both u_{C_1} and u_{C_2} are assessed, a number of discrete points are generated on the curve segment between them, to be subsequently used in the geometric feature evaluation. Minor adaptations of the search directions/boundaries in Eq. (3.15) are required when switching between left and right hand humeral specimens.

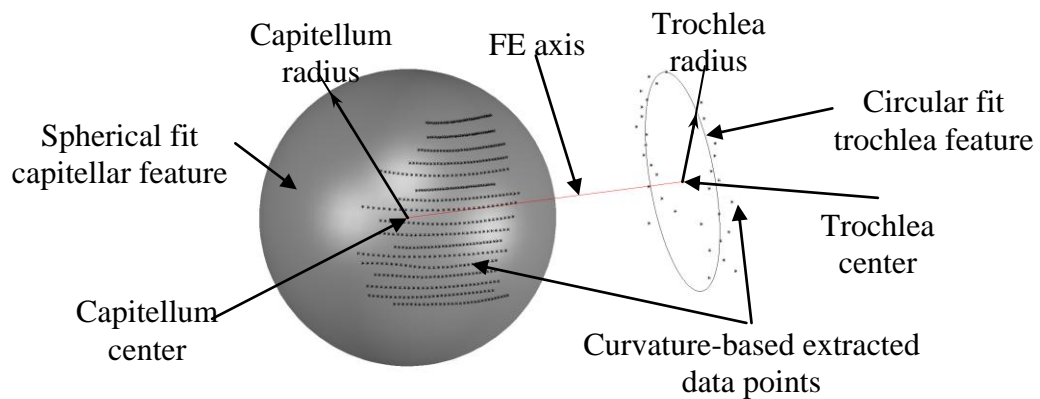


Figure 3.5: Determination of the geometric characteristics of FE axis through least squares fitting.

After all relevant capitellum and trochlea points are identified and then extracted from closed B-Splines, standard least squares fitting methods based on Gauss Newton searches were employed to establish the geometric characteristics of the spherical and circular features associated with capitellum and trochlear shapes (Figure 3.5). The circular profile of the trochlea requires determination of its characteristic plane prior to other geometric computations. As mentioned in the introductory section, the line connecting capitellum and trochlea centers is generally acknowledged as the FE axis of the elbow articulation. In addition to their positional attributes, the fitting technique facilitates radius-based dimensional characterization of the two anatomical landmarks of interest.

3.4 Conventional Voxel-based Determination of FE axis

This imaging-oriented method was used to provide a comparison basis for the original B-Spline based approach described in previous section. The conventional technique, originally developed in a clinical study [King *et al.*, 1999], was subsequently tested also in a navigated implantation and/or computer simulated context [McDonald *et al.*, 2008; Tutunea-Fatan *et al.*, 2010].

Similar to parametric geometry approach, the procedure relies on an input consisting of CT scans of the analyzed humeral specimen. Following image acquisition and thresholding/segmentation, the polygonal mesh representation of the distal humerus is generated by means of a custom-written numerical code developed in conjunction with Visualization Toolkit graphic libraries [Schroeder *et al.*, 2006]. The core of the polygonal mesh generation engine consists of marching cubes algorithm [Lorensen and Cline, 1987]. Once the humeral surface has been constructed, the user is required to roughly

locate in a graphically interactive manner the capitellum and trochlea regions. This operation is performed by selecting manually nine and three points on capitellum and trochlea respectively that are capable to delimit the shape of the analyzed anatomical features (Figure 3.6).

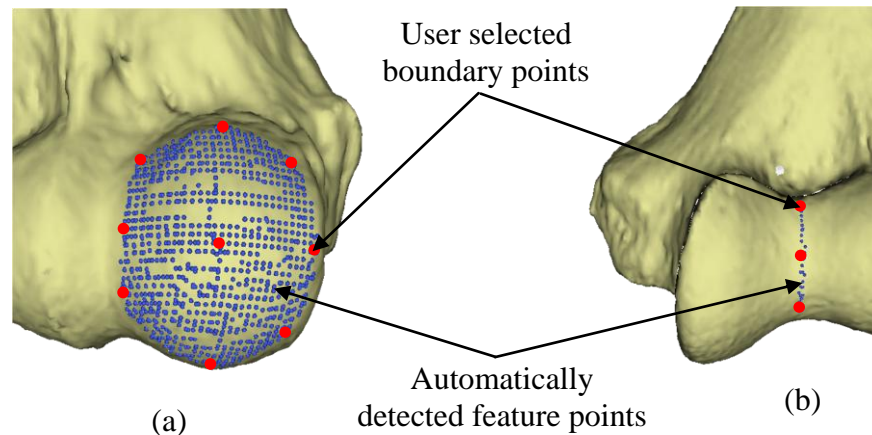


Figure 3.6: Graphical localization of the anatomical features of interest through manual delimitation of their boundaries for: (a) capitellum, and (b) trochlea.

Once their boundaries have been identified, the developed numerical algorithm employs a proximity search to determine all polygonal mesh vertices that are placed within the previously selected limits of the feature. Once the coordinates of all relevant points of the humerus have been found (Figure 3.6), least squares method was once more used to establish the posture of the FE axis, along with dimensional characteristics of the capitellum and trochlea.

3.5 Results and discussion

In order to compare the two approaches, fresh-frozen specimens of distal humerus were acquired with a 64-slice GE LightSpeed Ultra computer tomography. The CT scans were acquired by placing the humeral bone in a position of approximate coaxiality between its

longitudinal canal “axis” and that of the CT scanner. The scanning parameters were set to approximately replicate the clinical settings with a field of view of 16x16 cm and a power of 120 kVp at 90 mAs. The stack of raw CT slices generated was characterized by a resolution of 512x512 pixels and a voxel size of 0.3125x0.3125x0.625 mm. Once the images were acquired, the position and orientation of the FE axis was determined through parametric and voxel-based techniques detailed in Sections 3.3 and 3.4, above. The two end tolerances for Steps 2 and 3 of the parametric approach were set at $\Delta_{\text{global}} = 0.2$ and $\Delta_{\text{local}} = 0.5$ respectively.

A visual comparison of the results for one of the analyzed specimens is presented in Figure 3.7. As it can be noticed, the size and location of the two relevant features determined through the B-Spline approach matches reasonably well both the position of the real anatomical landmarks, as well as the set of points used to determine the FE axis through the conventional approach that will be further used as a baseline in the following quantitative comparisons.

It should be noted here that the term “error” is intentionally avoided from the upcoming discussion, as it would somehow imply that a “golden standard” has been used as a baseline - perhaps in the form of hard measurements performed directly on physical specimens. While this type of investigations is possible, they were simply regarded as out of the scope of the current study since they would require a more detailed understanding of the effect of environmental conditions (temperature, humidity) on the surface hardness and dimensional characteristics of the distal humerus. Because of these considerations, the conventional voxel-based approach will be treated as a reliable reference, since it was previously validated in the clinical context.

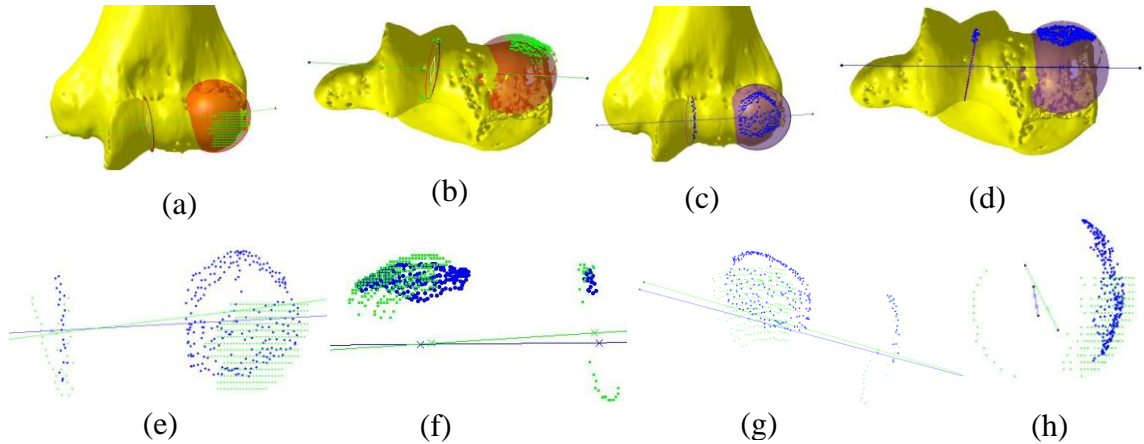


Figure 3.6: Qualitative comparisons between the resulting point datasets obtained through B-Spline (green) and conventional (blue) approaches achieved through: (a)-(d) combined fitted features and bone overlay, (e)-(h) direct result overlay.

To better quantify the differences in output between the two techniques, three different specimens were processed in parallel through both methods and Table 3.1 summarizes the main geometric discrepancies between them.

Table 3.1: Quantitative comparisons between B-Spline and voxel-based methods

<i>Feature Name</i>	<i>Conventionally Determined Feature Size</i>	<i>Difference between Methods</i>	<i>Difference between Methods [%]</i>
Capitellum radius	9.02 – 11.24 mm	0.39 – 1.78 mm	4.31 – 15.83
Trochlea radius	6.95 - 8.98 mm	0.48 - 0.76 mm	6.94 – 8.51
FE axis length	17.67 – 22.03 mm	0.34 – 0.77 mm	1.52 - 4.34
Capitellum center location	-	1.23 – 3.16 mm	-
Trochlea center location	-	1.35 – 1.67 mm	-
FE axes misorientation	-	4.11 – 7.71°	-
Troch planes	-	4.53 - 7.31°	-

The main goal of this validation was to provide a more qualitative comparison rather than a quantitative comparison. As it can be observed, while the two techniques

will yield comparable results, their output does not overlap perfectly. The numbers presented in Table 3.1 seem to imply that while a better match and consistency exists for trochlea geometry, larger variations are generally present in conjunction with capitellar geometry. Given the inherent complexity of the two procedures presented for FE axis determination, the differences between them are somewhat expectable, especially since their only commonalities are related to the initial stack of raw CT slices and least squares fitting procedure, among which the latter one is prone to yield different results when initialized with different guess values. Among the other factors that can be deemed responsible for result variability, the differences in segmentation and outer bone surface generation techniques would most likely play a major role. The difference in thresholding parameters would explain well the consistently smaller size of the features obtained through the parametric approach. Furthermore, some supplementary inconsistencies were probably also introduced via the manual input required from the user in the conventional approach in order to delimit the two relevant anatomical features.

On the other hand, given the stability of the anatomical conformation of the distal humerus, the automated feature recognition method described in Section 3.3.3 can be automatically applied to different humeral specimens, since it requires a minimal input from the user. However, this pattern-oriented method assumes that: 1) the analyzed planar slices are characterized by a certain morphological consistency, and 2) the CT data was acquired in a certain orientation of the humeral specimen. While assumption 2 can be easily corrected through successive coordinate transformations, assumption 1 prevents the application of this technique in regions of the distal humerus where cross sectional slices are truncated/incomplete with respect of the standard shape shown in Figure 3.3.

As such, the extreme top and bottom slices through capitellum and trochlea regions cannot be included in the developed parametric-based determinations of FE axis and this will cause additional result deviations. This limitation of the developed method becomes obvious in Figure 3.7e and 7h, but – taken alone – it should not represent a major source of result mismatch, provided that the capitellum shape is indeed spherical, as assumed.

3.6 Conclusions

The present study presents a novel method capable to automatically determine the posture of elbow flexion-extension axis by starting off with a minimal input consisting of a stack of raw of CT slices of the distal humerus. A three-specimen validation of the proposed approach against a conventional voxel-based determination revealed that while their outcomes are reasonably comparable, a number of factors might cause deviations between results that could add up to 15%. However, while from a pure engineering perspective the magnitude of the discrepancies might be regarded as borderline satisfactory, the current medical practices will likely treat them as acceptable, since surgeons generally lack the adequate means to accurately position the two relevant centers during surgery. Future extensions of this work will aim the validation of the proposed methodology via physical measurements, in an attempt to improve further its inherent reliability and precision.

3.7 References

- Alavala, C. R. (2008). *CAD/CAM: Concepts and applications*. PHI Learning Pvt. Ltd..
- Ameddah, H., and Assas, M. (2011). Bio-CAD reverse engineering of free-form surfaces by planar contours. *Computer-Aided Design and Applications*, 8(1), 37-42.

- Anderson, C. W., and Crawford-Hines, S. (2000). Fast generation of nurbs surfaces from polygonal mesh models of human anatomy. Colorado State University Computer Science Technical Report CS-99-101.
- Ane, B. K., and Roller, D. (2010, September). CAD modelling in reverse engineering: Generating C²-continuous planar B-spline curves for free-form shapes. In *World Automation Congress (WAC), 2010* (pp. 1-1). IEEE.
- Bağci, U., Udupa, J. K., and Chen, X. (2011, March). Orientation estimation of anatomical structures in medical images for object recognition. In *SPIE Medical Imaging* (pp. 79622L-79622L). International Society for Optics and Photonics.
- Bhatt, A. D., and Warkhedkar, R. M. (2008). Reverse engineering of human body: a B-spline based heterogeneous modeling approach. *Computer-Aided Design and Applications*, 5(1-4), 194-208.
- Bottlang, M., O'Rourke, M. R., Madey, S. M., Steyers, C. M., Marsh, J. L., and Brown, T. D. (2000). Radiographic determinants of the elbow rotation axis: experimental identification and quantitative validation. *Journal of Orthopaedic Research*, 18(5), 821-828.
- Brownhill, J. R., Furukawa, K., Faber, K. J., Johnson, J. A., and King, G. J. (2006). Surgeon accuracy in the selection of the flexion-extension axis of the elbow: an in vitro study. *Journal of shoulder and elbow surgery*, 15(4), 451-456.
- Brownhill, J.R., King, G.J., and Johnson, J. A. (2007) Morphologic analysis of the distal humerus with special interest in elbow implant sizing and alignment. *J.Shoulder.Elbow.Surg.* 16[3 Suppl], S126-S132.
- Duck, T.R., Dunning, C.E., Armstrong, A.D., Johnson, J.A., and King, G.J. (2003) Application of screw displacement axes to quantify elbow instability. *Clin.Biomech. (Bristol, Avon.)* 18[4], 303-310.
- Ericson, A., Arndt, A., Stark, A., Wretenberg, P., and Lundberg, A. (2003) Variation in the position and orientation of the elbow flexion axis. *J.Bone Joint Surg.Br.* 85[4], 538-544.
- Floater, M. S. (2008). On the deviation of a parametric cubic spline interpolant from its data polygon. *Computer Aided Geometric Design*, 25(3), 148-156.
- Gramstad, G.D., King, G.J., O'Driscoll, S.W., and Yamaguchi, K. (2005) Elbow arthroplasty using a convertible implant. *Tech.Hand Up Extrem.Surg.* 9[3], 153-163.
- Grove, O., Rajab, K., Piegl, L. A., and Lai-Yuen, S. (2011). From CT to NURBS: contour fitting with B-spline curves. *Computer-Aided Design and Applications*, 8(1), 3-21.
- Hangartner, T. N. (2007). Thresholding technique for accurate analysis of density and geometry in QCT, pQCT and μ CT images. *Journal of Musculoskeletal and Neuronal Interactions*, 7(1), 9-16.

- King, G. J., Zarzour, Z. D., Rath, D. A., Dunning, C. E., Patterson, S. D., and Johnson, J. A. (1999). Metallic radial head arthroplasty improves valgus stability of the elbow. *Clinical orthopaedics and related research*, 368, 114-125.
- London, J.T. (1981) Kinematics of the elbow. *J.Bone Joint Surg.Am.* 63[4], 529-535.
- McDonald, C. P., Beaton, B. J., King, G. J., Peters, T. M., and Johnson, J. A. (2008). The effect of anatomic landmark selection of the distal humerus on registration accuracy in computer-assisted elbow surgery. *Journal of Shoulder and Elbow Surgery*, 17(5), 833-843.
- McDonald, C.P., Johnson, J.A., Peters, T. M. and King, J. W. (2010) Image-based navigation improves the positioning of the humeral component in total elbow arthroplasty. *J Shoulder Elbow Surg.* 19, 533-543.
- Morrey, B.F. and Hotchkiss, R.F. (2000) External fixators of the elbow. In: *The elbow and its disorders*, edited by B.F. Morrey, Saunders, Philadelphia, 457–467.
- Mundy, J. L. (2006). Object recognition in the geometric era: A retrospective. In *Toward category-level object recognition* (pp. 3-28). Springer Berlin Heidelberg.
- Park, H. (2001). Choosing nodes and knots in closed B-spline curve interpolation to point data. *Computer-Aided Design*, 33(13), 967-974.
- Piegl, L. A., and Tiller, W. (1999). Computing offsets of NURBS curves and surfaces. *Computer-Aided Design*, 31(2), 147-156.
- Schroeder, W., Martin, K., and Lorensen, B. (2006) *The Visualization Toolkit*.
- Shiba, R., Sorbie, C., Siu, D. W., Bryant, J. T., Cooke, T. D. V., and Wevers, H. W. (1988). Geometry of the humeroulnar joint. *Journal of orthopaedic research*, 6(6), 897-906.
- Stokdijk, M., Meskers, C. G. M., Veeger, H. E. J., De Boer, Y. A., and Rozing, P. M. (1999). Determination of the optimal elbow axis for evaluation of placement of prostheses. *Clinical Biomechanics*, 14(3), 177-184.
- Tutunea-Fatan, O.R., Bernick, J.H., Lalone, E., King, G.J., and Johnson, J.A. (2010) Application of Collision Detection to Assess Implant Insertion in Elbow Replacement Surgery. SPIE.

Chapter 4

4 Assessment of the insertability of a certain implant within the endosteal canal of the bone

4.1 Overview

In this chapter a genetic algorithm based method is developed to assess a certain humeral implant insertion possibility into the humerus cavity. Nine humeral specimens were then employed in an experimental implantation setup to validate the results of the developed method. We hypothesized that by using this computer-assisted insertion technique, the malalignment between flexion-extension axes of the elbow and the corresponding implant can be decreased significantly.

4.2 Introduction

Recent developments in navigation technologies along with the advancements in medical imaging technology have created ample opportunities for computer-assisted orthopedic surgeries to be routinely employed in healthcare industry. Pre-operatively, the use of such simulation techniques assists orthopedic surgeons in not only planning for the appropriate surgical procedure but also deciding about proper size of artificial components to be used during the surgery instead of routine intra-operative trial-and-error implant insertions. Although, this pre-planning can lower the risk of joint replacement failures in the future, due to low incidence of upper limb joint replacement surgeries, the effectiveness of surgical procedures still highly depends on the expertise of the surgeon for upper limb joints like elbow versus lower limb joints such as knee or hip. Intra-operatively, advance employments of computer-assisted technologies can diminish the peril of dependency on

surgeons' expertise to help both surgeons by fitting the implants in bones more accurately as well as patients by having a better joint functionality, shortening hospital stay, and reducing hospital costs and the demand for repeating the surgery [Sankupellay *et al.*, 2005].

In the occurrence of various types of arthritis such as rheumatoid arthritis and different fractures to the elbow, one possible treatment option is elbow replacement surgery decided by surgeons based on the situation of the patient, severity of elbow disorder and ultimate clinical outcome of the surgery in order to enhance the elbow functionality. Clinically, the ultimate goal of this surgery is to accurately replicate the native articulation of the elbow, provided by a hinge joint connecting humeral and ulnar implants being inserted into medullary canals of the humerus and ulna. However, there are some limitations during this type of joint replacement which debilitates the surgical procedure. For the broad anthropomorphic distribution of the general population, the off-the-shelf implants with a limited number of sizes should fit everyone. Moreover, other than dependency on the surgeon's experience, the complexity of the elbow joint comparing to knee and hip makes the associated replacement procedure more and more challenging. Due to low incidence of this type of surgery, i.e., only less than several thousand of these procedures are carried out in the United States annually, presence of a skilled elbow arthroplasty surgeon capable of performing the aforementioned surgery many times each year is uncommon.

Since the position of the humeral implant in the canal determines the flexion-extension (FE) axis of the artificial joint, the overall success of the joint arthroplasty can be improved by bringing pre-operative planning into the picture. Indeed, establishing the

existence of a feasible position of the implant that will essentially cause a minimal malalignment of the prosthetic flexion-extension (FE) axis of the joint with respect to the native one aids surgeons to guide the humeral implant toward its final position. Complications of improper fit of the implant and change in the kinematic of the elbow include fracture, instability of the joints, loosening or wear of implants, implant failure due to excess moments, and need for a revision surgery. Although there exist limitations in studies reporting the complication rates after elbow replacement, they all indicate higher values ranging from 8%-45%, comparing to other joint replacements [Voloshin *et al.*, 2011; Krenek *et al.*, 2011].

Current routine practices provide the orthopedic surgeon with relatively few means to accurately assess whether a certain implant fits within the endosteal canal of the articulation bones. As such, the preliminary assessment of the fit relies heavily on the experience of the surgeon, and is generally perceived as a relatively challenging task due to the convoluted geometry of the canal in which loose fit, excessive bone removal or bone splitting may happen for 5.1% of cases as reported in [Krenek *et al.*, 2011; Joskowicz and Taylor, 1994].

Intra-operatively, surgeons face three situations: i) the fit is possible with an acceptable joint malalignment at the articulation; ii) the fit is possible, but the canal needs to be reamed, in order to reduce the amount of malalignment; or iii) the fit is not possible with the current stem length, which thereby needs to be shortened with negative consequences on the implant durability. The actual decision related to these scenarios often involves repeated impingements of the implant into the canal walls, through trial-and-error explorations that are not optimal.

In this chapter, a computer-assisted simulation technique is proposed in the context of humeral implant insertion in intramedullary canal of humerus. This method is capable of both assessing implant/bone fit possibility and finding a collision-free trajectory starting from an initial random implant pose located outside the bone cavity to one predicted as the final feasible position inside the bone. To make this accurate prediction on the feasibility of a certain implant/bone pair, the current study benefits from a local path planning algorithm aiming to minimize the malalignment between native FE axis of elbow joint and humeral implant artificial FE axis. The core of this algorithm is based on constrained search using genetic algorithm (GA) as an optimization technique, considering the humeral cavity as the constraint while targeting to determine feasible implant postures in each iteration. We hypothesized that implantation of a humeral stem using this approach will be an accurate solution, and can decrease the malalignment significantly.

Assuming that a feasible final position of the humeral implant in humerus has been investigated, determination of the optimal insertion path of the implant into the intramedullary convoluted canal with no collision is the complementary step towards completing the insertion procedure. Determination of the optimal insertion trajectory can be regarded as a classical peg-in-hole path planning problem, in which the primary goal is to determine a collision-free trajectory of a moving object (peg) from an outside position to the final inside position within confined spaces (hole) [Latombe, 1991]. In humeral implant insertion application, the confined space can be derived from imaging scans of humerus canal. Generally speaking, determination of a collision-free trajectory involves identification within the pool of instantaneously possible object position and

orientations (*i.e.* poses or postures) of those who are characterized by a non-overlapping status with neighboring objects. Obviously, once such a posture has been identified, the object has to continue its motion towards a finally desirable position that satisfies spatial constraints. The succession of the individual poses of the object between its initial and final configurations describes a collision free trajectory [Joskowicz and Taylor, 1993].

While numerous physical and/or kinematic constraints have been used in prior collision detection studies to restrict the pool of instantaneous poses associated with movable object configurations, most of them are simply inapplicable in context of implant insertion motion to be performed by the surgeon. During insertion, the implant stem can take practically any orientation and position as long as it does not come in contact with inner canal of the bone. Currently, this procedure is performed “quasi-blindly”, since the only information available to the surgeon is represented by the offline CT images acquired prior to surgery.

One of the typical solutions proposed to address this type of problems relies on the use of global strategies. They involve an initial construction of a configuration space connectivity graph followed by its search for the desired path. Global methods require computation of the configuration space, whose complexity increases proportionally with geometric size of the objects analyzed and exponentially with their total number of degrees of freedom. The circumstances associated with implant insertability such as: complex 3D shapes, six degrees of freedom, tight fit and fine motion planning – practically rule out global strategies and their variations as it is, for instance, hierarchical configuration space decomposition [Lozano-Perez and Brooks, 1983; Faverjon, 1984] or planning in low-dimensional configuration space projections [Buckley]. In addition, any

global search strategy that would repeatedly invoke object overlap detection could be deemed impractical due to the geometric complexity of implant and intramedullary canal, coupled with the fact that unlike in most other collision detection related applications, the contact between the stationary (bone) and moving (implant) object should be avoided at all costs in order to reduce the number of patient-related side effects associated with surgical procedure.

One possible alternative to global strategies is represented by the local ones that attempt to identify collision free path in a more direct manner by performing numerous collision avoidance computations as the search progresses. Local strategies depend on the efficiency of the geometric computations and the effectiveness of the search strategy. To exemplify, Donald's algorithm for a moving six degree of freedom polyhedron [Donald] places a fine resolution grid on the configuration space and uses a set of heuristics based on the local configuration space geometry to search for the path. For a tight fit, this method requires a very fine grid resolution and precise geometric computations which will significantly affect the overall efficiency. The potential field methods reported in the literature also tend to make similar assumptions [Joskowicz and Taylor, 1993; Joskowicz and Taylor, 1994].

In an extremely related, but almost singular study, [Joskowicz and Taylor, 1993] developed a numerical algorithm to determine femoral stem insertability. Their program was able to determine, based on the known shapes and dimensions of implant and inner femoral cavity, a collision/penetration free insertion trajectory. Subsequently, they developed a tool for computing and visualizing the interface free insertion path for an implant into a canal from a CAD description of their shapes [Joskowicz and Taylor,

1994]. As a notable simplification, these studies assumed a perfect match between implant and bone canal, such that the option of an impossible complete insertion was practically excluded. The previously developed navigated implantation procedures for total elbow arthroplasty [McDonald *et al.*, 2010, McDonald *et al.*, 2009a] have already outlined the importance of imaging data in the context of implant insertion. While the insertion trajectory is by no means optimized in case of navigated implantation and this might not be a viable option in case of live patients due to the impracticability required sensorized equipment, these studies revealed that superior implant alignments can be achieved by employing visualization principles. Implant insertion trajectory can also be generated by means of collision detection algorithms available in commercial CAE systems capable of motion analysis [Tutunea-Fatan *et al.*, 2010], but in this case a minimal user control exists on the insertion trajectory, that is generated automatically by the software based on predefined inputs (geometry, external forces and moments) as well as constraints (3D contact at bone/implant interface). Since the user cannot adequately control insertion trajectory, the collision between implant and bone is in fact unavoidable and this represents in fact on the major limitations of this method.

Since the amount of insertability studies available in the literature is extremely limited it seems logical to assert that this area needs more development. Compared to hip, elbow arthroplasty procedures are rare, and perhaps because of that, the surgeon feels more the need to visualize, be guided, be trained and practice the implant insertion maneuvers before the actual start of the surgical procedure. Compared to femur, the intramedullary canal of the humerus has a more convoluted shape, which makes insertion of a predefined stem length much more difficult [McDonald *et al.*, 2009b] As a result, a

preoperative prediction of the relative fit between implant and inner bone cavity would significantly increase long term outcomes of any type of joint arthroplasty, and in particular those of the elbow.

In this study, a computer-assisted simulation technique is proposed in the context of humeral implant insertion in intramedullary canal of humerus capable of both assessing implant/bone fit possibility and finding a collision-free trajectory starting from an initial random implant pose located outside the bone cavity to one predicted final feasible position inside the bone. To make this accurate prediction on the feasibility of a certain implant/bone pair, the current study benefits from a local path planning algorithm aiming to minimize the malalignment between native FE axis of elbow joint and humeral implant artificial FE axis. The core of the this algorithm is constrained genetic algorithm (GA) optimization searches, considering the humeral cavity as the constraint while targeting to determine feasible implant postures in each iteration. We hypothesized that implantation of a humeral stem using this technique would be an accurate way and can decrease the malalignemnt significantly.

4.3 Genetic Algorithm Based Search on the feasibility of the Implant Insertion

4.3.1 Materials

We acquired computer tomography (CT) images of 9 fresh frozen cadaveric distal humeri using a 64-slice clinical scanner (GE-Light SpeedUltra, New Berlin, WI). The scanning parameters were set to a field of view of 16x16 cm and a power of 120 kVp at 90 mAs. While the longitudinal canal “axis” of each specimen was placed coaxial with the axis of CT scanner during the imaging procedure, the stack of generated raw CT slices was

characterized by a resolution of 512x512 pixels and a voxel size of 0.3125x0.3125x0.625 mm.

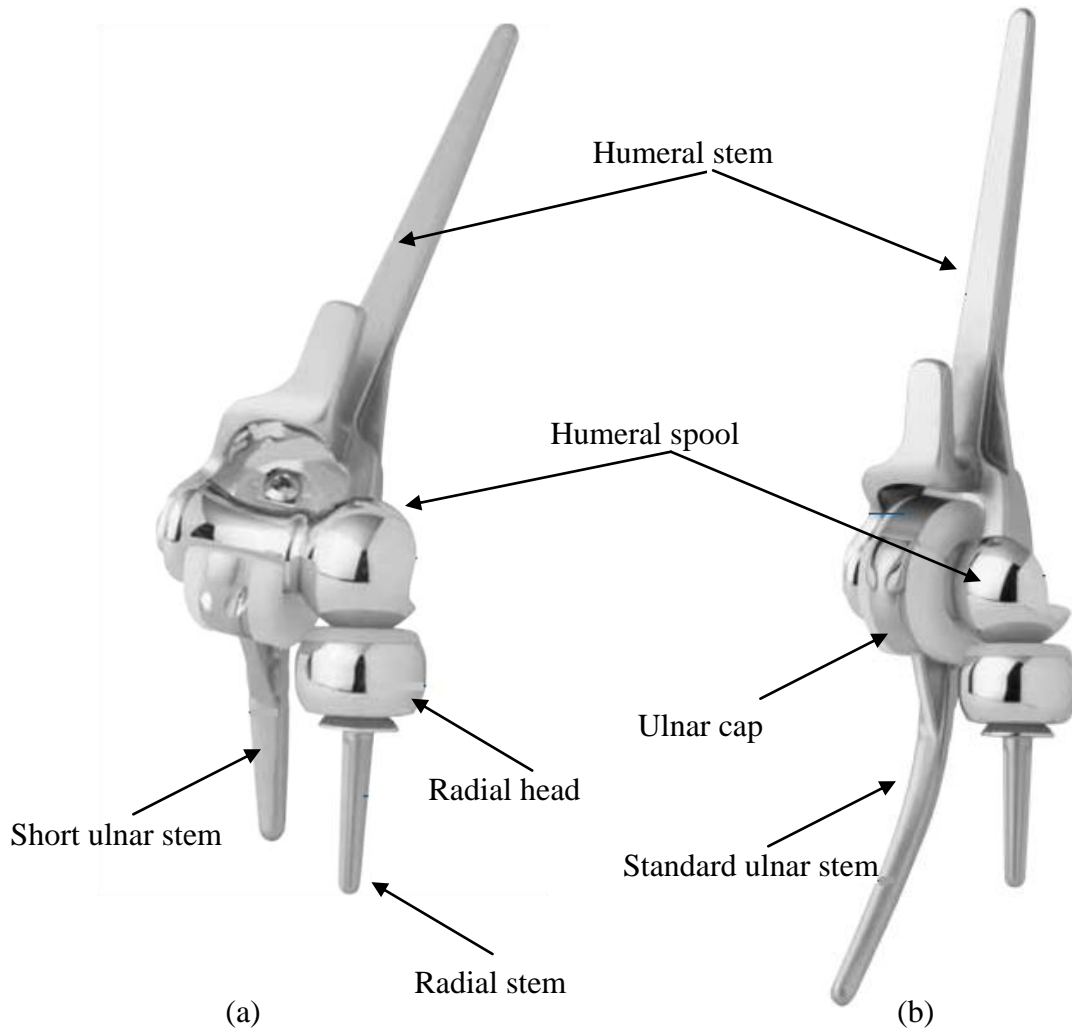


Figure 4.1: : Latitude implant configurations: (a) unlinked, and (b) linked versions

Adapted from [<http://www.tornier-us.com/upper/elbow/elbrec001/index.php>].

4.3.2 Elbow Implants

Although both linked and unlinked implants carry various advantages and disadvantages, the selection of linked or unlinked implant types mainly depends on the intra-operative patient situation likewise the amount of bone loss. Linkable implants are a new generation of implants capable of (1) converting into a linked or unlinked implant (Figure 4.1) based on the intra-operative decision of the surgeon; and (2) providing better clinical outcome due to thicker bearing surface and better anatomical reproduction.

As a result, linkable Latitude left elbow prostheses were selected for implantation procedure of this study. Humeral portion of this implant, being fit into medullary canal of the humerus, includes three main components; (1) humeral implant, (2) Spool, and (3) Screw (Figure 4.3). Indeed, the humeral implant and spool connect with the cannulated screw to form the implant humeral portion and flexion-extension axis. Since valgus angle of elbow FE axis varies from 2° to 9° with the mean of 6° , the articulation axis of humeral implant has a fixed 6° valgus angulation.

In order to secure stability of the humeral implant in its final position after the surgery, humeral implant (Figure 4.3) consists of medial and lateral fins to prevent intramedullary rotation and anterior flange accepting bone graft to prevent posterior movements. Off-the-shelf humeral implant stems come in 3 different sizes of small, medium and large while they should match corresponding spool sizes (small, medium, large and large plus) with three offsets (anterior, posterior and centered) in order to shape articulation in Latitude implants (Figure 4.2). What makes the implantation challenging is that unlike knee and hip joints replacements in which surgeons insert implants in a simple straight canal, the elbow has a more complex canal. Moreover, the bone size in the elbow

is smaller than in knee and hip which in turn makes the implantation more sensitive because of restricted room for implantation.

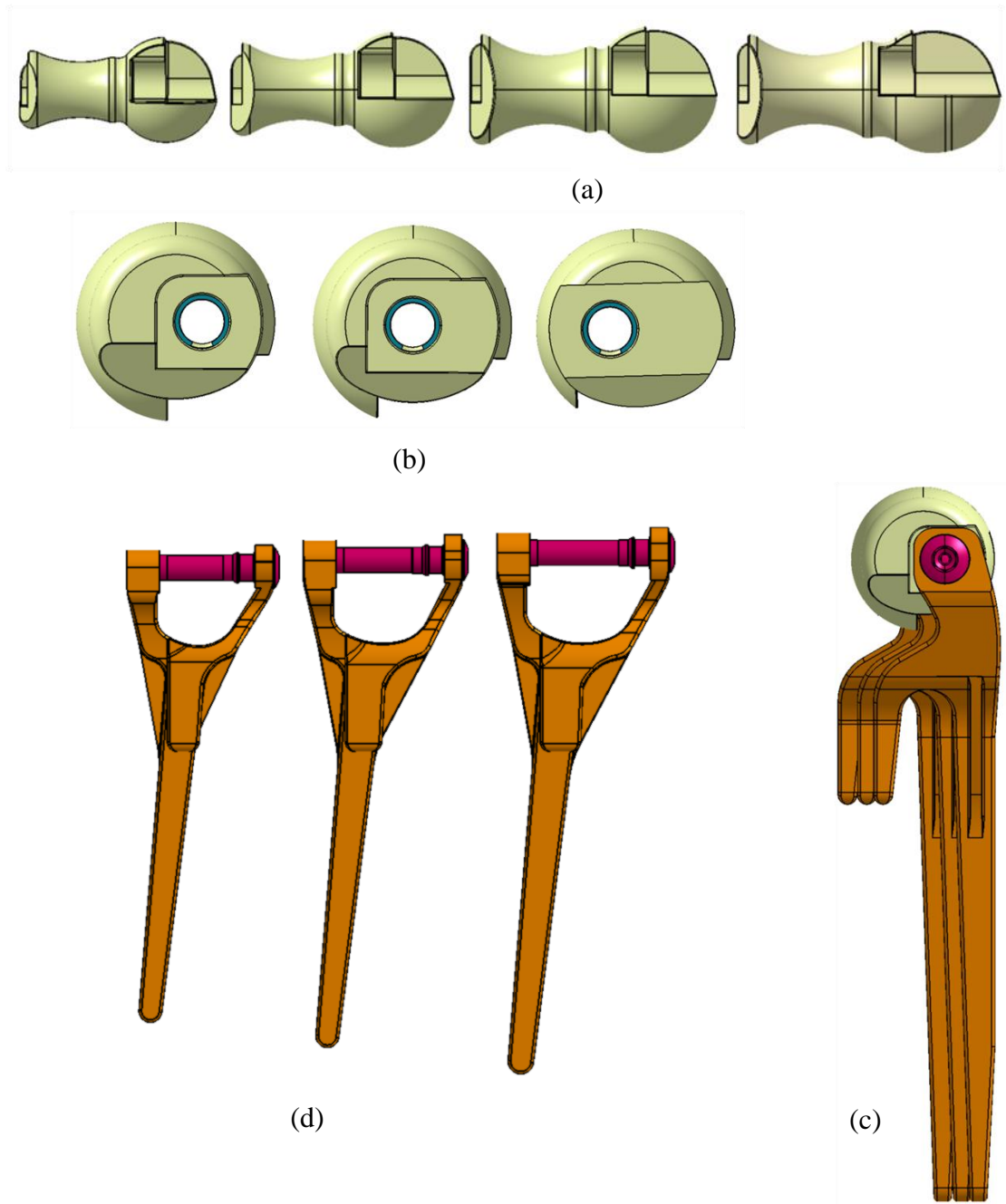


Figure 4.2: Implant Components: (a) small, medium, large and X-large spool sizes, (b) anterior, centered and posterior offset spools, (c) different stem locations based on offset spools, and (d) small, medium and large stem sizes.

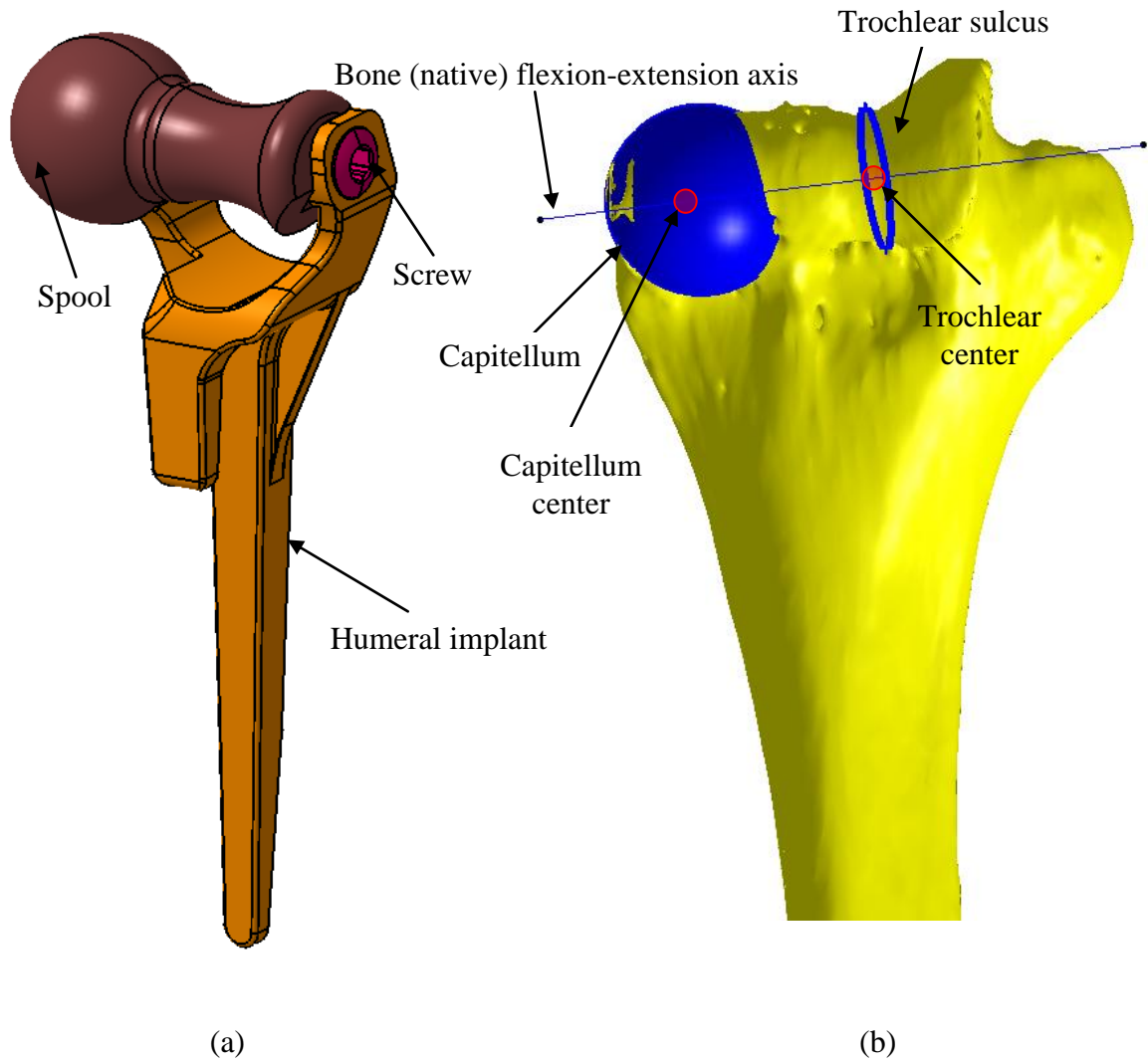


Figure 4.3: 3D representations of the humeral implant and the distal humerus: (a) Latitude humeral portion components containing humeral implant, spool and screw, and (b) anterior view of the distal humerus.

4.3.3 Bone Geometry Reconstruction

As it is shown in Figure 4.4, the convoluted canal shape of the humerus prevents the surgeon to perfectly align implant FE axis with native FE axis of the humerus. Intra-operatively, surgeons perform implantation by forcing the implant to sit in the canal with no prior knowledge of humeral walls and then try to orient the implant properly based on anatomical features. Unfamiliarity with implantation may lead to implant penetration into wall of the bone causing bone fractures (Figure 4.5). Not only proper insertion trajectory is essential for a perfect implantation, but also selecting the suitable size of the implant for insertion is difficult.

To address this objective, the first task to be accomplished is precise reconstruction of the bone geometry from axial slices of each specimen acquired through CT scanning. The reconstruction is carried out by means of a control polygon deformation technique developed in the past [Mostafavi *et al.*, 2012] and also described in Chapter 2. The thresholding technique is initially used to extract the inner contours of the humeral canal, and then a novel closed B-Spline fitting technique is proposed which enables us to approximate the extracted data points with a certain tolerance/accuracy in order to generate humerus 3D model [Mostafavi *et al.*, 2012] (Figure 4.6). This intended parametric representation enables robust and fully-controlled geometry discretization techniques to be further employed in the context of optimization algorithm.

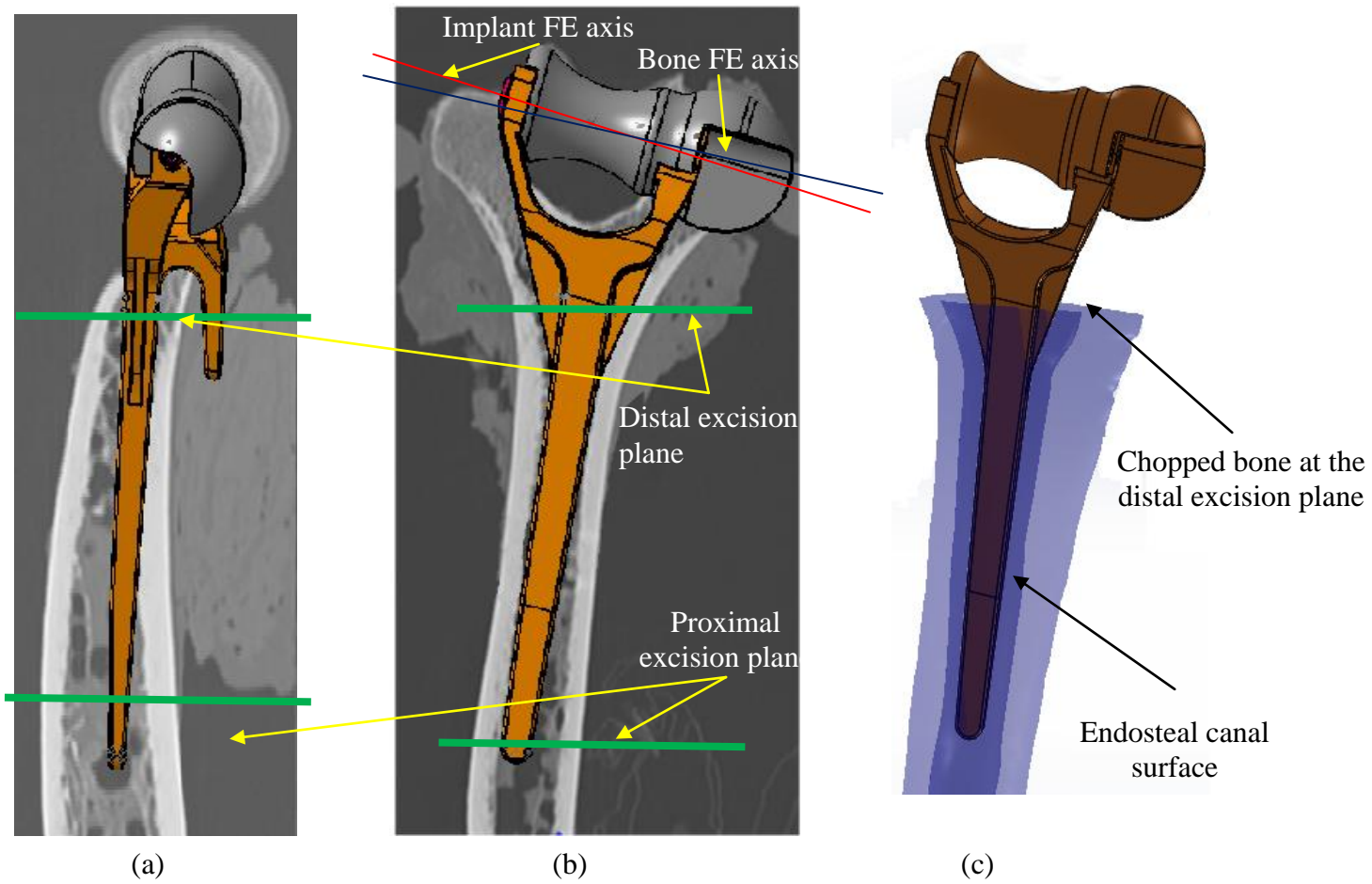


Figure 4.4: Relative position of Latitude humeral implant in: (a) medial-lateral (ML) view (b) anterior-posterior (AP) view of the distal humerus, and (c) 3D model of implant position in medullary canal of the humerus.

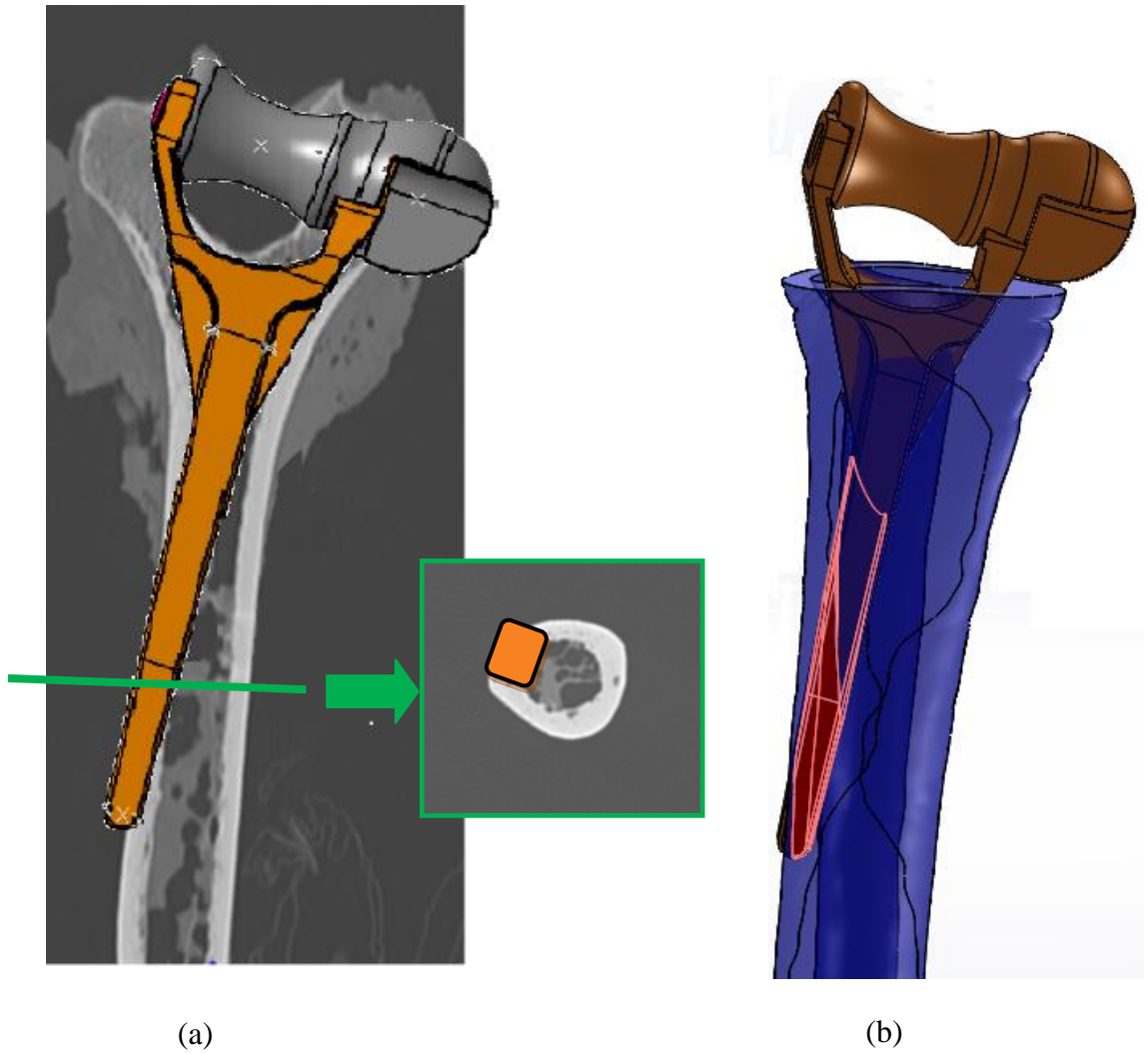


Figure 4.5: (a) Implant penetration into the humerus due to improper fitting, and (b) 3D model of implant penetration, showing interference areas in red.

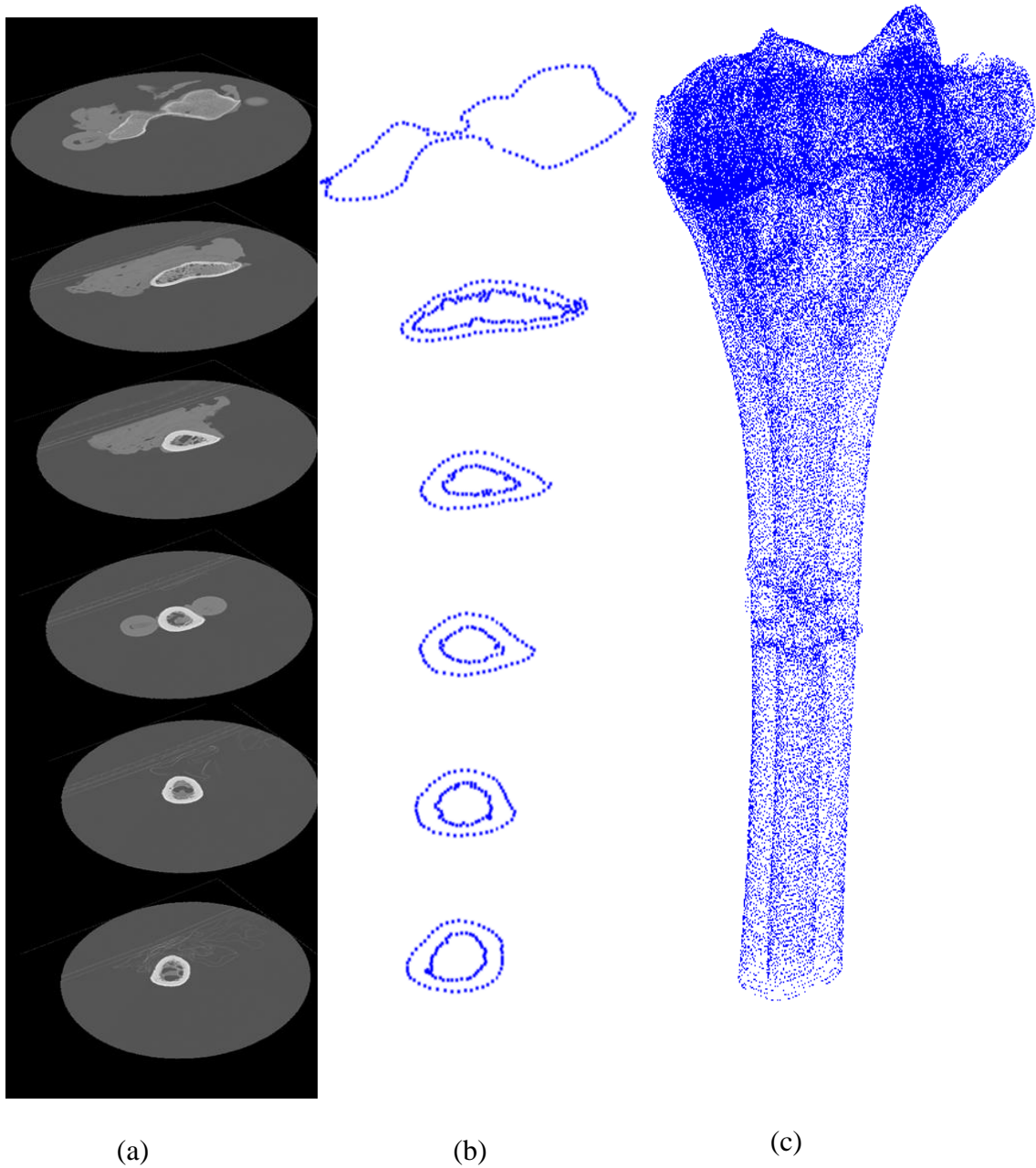


Figure 4.6: Reconstruction of the distal humerus geometry: (a) DICOM images of the humerus acquired from CT scan, (b) generated inside and outside contours from DICOM images using developed control polygon technique, and (c) full 3D model of the humerus from contours.

4.3.4 Genetic Algorithm

The problem of fitting one object (implant) inside another object (canal) with the goal of matching two corresponded features (FE axes) is a six variables constrained nonlinear minimization problem. The minimization algorithm used in this study is Genetic Algorithm (GA) which mimics the metaphor of natural biological evolution (Figure 4.9). This algorithm is a stochastic global search method that can best minimize the objective functions that are highly nonlinear in the domain of large number of variables. Since the output of this search should be the spatial location of the implant, six variables were set for this problem; three for position ($\mathbf{\Pi}$) and three for orientation ($\mathbf{\Omega}$) (Figures 4.10 and 4.11) with respect to a unique coordinate system [Mostafavi *et al.*, 2013].

To simplify the inputs, the fit of a particular implant/bone combination was evaluated by means of only three critical cross sections of bone model (Figure 4.7) and two distal and proximal cross sections of humeral implant stem (Figure 4.8) for the intended feasibility assessment. For the humerus, all cross sections were presented in the form of convex polygons $\mathcal{P}^{D,I,P}$; the top (distal, D) and bottom (proximal, P) cross sections were selected to match the location of the two ends of the stem, provided that the alignment between prosthetic and native FE axes is enforced. In addition to them, a third and intermediate (I) cross section was identified as the most constraining/narrowest through iterative comparisons of consecutive slice geometries as determined from multiple visualization directions. The visual determination of intermediate cross section is just a rough intermediate posture limitation for the implant orientation to better position the implant inside the humerus cavity.

Both humerus critical cross sections and distal and proximal end cross sections of the implant are located in their local coordinate systems of BCS (Bone Coordinate System) and ICS (Implant Coordinate System), respectively (Figure 4.10). By translating the ICS origin to the BCS origin, implant cross sections are defined in BCS. In order to place the implant cross sections in proper initial location, the centroid of proximal cross section of the implant was then translated to centroid of distal cross section of the bone. In fact, the only limitation that helps GA in generating final implant position is to keep the proximal cross section of the implant inside the convex polygon of distal cross section of the bone (

$$P_{C_i}(I_P, \mathbf{\Pi}_j, \mathbf{\Omega}_j) \in \mathcal{P}^D).$$

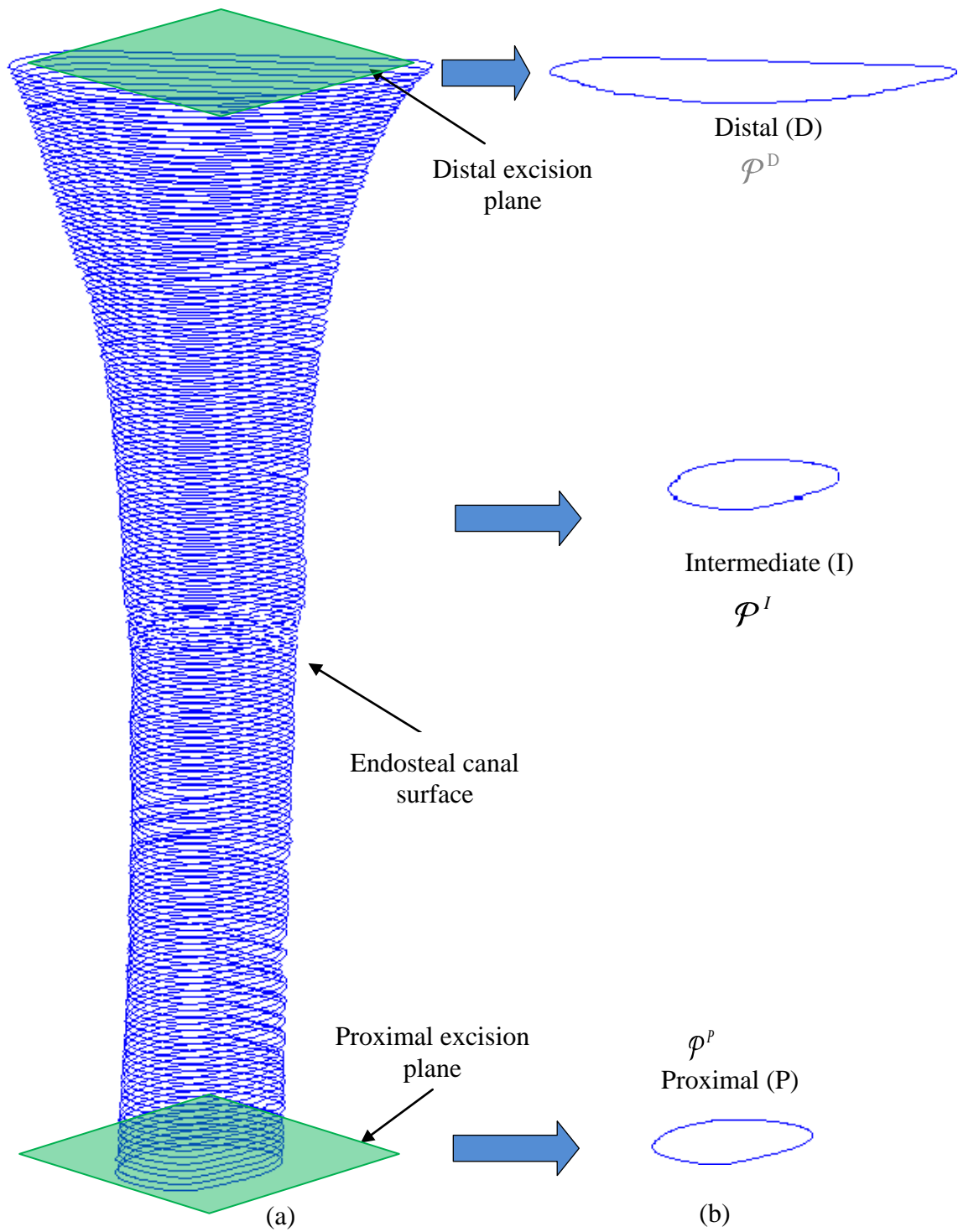


Figure 4.7: Reconstructed bone model: (a) control polygon form and (b) selection of three critical cross sections as the GA input.

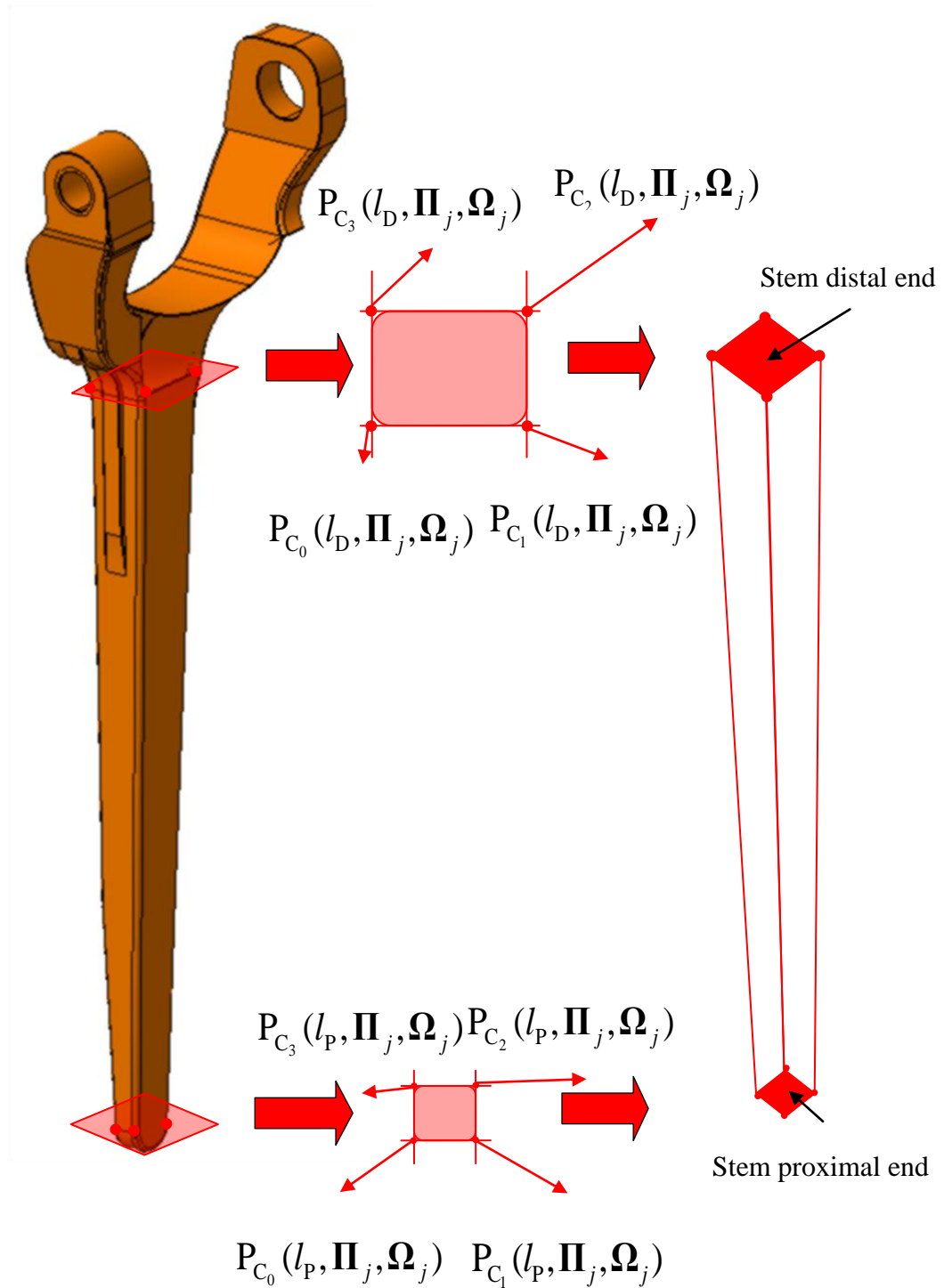


Figure 4.8: Selection of two distal and proximal ends of humeral implant stem as the GA input.

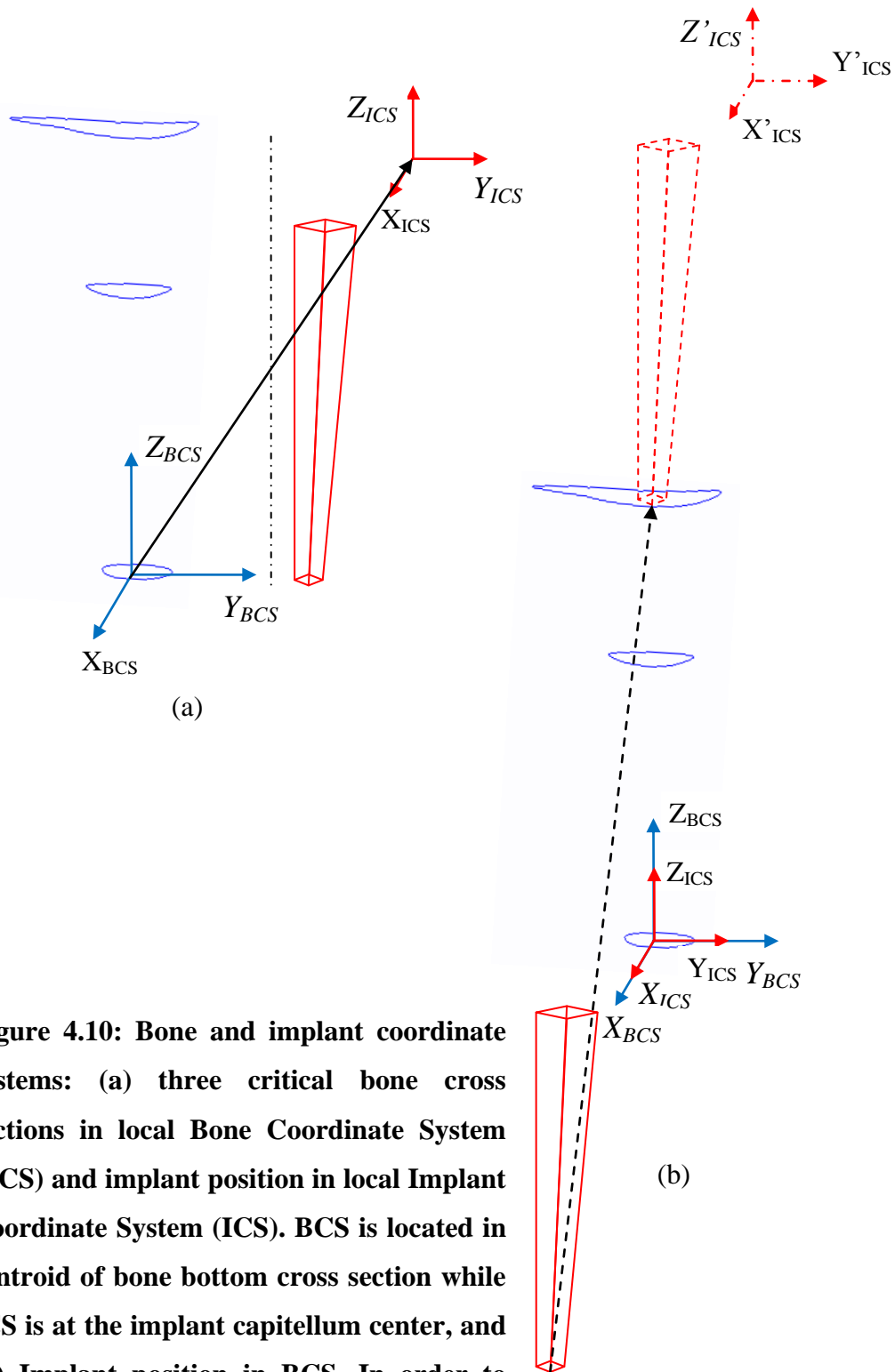


Figure 4.10: Bone and implant coordinate systems: (a) three critical bone cross sections in local Bone Coordinate System (BCS) and implant position in local Implant Coordinate System (ICS). BCS is located in centroid of bone bottom cross section while ICS is at the implant capitellum center, and (b) Implant position in BCS. In order to position the implant in initial position for GA technique, the centroid of implant bottom cross section should match the centroid of bone top cross section.

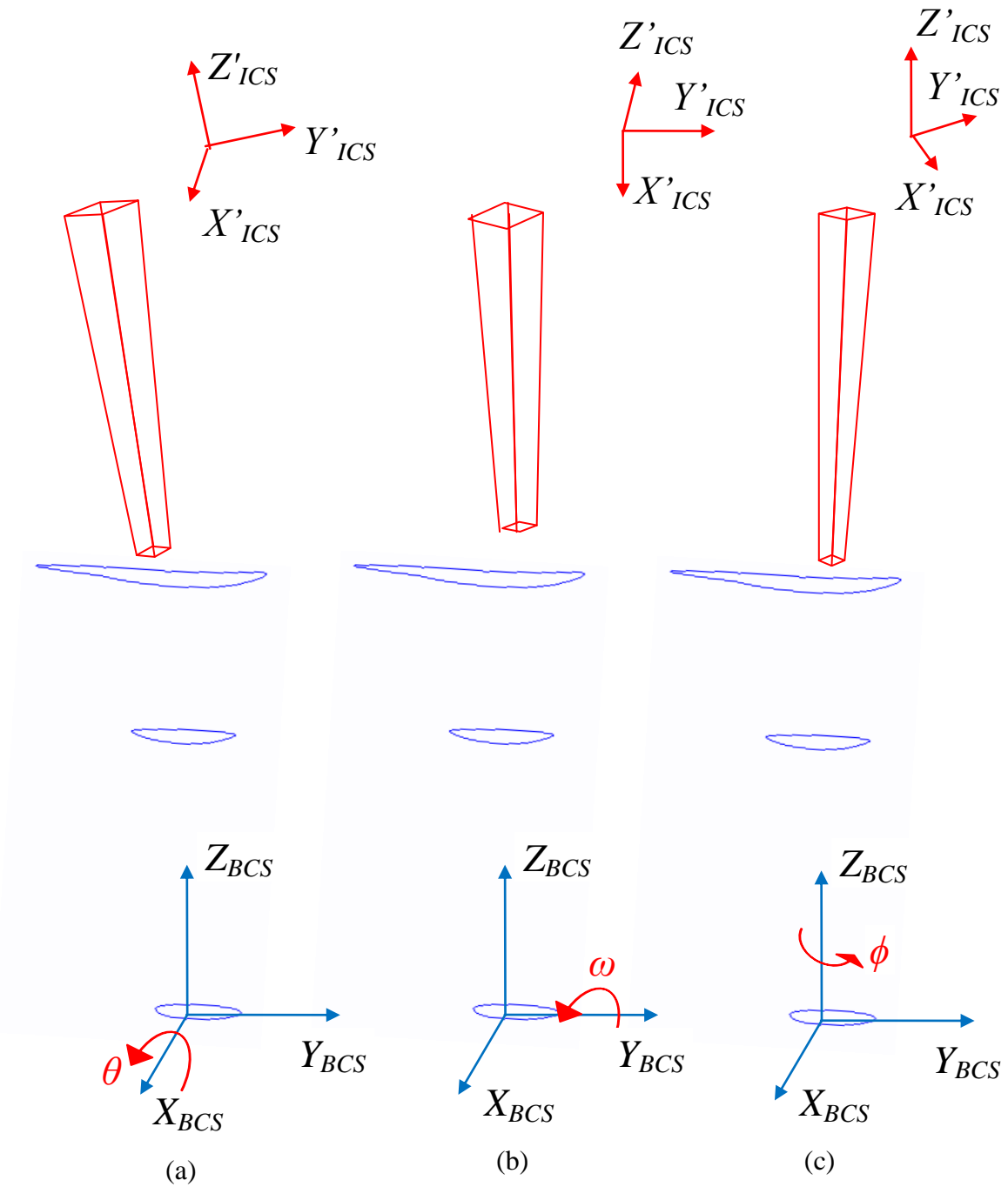


Figure 4.11: Implant Coordinate System (ICS) orientation with respect of Bone Coordinate System (BCS) over: (a) θ rotation about X_{BCS} axis, (b) ω rotation about Y_{BCS} axis, and (c) ϕ rotation about Z_{BCS} axis.

By having the two end cross sections of humeral stem, the spatial location of four corner points $\mathbf{P}_{C_i}(l, \mathbf{\Pi}_j, \mathbf{\Omega}_j)$ with $i \in \{0,1,2,3\}$ of the stem for its entire length ($L, l \in [0, L]$) can be identified as a result. The last input was the location of the native and prosthetic FE axes, defined through their two end points (*e.g.* geometric centers of capitellum and trochlea, respectively). All prior geometric elements were expressed in BCS, which represents a data consistency requirement to be acquired through appropriate coordinate transformations.

The GA-based search aims at the minimization of the implant malalignment with respect to the native FE axis of the humerus by enforcing non-interfering conditions in all three critical cross sections. The main role of these constraints is to ensure that the implant postures never penetrate into the bone canal envelope.

The implant malalignment was calculated as the difference between native FE axis location and position and the implant FE axis. In order to report this malalignment one translation d_{CC} (the distance between implant and native centers of capitella) and two angles: varus-varus α_{VV} and internal-external α_{IE} (Figure 4.12) were recorded to shape the objective function. Based on all these parameters, the mathematical formulation of the optimized search becomes:

$$\left\{ \begin{array}{l} \text{minimize}(\omega_1 \overline{d_{CC}} + \omega_2 \overline{\alpha_{VV}} + \omega_3 \overline{\alpha_{IE}}) \\ \mathbf{P}_{C_i}(l_D, \mathbf{\Pi}_j, \mathbf{\Omega}_j) \in \mathcal{P}^D \\ \text{Subject to: } \mathbf{P}_{C_i}(l_I, \mathbf{\Pi}_j, \mathbf{\Omega}_j) \in \mathcal{P}^I \\ \mathbf{P}_{C_i}(l_P, \mathbf{\Pi}_j, \mathbf{\Omega}_j) \in \mathcal{P}^P \end{array} \right. \quad (4.1)$$

where $i \in \{0,1,2,3\}$ and iteration number varies from 1 to a maximum convergence limit. The ω scalars in Eq. (4.1) are the weights associated with each of the malalignment components that are quantified in a normalized form with respect to their maximum allowable values. To determine these values, a number of previous studies were reviewed but due to existing insufficient information in this regard, arbitrary limits were chosen for the three malalignment values as below:

$$\begin{cases} \omega_1 = 1mm \\ \omega_2 = 1/2^\circ \\ \omega_3 = 1/2^\circ \end{cases} \quad (4.2)$$

The proposed GA method was tested over 9 humeri with the best corresponding implant to be fit properly (Figure 4.13). A population size of 100 was used for this algorithm, while the generation was set to 100 too. The mutation rate was 1% and the crossover probability was set to 100%. The constraint tolerance was 0.001. When convergence occurred in each optimization search, the implant final position was checked against all bone cross sections taken from DICOM images in order to make sure the implant had no penetration into the bone from distal to proximal ends. If penetration was observed in one or couple of slices, the corresponding cross sections were added to the list of intermediate cross sections. In case the implant was positioned fully inside the bone, the malalignment parameters were recorded to be validated against the results of experimental setup [McDonald *et al.*, 2009a]. The overall schematic of the proposed algorithm is shown by Figure 4.14.

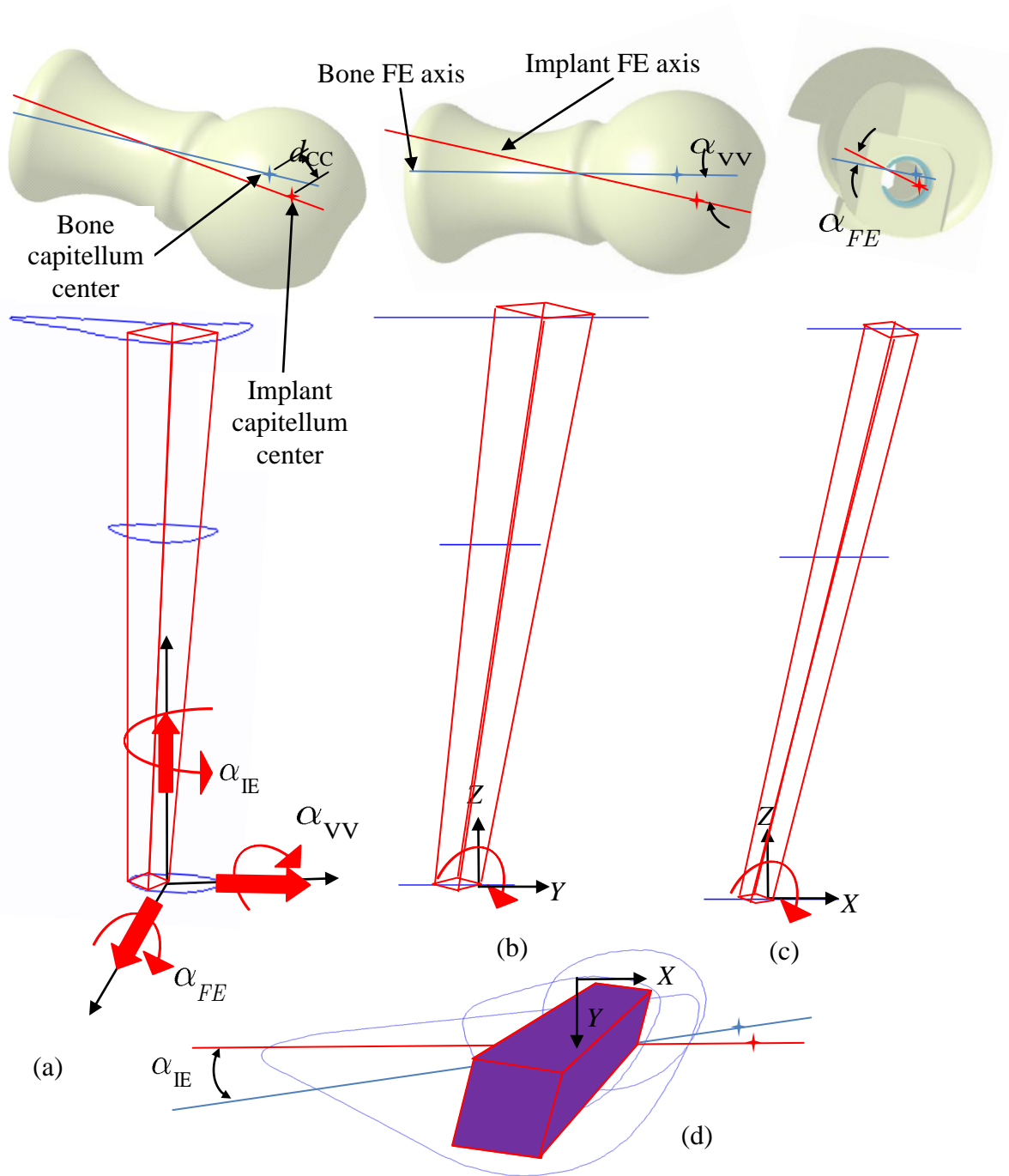


Figure 4.12: Geometric interpretation of implantation malalignment: (a) 3D view of implant position in bone cavity showing the translation error d_{CC} , (b) anterior-Posterior view of implant insertion showing varus-varus angulation error α_{VV} , (c) medial-lateral view of implant insertion showing flexion-extension angle α_{FE} and (d) distal-proximal view of implant insertion showing internal-external angulation error α_{IE} .

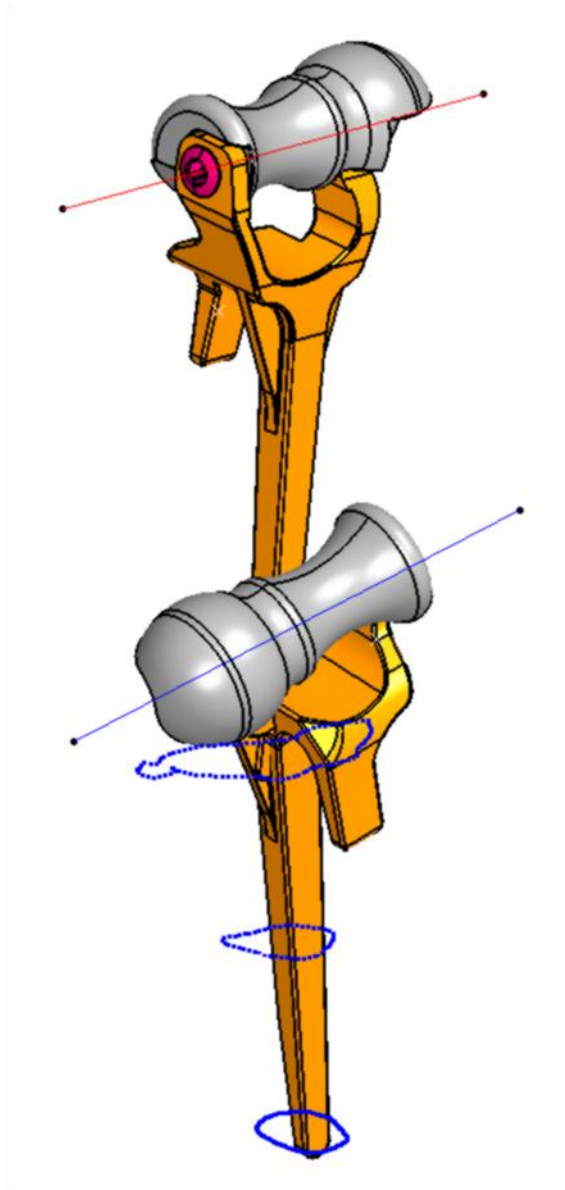
4.3.5 Experimental Setup

The experimental setup used for this study is in fact a navigated implantation setup developed by [McDonald *et al.*, 2009a]. This setup benefits from a pre-operative plan for generating 3D model of target implant. Herein, intra-operative alignment is then performed by placing the tracked implant inside the medullary canal and adjusting its position such that the source implant was superimposed on top of the target implant. In order to perform the registration of each specimen, physical landmarks were screwed to the distal humerus and then by using ICP (iterative Closest Point algorithm) a surface-based registration of the digitized landmark to corresponding CT surface was carried out. To obtain implant alignment error in translational and rotational directions, the position and orientation of the native FE axis were first achieved by digitizing capitellum and trochlea. Following each implantation and recording position and orientation of the implant FE axis with respect to humeral receiver, the implantation error is calculated subsequently.

4.4 Result

In order to validate the accuracy of the developed GA-based technique in identifying the optimized implantation described in the previous section, all 9 physical specimens were tested in the experimental setup while the CT images acquired from each subject were used in the proposed optimization technique, respectively. For the experimental setup, an expert surgeon was asked to perform the implantation in the context of a navigated implantation procedure aiming to find a possible final position for the humeral implant using landmarks, receivers and a set of implants and spools. In the event of a successful implantation, the final position and orientation of the implant and its FE axis were

recorded for both methods. In Figure 4.13a the initial and final positions of the implant during an insertion procedure are shown while Figure 4.13b demonstrates all the intermediate steps that the implant takes to reach its final position starting from the assumed initial position.



(a)

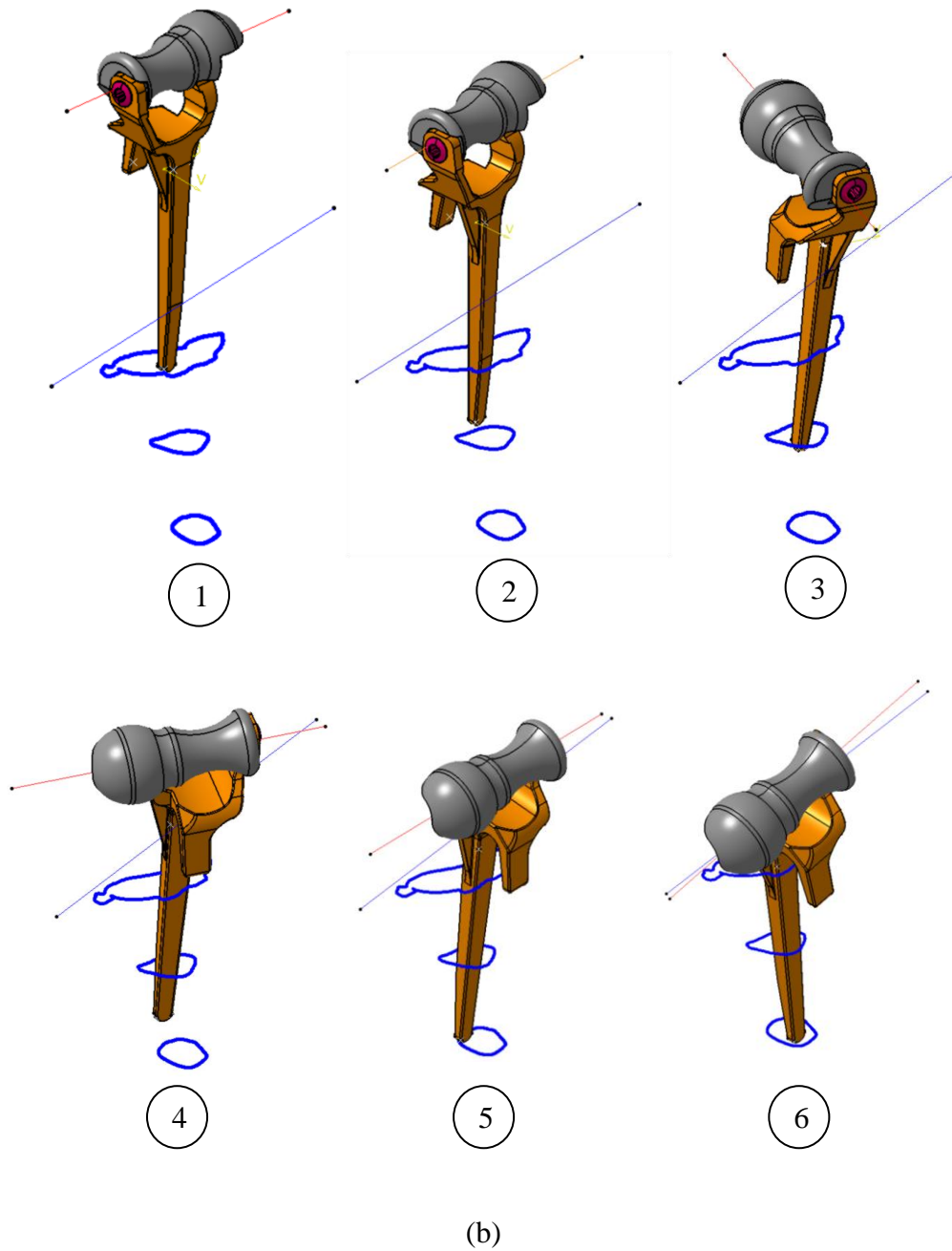


Figure 4.13: Implant insertion procedure using GA technique: (a) 3D view of the humeral implant from initial to final position, and (b) intermediate steps of implant insertion.

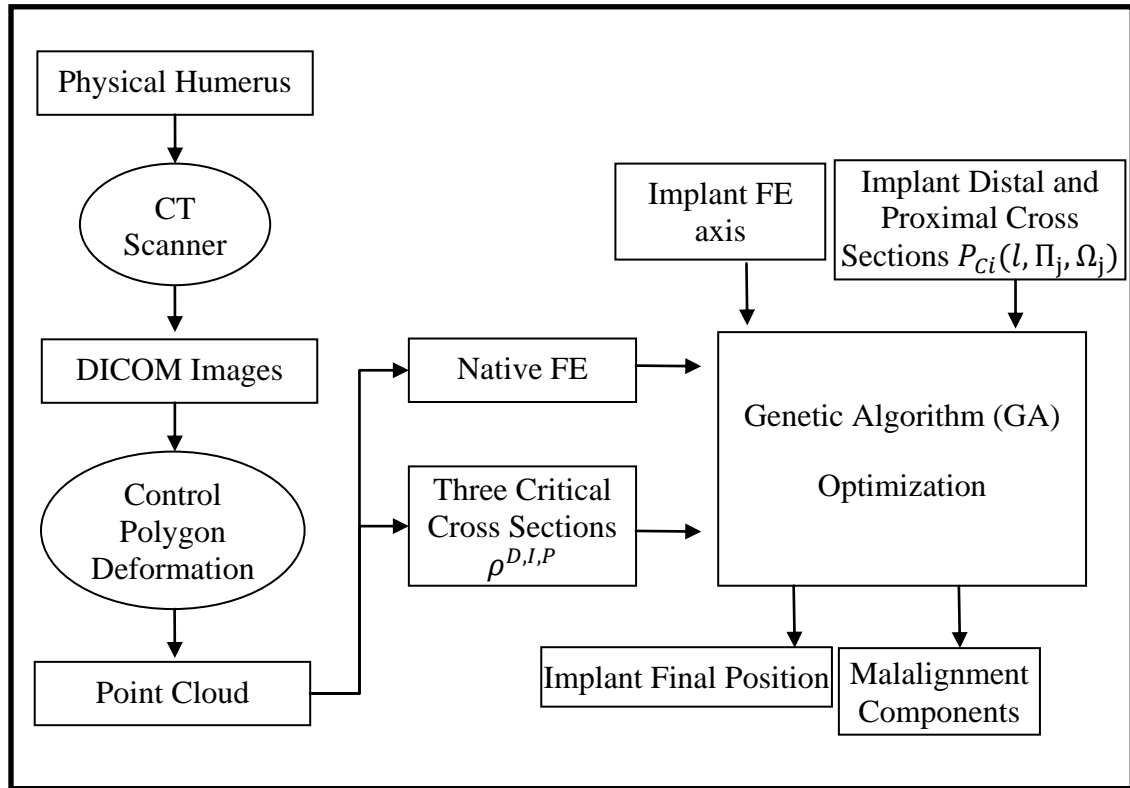


Figure 4.14: Schematic presentation of GA algorithm.

It can be observed that although implant and bone capitellum centers are far away in almost 180 degree orientation, the developed genetic algorithm initiates to rotate the implant and make it closer to the capitellum center of the bone as the insertion procedure is advancing.

Results of the implant alignment error represent a promising conclusion comparing to the results of the experimental setup (Figure 4.15). The translational error defined as the distance between capitella centers was 2.72 ± 1.66 mm for the developed method while for the experimental setup was 2.63 ± 0.83 mm. Although translational malalignment in medial-lateral direction for the developed method (2.25 ± 1.65 mm) is higher than experimental setup (0.83 ± 0.77 mm), the anterior-posterior and proximal-distal translational errors (1.43 ± 1.34 mm and 0.31 ± 0.38 mm) are lower compared with the corresponding malalignment in the experimental setup (2.19 ± 1.00 mm and 0.63 ± 0.52 mm). Maximum implant malalignment in translation occurred in medial-lateral direction (sagittal plane) for the developed method while for the experimental setup anterior-posterior direction (coronal plane) exhibited the maximum malalignment. In both methods, only 3 out of the 9 examined specimens showed a total implant alignment error of less than 2 mm whereas the remaining specimens had the error values ranging from 2 mm to 5 mm.

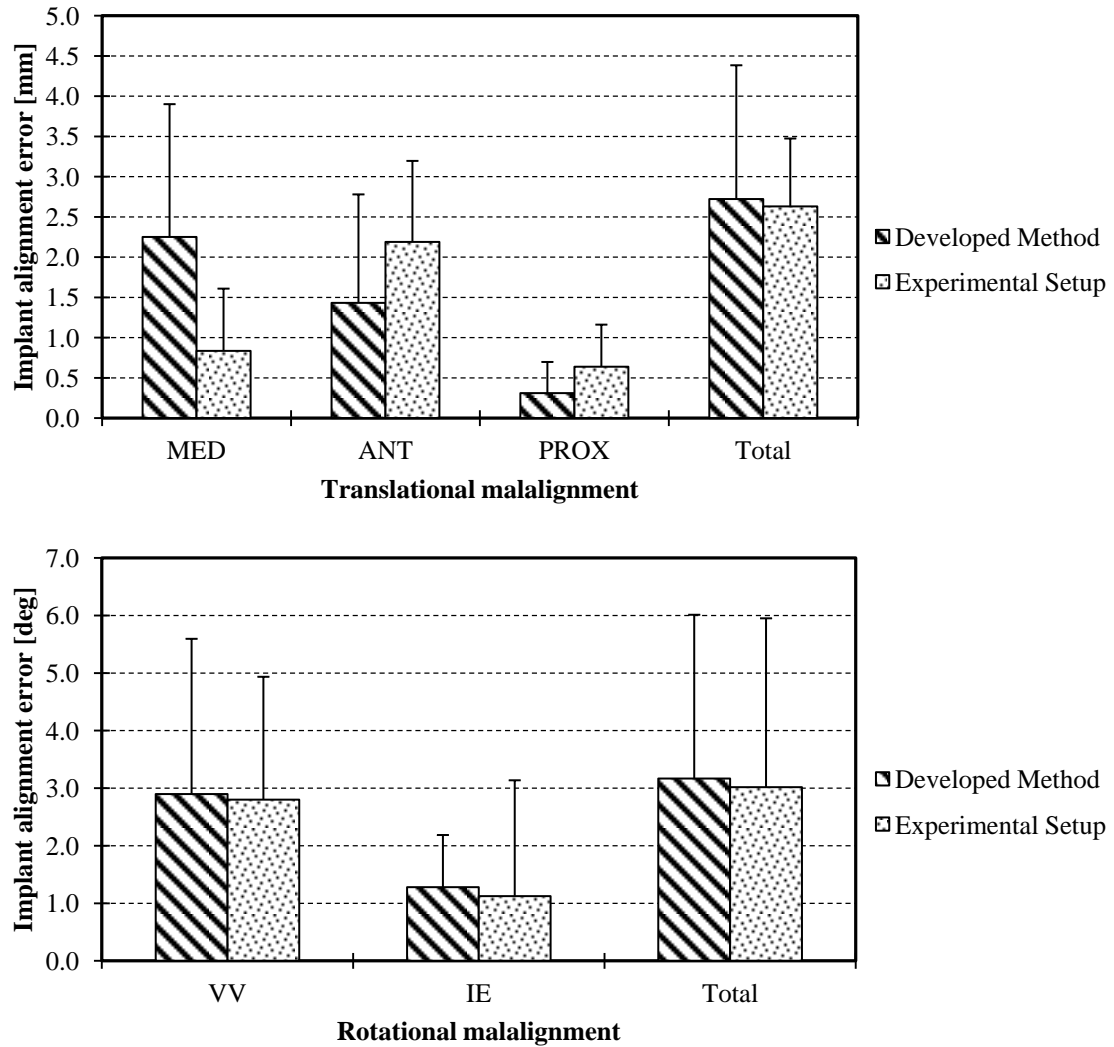


Figure 4.15: Validation of the developed method results in comparison with experimental setup results: (a) implant alignment error in translation (mean + 1 standard deviation) for both developed method and experimental setup. Translational malalignment was reported in three directional components of medial-lateral (MED) error, anterior-posterior (ANT) error and proximal-distal (PROX) error while Total represents square root of error components, and (b) implant alignment error in rotation (mean + 1 standard deviation) for both developed method and experimental setup. Rotational malalignment was reported in two components of varus-valgus (VV) error and internal-external (IE) error while Total represents square root of error components in rotation.

As it is observed, there was no significant difference in malalignment for both translation and rotation. In rotation, the amount of malalignment was $2.9^{\circ} \pm 2.7^{\circ}$ for the developed method and $2.8^{\circ} \pm 2.13^{\circ}$ for the experimental setup. Despite translational error, there was no significant difference in rotational angles between both developed method and experimental setup. Varus-valgus angulation error was $2.89^{\circ} \pm 2.69^{\circ}$ for the developed method and $2.79^{\circ} \pm 2.13^{\circ}$ for experimental setup. Malalignment in internal-external angulation for the developed technique and experimental setup were $1.27^{\circ} \pm 0.9^{\circ}$ and $1.12^{\circ} \pm 2.01^{\circ}$, respectively. Moreover, for both methods varus-valgus angulation showed the maximum contribution in rotational malalignment. For both methods, 3 out of 9 specimens exhibited the rotational misalignment of less than 2° and the rest of the specimens had the error between 2° to 6° . Figures imply that while a better consistency exists for proximal-distal translational alignment and internal-external rotational alignment, large variations are generally present in conjunction with medial-lateral and anterior-posterior translational alignments and varus-valgus rotational alignment.

Once the best possible final positions for each pair of the implant and the humerus specimen were found, the positioning of the implant inside the canal was analyzed for three random specimens. Accordingly, it was investigated that how the implant cross section is positioned with respect to inner boundary of the bone in each cross section. This analysis assists to assess both the efficiency of the insertion algorithm as well as the current shape of the implant based on the morphological characteristics of the distal humerus. As it is shown in Figure 4.16, a new parameter defined as the minimum distance from four corners of the implant to the inner boundary of the bone in each cross section, was calculated, and then was plotted for all distal to proximal bone cross

sections. This figure first of all shows that there is no penetration in any of the bone cross sections in all three specimens since no negative distance value was recorded for distal to proximal cross sections. However, for the majority of bone cross sections the implant was positioned very close (less than 0.5 mm) to the bone cavity. It shows that although there has been no penetration, a reasonable malalignment can be achieved only by positioning the current implant in the close vicinity of the bone cavity. Therefore, the current shape of the implant has an incompatible design with the inner space of the bone.

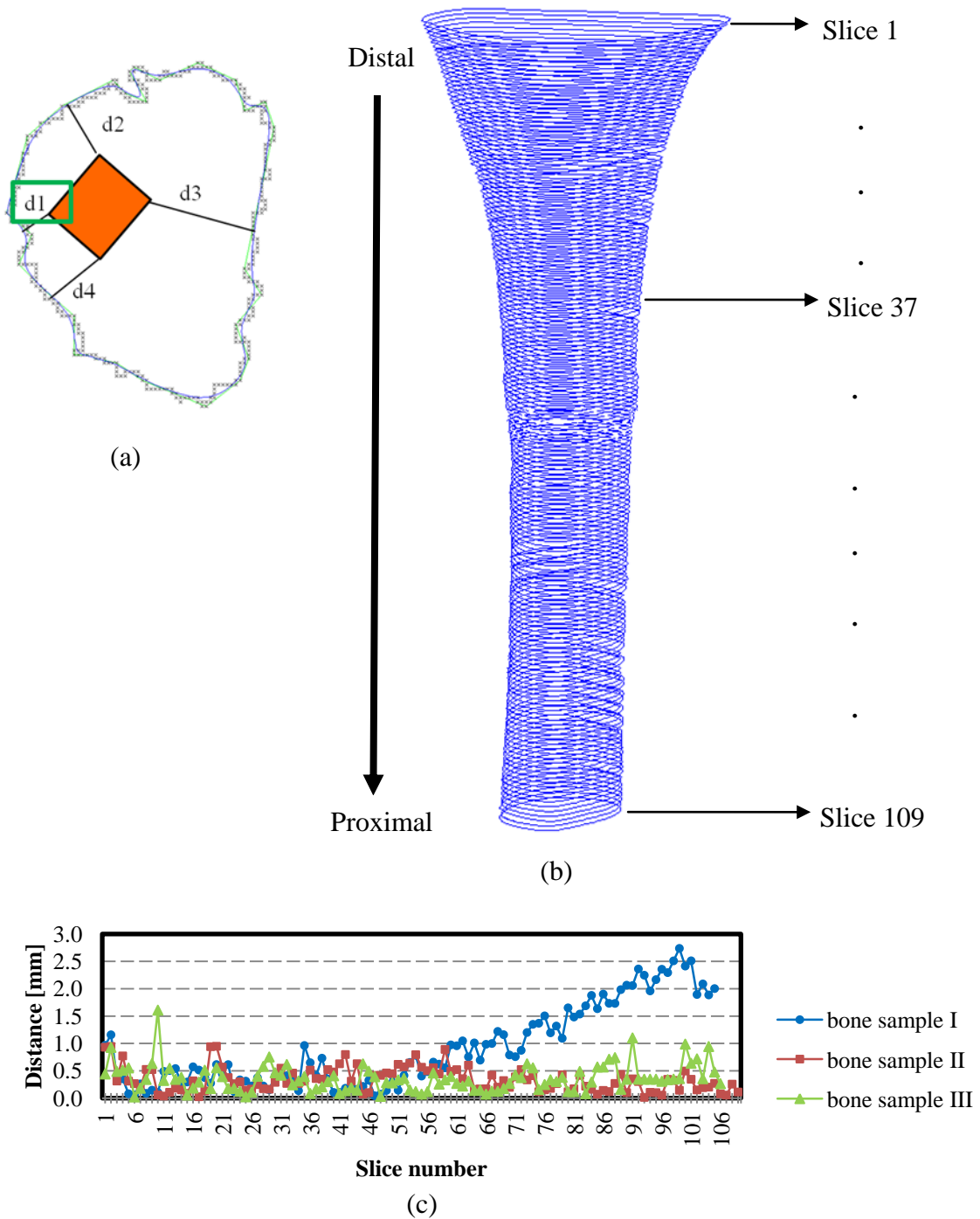


Figure 4.16: Definition of minimum implant distance to bone: (a) d1 to d4 represent the distances of each implant corner to bone inner boundary in one cross section while d1 denotes the minimum implant distance to bone, (b) relation between slice numbers and bone model, and (c) minimum implant distance to bone in each cross section from distal to proximal end of the bone.

In order to better assess the positioning condition of the implant, Figure 4.17 represents another new parameter defined as area ratio of the implant to bone in each cross section from distal to proximal ends for the same humeral specimens as in previous figure. The implant area was considered to be the area within the rectangular shape formed by four corners of the implant while the cross sectional area of the bone was denoted as the bone area delimited within the parametric definition of bone inner boundary in each cross section. The parameter of area ratio of the implant to bone from the distal to proximal ends of the bone represents the space that implant occupies in each cross section. The ideal design of the shape of the implant based on morphological characteristic of the distal humerus cavity should have a constant area ratio from the distal to proximal cross sections. However, as it can be seen from this figure, the area ratio for all these three specimens vary a lot showing that although implant does not have enough room for distal cross section, there is a large area ratio for proximal cross section. Considering Figures 4.16 and 4.17, it can be concluded that although for the majority of cross sections there is a large area ratio, the minimal distance from the implant to bone is less than 0.5 mm and thus is close to the wall of the bone. Therefore, the current design for the shape of the implant needs to be modified to make its positioning inside the bone optimal.

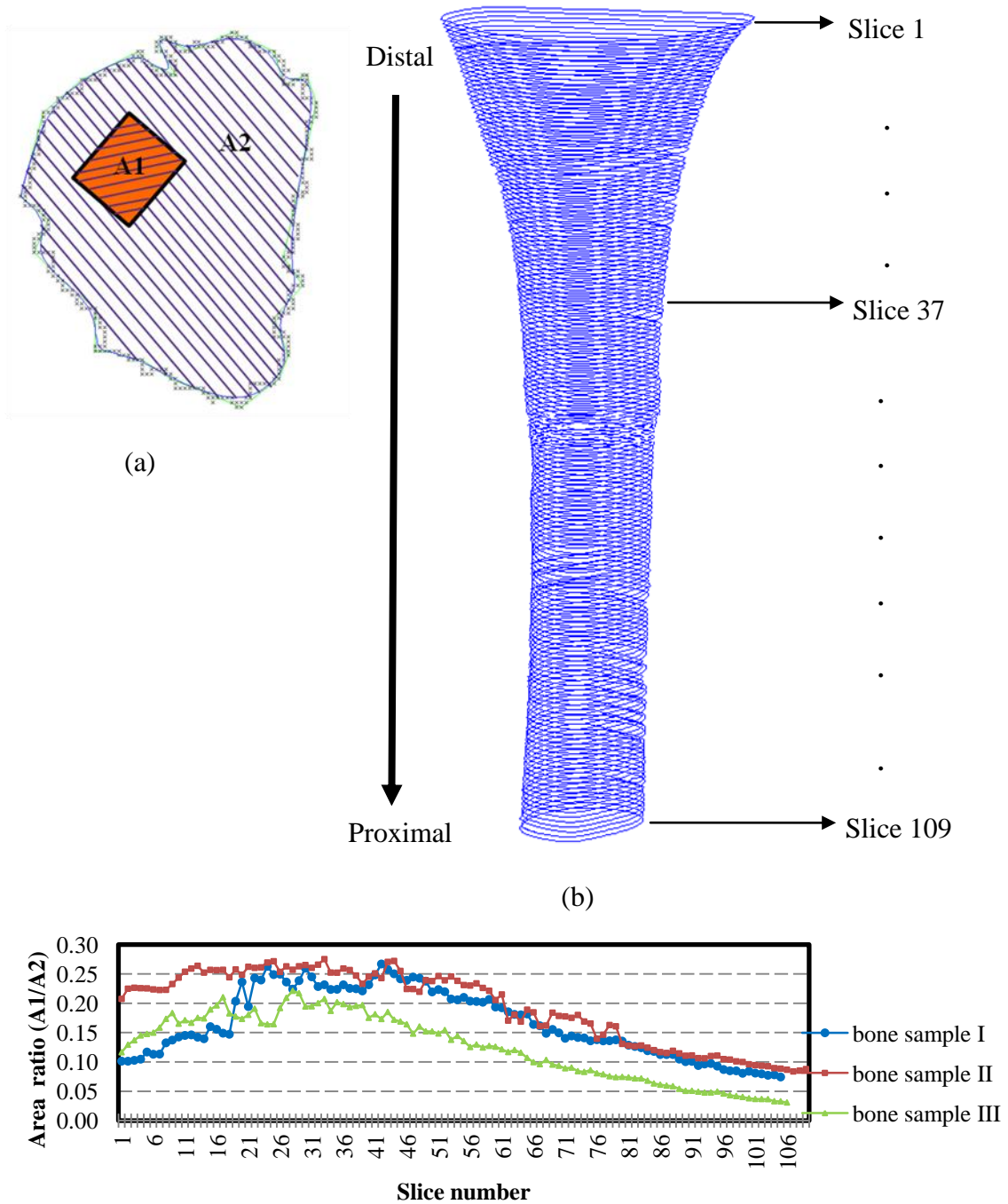


Figure 4.17: Definition of area (c) (a) A1 denotes implant area while A2 represents bone area delimited within the parametric definition of bone inner boundary in one cross section, (b) relation between slice numbers and bone model, and (c) Area ratio of implant to bone behaviour from distal to proximal end of bone.

In order to evaluate the efficiency and productivity of the genetic algorithm developed in this study, couple of tests were accomplished as following.

The first test belongs to insertion of a smaller size of the stem into the cavity of one random humeral specimen. Theoretically, smaller implant should lead to a better insertion and therefore a better malalignment, but in practice the story becomes a bit different. Note that a better insertion depends on the stem size of the implant, and better malalignment relies on relative position and orientation of the implant and bone FE axes. As it can be seen in Figure 4.18 although for initial iterations a better objective function/malalignment was achieved, and the algorithm converged faster, the final outcome depicted the fact that a smaller size of the stem would not necessarily lead to a better insertion and malalignment. Therefore, in order to provide a better implantation, both implant size and spool size have to be modified.

The second test performed was the repeatability test. In this test, the current proper implant for insertion into one corresponded humeral specimen was tested five consecutive times with exactly the same initial position for the implant. The translational and rotational malalignment values were reported in Figure 4.19. This test reveals the consistency and repeatability of the developed genetic algorithm. Although the malalignment for rotational error was not significantly different for both varus-valgus and internal-external angles, less consistency was observed for translational malalignment especially for anterior-posterior direction. Accordingly, the maximum difference in translational malalignment between these five cases is approximately 0.3 mm; thus, it can be strongly concluded that despite non-linear behavior of genetic algorithm itself, the

presented algorithm is consistent and reliable. Moreover, the objective function for all these five runs shows a close value representing the consistency of this method.

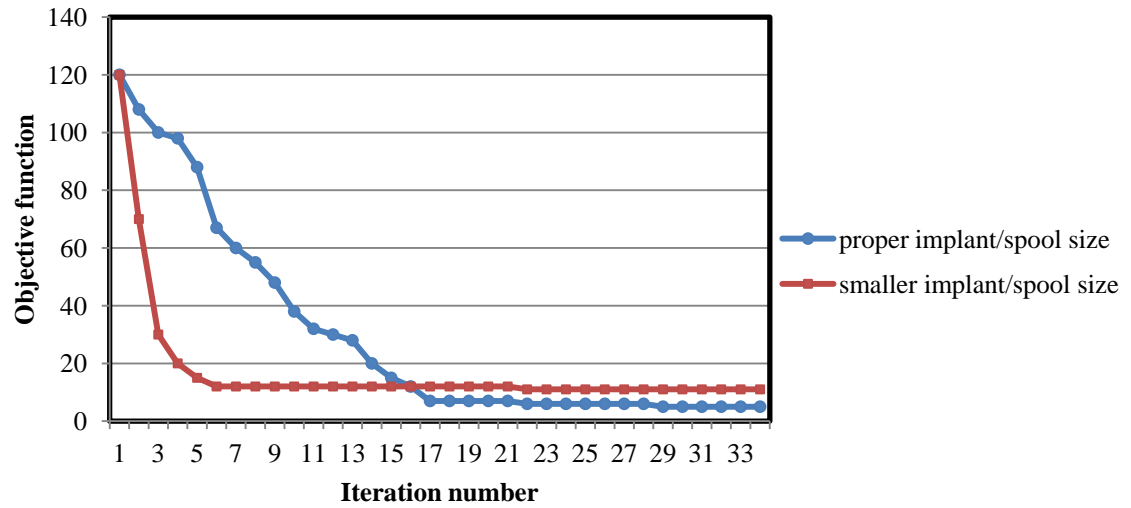
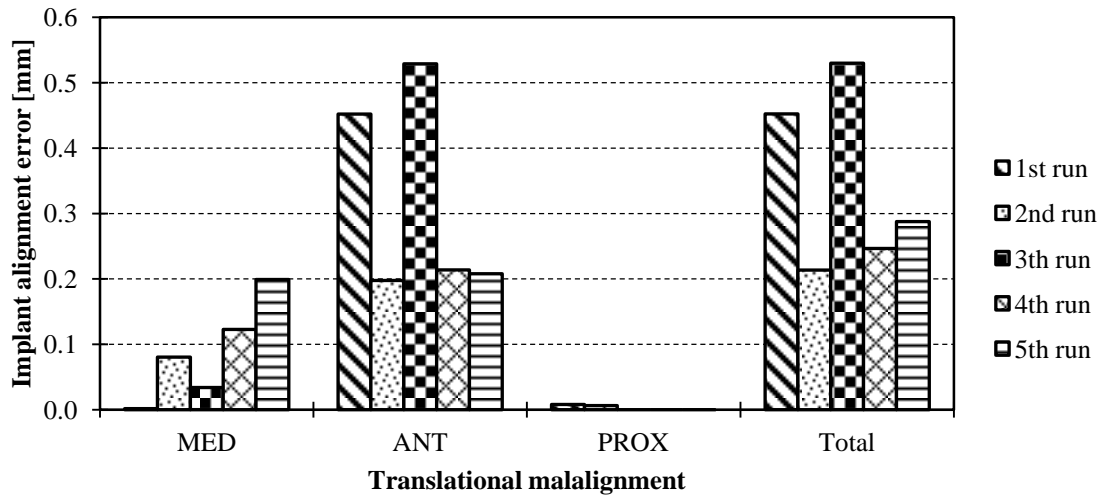
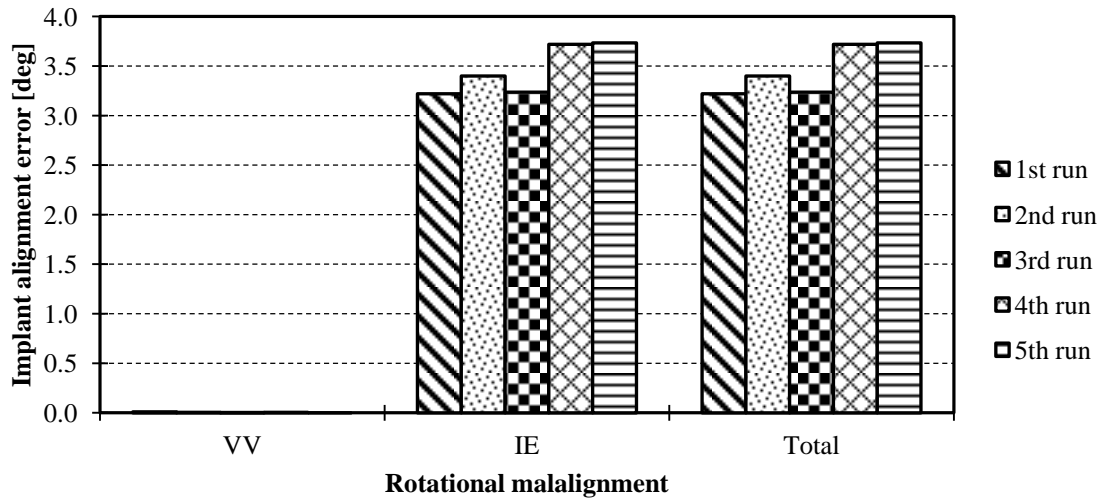


Figure 4.18: Impact of implant/spool size change in objective function value and final implant position



(a)



(b)

Figure 4.19: Repeatability test: (a) implant alignment error in translation (mean + 1 standard deviation) for developed method starting from the same implant position in 5 runs, and (b) implant alignment error in rotation (mean + 1 standard deviation) for developed method starting from the same implant position in 5 runs.

The third test conducted was similar to the second test with the difference that the initial implant orientation was selected to be different in five consecutive runs. As it was described in the previous section, the initial position of the implant was set in a sense that the centroid of proximal cross section of the implant matches the centroid of distal cross section of the bone. This was a consistent setup for all 9 humeral specimens that tested in this study within the developed genetic algorithm. In this test, the impact of different initial posture of the implant at the same initial position was evaluated, and the resultant translational and rotational malalignment was reported in Figure 4.20. As it was shown in this figure, the final malalignment values obtained in the current test is identical to the outcome of the previous one. Again the translational malalignment especially for anterior-posterior direction is much more significant than the rotational malalignment. However, since the values of the objective function for all five runs in this test were close enough to each other, it can be concluded that in spite of large deviations in the translational malalignment, the overall malalignment was compensated by rotational malalignment components.

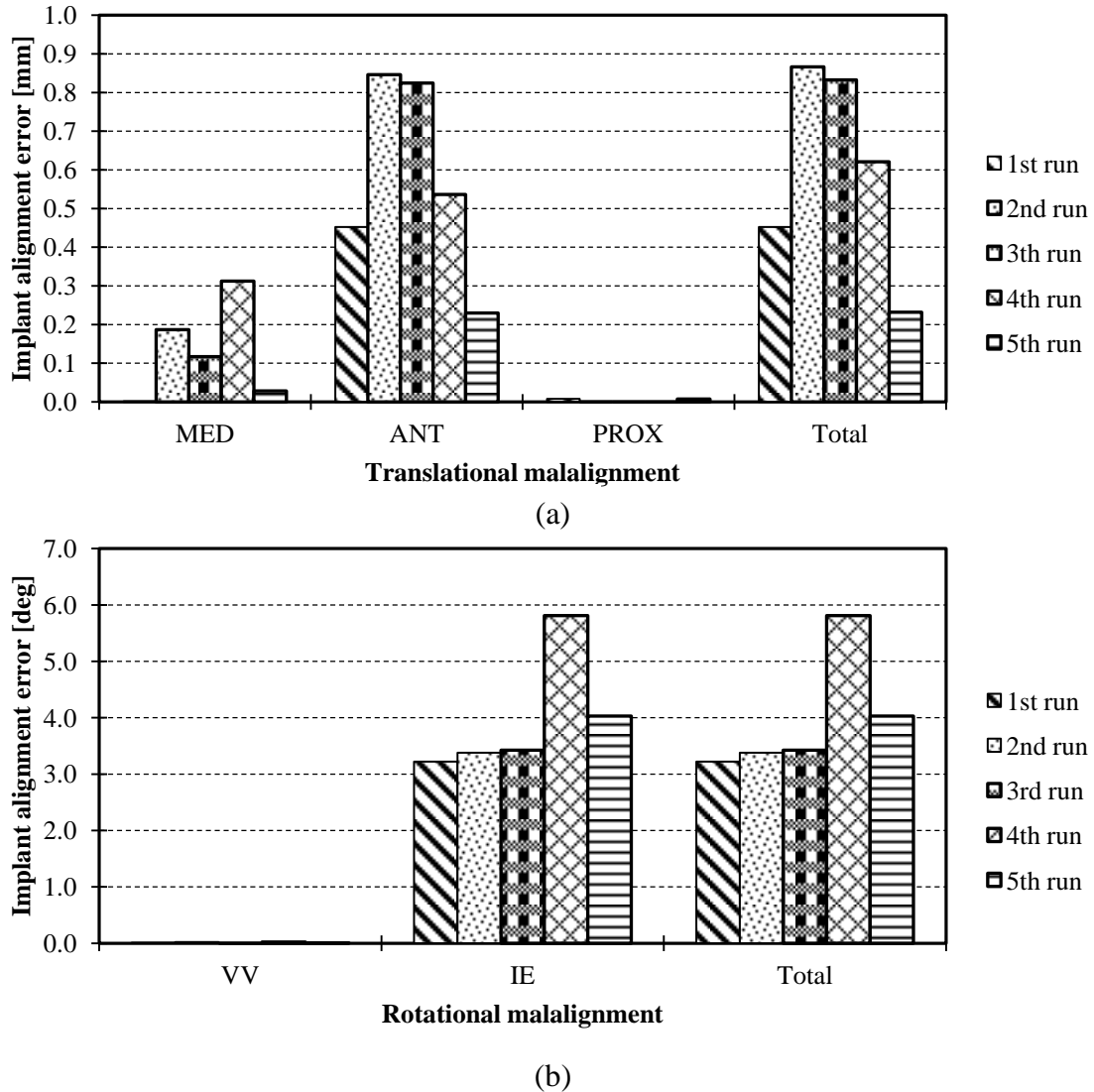


Figure 4.20: Sensitivity to initial implant position in the developed GA technique: (a) implant alignment error in translation (mean + 1 standard deviation) for developed method starting from different implant orientation in 5 runs, and (b) implant alignment error in rotation (mean + 1 standard deviation) for developed method starting from different implant position and orientation implant position in 5 runs.

4.5 Discussion

Given the fact that both techniques presented for accurate implantation include completely different procedures, slightly higher alignment errors are extremely acceptable especially when the only commonality is related to initial stack of raw CT images. It should be noted that here the rationale behind the comparison of the developed technique to the experimental setup will not entail the fact that this study considers the experimental setup as the golden standard. However the only reason for making such a comparison was to validate and evaluate the developed technique. Therefore, although the malalignment and standard deviation of the developed method is to some extent higher than the experimental setup, it results in consistency and accuracy but less improvement in accurate implantation.

Unlike the technique utilized in the experimental setup which cannot be applied in real surgical operations due to its dependency on landmarks being screwed to the distal humerus, the GA technique can be employed both pre-operatively and intra-operatively to better help surgeons complete implantation procedure in a more efficient way rather than the current semi-blind implantation. The other advantage of this technique is providing a simulation tool capable of deciding which size and combination of spool and stem can provide more accurate replication of flexion-extension axis of distal humerus with no damage to the physical bone. Due to the fact that the presented scheme can be applied to different humeral specimens with minimal user input, the generated tool can predict the best implant/bone fit in a quick time frame to help surgeons pre-operatively have a better plan for the surgery.

The selection of the intermediate cross section of the bone as one of the constraints of the algorithm was also investigated for all 9 humeral specimens. As a result, 40% of the distance from distal to proximal cross section is a region where the narrowest cross section of the bone exists. In order to ensure the selection of the narrowest cross section in 3 humeral specimens, various intermediate cross sections were selected and the resultant malalignment was assessed. This assessment revealed the fact that as long as the intermediate cross section is chosen within the region which is 40% of the way from distal to proximal cross section, there will be no significant impact on the implant insertion and final malalignment between the implant and bone FE axes. However, since the insertion algorithm checks the interference of the implant into the bone for all cross sections from distal to proximal ends, if the algorithm finds that after the insertion there is a penetration in one or couple of the cross sections, it adds this/those cross sections to the list of constraints, and starts the insertion procedure again until no penetration is found.

It should be noted here that based on Eq. (4.1), the weights associated with malalignment components play a major role in convergence point of the genetic algorithm. The reason behind this statement is that since genetic algorithm minimizes the objective function which depends highly on the values of both the weights and the malalignment components, inaccurate determination of the weights may lead to a convergence point with larger amounts for the malalignment components. Therefore, various combinations and limits were chosen for the weights, and the resultant objective function was tested within the scope of the genetic algorithm until it was decided that

normalizing d_{CC} with 1mm value and α_{VV} and α_{IE} with 2 degrees value will provide a reasonable range of malalignment at the end of insertion.

4.6 References

- Buckley, S.J. (1990) Fast Motion Planning for Multiple Moving Robots, *IEEE Int. Conf. on Robotics and Automation*, Scottsdale.
- Donald, B. (1987) A Search Algorithm for Motion Planning with Six Degrees of Freedom. *Artificial Intelligence in Engineering*, 31, 295-353.
- Faverjon, B. (1984) Obstacle Avoidance Using an Octree in the Configuration Space of the Manipulator. *IEEE Int. Conf. on Robotics and Automation*, Atlanta.
- Joskowicz, L. and Taylor, R. (1993) Hip Implant Insertability Analysis: A Medical Instance of the Peg-In-Hole Problem. *IEEE*, 901-908.
- Joskowicz, L. and Taylor, R. (1994) Preoperative insertability analysis and visualization of custom hip implant designs. *IBM TJ Watson Research Center*.
- Krenek, L., Farnig, E., Zingmond, D., and Soohoo, N. (2011) Complication and Revision Rates Following Total Elbow Arthroplasty. *The Journal of Hand Surgery*, 36[1],68-73.
- Latombe, J.C., (1991) Robot Motion Planning. *Kluwer Academic Publisher*.
- Lozano-Perez, T. and Brooks, R.A. (1983) , A Subdivision Algorithm in Configuration Space for Find-Path with Rotation. *8th Intl. Joint Conference on Artificial Intelligence*. Karlsruhe, FRG.
- McDonald, C.P., Johnson, J.A., King, J. W. and Peters, T. M. (2009a) Implant alignment in total elbow arthroplasty: conventional vs. navigated techniques. *SPIE*.
- McDonald, C.P., Johnson, J.A., Peters, T. M. and King, J. W. (2009b) The effect of Stem Length on the Alignment of the humeral component in computer-assisted total elbow arthroplasty, *Orthopaedic Research Society*. Las Vegas, USA (Poster)
- McDonald, C.P., Johnson, J.A., Peters, T. M. and King, J. W. (2010) Image-based navigation improves the positioning of the humeral component in total elbow arthroplasty. *J Shoulder Elbow Surg.* 19, 533-543.
- Mostafavi, K., Tutunea-Fatan, O. R., King, G. J., and Johnson, J. A. (2013, June). Prediction of Interference Free Positions of the Humeral Implant in Preparation of Joint Replacement Procedures. In *ASME 2013 Summer Bioengineering Conference* (pp. V01AT20A024-V01AT20A024). American Society of Mechanical Engineers.
- Mostafavi, K., Tutunea-Fatan, O. R., Lalone, E., King, G. J., and Johnson, J. A. (2013). Determination of Elbow Flexion-Extension Axis Based on Planar and Closed B-Splines. *Computer-Aided Design and Applications*, 10(4), 551-565.

- Sankupellay, M., Narainasamy, S., and Ismail, N. (2005) Simulation of implant fitting in the femur bone. *Sunway Academic Journal*, 2, 67-65.
- Tutunea-Fatan, O.R., Bernick, J.H., Lalone, E., King, G.J., and Johnson, J.A. (2010) Application of Collision Detection to Assess Implant Insertion in Elbow Replacement Surgery. SPIE.
- Voloshin, I., Schippert, D.W., Kakar, S., Kaye, E.K., and Morrey B.F. (2011) Complications of total elbow replacement: A systematic review. *J Shoulder Elbow Surg*, 20, 158-168.

Chapter 5

5 On the Design of Customized Implant Geometries

5.1 Overview

This chapter focuses on the shape optimization of the current humeral implants with the target of achieving minimum malalignment between native and prosthetic flexion-extension axes. Four different optimization methods are introduced to modify the current shape of the humeral implant while the results of the new customized implant shapes are reported. We hypothesized that this optimization approach can significantly lower the malalignments between bone and implant axes.

5.2 Introduction

Recent developments in manufacturing technologies, alongside the advancements in engineering and imaging software have created ample opportunities for personalized medicines to emerge in the healthcare industry. As a tool for tailoring of treatments as per individuals, personalized medicine can eliminate trial-and-error inefficiencies that inflate health care costs and undermine patient care. Industry players have also rapidly adopted this field and are progressing towards achieving higher goals in the same approach. Meanwhile, it became clear that the growing applications of computer-assisted and simulation techniques in orthopedic surgeries not only allow surgeons to reliably replace the damaged joints with artificial components (implants), but they can also be the key element towards a desirable development of computer-based systems for optimized implant design for individuals. Although, in a perfect world successful clinical outcome of surgical joint arthroplasty relies on precise fit of an implant to a patient, in a real

world, the off-the-shelf implants come only in a limited number of sizes. As time went on, surgeons began to realize that this inefficient way of delivering implants should be replaced by using accurate implant size and geometry customized for each individual patient.

The benefit of creating a true patient-specific implant is that it potentially addresses the driving factors of patient dissatisfaction after a joint arthroplasty. While the implant being too big or too small would be no longer an issue and it fits right every time, since the implants are covering all the cut bone, less blood loss, reduced risk of transfusion, less swelling of the joint and more importantly a significant drop in dissatisfaction rate will be observed. In addition, because the shape of the joint is more accurately reproduced, patients function better, sooner, and at the end of the recovery process have joints that feel and move more natural. In this chapter, four methods were developed to optimize the design parameters involved in the overall shape of the humeral implant. The new designed implants were then compared to the current shape of the implant.

In conventional joint surgeries, the bone is customized to fit the off-the-shelf implants while in personalized surgeries the idea is to employ a customized implant to fit the patient's bone. Studies reported that using standard artificial components for younger patients lead to a lower success rate comparing to older patients and that is why in so many countries delay the surgery time for younger patients [Harrysson *et al.*, 2007]. The most common reason for surgical failure of younger patients is aseptic loosening which is caused by more daily activities of younger patients versus older patients. Since the relative fit between implant and bone is not guaranteed, routine activities cause implant

micro motions in the bone canal. On the other side, reshaping the bone canal alters the rounded shape into an irregular shape. These two factors end up with uneven stress distribution on the endosteal surface of the bone, and therefore, uneven growths of bone (bone remodelling) on the implant-bone interface and loosening of the implant over time.

The other benefit of using customized implants is for patients having abnormal anatomy or asymmetric bone loss. Using customized implants can compensate the abnormal anatomy of the bone or asymmetric bone loss by avoiding challenging surgeries and poor outcome after the surgery for these types of patients. Despite of major obstacle for extensive using of customized implants which is associated with the cost, many reports have emphasized this fact that custom-designed implant can solve complicated orthopedic surgeries and lead to a better outcome. Most of these studies reported using custom implants on knee and hip joints and rare studies were conducted on elbow joint [Cil *et al.*, 2011].

Cil *et al.* [Cil *et al.*, 2011] designed a new shape for the ulnar implant to be used in total elbow arthroplasty. They believed that this triflange outrigger ulnar component can provide roll stability by having a righting moment that resists any disturbance in the roll moment. This idea was perceived from the concept of roll stability in outrigger canoes. They tested these new types of ulnar implant in the revision surgery of 5 patients who had failure of Coonrad-Morrey total elbow prosthesis. The result of this new shape for ulnar implant was bigger range of motion and also reducing the amount of pain in the elbow. However, for one of the patients an extra humeral component revision surgery became needed after 4 years of the revision surgery. Cil *et al.* also suggested this new shape of the ulna implant for patients with absent humeral epicondyles. They believe that

this new type can delay the failure of total elbow arthroplasty due to bushing wear in these patients [Cil *et al.*, 2011].

Gotze *et al.* analyzed the stability of custom-made femoral stem (Adaptiva) in seven pairs of fresh frozen cadaveric femurs for a hip replacement surgery. From CT scans, they derived the 3D model of the canal and by benefiting from CAD/CAM techniques they manufactured custom-made femoral implants. They added three ribs on the anterior surface of the implant in order to interdigitate with the metaphyseal cancellous bone. After positioning the implants into cadaveric femurs, they secured the bone in a biomechanical testing system which applied various load patterns on the femur. In order to validate this study, they compared the results of micromotions with conventional femoral stem implanted into femurs [Gotze *et al.*, 2002].

Gunther *et al.* employed custom insert glenoid implants in deficient glenoid bones during total shoulder replacement surgery for 7 patients. Indeed, deficiency in glenoid bone limits the treatment options and outcome of surgery because of lack of support for glenoid implant. Upon these circumstances surgeons usually prefer to perform a hemiarthroplasty instead of resurfacing the glenoid and current studies show that clinical results of hemiarthroplasty comparing to total shoulder arthroplasty is worse in patients with nonconcentric glenoid with bone loss. After these surgeries with new glenoid implants, patients had a better range of motion including 33 degrees for forward flexion and 34 degrees for external rotation. The pain level of patients after these surgeries dropped significantly from 6.9 to 0.1 (assuming that 10 represents the most severe pain and 0 to represent no pain situation) at the final follow-up [Gunther and Lynch, 2012].

Viceconti *et al.* introduced a new software program named as HIDE for the design of custom-made hip prosthesis. This software program is able to design the shape of the femoral stem from CT images in a single operation. The operator can also control the shape of the stem by imposing control section directly on CT images. CAM part of this software is able to generate the Gcode needed to manufacture this part using CNC machines [Viceconti *et al.*, 2001]. Similar to this software Jun and Choi [Jun and Choi, 2010] developed another new software for designing custom-made hip implant out of 3D geometry parameters related to Patient's 3D bone geometry. Some of these parameters are femoral shaft isthmus, anatomical femoral axis, femoral head center/radius, head offset length and femoral neck. By manufacturing and designing this implant the contact area between implant and bone has been maximized.

Harrysson *et al.* customized the shape of articulating surface and bone-implant interface for total knee arthroplasty implants and then used finite element analysis to verify this design in comparison with the conventional femoral implants. The advantages of such customized shape include better imitation of the shape of distal femur for articulating surface, even bone remodelling due to even distribution of stress and also less bone removal because of better bone-implant fit. They believe that this type of implant can be used for younger patients and those who have a more active life style [Harrysson *et al.*, 2007].

Some of the studies have focused on patient-specific pre-operative and intra-operative procedures such as computer-assisted surgeries or using navigation systems to better position the implant into the bone [Lombardi *et al.*, 2008; O'connor and Kransdorf, 2013] instead of changing the shape of the implant to fit the bone cavity.

5.3 Optimization Techniques on Elbow Implant Shape

The main goal of this chapter is to define the numerical techniques developed to optimize the shape of the implant, aiming at minimizing the amount of malalignment between FE axis of the bone and implant. In Chapter 4, a numerical algorithm was developed to find an optimal final position of the current implants inside the cavity of the distal humerus using genetic algorithm as the optimization function. Comparison of these results with experimental ones reveals the fact that the current design and shape of the implants can decrease the amount of FE axes malalignment to some extent while efforts on lowering this malalignment seems to be impossible with the current shape of the implant.

To our knowledge a limited number of researches have been published on the study of the humeral implant shape and also implant positioning to fit the endosteal cavity of the distal humerus. It should also be noted that the results achieved in the last chapter using cadaveric experiment and the numerical technique is really hard to achieve with intra-operative decisions of a surgeon during an elbow replacement surgery. Therefore a higher amount of malalignments should be expected as a result of the current shape of the implants and limitations of a real surgery. In order to avoid larger malalignment and achieve reasonable clinical results out of implantation during a surgery, a new shape of the humeral implant is required to be designed that theoretically results in a close to zero malalignment. In this way it can be ensured that this new design in a real surgical operation provides a minimum malalignment.

The issue of optimizing the shape of the current implant with the target of matching FE axis of the implant to the native FE axis of the bone during implant insertion into the bone cavity is a constrained nonlinear optimization problem. The mathematical

formulation for describing this problem is the same as equation Eq. (4.1) in the previous chapter,

$$\left\{ \begin{array}{l} \text{minimize}(\omega_1 \overline{d_{CC}} + \omega_2 \overline{\alpha_{VV}} + \omega_3 \overline{\alpha_{IE}}) \\ \mathbf{P}_{C_i}(l_D, \mathbf{\Pi}_j, \mathbf{\Omega}_j) \in \mathcal{P}^D \\ \text{Subject to: } \mathbf{P}_{C_i}(l_I, \mathbf{\Pi}_j, \mathbf{\Omega}_j) \in \mathcal{P}^I \\ \mathbf{P}_{C_i}(l_P, \mathbf{\Pi}_j, \mathbf{\Omega}_j) \in \mathcal{P}^P \end{array} \right. \quad (5.1)$$

The only difference between this problem and the fitting problem of the previous chapter is in terms of the problem input, which contains an optimized shape of the implant, instead of the current shape of the problem. As indicated in the previous chapter the core algorithm that fits the implant into the distal humerus cavity is the genetic algorithm. In order to customize the shape of the current implant a global search solver was used on top of the local genetic algorithm.

Global search benefits from a scatter-search mechanism to generate start points. Once it converges, the global search records this point and the end point and then estimates the radius of a basin of attraction. Based on the scatter-search mechanism, the global search tries a set of trial points and then evaluates where these initial points converges to. If these points converge reasonably well, the algorithm then checks to see if these points are local or global minima in the problem space. In case that a global minimum is found, the global solver stops the search and set this point as the output.

The parameters that define the shape of the humeral implant can be divided into two groups. First group contains parameters that control the shape of the distal end of the implant on where the spool sits and second group includes parameters that control the

shape of the stem (proximal part) which fits into the bone canal. Optimizing the parameters of both groups change the implant shape, and therefore, can impact on the final result of the implant insertion in a sense that the first group can directly effect on the minimization function which is the function of malalignment while the second group alters the constraints of the optimization problem.

In the context of this optimization problem, three different selection methods were decided to be considered for these parameters.

5.3.1 Stem-Focused Optimization

In the stem-focused optimization method, optimization variables were selected from the second group of parameters. In other words, only the stem shape of the implant was targeted for global optimization while the distal end of the implant was assumed to have the current shape. Among entire parameters that define stem length, stem posture, and cross sectional size and orientation of the stem, it was assumed that only those parameters that are related to stem posture should be optimized.

As it has been shown in Figure 5.1, the stem is supposed to have five degrees of freedom which includes two for translation and three for rotation. As Figure 5.1 indicates, the three rotations were defined with respect to the three axes of Stem Coordinate System (SCS with the origin at the center of distal implant stem) as rotation about X_s (β angle), rotation about Y_s (γ angle), and finally rotation about Z_s (θ angle).

The translation vector \mathbf{P}_{SS} is also defined as a planar vector in $X_s - Y_s$ plane capable of translating center of distal implant stem in both X_s and Y_s directions by

corresponding values of ΔX_s and ΔY_s . Therefore, the transformed posture of the implant stem can be expressed by T_s transformation matrix,

$$\begin{aligned} T_s &= R_{\hat{i}_s}(\beta) \cdot R_{\hat{j}_s}(\gamma) \cdot R_{\hat{k}_s}(\theta) \cdot T(P_{SS}) \\ P_{SS} &= [\Delta X_s \quad \Delta Y_s \quad 0] \end{aligned} \quad (5.2)$$

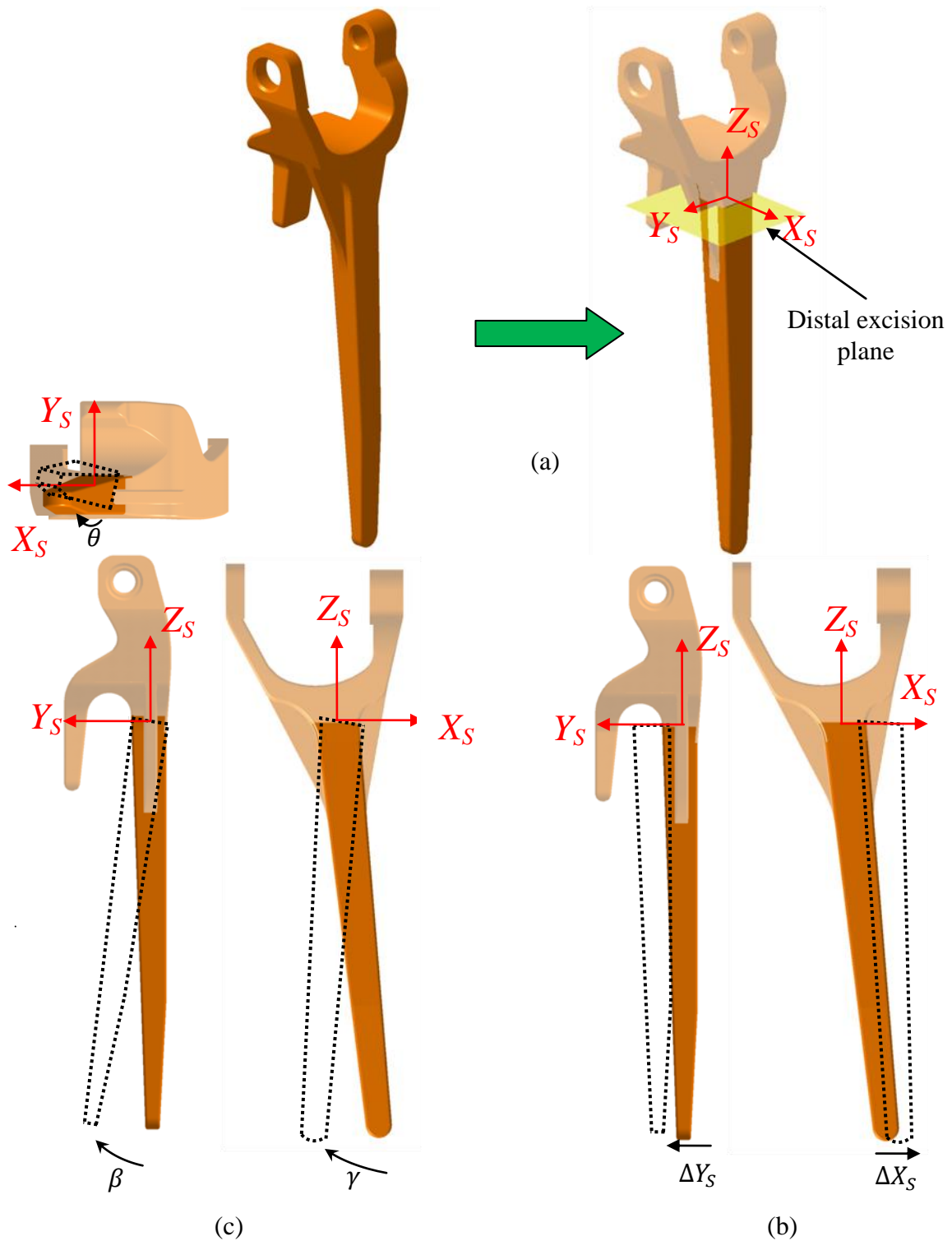


Figure 5.1: Stem-focused optimization variables: (a) Stem Coordinate System (SCS) located in the centroid of distal implant cross section, and (b) and (c) represent two translational and three rotational variables defined for the change in the shape of the stem.

The calculation of this transformation matrix enables the calculation of eight vertices of implant stem in the new stem shape as described in Eq. (5.3).

$$\begin{aligned}\mathbf{P}'_{C_i}(l_D, \mathbf{\Pi}_j, \mathbf{\Omega}_j) &= \mathbf{T}_S \cdot \mathbf{P}_{C_i}(l_D, \mathbf{\Pi}_j, \mathbf{\Omega}_j) \\ \mathbf{P}'_{C_i}(l_P, \mathbf{\Pi}_j, \mathbf{\Omega}_j) &= \mathbf{T}_S \cdot \mathbf{P}_{C_i}(l_P, \mathbf{\Pi}_j, \mathbf{\Omega}_j)\end{aligned}\quad (5.3)$$

Indeed, initial coordinates of implant vertices $\mathbf{P}_{C_i}(l_D, \mathbf{\Pi}_j, \mathbf{\Omega}_j)$ and $\mathbf{P}_{C_i}(l_P, \mathbf{\Pi}_j, \mathbf{\Omega}_j)$ relate to distal and proximal cross sections of current implant shape, respectively. The transformed coordinates of implant vertices $\mathbf{P}'_{C_i}(l_D, \mathbf{\Pi}_j, \mathbf{\Omega}_j)$ and $\mathbf{P}'_{C_i}(l_P, \mathbf{\Pi}_j, \mathbf{\Omega}_j)$ denotes distal and proximal vertices of implant cross sections in the context of new shape of the stem. While forcing the change in the coordinates of implant vertices for intermediate cross too ($\mathbf{P}'_{C_i}(l_I, \mathbf{\Pi}_j, \mathbf{\Omega}_j)$) section. By changing the shape of the stem, the problem constraints vary at each iteration, and so, the problem converts into below formulation:

$$\left\{ \begin{array}{l} \text{minimize}(\omega_1 \overline{d_{CC}} + \omega_2 \overline{\alpha_{VV}} + \omega_3 \overline{\alpha_{IE}}) \\ \mathbf{P}'_{C_i}(l_D, \mathbf{\Pi}_j, \mathbf{\Omega}_j) \in \mathcal{P}^D \\ \text{Subject to: } \mathbf{P}'_{C_i}(l_I, \mathbf{\Pi}_j, \mathbf{\Omega}_j) \in \mathcal{P}^I \\ \mathbf{P}'_{C_i}(l_P, \mathbf{\Pi}_j, \mathbf{\Omega}_j) \in \mathcal{P}^P \end{array} \right. \quad (5.4)$$

The problem defined in Eq. (5.4) is now again a classical problem of optimization which was solved through genetic algorithm. On top of this local algorithm, the master optimization algorithm, which is the global search algorithm, optimizes the five variables that are described in Eq. (5.2) in order to find a global minima.

In order to make this global optimization work it is needed to specify the initial guess along with the bounds for all the five variables that form the new shape of the stem.

The initial guess for this problem was set to be the current shape of the stem which is available in the market for elbow joint replacements. In fact, the algorithm starts with this shape and tries to optimize the five variables and converge into a new implant stem. On the other hand, bounds for each of the five variables specify the domain for the global solver to search the initial trial points. The primary goal behind selection of bounds was to achieve a new optimized stem shape with minimal possible change/deformation in the current shape of the stem aiming at lowering the malalignment significantly. In the area of selecting proper bounds, the literature lacks the information needed to characterize the domain of the variables. Therefore, arbitrary limits were chosen for each of the five variables, specifically,

$$\begin{aligned}
 \Delta X_{S_{\min}} &= \Delta Y_{S_{\min}} = -0.5mm \\
 \Delta X_{S_{\max}} &= \Delta Y_{S_{\max}} = 0.5mm \\
 \beta_{\min} &= \gamma_{\min} = \theta_{\min} = -2^{\circ} \\
 \beta_{\max} &= \gamma_{\max} = \theta_{\max} = 2^{\circ}
 \end{aligned} \tag{5.5}$$

5.3.2 Spool-Focused Optimization

The second method is spool-focused optimization technique that optimizes the parameters of the first group. In this way only the distal end of the implant was targeted for global optimization while the implant stem was supposed to keep the current shape. The rationale behind the optimization of these parameters is that one of the main reasons that may result in larger malalignment is the posture of the distal end of the implant

where the spool is attached to the implant and therefore the location of capitellum and trochlea centers along with implant FE axis are specified.

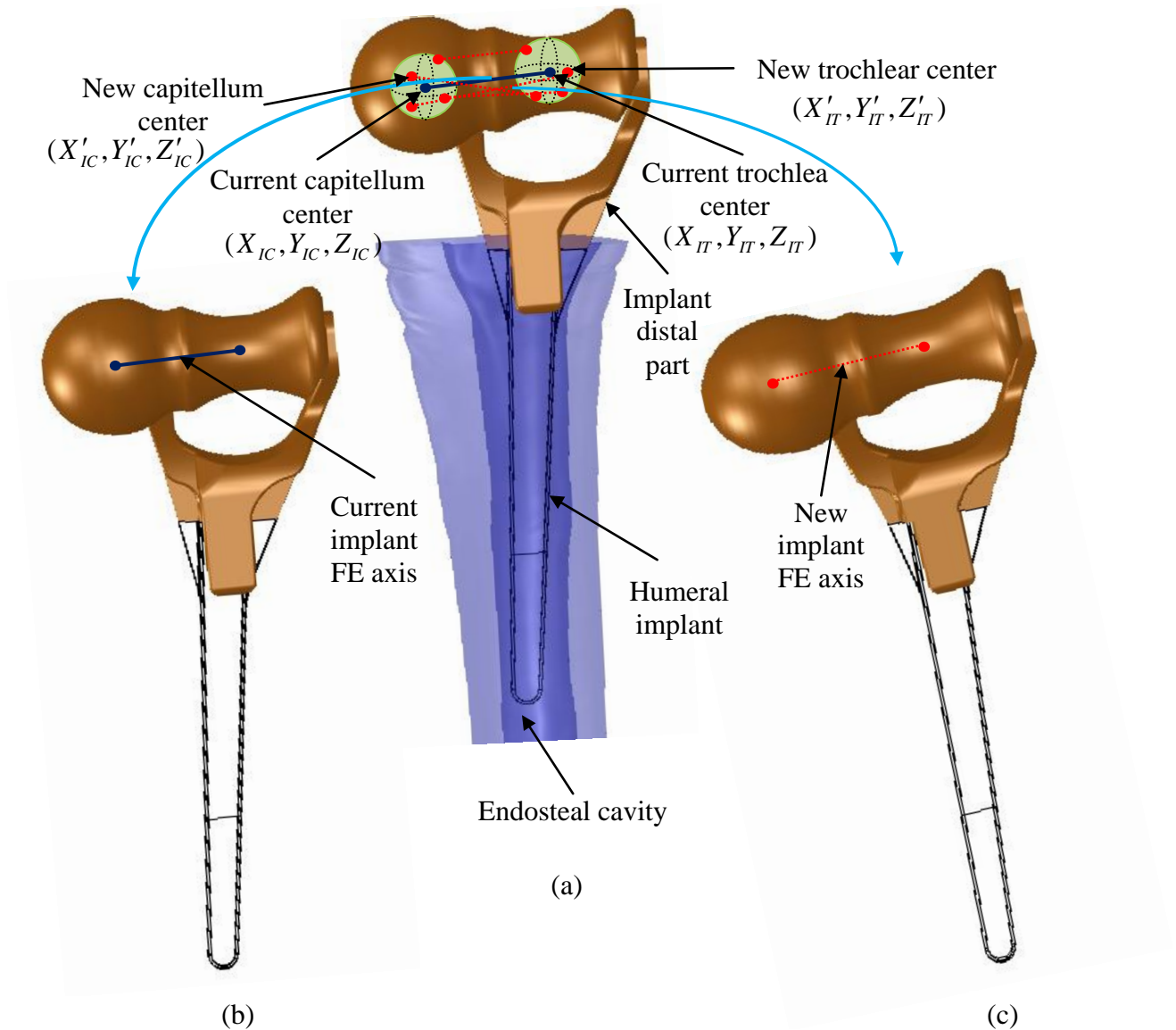


Figure 5.2: Spool-focused optimization method representation: (a) change in the position of the capitellum and trochlea centers of the current shape of the implant, (b) current design of the implant with its FE axis, and (c) new design for the implant distal part (where spool is attached) with new FE axis.

In this method, it was believed that by optimizing the position of the implant capitellum and trochlea, it can be ensured that the resultant shape of the new implant lead to less malalignment. The problem of optimizing capitellum and trochlea spatial coordinates is a six-variable problem in which three variables (X_{IC}, Y_{IC}, Z_{IC}) locate the position of capitellum center, and other three variables (X_{IT}, Y_{IT}, Z_{IT}) define the spatial position of trochlea center.

Again a global solver was employed to search possible new spatial locations for capitellum and trochlea centers and then a local genetic algorithm carried out finding the optimal final position of the new designed implant within the bone cavity in order to minimize the malalignment. Initial guess for the starting point of the global solver was set again to be the current shape of the implant. To specify the bounds of the six variables, it was assumed that each of the capitellum and trochlea centers can independently move within a sphere of radius 2mm with the center at the corresponding capitellum or trochlea center (Figure 5.2). Indeed, for each variable a bound of 2mm was applied as follows,

$$\begin{aligned}
 \Delta X_{IC_{\min}} &= \Delta Y_{IC_{\min}} = \Delta Z_{IC_{\min}} = -2mm \\
 \Delta X_{IC_{\max}} &= \Delta Y_{IC_{\min}} = \Delta Z_{IC_{\min}} = 2mm \\
 \Delta X_{IT_{\min}} &= \Delta Y_{IT_{\min}} = \Delta Z_{IT_{\min}} = -2mm \\
 \Delta X_{IT_{\max}} &= \Delta Y_{IT_{\min}} = \Delta Z_{IT_{\min}} = 2mm
 \end{aligned} \tag{5.6}$$

To set these bounds in the numerical algorithm, the Cartesian components of capitellum and trochlea centers were implemented and converted into spherical coordinates of (R, θ, ϕ) . Therefore, the new positions of capitellum and trochlea centers at each iteration were implemented as follows,

$$\begin{aligned}
\text{Capitellum:} & \begin{cases} X'_{IC} = X_{IC} + R_C \cos \theta_C \sin \phi_C \\ Y'_{IC} = Y_{IC} + R_C \sin \theta_C \sin \phi_C \\ Z'_{IC} = Z_{IC} + R_C \cos \phi_C \end{cases} \\
\text{Trochlea:} & \begin{cases} X'_{IT} = X_{IT} + R_T \cos \theta_T \sin \phi_T \\ Y'_{IT} = Y_{IT} + R_T \sin \theta_T \sin \phi_T \\ Z'_{IT} = Z_{IT} + R_T \cos \phi_T \end{cases}
\end{aligned} \tag{5.7}$$

in which $(X'_{IC}, Y'_{IC}, Z'_{IC})$ and $(X'_{IT}, Y'_{IT}, Z'_{IT})$ are the new locations of capitellum and trochlea centers and (R_C, θ_C, ϕ_C) and (R_T, θ_T, ϕ_T) are variables that define the spheres around current capitellum center (X_{IC}, Y_{IC}, Z_{IC}) and trochlea center (X_{IT}, Y_{IT}, Z_{IT}) . The bounds for this spherical coordinates change to following values,

$$\begin{aligned}
R_{C_{\min}} &= R_{T_{\min}} = 0mm \\
R_{C_{\max}} &= R_{T_{\max}} = 2mm \\
\theta_{C_{\min}} &= \theta_{T_{\min}} = 0^\circ \\
\theta_{C_{\max}} &= \theta_{T_{\max}} = 360^\circ \\
\phi_{C_{\min}} &= \phi_{T_{\min}} = 0^\circ \\
\phi_{C_{\max}} &= \phi_{T_{\max}} = 180^\circ
\end{aligned} \tag{5.8}$$

5.3.3 Overall Implant Optimization

This method covers parameters of both groups related to the distal end of the implant and as well as to the shape of the implant stem. In order to generalize the problem and provide enough degrees of freedom for the deformation/change of the implant shape, an optimization problem with twelve variables was considered for this method.

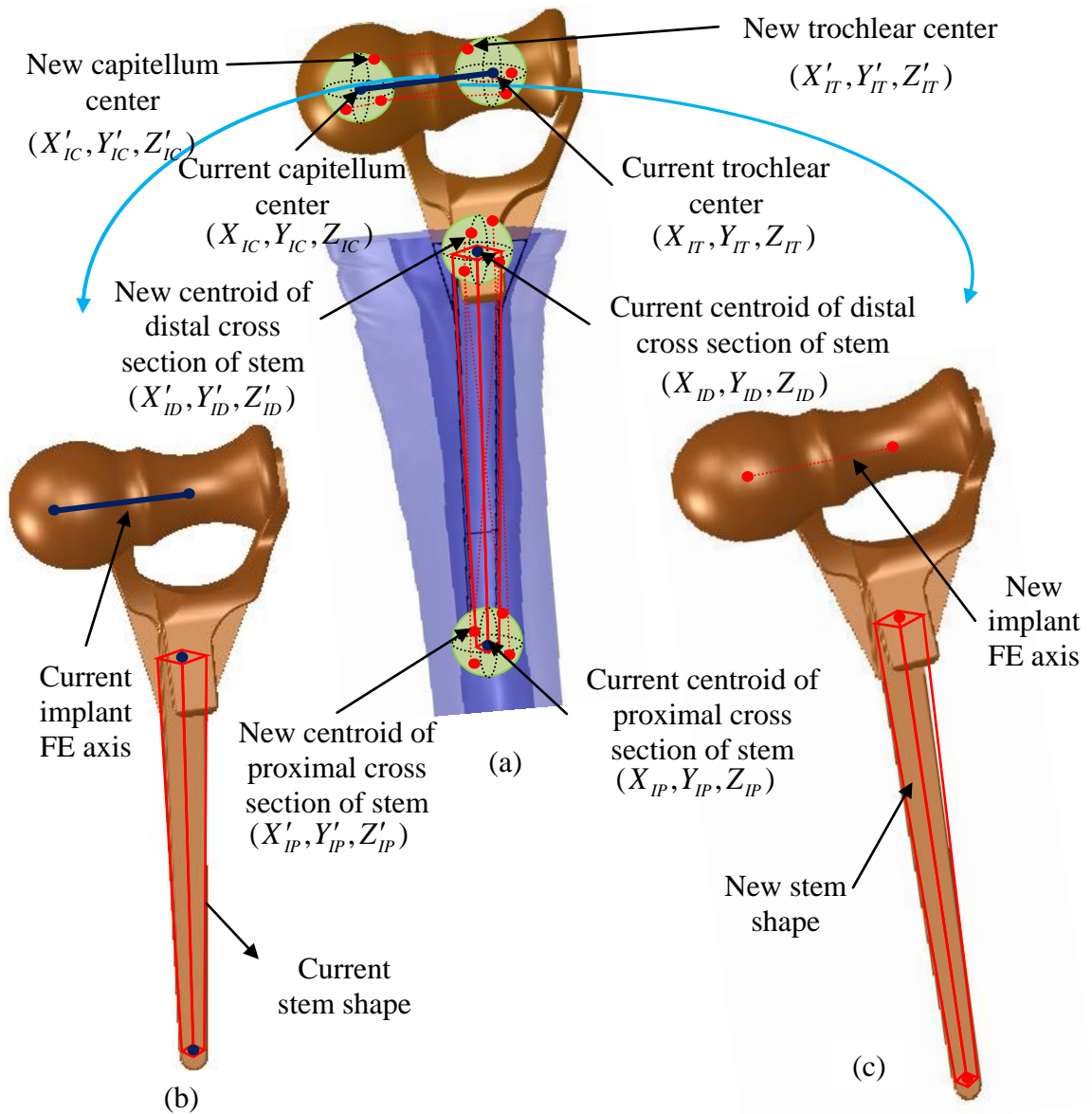


Figure 5.3: Overall implant optimization method representation: (a) change in the positions of the capitellum and trochlea centers and also centroids of the distal and proximal cross sections of stem for current shape of the implant, (b) current design of the implant with its current FE axis and current stem shape and (c) new design for the implant with new FE axis and new stem shape.

Out of these twelve variables, six variables define the new shape of the implant stem while the other six variables are related to the distal end of the implant and specifically implant capitellum and trochlea centers, similar to what was described in the second method. The six variables that are related to the implant stem are spatial coordinates of centroids of distal (X_{ID}, Y_{ID}, Z_{ID}) and proximal (X_{IP}, Y_{IP}, Z_{IP}) implant cross sections, as described in Figure 5.3.

The bounds for all these twelve variables are similar to the second method in a sense that 2 mm limit was set for each variable. Therefore, the domain of this optimization problem is a 12D space in which capitellum and trochlea centers and centroids of distal and proximal implant cross sections can vary within a sphere with radius of 2mm to be positioned at the center of each corresponding centers. The methodology for solving this optimization is the same as previous methods. While a local genetic algorithm is responsible for finding an optimal position for a selected shape of the implant as input, a master global solver optimizes the shape of the implant in order to minimize the malalignment.

Spherical coordinates were used for this method too in order to specify bounds for the variables. The new positions of capitellum and trochlea centers were named as $(X'_{IC}, Y'_{IC}, Z'_{IC})$ and $(X'_{IT}, Y'_{IT}, Z'_{IT})$ in each iteration and centroids of distal and proximal implant cross sections were implemented as $(X'_{ID}, Y'_{ID}, Z'_{ID})$ and $(X'_{IP}, Y'_{IP}, Z'_{IP})$ and therefore their relation to the original corresponding centers can be calculated as,

$$\begin{aligned}
\text{Capitellum : } & \begin{cases} X'_{IC} = X_{IC} + R_C \cos \theta_C \sin \phi_C \\ Y'_{IC} = Y_{IC} + R_C \sin \theta_C \sin \phi_C \\ Z'_{IC} = Z_{IC} + R_C \cos \phi_C \end{cases} \\
\text{Trochlea : } & \begin{cases} X'_{IT} = X_{IT} + R_T \cos \theta_T \sin \phi_T \\ Y'_{IT} = Y_{IT} + R_T \sin \theta_T \sin \phi_T \\ Z'_{IT} = Z_{IT} + R_T \cos \phi_T \end{cases}
\end{aligned} \tag{5.9}$$

$$\begin{aligned}
\text{Distal Implant : } & \begin{cases} X'_{ID} = X_{ID} + R_D \cos \theta_D \sin \phi_D \\ Y'_{ID} = Y_{ID} + R_D \sin \theta_D \sin \phi_D \\ Z'_{ID} = Z_{ID} + R_D \cos \phi_D \end{cases} \\
\text{Proximal Implant : } & \begin{cases} X'_{IP} = X_{IP} + R_P \cos \theta_P \sin \phi_P \\ Y'_{IP} = Y_{IP} + R_P \sin \theta_P \sin \phi_P \\ Z'_{IP} = Z_{IP} + R_P \cos \phi_P \end{cases}
\end{aligned} \tag{5.10}$$

In the Eqs. (5.9) and (5.10), (R_D, θ_D, ϕ_D) and (R_P, θ_P, ϕ_P) are variables that define the spheres around current centroids of distal and proximal implant cross sections. The bounds for this spherical coordinates change to the following values,

$$\begin{aligned}
R_{C_{\min}} &= R_{T_{\min}} = R_{D_{\min}} = R_{P_{\min}} = 0mm \\
R_{C_{\max}} &= R_{T_{\max}} = R_{D_{\max}} = R_{P_{\max}} = 2mm \\
\theta_{C_{\min}} &= \theta_{T_{\min}} = \theta_{D_{\min}} = \theta_{P_{\min}} = 0^\circ \\
\theta_{C_{\max}} &= \theta_{T_{\max}} = \theta_{D_{\max}} = \theta_{P_{\max}} = 360^\circ \\
\phi_{C_{\min}} &= \phi_{T_{\min}} = \phi_{D_{\min}} = \phi_{P_{\min}} = 0^\circ \\
\phi_{C_{\max}} &= \phi_{T_{\max}} = \phi_{D_{\max}} = \phi_{P_{\max}} = 180^\circ
\end{aligned} \tag{5.11}$$

All aforementioned methods follow the below optimization chart:

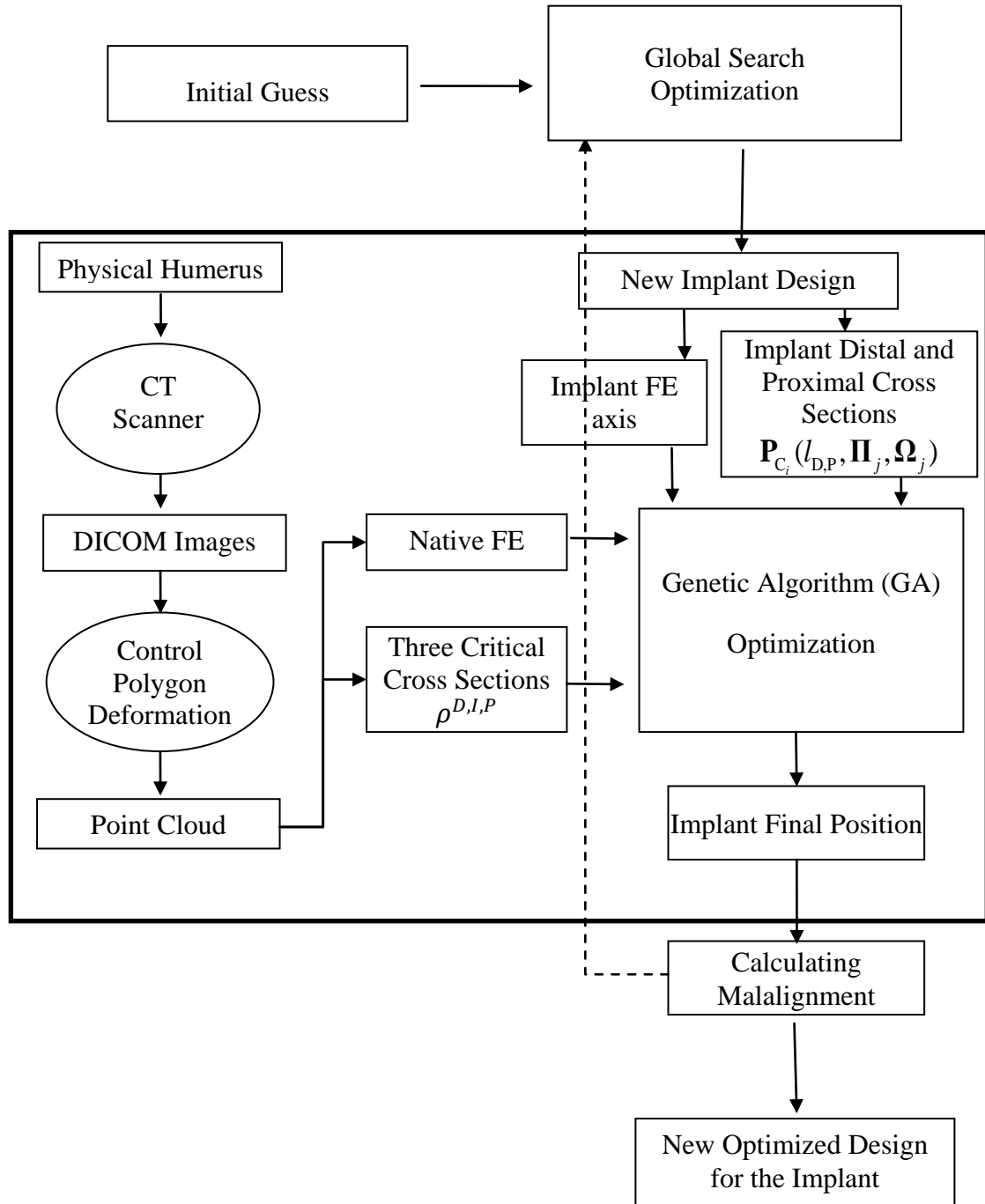


Figure 5.4: Schematic chart of the first three methods (stem-focused, spool-focused and overall implant optimization) for optimizing the shape of the implant.

Beside all these global optimization methods, brute force method was also used primarily for comparison and reference purposes and in order to make sure it can potentially converge to a reasonable result with all the information provided for the global search method.

All the methods described so far benefit from a global solver for shape optimization and a local genetic algorithm. Since these methods encounter as double-optimization problems, the computation time grows significantly. In order to make such a double-optimization problem converges, it might be needed to wait for weeks in some cases. Although there are ways to optimize the coding behind these numerical algorithms in order to speed up the convergence, still the computation time is considerable. In the fourth method a new method will be introduced that avoids such double optimization problem and is capable of calculating the optimized shape of the implant in a different approach.

5.3.4 Customized Implant Design

Unlike previous methods that try to optimize current shape of the implant, the logic behind this method is sort of out-of-the-box idea aiming at shaping a new implant starting from scratch. Assuming that the endosteal canal of the distal humerus with its FE axis is provided, the problem only focuses on the challenge of obtaining the shape of the implant which best fits into this cavity while FE axes match perfectly. For starting point of the solution, it can be considered that the FE axis of the implant match exactly the FE axis of the bone. Therefore, the problem can be easily narrowed down to finding the best shape for the stem that fits well in the bone cavity. Once it is ensured that the stem inserts the cavity with no challenge, since the FE axis of the proposed implant matches already with

FE axis of the bone, minimum possible malalignment (ideally close to zero) is guaranteed.

Finding an optimal shape for the stem that from a starting point out of the bone canal can be transferred to a final point in the bone cavity with no penetration into the walls seems to be challenging. In order to solve this problem, it can be presumed that a final solution has been achieved and so there is a final position/posture for the implant stem in which all the constraints are satisfied. Due to the fact that most of the common implant stems have regular straight edges in the distal-proximal direction, the most accessible starting point out of the bone cavity based on the achieved final position of the implant stem, is a point that lies on the centerline of the implant stem. This centerline also represents the optimal insertion trajectory that provides the surgeon a linear direction for implantation. That being said, the problem can be converted to finding a 3D axis of the canal that best represents the centerline of the implant stem and satisfies all constraints. The optimal 3D axis lies where the largest volumetric envelope inside the bone cavity occurs for the linear insertion of the implant stem.

To better calculate this volumetric envelope, it can be presumed that this envelope is close to a cylinder with an irregular cross sectional shape while the 3D axis characterizes the centerline of this cylinder. In order to maximize the volume of this envelope, it is required to search for the biggest cross sectional area of the cylinder. Indeed, this maximum irregular cross section of the cylinder-shape envelope is the biggest common area of the projections of all inner boundaries of the distal humerus onto a plane which is normal to the aforementioned optimal 3D axis, as shown in Figure 5.5.

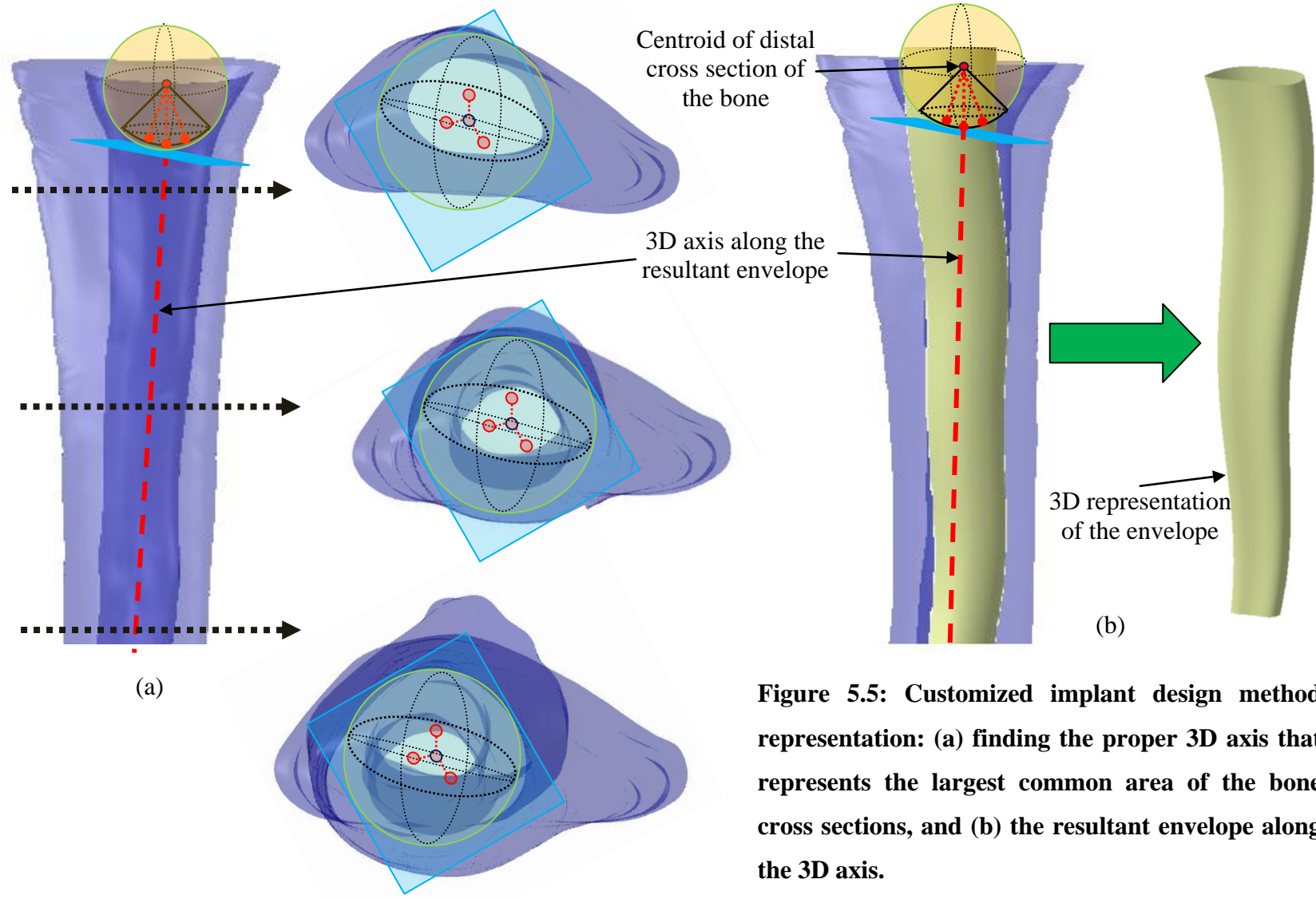


Figure 5.5: Customized implant design method representation: (a) finding the proper 3D axis that represents the largest common area of the bone cross sections, and (b) the resultant envelope along the 3D axis.

The method developed within this section searches for the optimal 3D axis that maximizes the common area of projections of all inner boundaries of the bone onto the plane normal to this axis. The algorithm employs a simple searching function to search among all 3D axes that start from the geometric center of the distal cross section of the bone (X_{BD}, Y_{BD}, Z_{BD}) and ends on a sphere with the arbitrary radius of 1mm positioned at the geometric center of the distal cross section. To decrease the computational complexity of this search, the bounds were set in a way that only a portion of the sphere that observes proximal cross section of the bone, was included in the search domain. The 3D axis $\mathbf{A}_{insertion}$ can be implemented as,

$$\begin{aligned} \mathbf{A}_{insertion} &= [\cos \theta \sin \phi \quad \sin \theta \sin \phi \quad \cos \phi] \\ 0 &\leq \theta \leq 2\pi \\ \phi_{min} &\leq \phi \leq \phi_{max} \end{aligned} \quad (5.12)$$

To find the projection $proj_{plane}(\rho_k^m)$ of k^{th} point on m^{th} inner bone cross section ρ_k^m onto a plane with the $\mathbf{A}_{insertion}$ as the normal vector and tangent to the sphere at $(X'_{BD}, Y'_{BD}, Z'_{BD})$ point, the following calculations are needed,

$$\begin{cases} X'_{BD} = X_{BD} + \cos \theta_i \sin \phi_j \\ Y'_{BD} = Y_{BD} + \sin \theta_i \sin \phi_j \\ Z'_{BD} = Z_{BD} + \cos \phi_j \end{cases} \quad (5.13)$$

$$\mathbf{P}'_{BD} = [X'_{BD} \quad Y'_{BD} \quad Z'_{BD}] \quad (5.14)$$

$$\text{proj}_{plane}(\rho_k^m) = \rho_k^m - (\mathbf{A}_{insertion} \cdot (\rho_k^m - \mathbf{P}'_{BD})) \mathbf{A}_{insertion} \quad (5.15)$$

Once all points on each inner bone cross section were projected on the plane, the problem equation is converted to,

$$\text{maximize}(\text{Area}(\text{proj}_{plane}(\rho_k^{m_D}) \cap \dots \cap \text{proj}_{plane}(\rho_k^{m_P}))) \quad (5.16)$$

Once this optimal axis is defined, there are couple of approaches that can be taken for finding the shape of the stem. Among all possibilities, it was decided to follow the cross sectional sizing of the current implant shape for this new method. By having this optimal axis, the algorithm then starts to rotate the implant stem along that axis until it finds an orientation for the implant stem that has no penetration into the bone.

If we put the resultant two sections of implant FE axis, which was supposed to match bone FE axis and implant stem shape together, the new optimized shape of the implant can be achieved which can ensure a minimum malalignment. In order to check the efficiency of this method, the resultant shape of the implant was inserted into the bone cavity form a starting point out of the cavity using the method described in the previous section.

5.4 Result

All the four methods described in the previous section were tested on a bone sample to evaluate their performances. For all the methods, the same input was provided including bone cross sections, initial implant position, and information on native FE axis and as the

output optimized variables, solving time, and malalignment values were reported in Tables 5.1-5.4. The only difference is that for the first three methods the first three best solutions were provided while for the last method only the final result was reported.

Table 5.1: Summary of the best three implant designs with minimum malalignment developed by the stem-focused optimization method.

Stem-Focused Optimization Method	Optimized Variables					Malalignment			fval	Solving Time [min]
	X [mm]	Y [mm]	β [rad]	γ [rad]	θ [rad]	d_{cc} [mm]	α_{VV} [rad]	α_{IE} [rad]		
	-0.29	-0.04	-0.02	-0.03	-0.02	0.55	0.41	1.29	1.40	24060
	-0.25	-0.27	-0.02	-0.03	0.00	0.001	1.10	1.82	1.46	22480
	-0.08	-0.48	-0.02	-0.01	-0.01	0.001	0.22	2.74	1.48	22120

Table 5.2: Summary of the best three implant designs with minimum malalignment developed by the spool-focused optimization method.

Spool-Focused Optimization Method	Optimized Variables						Malalignment			fval	Solving Time [min]
	R_C [mm]	θ_C [rad]	ϕ_C [rad]	R_T [mm]	θ_T [rad]	ϕ_T [rad]	d_{cc} [mm]	α_{VV} [rad]	α_{IE} [rad]		
	1.74	0.63	0.55	0.94	1.10	2.26	0.00	0.01	0.01	0.01	17745
	1.76	0.07	0.58	0.92	1.24	2.25	0.01	0.04	0.12	0.09	12890
	1.74	0.63	0.55	0.94	1.10	2.26	0.05	0.01	0.13	0.12	9783

Table 5.3: Summary of the best three implant designs with minimum malalignment developed by the overall implant optimization method.



Overall Implant Optimization Method	Optimized Variables												Malalignment			fval	Solving Time [min]
	R_C [mm]	θ_C [rad]	ϕ_C [rad]	R_T [mm]	θ_T [rad]	ϕ_T [rad]	R_D [mm]	θ_D [rad]	ϕ_D [rad]	R_P [mm]	θ_P [rad]	ϕ_P [rad]	d_{cc} [mm]	α_{VV} [rad]	α_{IE} [rad]		
	0.57	0.00	2.23	1.97	0.12	2.73	1.51	3.68	2.50	0.15	2.23	2.43	0.01	0.00	0.00	0.01	18250
	0.64	0.05	2.93	1.99	0.89	2.93	1.33	5.36	3.14	0.19	2.10	2.62	0.01	0.04	0.18	0.12	12524
	0.65	0.18	2.89	1.96	0.92	2.91	1.32	5.15	3.13	0.20	2.12	2.51	0.10	0.10	0.02	0.16	10371

Table 5.4: Summary of the best three implant designs with minimum malalignment developed by the customized implant design method.

Customized Implant Design Method	θ [rad]	ϕ [rad]				Malalignment			fval	Solving Time [min]
			X [mm]	Y [mm]	Z [mm]	d_{cc} [mm]	α_{VV} [rad]	α_{IE} [rad]		
	0.43	0.14	0.13	0.06	0.98	0.00	0.00	0.02	0.01	1

As expected, differences in results are visible between various methods. However, the customized implant design method provides a more efficient solution to this problem. Not only this method decreases the amount of solving time significantly, it will also lead to a better (almost zero) malalignment since the rationale behind the solution of this method originates from the fact that the two FE axes should be matched in the primary stage. To better visualize the impacts of such solutions onto final optimized designs of the current implant, Figures 5.6 – 5.10 provide a 3D representation of all implant designs derived by the best solution obtained with each single method.

It should be noted here that since the implant body is a single solid body, change in the design of the stem (parameters of group2) is convertible to change in the design of the distal section of humerus (parameters of group1). However, in order to make the results of all methods comparable, for all solutions the distal cross section of the stem part of the humerus matched in 3D representation. All these figures reveal the fact that current shape of the implant can be converted to a better design through multiple ways in different angular directions. The severe difference belongs to the result of the last method in which the current shape of the implant needs to be modified considerably to be able to minimize the malalignment.

 Current implant shape
 New implant shape by the stem-focused optimization method

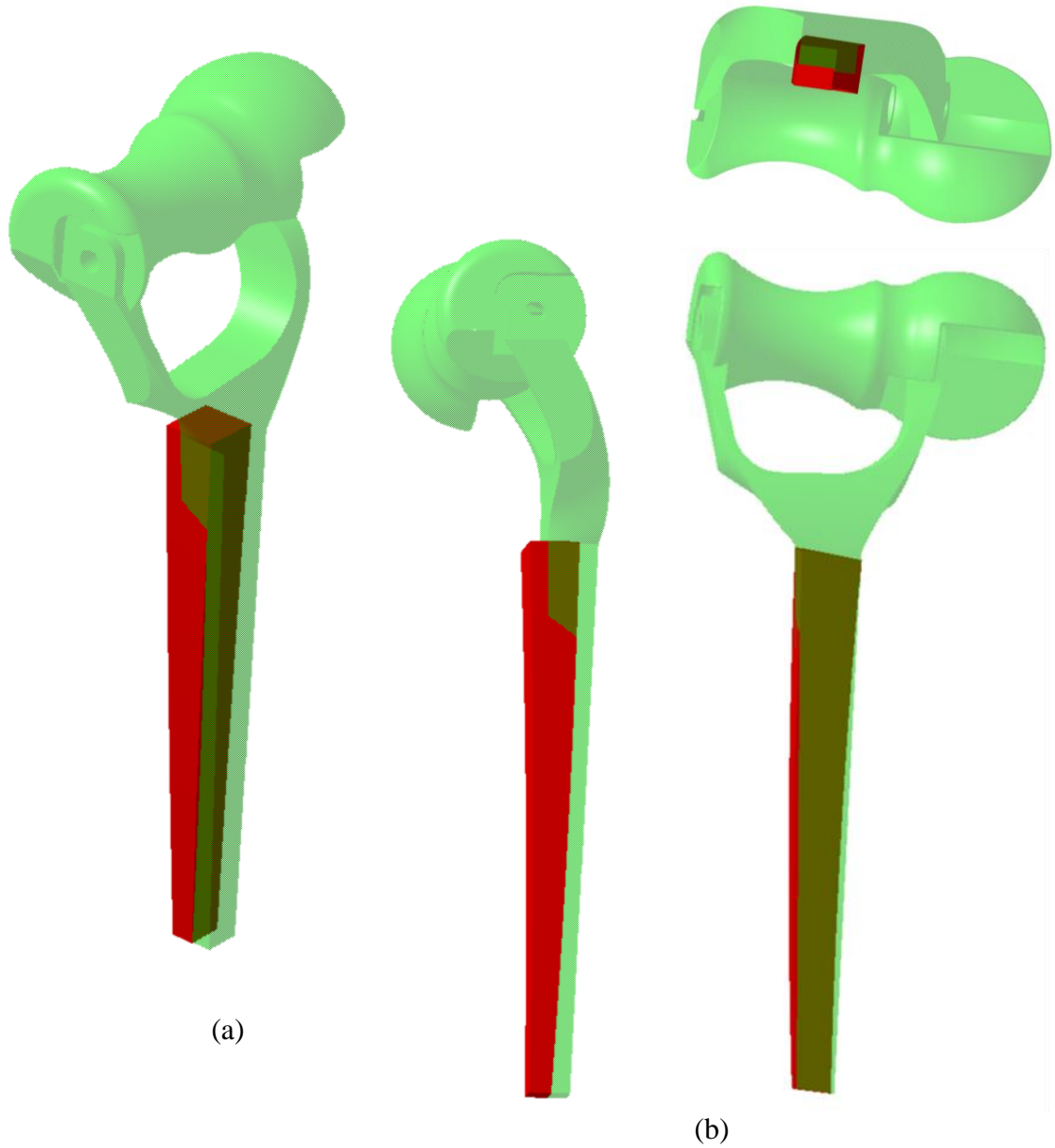


Figure 5.6: Comparison of the developed implant design in the stem-focused optimization method versus current design (green): (a) 3D view, and (b) side views of this comparison implant designs.

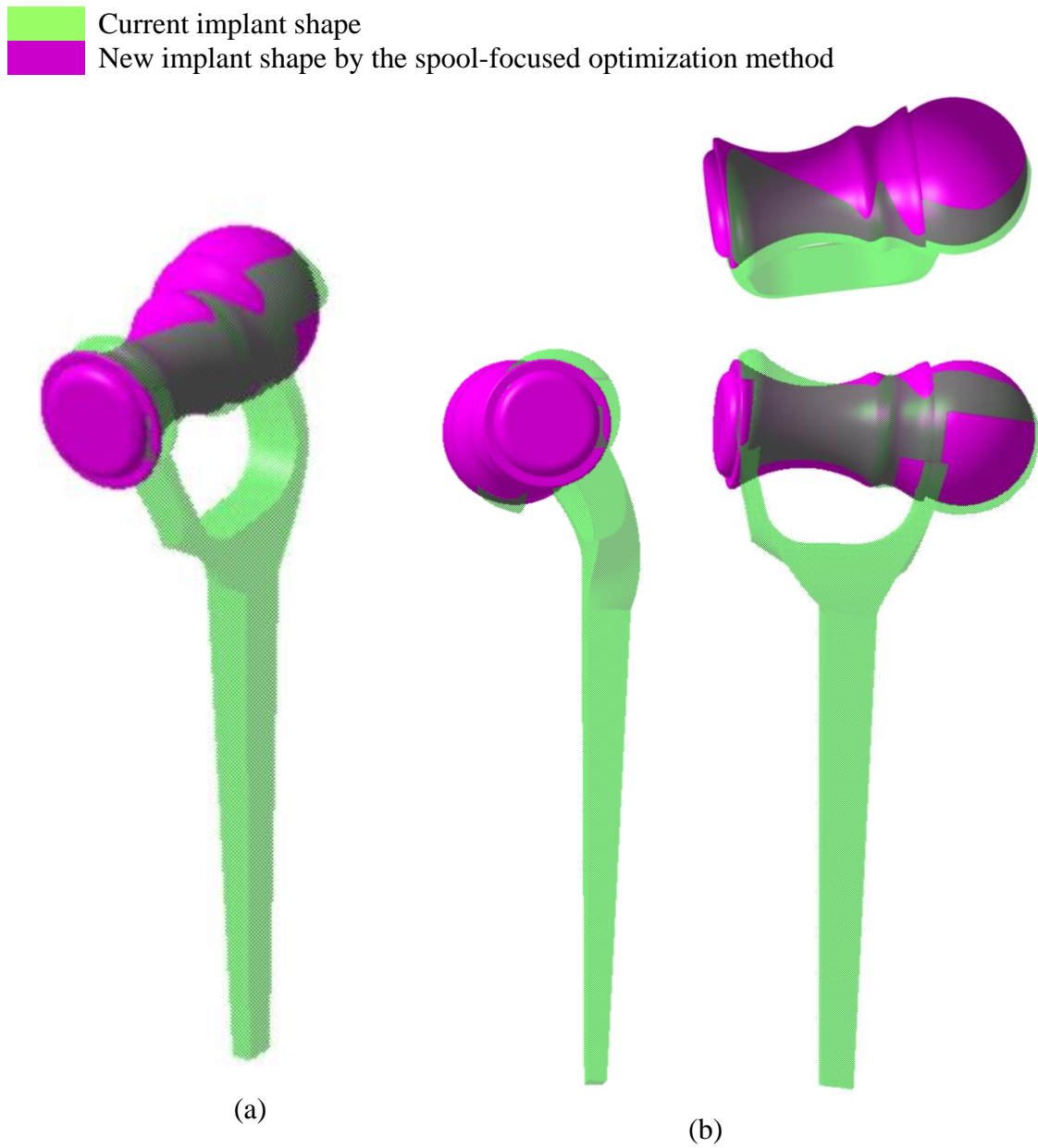


Figure 5.7: Comparison of the developed implant design in the spool-focused optimization method versus current design (green): (a) 3D view, and (b) side views of this comparison implant designs.

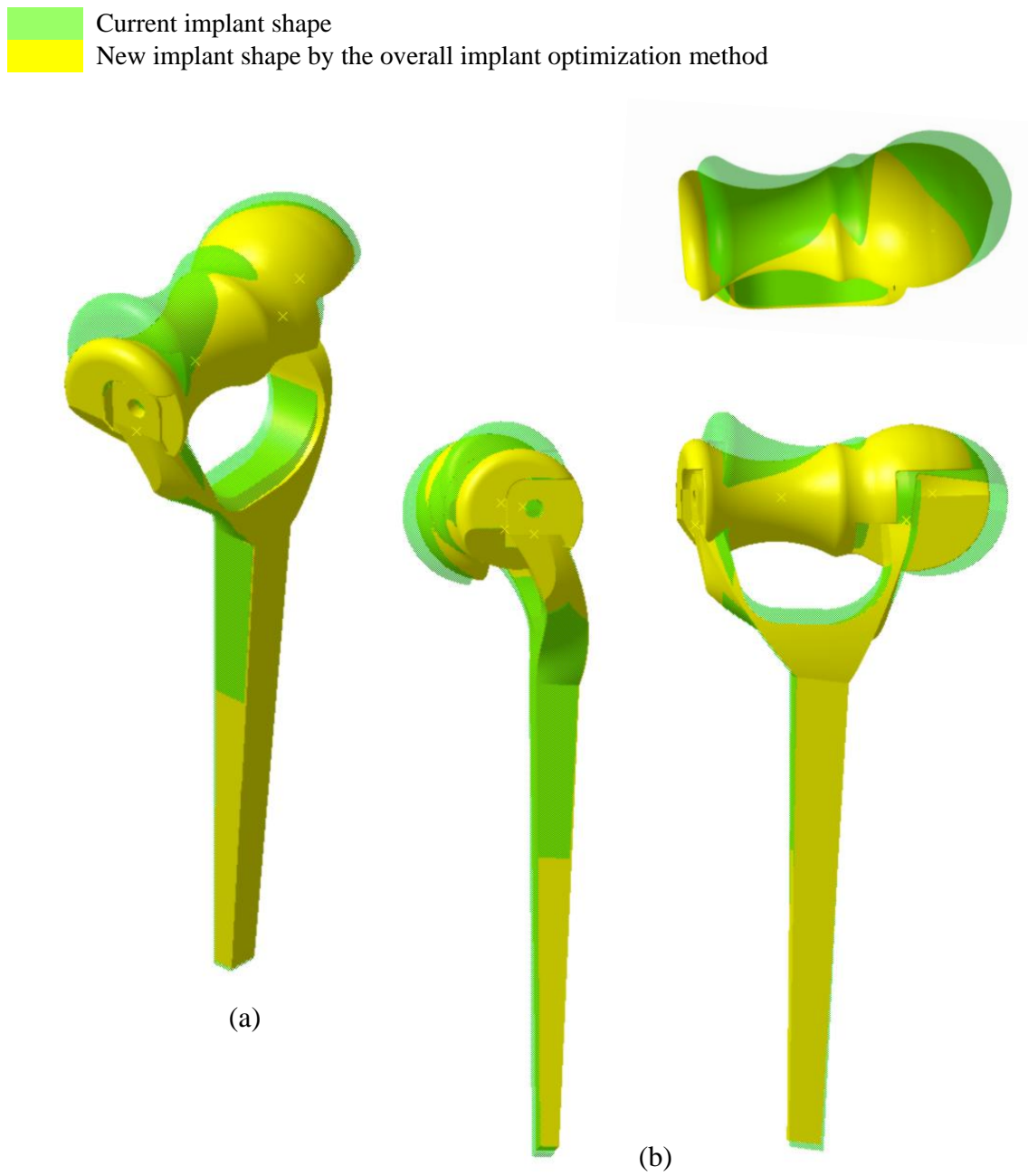


Figure 5.8: Comparison of the developed implant design in the overall implant optimization method versus current design (green): (a) 3D view, and (b) side views of this comparison implant designs.



Figure 5.9: Comparison of the developed implant design in the customized implant design method versus current design (green): (a) 3D view, and (b) side views of this comparison implant designs.

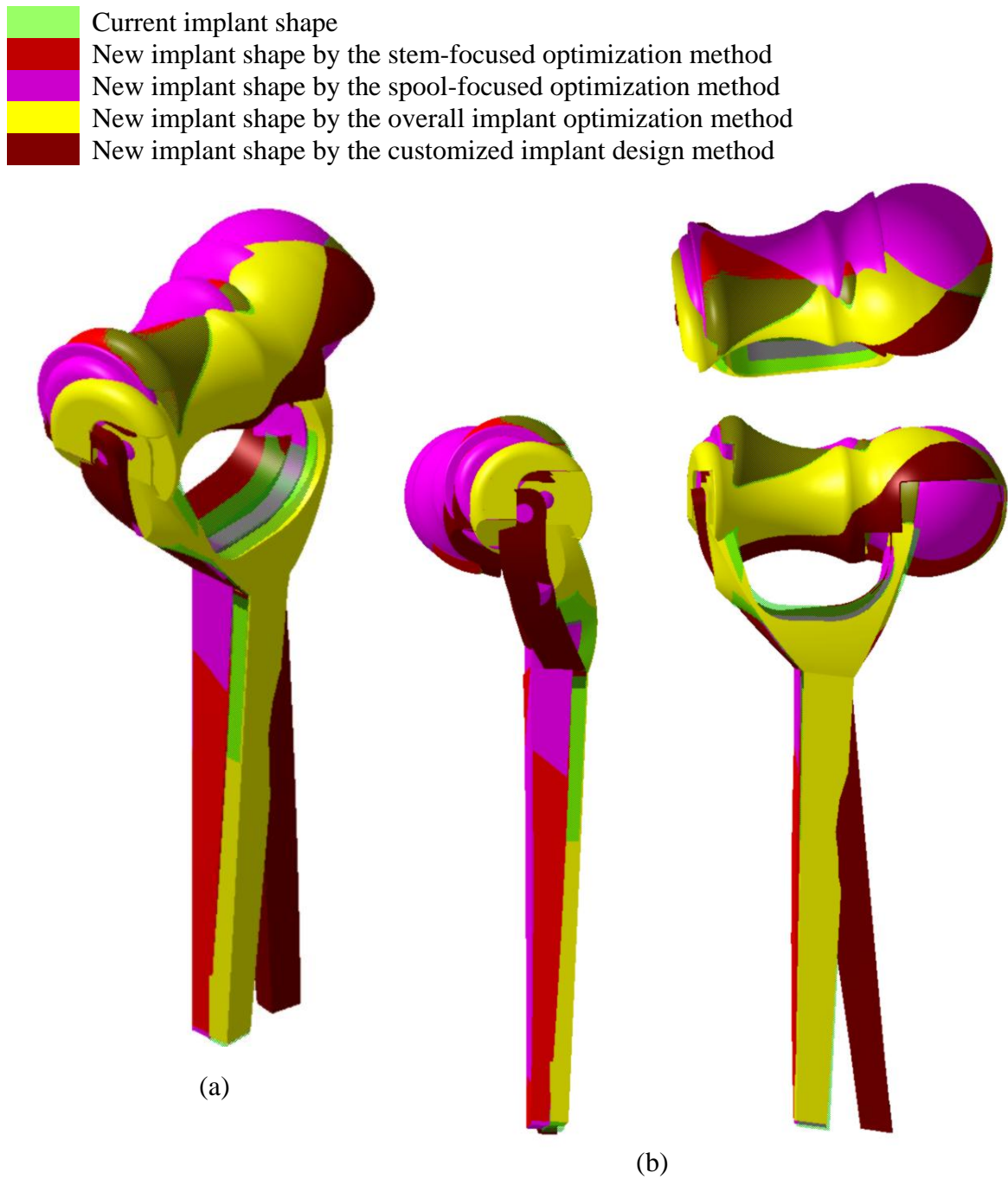


Figure 5.10: Comparison of the four developed implant designs versus current design (green): (a) 3D view, and (b) side views of the comparison of all implant designs.

For the first three methods, the first three best solutions (optimized variables) are interestingly close to each other and in the same range. This represents that the global search algorithm for these three methods and based on the variable range provided is convergent. Comparing the solutions for all the methods from Table 5.1 – 5.4 and Figure 5.6-10 shows that the optimized shape of the implant can be reached in a variety of ways for each of the humeral specimens. In the stem-focused optimization method it has been suggested that a small change in the medial- lateral and anterior-posterior offset values can improve the malalignment by 50%. Solutions of the spool-focused optimization method focus more on the change in capitellum center position rather than trochlea position and try to make the implant FE axis more compatible with the native one, especially for varus-valgus angulation. In the overall implant optimization method other than correcting the implant FE axis by prominently changing the position of the trochlea, shortening of the stem length was highly recommended, by moving the two ends of stem toward each other, in order to provide a better alignment. In the customized implant design method, the insertion axis was found to have a small angulation with the z direction normal to the cross sectional planes.

It needs to be noted here that in a broad population, the morphological characteristics of bone cavities of the distal humerus are all over the place and fitting a unique and single shape of the implant into all the canals with minimum malalignment can be problematic. However, the fact that there are a number of ways that can correct the overall shape of the implant and modify it for more efficient insertion into the bone cavity, implies that although these methods were only evaluated on one sample bone, the mitigation of all the results for a broad population of the humerus is not a hard goal to

achieve. Therefore, a final optimized shape for the implant can be reached by applying these methods on more samples, capable of fitting in all the distal humerus canals while providing a reasonable malalignment comparing to the current shape of the implant.

5.5 References

- Bugbee, W., Mizu-uchi, H., Patil, S., and D'Lima, D. (2013) Accuracy of Implant Placement Utilizing Customized Patient Instrumentation in Total Knee Arthroplasty, *Advances in Orthopedics*, 2013.
- Cil, A., An, K., and O'Driscoll, S. (2011) Custom triflange outrigger ulnar component in revision total elbow arthroplasty. *Journal of Shoulder and Elbow Surgery*, 20(2), 192-198.
- Götze, C., Steens, W., Vieth, V., Poremba, C., Claes, L., and Steinbeck, J. (2002). Primary stability in cementless femoral stems: custom-made versus conventional femoral prosthesis. *Clinical Biomechanics*, 17(4), 267-273.
- Gunther, S. B., and Lynch, T. L. (2012). Total shoulder replacement surgery with custom glenoid implants for severe bone deficiency. *Journal of Shoulder and Elbow Surgery*, 21(5), 675-684.
- Harrysson, O. L., Hosni, Y. A., and Nayfeh, J. F. (2007). Custom-designed orthopedic implants evaluated using finite element analysis of patient-specific computed tomography data: femoral-component case study. *BMC Musculoskeletal Disorders*, 8(1), 91.
- Jun, Y., and Choi, K. (2010). Design of patient-specific hip implants based on the 3D geometry of the human femur. *Advances in Engineering Software*, 41(4), 537-547.
- Lombardi Jr, A. V., Berend, K. R., Adams, J. B., White, D., Chelule, K. L., and Seedhom, B. B. (2008). Patient-specific approach in total knee arthroplasty. *Orthopedics*, 31(9), 927.
- O'Connor, M. I., and Kransdorf, M. J. (2013). Customized knee arthroplasty and the role of preoperative imaging. *American Journal of Roentgenology*, 201(3), 443-450.
- Okazaki, Y. (2012). Development trends of custom-made orthopedic implants. *Journal of Artificial Organs*, 15(1), 20-25.
- Slamin, J., and Parsley, B. (2012). Evolution of customization design for total knee arthroplasty. *Current reviews in musculoskeletal medicine*, 5(4), 290-295.
- Unwin, P. S., Cannon, S. R., Grimer, R. J., Kemp, H. B. S., Sneath, R. S., and Walker, P. S. (1996). Aseptic loosening in cemented custom-made prosthetic replacements for bone tumours of the lower limb. *Journal of Bone & Joint Surgery, British Volume*, 78(1), 5-13.

- Viceconti, M., Testi, D., Gori, R., Zannoni, C., Cappello, A., and De Lollis, A. (2001). HIDE: a new hybrid environment for the design of custom-made hip prosthesis. *Computer methods and programs in biomedicine*, 64(2), 137-144.
- Werner, A., Lechniak, Z., Skalski, K., & Kedzior, K. (2000). Design and manufacture of anatomical hip joint endoprotheses using CAD/CAM systems. *Journal of Materials Processing Technology*, 107(1), 181-186.

Chapter 6

6 Conclusion

6.1 Overview

The demand for joint replacement surgery is expected to gradually increase over the next years as a result of a growingly aging population. However, the long term success of these surgical procedures is critically dependent upon the familiarity of the surgeon with elbow anatomy, his/her experience with respect to the available options in terms of implant design as well as with his/her overall expertise with respect to implantation protocols [Sanchez-Sotelo, 2011]. Since improper implant insertions often lead to failure of the prosthetic components which in turn translate into costly revision surgeries, accurate implant design and positioning represents an issue of paramount importance in surgical joint replacement procedures. As such, careful preoperative planning becomes a key element to ensure their success, from both patient and health care provider perspectives.

The work presented in this thesis provides orthopedic surgeons with tools meant to enable them to better plan an upcoming elbow joint replacement surgery. To address this, a number of original computational techniques have been developed to determine the “insertability” of a certain implant design, to identify adequate insertion trajectories for specific implant/endosteal canal geometries or to propose patient-specific implant shapes capable to ensure superior replicas of the native kinematics of the articulation. Similar to the many other economic sectors which have benefited tremendously in the recent years from the advent of computer-assisted technologies, it is believed that the

implementation of such advanced computational/simulation tools in the current clinical practice could potentially translate into significant cost reductions for the health care system. These systems are relatively inexpensive compared to the overall costs associated with initial and revision surgeries and being exclusively in a preoperative manner – and typically outside of the operating room – they would pose a relatively small risk to the patient. Also,

This study is virtually divided into two different sections characterized by distinct approaches. The first section is primarily concerned with the assessment of the insertability in the context of a specific geometric combination between implant and endosteal canal. By contrast, the second part of the study has slightly reversed the definition of the problem in a sense that implant geometry was treated as unknown in an attempt to find means to determine an implant shape that would ensure the least amount of malalignment for a patient-specific canal configuration. This latter idea is rather inline with a growing trend in the medical field arguing that the present “one size fits all” approach taken regardless if with respect to medication or orthopaedic implants is clearly not an optimal therapeutic strategy.

For computer-assisted joint replacement surgeries, accurate representation of the endosteal cavity represents a mandatory and preliminary step towards adequate implant positioning since its stem needs to be immobilized into a bed of dense cortical bone to provide a maximized mechanical stability to the implant. A two-step approach was used for the first section of the study. During the first step, an accurate parametric-based representation of the humerus geometry was reconstructed from patient-specific CT scans and then the theoretical location of the native flexion-extension axis of the elbow was

determined by means of automatic curvature detection methods performed on capitellum and trochlea geometries. The core of the automatic reverse engineering of the bone shape consists of a global B-Spline fitting procedure based on control polygon deformation performed in such a way to ensure a minimal deviation between the fitted curve and given CT data set. In order to verify the accuracy of the proposed bone reconstruction methodology, the generated parametric representation was validated against a control dataset acquired through CMM-based measurements performed on the outer surface of the bone. Once the reconstruction of the osseous geometry was accomplished for the analyzed distal humerus, an in-depth analysis of their local curvature patterns was performed to identify the geometric centers of capitellar and trochlear landmarks involved in FE axis definition. A three-specimen validation of the proposed approach against a conventional voxel-based determination revealed that their outcomes are reasonably comparable.

The second developmental step of the initial section of the thesis was focused on devising a numerical method capable to predict whether a particular straight stem design can be inserted to an acceptable level into a particular endosteal canal of a distal humerus and if so, what would be the final malalignment to be expected between the native and prothetic FE axes. The developed numerical technique, primarily relying on genetic algorithm, was capable to establish the final implant posture based on collision detection/avoidance criteria set with respect to the two objects, all in the context of a targeted minimal malalignment between the FE axes of implant and bone. The numerical outcome of this technique was then compared to a previously devised experimental setup involving navigated implantation and the results obtained for nine different humeral

specimens have indicated that the precision of the developed insertion algorithm is comparable to that obtained through the experimental setup. The fact that no further reductions in the malalignment levels obtained through computational approaches was possible suggested that: i) the precision of the present manual insertion approaches is comparable to that yielded through automated methods and ii) lower implant malalignments can only be obtained if design changes are brought to the implant shape. However, by contrast with navigated implantation methods which are not yet easily transferrable to the operating room to the variety of invasive tracking devices required for registration purposes, the developed 3D simulation of an upcoming implant insertion procedure can be previewed by surgeons in context of patient-specific bone data.

The idea of optimal implant design was taken further in the last section of study in which all previously developed numerical techniques have been employed to propose a geometry that will ensure a minimal (possible zero) malalignment with the native FE axis but without sacrificing much (if any) of the stem length. While the obvious solution in case of an inadequate alignment between natural and prosthetic FE axes is represented by total or partial stem abutment, this constitutes in fact an undesirable path to be taken since it will decrease the contact interface between implant and bone and thereby worsens the long term outcome of the surgical joint arthroplasty procedure. The four different optimization approaches tested revealed that a broad variety of optimal solutions can be identified. Ultimately, the absolute best implant design for a certain patient will be the one that warrants a zero malalignment between native and prosthetic FE axes. However, since this might not necessarily be a cost-effective solution, the question will practically revert to the amount of modifications that could be brought to the current implant shape

and Chapter 5 has indicated that different optimums will be obtained if only the stem orientation, spool size and/or both of them will be allowed to change.

6.2 Limitations

Like many other studies in the field, the work presented in this thesis is neither annulled by unrealistic assumptions nor limitations-free. Although the results of the numerical algorithms developed can be warranted in terms of correctness and accuracy, there are a number of errors that can be anticipated to affect to a certain degree the overall precision of the developed techniques. Most of these errors are commonly encountered in reverse engineering processes involving reconstructions of the physical objects and are caused by the inherent imprecision of the approaches used to collect and then to process the scanned data.

In terms of CT data acquisition, the low intensity of the beam used for clinical purposes – which was used for all scans performed reported in this study – is known to introduce relatively large amounts of noise that typically prevent accurate segmentation of the bone contours. While arguably, more advanced/accurate scanning techniques could have been used – such as microCT - the amount of radiation involved in this case would have likely diminished the clinical relevance of the results. It is also logical to postulate that possible extrapolations of the developed techniques to patients will have to account for the difficulties associated with extraction of the relevant geometry from larger amount of data collected, an issue which was not present in the context of this work which relied exclusively on cadaveric specimens. All humeral samples were scanned by means of a special jig meant to ensure a certain degree of collinearity between the axis of the scanner

and that of the humeral shaft. However, since this particular and desirable orientation of the specimen with respect to the beam direction is difficult to obtain for a patient whose upper arms will be scanned in a different orientation. Furthermore, the inherent discrete nature of the voxelized data collected with the CT scanner combined with resolution (*e.g.* mm/pixel) of the images constituting the initial input into the reverse engineering process will contribute to further error buildup.

With respect to data processing, it is reasonable to expect that the tolerances used to control the accuracy of the B-Spline fitting process are another likely source of error affecting the precision of the digital model of the bone that in turn will translate in slight variations of the FE axis location whose end points are in fact dependent on outer bone contours. Evidently, the fitting precision can be increased by means of tighter fitting tolerances, but this will inevitably translate in more control points and thereby more undulations on the curve – especially for inner contour – possibly leading to unacceptable singularities in terms of radius of curvature of the curve.

Despite of all these errors, the validations performed against CMM data – presumably of high accuracy – have revealed fairly low differences in terms of outer bone geometry even when considering various sources of registration errors between the two datasets. However, although there are few reasons to believe that the accuracy of the inner contour would be different than the one measured for the outer contour, direct contact measurements – which is difficult to perform on convoluted and deep geometries such as that of the endosteal canal – would represent a more trustworthy verification. Along the same line of thoughts, the accuracy of the subsequent validations performed against navigated implantation methods could be challenged given that these methods are

affected by their own inherent imprecision. However, until comparison data acquired through different techniques will become available, the present study has revealed that comparable results can be expected through dissimilar methods.

6.3 Future Direction

As emphasized throughout the thesis, the position of the humeral implant into the humeral cavity represents one of the determining factors for the magnitude of the malalignment and the developed computational techniques are not only capable to predict its final value, but also the overall insertion trajectory. While – other than the associated inconveniences associated with trial and error procedures – the surgeon will almost always be capable to identify an insertion path, its prior knowledge will become of particular importance in the context of future robotic-assisted surgeries in which this information will have to be conveyed in details to the main controller.

Another possible future extension of the current work would involve the extension of the developed algorithms to other optimal design geometries, possibly involving curved rather than straight stems, as well as different cross sectional shapes. While all techniques presented in this thesis have exclusively relied on straight and rectangular stems, they could be reconsidered from a different implant design perspective. With respect to the straight stems, one of the most interesting avenues that would not require extensive efforts would involve the application of the developed techniques to a much broader population, especially since the reasoning behind the current implant design is either inexistent or covered by proprietary and thereby confidential information.

Although for the purpose of this thesis, all computational methods were assumed to be useful primarily from a preoperative planning procedure, it could be inferred that their coupling with navigated implantation would convert them into more complex simulation packages to be also used also in an intraoperative environment. However, regardless if used in an pre or intra-operative manner, better simulation capabilities would likely increase the proficiency of both novice and experienced surgeons, especially if included in their training programs. Evidently, prior to any possible extensions towards clinical applications further validations of the techniques will have to be performed.

Finally, one of the most interesting directions to be pursued in the future would be the extension of these techniques to other upper or lower articulations. While the exclusive focus of the current thesis on the elbow is fully justifiable by means of its complexity, the other joints are also interesting, especially due to their higher incidences.

To conclude, the work presented in this thesis proposes a comprehensive platform capable to predict, simulate and validate the insertion of the implant stem into the endosteal canal of the humerus. Unlike most previously developed methods addressing similar topics and typically relying on relying on oversimplified insertion trajectories/implant designs, the algorithms developed in this thesis are capable to enhance surgeon's confidence as well as precision with respect to joint replacement procedures. Owing to their versatility, these computer-assisted tools are expected to become in the future one of the essential components of surgeon's armamentarium, regardless if used in the context of "virtual previews" of an upcoming surgery or the one related to validation of the customized implant designs.

6.4 References

- Aamodt, A., Kvistad, K. A., Andersen, E., Lund-Larsen, J., Eine, J., Benum, P., and Husby, O. S. (1999). Determination of the Hounsfield value for CT-based design of custom femoral stems. *Journal of Bone & Joint Surgery, British Volume*, 81(1), 143-147.
- Laine, H. J., Kontola, K., Lehto, M. U. K., Pitkänen, M., Jarske, P., and Lindholm, T. S. (1997). Image processing for femoral endosteal anatomy detection: description and testing of a computed tomography based program. *Physics in medicine and biology*, 42(4), 673.
- McDonald, C.P., Johnson, J.A., King, J. W. and Peters, T. M. (2009a) Implant alignment in total elbow arthroplasty: conventional vs. navigated techniques. *SPIE*.
- McDonald, C. P., Peters, T. M., Johnson, J. A., and King, G. J. (2011). Stem abutment affects alignment of the humeral component in computer-assisted elbow arthroplasty. *Journal of Shoulder and Elbow Surgery*, 20(6), 891-898.
- Sanchez-Sotelo, J. (2011) Total elbow arthroplasty. *The Open Orthopaedics Journal*, 5, 115-123.
- Smith, H. W., De Smet, A. A., and Levine, E. (1982). Measurement of cortical thickness in a human cadaver femur: conventional roentgenography versus computed tomography. *Clinical orthopaedics and related research*, 169, 269-274.

Curriculum Vitae

Name: Seyed Kamaleddin Mostafavi Yazdi

EDUCATION

The University of Western Ontario, London, Ontario, Canada

Ph.D., Mechanical and Material Engineering
Jan. 2010- Apr. 2014

- NSERC CAMI Program Scholar
- Thesis Title: **Computational Techniques to Predict Orthopaedic Alignment and Fit in Bone**
- Research: Medical Imaging, Robotic Surgery, Path Planning & Haptics
- Supervisors: Prof. Jim Johnson and Prof. Remus Tutunea-Fatan
- Average: 92/100

Sharif University of Technology, Tehran, Iran

M.Sc., Mechanical Engineering
Sep.2006-Mar.2009

- Thesis Title: **Estimation of 3-D Kinematics of Joints Using Surface Registration Technique**
- Research: Navigation Systems, Registration, Medical Imaging, Kinematics
- Supervisors: Prof. Farzam Farahmand & Dr. Ali Jafari
- Average: 17.9/20

B.Sc., Mechanical Engineering

Sep. 2002-Sep. 2006

- Thesis Title: **Estimating load center in deep drawing dies using CATIA software**
- Research: Metal Forming, Deep Drawing
- Supervisors: Prof. Ahmad Assempour
- Average: 16.2/20

HONORS, AWARDS & GRANTS

- Ontario Graduate Scholarship, UWO, \$15000
2013-2014
- Graduate Research Thesis Fund, UWO, \$1500
2013
- NSERC CAMI Program Scholarship (\$10,500/y)
2010- 2014
- Western Graduate Research Scholarship (WGRS, \$10,500/y),
UWO 2010-2014

PUBLICATIONS

- **Peer-Reviewed Journal Papers**
- **Mostafavi, K.**, Tutunea-Fatan, O.R., Lalone, E., King, G.J.W, and Johnson, J.A. (2013) Determination of Elbow

Flexion-Extension Axis Based on Planar and Closed B-Splines. *Computer-Aided Design and Applications*. 10. 4: 551-565 , DOI: 10.3722/cadaps.2013.551-565

- **Mostafavi, K.**, Tutunea-Fatan, O.R., and Johnson, J.A. (2014) Efficient and Accurate Bone Geometry Reconstruction through Deformable Control Polygon Technique. submitted to *Computer-Aided Design and Applications*.
- **Mostafavi, K.**, Jafari, J., Farahmand, F., A Surface Registration Technique for Estimation of 3-D Kinematics of Joints, *Studies in Health Technology and Informatics*, 142:204-206, PMID: 19377149, 2009
- Najmaei N., **Mostafavi K.**, Shahbazi S., Azizian M., Image-Guided Techniques in Hepatic and Renal Interventions, *IJMRCAS*, 2012 Jun 27. doi: 10.1002/rcs.1443
- Rahemi, H., **Mostafavi, K.**, Esfandiarpour, F., Parnianpour, M., Shirazi-Adl, A., Review of Finite Element Model Studies in Knee Joint Biomechanics, *Modern Rehabilitation*, 2011;5(3)
- **Peer-Reviewed Conference Papers**
- **Kamal Mostafavi**, O. Remus Tutunea-Fatan, Graham J.W. King, James A. Johnson (June 26-29, 2013) Prediction of Interference Free Positions of the Humeral Implant in Preparation of Joint Replacement Procedures. *Proceedings of the ASME 2013 Summer Bioengineering Conference, SBC2013*, Sunriver, Oregon, USA, doi:10.1115/SBC2013-14606
- **Mostafavi, K.**, O. Remus Tutunea-Fatan, Emily Lalone, Graham J. W. King, James A. Johnson, Determination of Elbow Flexion-Extension Axis Based on Planar and Closed B-Splines, *USB Proceedings of CAD'12 Conference*, Jun. 2012, Niagara Falls, Canada, paper 79 (12 pages).
- **Mostafavi, K.**, Jafari, J., Farahmand, F., A surface registration technique for estimating of 3-D kinematics of joints, *The 17th Annual Medicine Meets Virtual Reality 17 (MMVR17) conference*, Long Beach, CA, USA, Jan 19-22, 2009.
- **University of Western Ontario**
- **Teaching Assistant**, Faculty of Engineering
Jan. 2010 – Apr. 2014
- Summer Academy Course
Summer 2012

ACADEMIC EXPERIENCES

- MME4480A, Computer Aided Design
Jan. 2011- Apr. 2014
- MME4459A CNC Machining,
Sep. 2010- Dec. 2013
- **Research Assistant**, Implant Insertion Simulation
Jan. 2010 – Apr. 2014
- **Sharif University of Technology**
- **Teaching Assistant**, Faculty of Engineering
Sep. 2006 – Sep. 2009
 - Die Design
spring 2006, 2007 & 2008
 - CAD/CAM
fall 2007
 - Advance Engineering Mathematics
winter 2008
- **Lab Assistant**, “Solid Mechanics” lab
spring 2006, spring & fall 2007
- **Instructor**
 - CATIA software
2005, 2006, 2007 & 2008
 - Mechanical Desktop software
spring 2006
 - Autocad software
2006-2007
- **Tehran Institute of Technology**
- **Instructor**, CATIA Software
Sep. 2007-Sep. 2009
- **Imam Hossein University**
- **Instructor**, Autocad Software
Sep. 2005-May 2006
- **Tehran University**
- **Instructor**, Stress Analysis in Dental Implants
Sep. 2007-Jan. 2008

PROFESSIONAL EXPERIENCES

- Mechanical Designer, Whilliams and White Co.,
Burnaby, Canada Apr.2013- Sep. 2013
- Senior Technical Engineer, Delta Co., Iran
Apr. 2009-Dec. 2009
- Senior Mechanical Engineer, Roshdsanaat Co., Iran
Jun. 2009- Sep. 2009
- Project Manager, Incubation Center of Pars Khodro Co., Iran
Jan. 2009-Dec. 2009

- Technical Manager, Incubation Center
Sep. 2006 - Dec. 2008
for Medical Equipments and Devices, Iran
- Project Manager, Studies Center of Sharif University of
Technology Sep. 2006 – Sep. 2008
- Project Manager, NAB Co., Iran
Apr. 2005 - Jan. 2006
- Junior Design Engineer, Niroo Studies Center, Iran
Jan. 2005- Jan. 2006
- Project Manager, Jahad Keshavarzi Center, Iran
Sep. 2004- Sep. 2005

**OTHER
ACADEMIC
ACTIVITIES**

- Global Student Advisor (GSA) of MITACS
Summer 2012
- Co-Chair of the 6th Annual Canadian Student Conference on
Biomedical Computing and Engineering,
2010-2011
- Elected as Scholarship Committee Member of GTA Union,
UWO Winter 2011
- Reviewer of the 6th Annual Canadian Student Conference on
Biomedical Computing and Engineering
2010-2011
- Lab Manual Designer and Coordinator, UWO
Fall 2011
- Member of Mechanical Engineering Department seminars
committee 2012
- Head of Electrical Car team, Sharif University of Technology
2007
- Workshop Lecturer on Pneumatics & Hydraulics, ISME
Conference, Iran 2003
- Member of Nameh Mechanic Magazine, the head of several
sections, Iran 2004-2007
- Providing an article on CATIA Software Manual, Nameh
Mechanic Magazine, Iran 2005

**OTHER
PROFESSIONAL
& COMMUNITY
ACTIVITIES**

- Elected as SOGS (Society Of Graduate Students) Councilor,
UWO Sep. 2010- Sep. 2012
- Elected as SOGS Councilor, UWO
Sep. 2011- Sep. 2012
- Elected as GTA (Graduate Teaching Assistant) Union
steward, UWO Sep. 2010- Sep 2011
- Member of ISLO (a Non-Profit Organization) radio group
performing in CHRW radio, University of Western Ontario
Sep. 2010- Sep 2011
- Organizer of ISLO philosophy committee
Sep. 2010- Sep 2011
- Selected as Food Committee member of GTA Union, UWO
Sep. 2010-Sep. 2011